Multi-scale remote sensing to characterize crustal faulting in the northern Pacific Cordillera

by

Guy William Salomon
MSc, University of Cape Town, 2019
BSc Honours, University of Cape Town, 2017
BSc, University of Cape Town, 2016

A Dissertation Submitted in Partial Fulfillment of the
Requirements for the Degree of

DOCTOR OF PHILOSOPHY

in the School of Earth and Ocean Sciences

We acknowledge and respect the Lək´ʷəŋən (Songhees and Xʷsepsəm/Esquimalt) Peoples on whose traditional territory the university stands, and the Lək´ʷəŋən and W̱SÁNEĆ Peoples whose historical relationships with the land continue to this day.

Multi-scale remote sensing to characterize crustal faulting in the northern Pacific Cordillera

by

Guy William Salomon
MSc, University of Cape Town, 2019
BSc Honours, University of Cape Town, 2017
BSc, University of Cape Town, 2016

Supervisory Committee

Dr. Edwin Nissen, Supervisor
School of Earth and Ocean Sciences

Dr. Lucinda Leonard, Departmental Member
School of Earth and Ocean Sciences

Dr. Andrew Schaeffer, Departmental Member
School of Earth and Ocean Sciences

Dr. Eva Kwoll, Outside Member
Department of Geography

Abstract

Crustal earthquakes pose significant hazard to people all around the world, and because these events occur infrequently, relative to interplate earthquakes, they remain poorly understood. This dissertation is composed of three projects which share common themes of characterizing the geometries, kinematics, and activity of crustal faults within the northern Pacific Cordillera by making use of remote sensing techniques, albeit at several spatial scales. This region is vast with limited access which makes traditional, boots-on-the-ground fieldwork challenging and expensive. Remote sensing allows us to gather significant insights into the region from afar and focus, or motivate, future research. I begin by using InSAR and seismological analyses to study a recent earthquake within the Koryak Highlands of eastern Siberia. This is one of the most northerly earthquakes to be studied using InSAR, with additional challenges of steep terrain and snow cover; these issues were overcome by the short revisit times offered by the Sentinel-1 satellites. Understanding this event has implications for seismic hazard assessment in other parts of the cordillera, such as Alaska and western Canada which have similar crustal structures. This study highlights that previously unknown, immature faults within known suture zones can produce moderate to large earthquakes. In the second project, I describe a novel uncrewed aerial vehicle (UAV) laser scanning (ULS) platform which can be used to collect inexpensive, high-resolution topography even beneath dense vegetation. I showcase four datasets collected by this platform, across several different landscapes and vegetation types in western Canada, comparing these with conventional airborne laser scanning (ALS) and Structure-from-Motion (SfM) datasets. The ULS offers improved point density and vegetation penetration compared to ALS and SfM, creating high-resolution topographic models and allowing fine-scaled features to be identified. It also offers opportunities for rapidly collecting perishable data such as along surface ruptures of recent earthquakes and potentially could be used to capture afterslip. The last project uses ALS and ULS, as well as near-surface geophysics and field observations, to investigate whether the San Juan fault on southern Vancouver Island has been active during the Quaternary. I find a 6 km long, 30 m high scarp cutting across glacial sediments. The up-thrown southern side being composed of rheologically weaker schists and volcanics, leads me to infer that the fault has been recently active in order to have generated this feature, and that this scarp likely represents many earthquake cycles. I also find an uphill-facing scarp offsetting colluvium, which may represent the most recent rupture (late Quaternary) along the San Juan fault. Several potential targets for future paleoseismic studies are identified. In all, these works demonstrate the importance of a multi-disciplinary approach when studying active tectonics, and highlight the usefulness of remote sensing techniques for initial observations of continental deformation.

Table of Contents

List of Tables

List of Figures

Acknowledgements

There are a lot of people I'd like to thank for their roles over the last five years. There were times when I seriously reconsidered why I had moved to the other side of the planet, but thanks to many of the people on this page I have many happy memories and would not have done things any other way.

Firstly, I'd like to thank my supervisor, Edwin Nissen, for his support, suggestions, enabling countless opportunities, and for his unfailing positive attitude. Beyond research interests, we also share a number of interests outside of academics, which has made working with Ed an absolute pleasure. I'm also grateful for my committee members, Lucinda Leonard, Andrew Schaeffer, and Eva Kwoll for their support and constructive feedback throughout this degree. I'd like to thank the TEARs group, as well as the PGC group, for all the shared meals, birthday 'quakes', coffees, and excellent conversations. It has been such a pleasure to be a part of a large group with similar research interests. In particular, I'd like to thank Theron Finley. Thank you for your positive attitude, your keen eye (in manuscripts and in the field), and for introducing me to so many good artists on long drives to and from fieldwork. Many thanks go to Roger Stephen, for painstakingly providing technical explanations of drones, GNSS, lidar, and processing workflows. I'm not sure if we would have gotten the drone working without Roger.

To my friends, Chad, Sejal, Wayne, Saif, Lorena, and Farhaan. Thank you for all the laughs, deep talks, shared frustrations, and games. Despite being separated by vast distances and annoying time zones you were always around, and for that I feel particularly lucky. Thank you Jo for always organizing trips and adventures around the island. I owe a great deal of gratitude to Kate and Ian Reston, whose home I lived in for over two years, and who I now think of as my Canadian family. You welcomed me in, just at the beginning of the pandemic, and for that I am forever grateful. Thank you for all the shared meals, laughs, debates, stories, furry friends, paddles, ski trips, and for introducing me to ice skating.

I would like to thank my family for loving and supporting me throughout my studies. Thank you Opie, for teaching me to be critical and question the world around me.

Finally, thank you Kirsten for coming into my life at just the right time. Thank you for all the love, support, and encouragement, especially throughout the last year.

Chapter 1
Introduction

Along the Cascadia subduction zone (from Vancouver Island, British Columbia to northern California), many people are aware that the region experiences megathrust earthquakes, which occur on the oceanic–continental plate interface within subduction zones. While these events can be very large and damaging, they are not the only significant earthquake hazard within the region. In fact, crustal faulting earthquakes (which in this dissertation include those that occur within the overriding continental plate of a subduction zone) may be more hazardous as they can occur on faults that are closer to cities and towns. There are numerous challenges to studying crustal faults; for one, many crustal faults accumulate strain slowly and only rupture in large earthquakes once every few thousand years. Lower magnitude seismicity may not be sufficiently concentrated to delineate active faults, as immature and slowly deforming faults can be associated with minor, mostly off-fault earthquakes. Geodetic measurements struggle to identify active faults in Cascadia where elastic deformation due to locking of the subduction interface overrides smaller signals from other types of crustal deformation. As large crustal earthquakes within the instrumental and historical records are relatively infrequent within northern Cascadia, I expand my study area to that of the northern Pacific Cordillera, a section of the circum-Pacific orogenic belt which has experienced broadly similar tectonic histories of subduction and terrane accretion to that of Cascadia. As such, lessons learned about the tectonics of this region can be used as analogues for similar scenarios within northern Cascadia. Remote sensing techniques allow us to observe the Earth's surface, and study landforms that were generated over the course of multiple earthquake cycles, allowing us to extend our knowledge of a region's seismicity well beyond that of instrumental and historic records. These observations provide an excellent first pass of a region, which, once the key features within have been identified, can be targets for follow-up investigation with geophysical techniques, and field observations. This multi-disciplinary approach is essential to provide a better understanding of fault systems in deforming continental regions.

1.1 Structure of this dissertation

This dissertation includes three projects, each formatted as a stand-alone journal manuscript. The aim of this thesis is to explore continental deformation through different lenses. I use a combination of remote sensing, seismology, field observations, and near-surface geophysics to investigate crustal deformation in the northern Pacific Cordillera at various scales (both spatial and temporal). While each of the chapters contain different research questions and techniques, they all fall under this theme. Short methodological descriptions are given within each chapter for each new technique; including InSAR, body-waveform modelling, back projections, multi-event hypocentre relocations, lidar collection/processing, electrical resistivity tomography, and Schmidt hammer measurements.

Two of the manuscripts (Chapter 2 & 3) have been peer-reviewed and published. The details of each publication can be found at the beginning of the respective chapter. Chapter 4 was submitted to *Seismica*, the Cascadia Subduction Zone Special Issue, at the end of March 2025. Below, I summarize the remaining chapters of this dissertation:

The remainder of **Chapter 1** provides an introduction to the northern Pacific Cordillera and its tectonic history as well as some background about the remote sensing techniques used in the subsequent chapters.

Chapter 2 is a detailed investigation into the 2020 M_w 6.4 Koryak Highlands earthquake, the largest event to have been recorded in this remote, poorly studied region. This is also one of the most northerly earthquakes to have been studied using InSAR, a particularly challenging case as the earthquake occurred in the mountains in mid-winter, with snow on the ground. Fortunately, the short revisit times of the Sentinel-1 satellites allowed for these challenges to be overcome. I use InSAR, elastic dislocation modelling, a teleseismic back-projection, calibrated hypocentre relocations and teleseismic moment tensor solutions to resolve the rupture of an immature, left-lateral fault striking NW–SE. I find that the fault likely ruptured unilaterally northwestwards, and estimate the seismogenic thickness for this area. This earthquake highlights how terrane boundaries within cordilleran belts can accommodate strain long after accretion, resulting in significant earthquakes even along hidden faults.

In **Chapter 3**, I present a new uncrewed aerial vehicle (UAV) laser scanning system that was developed to study landforms created by earthquakes. The platform, data acquisition and processing workflows are described, providing a practical guide for other researchers interested in developing their own systems. I then present four case studies along faults from a variety of terrain and vegetation types, located across the Canadian Cordillera, comparing our drone lidar with that of conventional airborne lidar and Structure-from-Motion datasets. The drone lidar is able to produce sub-metre digital terrain models, and offers improved vegetation penetration over the conventional methods, allowing for improved identification of fine-scale tectonic landforms.

Chapter 4 is an investigation into whether the San Juan fault on southern Vancouver Island has been active within the Quaternary. Recently acquired airborne and drone lidar reveals a linear set of scarps along the fault trace. Measurements of vertical separation along these scarps are obtained, as are Schmidt hammer measurements, to determine whether these features could be the result of differential weathering. Electric resistivity tomography is used to image the subsurface of one uphill-facing scarp, revealing an offset within the conductivity structure, evidence of seismogenic origin. Our results strongly motivate future paleoseismic investigations, which would be necessary to establish a long-term slip rate for incorporation into seismic hazard models.

In addition to the conclusions at the end of each chapter, I also include some final, more general, concluding remarks in **Chapter 5**.

I have had the opportunity throughout my PhD to collaborate with other students and researchers. While the following works are not a part of this dissertation, they have provided me with opportunities to expand and refine my skill set, observe and interact with experts in their field, and gain insights into other fault systems and tectonic settings. Muir et al. (2023) and Salomon et al. (2022) are works related to my Masters degree, and gave me experience in mapping tectonic geomorphology. Also related to seismicity in Namibia, I learned how to process InSAR time series to study some of Namibia's largest instrumented earthquakes for Angombe et al. (2025). Back on Vancouver Island, I had the opportunity to assist with the paleoseismic trench described in Harrichhausen et al. (2023), where I gained experience in logging trench walls, creating orthophotos and collecting radiocarbon samples. Finley et al. (2022a) details some of the research group's first data collections with our lidar drone. These datasets, and others collected during subsequent field trips to the Yukon, have allowed us to characterize two active fault systems, described in Finley et al. (2025a,b). In addition to drone lidar collections, fieldwork in the Yukon included making field observations, structural measurements, optically stimulated luminescence sampling, and radiocarbon sampling. These projects have taught me a lot about cordilleran tectonics, the geomorphology of strike slip faults, and the challenges associated with tectonic geomorphology in glaciated landscapes.

1.2 The northern Pacific Cordillera

The northern Pacific Cordillera is comprised of a section of the circum-Pacific orogenic belt where the oceanic Pacific plate, and the smaller Juan de Fuca plate, are being subducted below that of the continental North American plate. Starting in the eastern hemisphere, this region begins at the tectonic triple point of the North American, Eurasian and Pacific plates off the Kamchatka Peninsula in Siberia, and stretches across the Aleutians, along the Alaska and British Columbia coastlines, and down to northern California at the southernmost extent of the Juan de Fuca plate (Figure 1.1). The regions that comprise the northern

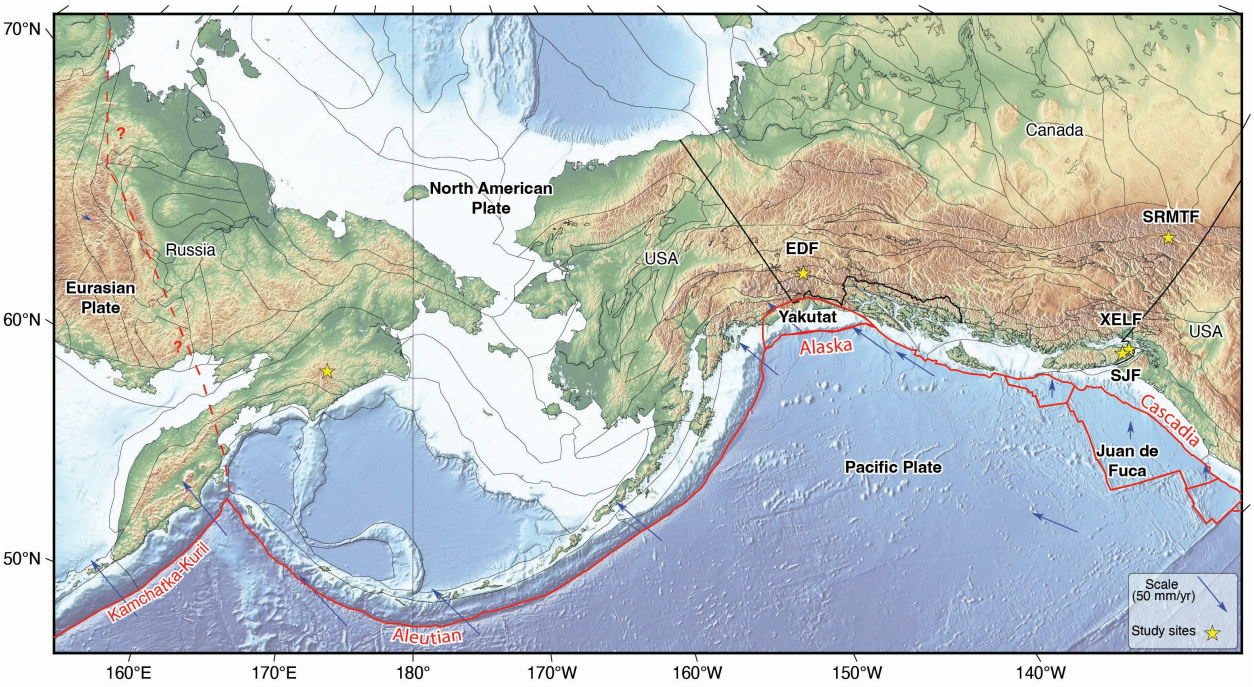

Figure 1.1: The north Pacific Cordillera; thin black lines show terrane boundaries from Hasterok et al. (2022), bold black lines are international borders, and yellow stars mark study locations in this dissertation. Blue vectors are ITRF2020 (Altamimi et al., 2023) plate velocities relative to a fixed North American plate. Topography is SRTM15+ (Tozer et al., 2019). Study sites include the EDF – Eastern Denali Fault, KH – Koryak Highlands, SJF – San Juan Fault, SRMTF – Southern Rocky Mountain Trench Fault, and XELF – XEOLXELEK–Elk Lake Fault.

Pacific Cordillera have experienced similar tectonic histories of deformation, terrane accretion of island arc systems, magmatism, and batholith emplacement (Dickinson, 2004; Miller et al., 2002), albeit the timing of these events varies along its extent.

This region is home to several large subduction zones, including Kamchatka–Kuril, Alaska–Aleutian and Cascadia, all capable of rupturing in megathrust earthquakes of greater than M 8 (Bilek and Lay, 2018; Satake et al., 1996); additionally, the forearcs of the subduction zones are also actively deforming and crustal faults within them can produce large damaging earthquakes (Bai et al., 2017; Hata et al., 2016; Morell et al., 2018). Many of the continental crustal earthquakes along this margin are associated with terrane boundaries (black lines in Figure 1.1) along which allochthonous blocks were accreted onto North America during the Mesozoic and early Cenozoic. This suggests that these first-order geological boundaries form long-lasting zones of weakness which are capable of reactivating from the accumulation of stresses within the crust. As such, the seismic hazard of these areas remains elevated long after terrane accretion.

1.2.1 Tectonic background

The northern part of the Pacific plate is currently moving to the northwest at a rate of 6–9 cm/yr (Figure 1.1, ITRF2020, relative to a stable North America (Altamimi et al., 2023)). This motion causes the plate to subduct beneath the North American plate along the Kamchatka Peninsula and the Alaska-Aleutian arc. In the Gulf of Alaska, the Yakutat microplate is moving north-northwest at approximately 5 cm/yr, partially subducting beneath and partially colliding with North America. Just offshore of Sitka, Alaska the Pacific plate is once again in contact with the North American plate, although here the margin is transform, a right-lateral strike-slip fault (Queen Charlotte fault) similar to that of the San Andreas fault in California. In Cascadia, from northern Vancouver Island to Cape Mendocino, California, the Juan de Fuca plate is moving east-northeast at a rate of ∼4 cm/yr, subducting beneath the North American plate.

The Koryak Highlands, the study site of Chapter 2, is an amalgamation of mountain ranges in eastern Siberia. Located in the westernmost part of the north Pacific Cordillera, and north of the diffuse triple junction with the Eurasian and Pacific plates, the active tectonics of this area are poorly understood. The Highlands were created by the accretion of the following terranes to the North American plate: the Khatyrka terrane (Upper Jurassic–Early Cretaceous), the Central Koryak terrane (Upper Jurassic—Larly Cretaceous volcanic and sedimentary rocks), and the Olyurtusky island arc (Late Cretaceous cherty and volcanic sequences, Chekhovich et al., 2008). The suture zones between these terranes form NE-trending topographic lineaments, such as the Khatyrka-Vyvenka zone and the Vatyna–Vyvenka thrust (Chekhovich et al., 2008; Imaeva et al., 2017).

The Canadian Cordillera, the study region for Chapter 3, is located on the western coast of Canada and is composed of five morphological belts, from east to west: the Foreland, Omineca, Intermontane, Coast, and Insular belts. Each of these domains has a unique geology and tectonic history, beginning with the breakup of Rodinia approximately 750 million years ago (Monger and Price, 2002). The majority of the Cordillera is made up of Paleozoic to Mesozoic magmatic arcs, microcontinents and ocean basins that accreted to western Laurentia during the Mesozoic and Cenozoic (Nelson et al., 2007).

Vancouver Island, the tectonic setting for Chapter 4, is within the Insular belt. On southern Vancouver Island, there are three distinct geologic terranes. The Wrangellia terrane is composed of Paleozoic (370 Ma – 185 Ma) island arc-related volcanics and sediments, overlain by Triassic ocean island basalts and marine sediments (Monger, 1977). Wrangellia was accreted onto North America during the late Cretaceous, creating a forearc basin into which the Nanaimo Group sediments were deposited between 85 Ma and 65 Ma (England and Calon, 1991). The Pacific Rim terrane, Jurassic to Paleocene metamorphosed sediments and volcanics, was accreted to North America along the San Juan and Survey Mountain faults from the Late Cretaceous to Eocene (Brandon, 1989; Rusmore and Cowan, 1985). Geological maps show that these faults have accommodated 60 km of left-lateral slip. Most

recently, Siletzia (also known as the Crescent terrane), composed of ocean island basalts, was accreted onto North America along the Leech River fault during the Eocene (England and Calon, 1991; Groome et al., 2003). The Carmanah Group, composed of marine sediments, was deposited on the outboard of accreted terranes (today the west coast of Vancouver Island) around 24 Ma (Monger, 1977; Muller, 1977; Rusmore and Cowan, 1985).

1.2.2 Challenges

There are several challenges to studying active tectonics and crustal faulting within the northern Pacific Cordillera. For one, assessing the hazard posed by crustal faults can be a challenge because many crustal faults within the region have low levels of historical seismicity (Balfour et al., 2011) and long recurrence intervals due to slow loading rates (Li et al., 2018). In areas outside of Cascadia and southern Alaska, this problem is exacerbated by sparse seismic instrumentation. Another challenge is that tectonic landforms may have been eroded by glacial action during the Pleistocene. Much of the Canadian Cordillera was glaciated during the last glacial maximum (Clague and James, 2002), as were parts of eastern Siberia (Glushkova, 2011). Similarly, the north Pacific Cordillera experiences high rates of precipitation, which may be responsible for removing fault related geomorphology, especially the landforms generated by strike-slip faults (channel offsets, etc., Reitman et al., 2022). Finally, much of the region is characterized by rugged topography and is often covered by dense vegetation which may obscure fault-related geomorphic features.

As a result of the challenges discussed above, identifying active faults within the north Pacific Cordillera, and characterizing their geometries and kinematics, remains an ongoing research objective. As much of the region is not easily accessible, traditional boots-on-the-ground research can become prohibitively expensive. By utilizing advances in seismology, geodesy and remote sensing we can continue to improve our understanding of crustal faults, their locations and behaviours within this region, over a range of different spatial scales — from regional studies of surface deformation all the way down to sub-metre cracks.

1.3 Remote sensing

Remote sensing involves acquiring information about a target without making physical contact with it. It is used throughout the Earth Sciences (e.g. geology, geophysics, geography, hydrology) for a multitude of applications including: land use mapping, weather forecasting, disaster management and collecting high-resolution topography. The field can be split into "active" and "passive" remote sensing. In the active case, energy is emitted by the instrument, and the reflection of that energy is measured. In passive remote sensing, sensors gather energy emitted or reflected by their target. Over the last three decades, remote sensing methods have become an increasingly useful way to study natural hazards such as earthquakes, floods, landslides, and volcanoes (Tralli et al., 2005). These data can easily

be integrated with seismic and geodetic monitoring as well as numerical modelling to better understand Earth system processes (e.g. the earthquake cycle).

There are several different acquisition methods for collecting remote sensing data, from satellite-based observations, crewed aircraft, and increasingly, uncrewed aerial vehicles (UAVs, or drones). Each of these platforms collects data at unique spatial scales and resolutions, which are discussed in the following sections. Due to the dense vegetation present throughout much of the northern Pacific Cordillera, photogrammetry is not often viable. As such, in this dissertation I primarily make use of two remote sensing techniques, interferometric synthetic aperture radar (InSAR) and light detecting and ranging (lidar), both of which are capable of penetrating vegetation.

1.3.1 InSAR

Synthetic Aperture Radar (SAR) is an active form of remote sensing used to produce high-resolution images of the Earth's surface, usually from right-looking satellites in sun-synchronous low Earth orbits (600–800 km). These satellites use side-looking radio detection and ranging (radar) antennae, illuminating the Earth below with microwave radiation (usually between 1 mm and 30 cm wavelengths) and recording the back-scattered energy (Rosen et al., 2000). The wavelengths used by SAR satellites were chosen as they can penetrate clouds and water vapour with minor path delays, allowing for observations to be made in any weather. As the technique is active source, data can be collected regardless of the time of day or night, although orbits are often optimized to be sun-synchronous, allowing the satellite's solar panels to be illuminated as much as possible. SAR data are incredibly versatile, and are broadly used for Earth surface studies. This technology allows us to detect surface deformation over large, regional areas (Sentinel-1 swath width is 250 km) regardless of accessibility.

The images collected by SAR satellites include two components; the amplitude, and the phase. The amplitude is a function of the surface roughness, and indicates the amount of energy that has returned to the sensor, while the phase for a single image is essentially random. Interferometric synthetic aperture radar (InSAR) refers to the differencing of phase data from SAR images collected at approximately the same location but at different times (Figure 1.2). The resultant image contains a map of phase changes across the imaged area, known as an interferogram. The phase can be affected by several factors including: slight differences in orbital path; perspective effect of topography; atmospheric delays (in both images); changes to the back-scattering abilities for each pixel; and surface deformation. As we are interested in the surface deformation, the other factors need to be accounted for during the preprocessing phase. This includes removing orbital ramps, and removing the effect of topography by subtracting a digital elevation model (DEM) from the image. The remaining phase differences appear as fringes (colour cycles) of deformation. Each fringe represents a contour of one half wavelength of line-of-sight (LOS) deformation, either towards

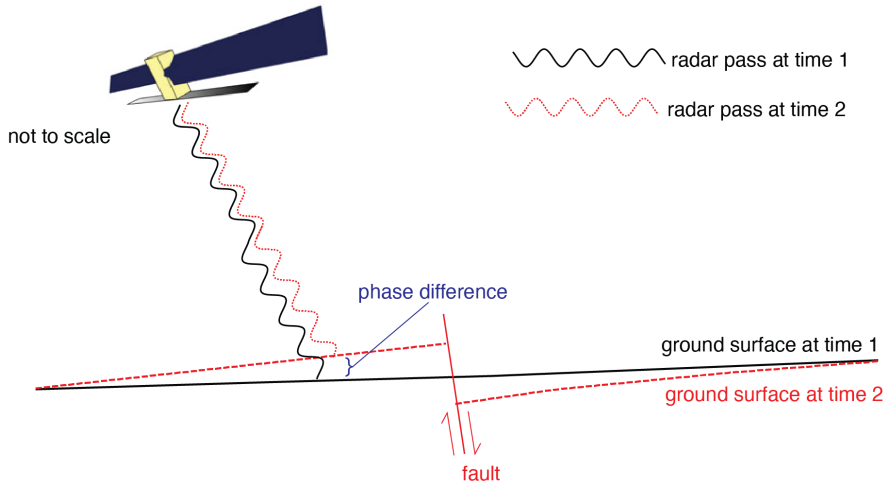

Figure 1.2: Measuring surface movement with InSAR, adapted from Biggs and Wright (2020). An orbiting satellite sends a coherent radar signal to the surface and measures the backscattered radiation. The phase difference (position in the wave cycle) between the signals returning at two different times (time 1 in black and time 2 in red) can be used to estimate ground movement caused by a range of mechanisms.

or away from the satellite. The total LOS displacement can be added up during a process called phase unwrapping. There are several sources of noise introduced to all interferograms, some of which are exacerbated by the environment, such as where there is steep topography and shadowed slopes (not facing the radar illumination) that may cause decorrelation (Lee and Liu, 2001). Areas that experience seasonal snow cover and ground freeze-thaw cycles undergo changes to the surfaces' ability to backscatter energy causing decorrelation (Wang et al., 2020), as do areas that have dense and rapidly growing vegetation (Ebmeier et al., 2013). However, recent SAR satellites like the Sentinel-1 pair offer shorter revisit times, and novel techniques to isolate signal from potential sources of noise have led to improved performance in challenging regions, such as the northern Pacific Cordillera.

InSAR was first used to study the 1992 Landers, California earthquake (Massonnet et al., 1993), and today is one of the prevalent techniques for mapping deformation associated with moderate to large (M_w>5.5) continental earthquakes (Elliott et al., 2016). There are now several SAR satellites (including; Sentinel-1, RadarSAT, ALOS-2 among others) that routinely monitor the Earth and achieve sub-millimetre accuracies allowing us to better understand how the Earth deforms. The surface deformation of more than 130 earthquakes have been mapped using InSAR, helping to constrain detailed models of fault slip and confirming that the Earth does behave like an elastic solid (Biggs and Wright, 2020). One surprising observation from many of these studies is that the faults which slipped during the earthquake are often hidden or not known to be active (e.g. Gaudreau et al., 2019; Sethanant et al., 2023). Another observation is that InSAR deformation maps have highlighted the location

uncertainty within seismic catalogues (Ghayournajarkar and Fukushima, 2022), and can be used to calibrate event relocations.

1.3.2 Lidar

Light detection and ranging (lidar) is another active remote sensing technique and is an immensely useful method of collecting high resolution topography. In this method, the return times of reflected laser pulses (Figure 1.3a) are combined with information on the location and orientation of the laser scanner to produce a dense point cloud containing the Cartesian (x, y, and z) co-ordinates of a geographic target (Glennie et al., 2013; Xiaoye Liu, 2008). The point clouds produced can have sub-metre point spacings, finer than the 2–10 m pixel dimensions typical of modern satellite derived DEMs (e.g. Hodge et al., 2019; Morin et al., 2016; Wang et al., 2019). Furthermore, since multiple returns can be distinguished from the same outgoing laser pulse, returns within the vegetation canopy can be filtered out (Figure 1.3b) to produce a bare Earth digital terrain model (DTM). This unique attribute of lidar remote sensing has allowed it to become the common mode of high resolution topography collection across many geospatial fields. Lidar is especially useful in northern Cascadia, where widespread forest cover may otherwise obscure fault scarps or other fault-related landforms (e.g. Harrichhausen et al., 2021; Haugerud et al., 2003; Hunter et al., 2011; Johnson et al., 2018; Morell et al., 2017; Nelson et al., 2017; Schermer et al., 2021; Witter et al., 2021).

There are typically two established methods of collecting lidar data, and one emerging method, which is the focus of Chapter 3 (Figure 1.3c). In Terrestrial Laser Scanning (TLS), landscapes are mapped from a laser scanner mounted to a tripod (Telling et al., 2017). TLS can achieve very dense point clouds with up to several thousands of points per square metre (pts/m^2), but to avoid shadowing of features of interest behind objects like tree trunks or undulating topography, the scanner typically needs to be deployed from several locations. As each location change and scan takes considerable time, TLS surveys are best suited for relatively small-scale outcrop or landform acquisitions (e.g. Bubeck et al., 2015; DeLong et al., 2015; Gold et al., 2013; Haddad et al., 2012; Jones et al., 2009; Wedmore et al., 2019; Wiatr et al., 2013). The second, more prevalent method of lidar data collection is Airborne Laser Scanning (ALS), where the laser scanner is mounted to a crewed aircraft and flown over the target area. This method is suitable for collecting much larger areal datasets, typically 1–2 km wide swaths that can extend for tens to hundreds of kilometres along linear targets, such as fault lines, coastlines, or infrastructure corridors (Clark et al., 2017; Johnson et al., 2018; Langridge et al., 2014). The point clouds generated by ALS are lower density than TLS, generally 10–15 pts/m^2 for modern acquisitions. These point spacings are generally considered good enough to produce DTMs with cell resolutions of 1 m. One of the main limitations of ALS surveys is the steep cost of deploying a crewed aircraft — a modest survey can cost tens of thousands of dollars. In the recent past, publicly accessible datasets have been released for large portions of Washington and British Columbia (e.g. LidarBC,

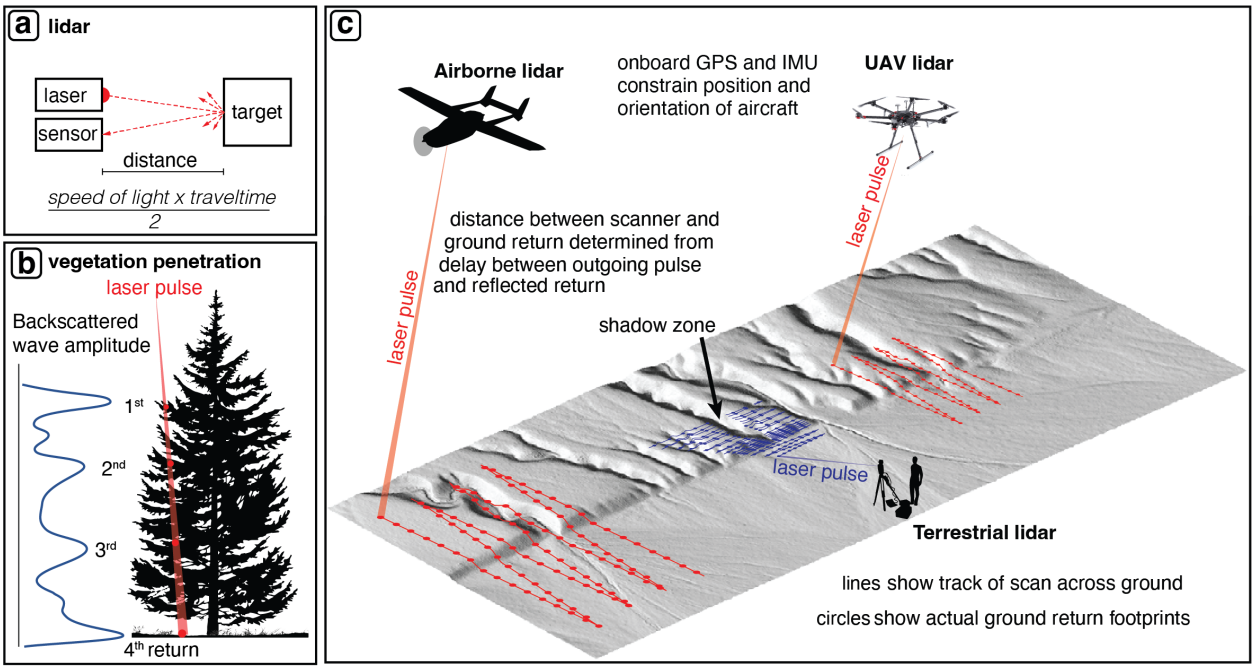

Figure 1.3: Light detection and ranging method schematic. a) Diagram explaining how light can be used to measure distances. b) Illustration of how a laser pulse can penetrate vegetation by returning several values. c) Popular methods of collecting lidar data at various scales. Adapted from Johnson et al. (2014).

2023) — making it possible to identify active faults and study surface deformation caused by crustal faulting in Cascadia at higher resolutions than ever before (e.g. Duckworth et al., 2021; Harrichhausen et al., 2023).

Recently, commercially available and inexpensive UAVs have become a popular method for terrain mapping. Initially these platforms used onboard cameras and computationally expensive, sophisticated photogrammetric algorithms to create Digital Surface Models (DSMs) (e.g. Harwin and Lucieer, 2012; James and Robson, 2012; Westoby et al., 2012). Unfortunately, photogrammetry has limited ability to map forested landscapes as the ground surface is obscured. Recent development of lighter laser scanners has enabled the possibility of collecting lidar datasets from UAV platforms referred to as UAV Laser Scanning (ULS). This technique offers a compromise between the scales and resolutions of the aforementioned established collection methods. The application of ULS data for tectonic feature mapping is demonstrated in Chapter 3 of this dissertation.

Chapter 2
The 2020 M_w 6.4 Koryak Highlands earthquake illustrates hidden seismic hazards in the northern Pacific Cordillera

2.1 Author names, affiliations and roles

Guy Salomon[1], Edwin Nissen[1,2], Fengzhou Tan[1,3], Eric Bergman[4], Alastair Sloan[5], & Léa Pousse-Beltran[1,6]

[1] School of Earth and Ocean Science, University of Victoria, BC, Canada
[2] College of Earth, Ocean, and Atmospheric Sciences, Oregon State University, Corvallis, OR, USA
[3] Scripps Institution of Oceanography, University of California San Diego, La Jolla, CA, USA
[4] Global Seismological Services, Golden, CO, USA
[5] Department of Geological Sciences, University of Cape Town, Rondebosch, South Africa
[6] Université Grenoble Alpes, Université Savoie Mont Blanc, CNRS, IRD, UGE, ISTerre, Grenoble, France

This chapter has been published in *Geophysical Journal International* (https://doi.org/10.1093/gji/ggaf031). I led the data processing, analysis, figure creation and wrote the manuscript. I was assisted in the following analyses by the co-authors in brackets; InSAR processing (Léa Pousse-Beltran), InSAR elastic dislocation modelling (Edwin Nissen), body waveform modelling (Alastair Sloan, Edwin Nissen), teleseismic back-projection (Fengzhou Tan), and calibrated hypocentral relocations (Eric Bergman). The co-authors listed above provided manuscript edits.

2.2 Abstract

On 9th January 2020, a M_w 6.4 earthquake struck the central Koryak Highlands of eastern Siberia, northeast of the diffuse triple junction between the North American, Pacific and Eurasian plates. The largest earthquake recorded in the central Koryak Highlands to date, it provides an excellent opportunity to study the little-known active tectonics of this remote, sparsely instrumented region. We mapped coherent, coseismic surface deformation with Sentinel 1 Interferometric Synthetic Aperture Radar (InSAR), making this one of the highest-latitude earthquakes to be captured successfully with satellite radar, in spite of the rugged, snow-covered terrain. Elastic dislocation modelling, teleseismic back-projections, calibrated hypocentral relocations, and teleseismic moment tensor solutions are used to resolve a left-lateral fault trending northwestwards, proximal but perpendicular to a regional geological suture zone, the Khatyrka-Vyvenka Thrust. The earthquake probably ruptured unilaterally northwestwards along a 20 km long segment that appears indistinct in the local topography, and likely generated no surface rupture. We interpret that these observations are indicative of a structurally immature fault zone and estimate a seismogenic zone thickness of 10–15 km. The Koryak Highlands earthquake illustrates how terrane boundaries within cordilleran belts may continue to accommodate tectonic strain long after accretion, resulting in significant earthquakes even along hidden faults.
Keywords: Seismology, Radar interferometry, Asia, North America, Seismicity and tectonics, Seismic cycle

2.3 Introduction

On 9th January 2020 at 08:38 UTC, a shallow, M_w 6.4 earthquake struck the Koryak Highlands of eastern Siberia, located in the westernmost North American Cordillera and within a diffuse triple junction with the Eurasian and Pacific plates. The Koryak Highlands are an amalgamation of mountain ranges created through the Mesozoic-Paleogene accretion of terranes onto the North American plate via northward subduction of the Pacific (Figure 2.1). A series of NE-trending sutures and faults such as the Khatyrka-Vyvenka zone (Imaeva et al., 2017), bounded in the south by the Vatyna–Vyvenka thrust (Chekhovich et al., 2008), are relics of this process. Modern day regional seismicity is concentrated in the south-western Khatyrka-Vyvenka zone adjacent to the Kamchatka peninsula (Figure 2.1), where notable events include the 2006 M_w 7.6 and 6.6 Olyutorskii and 1991 M_w 6.6 Khailino reverse faulting earthquakes (Lander et al., 1996, 2010; Rogozhin et al., 2007). Seismicity decays northeastwards towards the central Koryak Highlands, where the largest events prior to 2020 were M_w 5.6 and 5.3 strike-slip earthquakes in 1988 and 2007 (Lander et al., 1996; Rogozhin et al., 2021). The larger, M_w 6.4 2020 earthquake thus offers an opportunity to better understand the little known active tectonics of this region, and whether inherited geological structures

influence modern seismicity.

This latter question is of much broader relevance. The geological formation of the Koryak Highlands is characteristic of the northern Pacific Cordillera, defined here as the part of the circum-Pacific orogenic system where Pacific oceanic lithosphere subducts below the continental North American plate, and stretching from Kamchatka in the west to Haida Gwaii in the east (Figure 2.1, inset). Allochthonous terranes accreted onto the western margin of the North American continent throughout the Mesozoic and early Cenozoic eras (Akinin et al., 2020; Coney and Evenchick, 1994; Dickinson, 2004), with deformation apparently slowing into the late Cenozoic, but not stopping altogether. Understanding the causes and characteristics of crustal seismicity within the Koryak Highlands, and in particular its links to inherited geological structure, may therefore inform our understanding of the potential for large earthquakes in other parts of the northern Pacific Cordillera (e.g. Gaudreau et al., 2019; Wetmiller et al., 1988). Though very few people live in the Koryak Highlands, large earthquakes may pose risks to vulnerable population centres and critical infrastructure in these neighbouring regions.

The central object of this study is to characterize the 2020 earthquake sequence in as much detail as possible, notwithstanding its remote location which poses a number of methodological challenges. We build on a preliminary seismological analysis of the sequence by Rogozhin et al. (2021) and an Interferometric Synthetic Aperture Radar (InSAR) study of the mainshock by Svigkas et al. (2023), which notably disagree on which of the seismological nodal planes the earthquake ruptured. We resolve this by performing our own analysis and modelling of InSAR data, revealing the mainshock geometry and slip distribution and in doing so helping to constrain the regional seismogenic layer thickness. However, we also add a number of new seismological constraints, relying upon teleseismic data in the absence of local and regional station coverage. We use body waveform analysis to constrain and independently check the mainshock geometry and centroid depth, a phase-weighted back projection to reveal the mainshock kinematics, and a calibrated earthquake relocation in order to assess the aftershock distribution which has the potential to delineate other, neighbouring active structures. We finish by discussing implications for active tectonics and earthquake hazards within the northern Pacific Cordillera.

2.4 Methods

2.4.1 InSAR

The 2020 Koryak Highlands earthquake was captured by the European Space Agency's (ESA) Sentinel 1A satellite on descending track 118D and ascending tracks 125A and 154A. All of the available 12 or 24 day coseismic interferograms, including some postseismic pairs, were processed using GAMMA software (Werner et al., 2000), topographic effects were removed using the 30 m-resolution Copernicus digital elevation model (GLO-30), and the interfero-

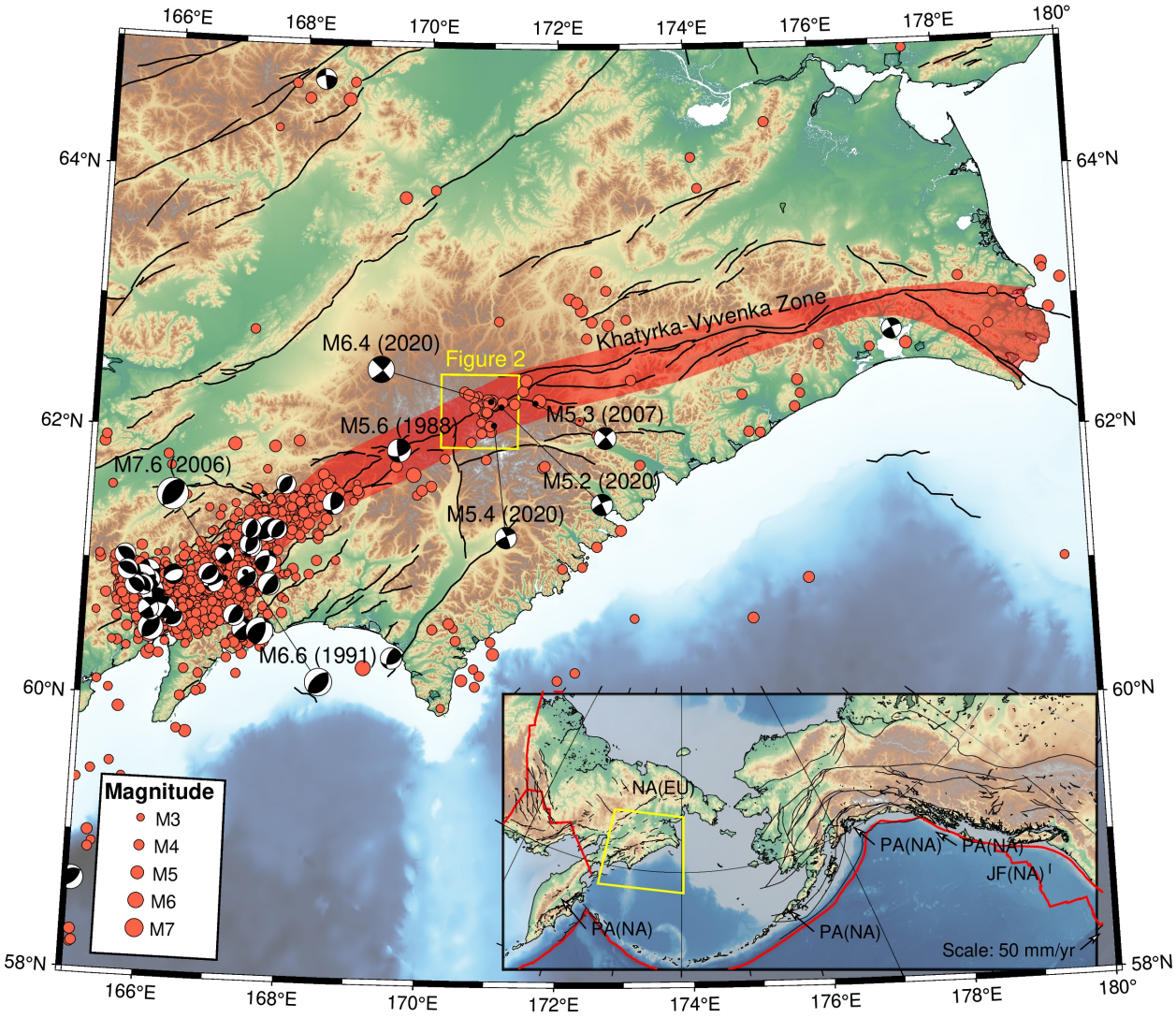

Figure 2.1: Seismicity and active faulting within the Koryak Highlands. Red dots are M 2.5+ epicentres for 1960–2024 from the International Seismological Centre (2024) and focal mechanisms are from the Global Centroid Moment Tensor catalog (Dziewonski et al., 1981; Ekström et al., 2012); note the change from predominantly thrust faulting in the SW (near the Kamchatka Peninsula) to strike-slip mechanisms within the central Koryak Highlands. Faults are from Zelenin et al. (2022)) with the Khatyrka-Vyvenka Zone marked by a red transparent polygon. Background topography is the Copernicus GLO90 DEM (European Space Agency, Singergise, 2021) and bathymetry is from the GEBCO Compilation Group (2023). Inset shows the location of the main map (yellow polygon) within the broader north Pacific Cordillera, with major structures in Alaska and Canada from the Yukon Geological Survey (2020). Vectors show relative velocities of the Pacific (PA), North American (NA), Eurasia (EU) and Juan de Fuca (JF) plates from the ITRF2020 plate motion model (Altamimi et al., 2023).

metric phase was unwrapped using the minimum cost flow algorithm (Werner et al., 2002) before being converted from radar to geographic coordinates (WGS-84) and from radians to line-of-sight (LOS) displacement. Large parts of many of the interferograms have poor coherency owing to the high latitude, rugged topography, and wintertime acquisitions, all of which can cause decorrelation (Wang et al., 2020). The shorter repeat acquisition times of Sentinel 1 over earlier generations of SAR satellites offer a vast improvement for wintertime imaging at high latitudes (e.g. Elliott et al., 2007; Mikhailov et al., 2023). A clear coseismic signal is evident on a 12 day interferogram (03/01/2020–15/01/2020) on descending track 118D and on a 24 day interferogram (23/12/2019–16/01/2020) on ascending track 125A. A 12 day interferogram on the adjacent track 154A also exhibited coseismic deformation but was too noisy to be useful in the modelling stage and is not discussed further.

To characterize the causative faulting, the LOS displacements were first downsampled using a quadtree algorithm (Jónsson et al., 2002) and then inverted for uniform slip on a rectangular dislocation embedded within an elastic half-space with Lamé parameters $\mu = \lambda = 3.2 \times 10^{10}$ Pa (Okada, 1985). Weighting the two datasets equally, we solved for the fault strike, dip, rake, slip, surface projection centre points, length, and top and bottom depths, using a non-linear, downhill Powell's algorithm (Press et al., 2007) with 100 Monte Carlo restarts to avoid local minima (Wright et al., 1999). To account for satellite orbital errors and different unwrapping reference points, we also jointly solved for linear ramps and static shifts in LOS displacement. To achieve the best possible fit to the observed data in a stable inversion, we found it preferable to fix the slip to 0.9 m to ensure that the modelled deformation had the same number of fringes as the observed interferogram. This value was chosen on the basis of fault scaling relationships (Kanamori and Anderson, 1975).

To resolve finer details, we solved for the distribution of slip across the model fault plane. The fault plane was first extended along strike and down dip, and then subdivided into 1 km × 1 km patches. The slip on each patch was estimated using a Laplacian smoothing operator (Funning et al., 2005; Wright et al., 2004) and a non-negative least squares algorithm to ensure positive slip (Bro and De Jong, 1997). A range of smoothing factors were tested so as to obtain a realistic, non-oscillatory slip gradient without unduly increasing the misfit.

2.4.2 Seismic body wave analysis

We used long-period teleseismic body-waveform modelling as an an independent check of the mainshock focal mechanism and centroid depth. Waveform data were restricted to epicentral ranges of 30°-90° for *P* waves and 30°-80° for *SH* waves in order to avoid complications from unmodelled lithosphere and core phases. 26 vertical component *P* wave seismograms and 24 transverse component *SH* wave seismograms were selected for modelling on the basis of high signal-to-noise ratios and an even global distribution without any large azimuthal gaps. We used the MT5 program (Zwick et al., 1994) developed from the algorithms of McCaffrey and Abers (1988) and McCaffrey et al. (1991) to minimize differences between the observed

waveforms and synthetic seismograms calculated using a half space with V_p = 6.0 km.s^{-1}, V_s = 3.5 km.s^{-1}, and density = 2800 kg.m^{-3} (values consistent with the elastic parameters used in our InSAR modelling). The synthetic seismograms incorporate direct *P* and *SH* phases and *pP*, *sP* and *sS* depth phases, thus providing sensitivity to centroid depth (Molnar and Lyon-Caen, 1989; Wimpenny and Watson, 2021), and represent the source time function as the combination of a series of triangular elements, with the moment being their integral. Before inversion, the synthetic *P* and *SH* waveforms were aligned against their observed arrivals on broadband vertical and transverse seismograms so as to remove any potential influence from epicentral mislocation. The program uses a least squares routine to solve for the centroid strike, dip, rake, depth, and source time function by minimizing misfits between observed and synthetic seismograms. To test the sensitivity of the solution to varying centroid depth, we then fixed this parameter in 1 km increments either side of the minimum misfit value and re-ran the inversion allowing the strike, dip, rake, and source time function to vary (Molnar and Lyon-Caen, 1989; Nissen et al., 2014a).

2.4.3 Back projection

We assessed the rupture kinematics using the phase-weighted relative back projection method (Schimmel and Paulssen, 1997; Tan et al., 2019; Zhang and Ge, 2010). Relative energy was back projected onto a 0.01° (≈1 km) grid across the source region using a teleseismic array in the contiguous United States and travel times estimated with the IASP91 reference model (Kennett and Engdahl, 1991). We also tested a European array, but the results showed considerable swimming artifacts (Meng et al., 2012), likely reflecting that while source–receiver paths to the US are approximately perpendicular to the NW-trending fault, those to Europe lie roughly along strike. An additional issue could be the epicentral distance to the EU array being significantly larger (62–77°) than to the US array (40–65°), as such, the signal to noise ratio for the EU array is lower than for the US array. The *P* seismograms were aligned using cross correlation, the waveforms were then stacked using a 10 s sliding window. A frequency band of 0.2–2 Hz was used, the waveform amplitudes were normalized, and the relative energy was calculated using phase-weighted stacking to reduce biases introduced by incoherent signals with large amplitudes. The sliding window produced some artifacts in the form of energy radiators centred upon the same source grid node but at different times; here, the mean source times were chosen and the rest were discarded.

2.4.4 Calibrated relocation

The hypocentral locations of the 2020 mainshock, a M_l 4.1 foreshock, fifteen aftershocks (m_b 3.6–M_l 5.4), and 22 other events located within a radius of 1.5 degrees were re-evaluated using the *mloc* calibrated earthquake relocation software (Bergman and Solomon, 1990; Walker et al., 2011). We acquired phase data from the ISC bulletin (International Seis-

mological Centre, 2024) and only included events with 30 or more phase readings in the relocation. The *mloc* program minimizes location bias by exploiting the fact that ray paths of events clustered in space and recorded at common stations sample roughly the same portion of the Earth, such that travel time differences more likely represent the relative epicentre locations within the cluster rather than the 3D velocity structure. The relocation is split into two independent steps, each using a specific, tailored set of arrival time data (Jordan and Sverdrup, 1981). The first step estimates the relative locations of each hypocentre within the cluster using differences in arrival times at common stations at all distances. For the second step, we used an indirect calibration to constrain the absolute location of the hypocentroid. Indirect calibration makes use of a precise, independent constraint on the epicentre of at least one earthquake in the sequence (Walker et al., 2011); we chose to place the mainshock epicentre along the trace of our InSAR model fault where it roughly bisects the cloud of well-located aftershocks.

Without any close-in stations or even much in the way of regional coverage, we are heavily reliant on teleseismic depth phases to solve for focal depths. Unfortunately, we find that those reported for earthquakes in our relocation cluster are often unreliable, with some stations offering only theoretical depth phase arrival times based on a preliminary hypocentre, and others listing identical pP and sP arrival times. Because of this, we were unable to solve for the best-fitting focal depths for most of the earthquakes within the 2020 cluster. We were able to constrain a focal depth for the mainshock, but for all other events the focal depth was set to 10 km, consistent with independent inferences of the mainshock centroid depth and seismogenic layer thickness, described below. Based on prior experience, we do not anticipate there to be any meaningful impact on epicentral accuracy from this choice of fixed focal depth (e.g. Ghods et al., 2012; Karasözen et al., 2016).

2.5 Results

2.5.1 Mainshock

The InSAR data and modelling provide the best constraints on the mainshock location and geometry. The interferograms are generally coherent, though steep topography and/or snow cover (Appendix A.1) may have introduced noise to the mountainous, eastern parts (Figure 2.2a, left panels). Both interferograms also contain a NW-trending band of partial decorrelation, clearest in the descending scene in which it is masked out in Figure 2.2a (lower left panel). Nevertheless, coseismic deformation appears clearly in both interferograms as two main fringe lobes, one on each side of the decorrelation band. The western lobes contain the peak displacements, which are toward the descending track satellite and away from the ascending satellite, while the eastern lobes show the opposing sense of motion. This pattern is consistent with left-lateral motion along a fault aligned northwest–southeast, roughly along the observed band of decorrelation. The ascending interferogram also exhibits smaller

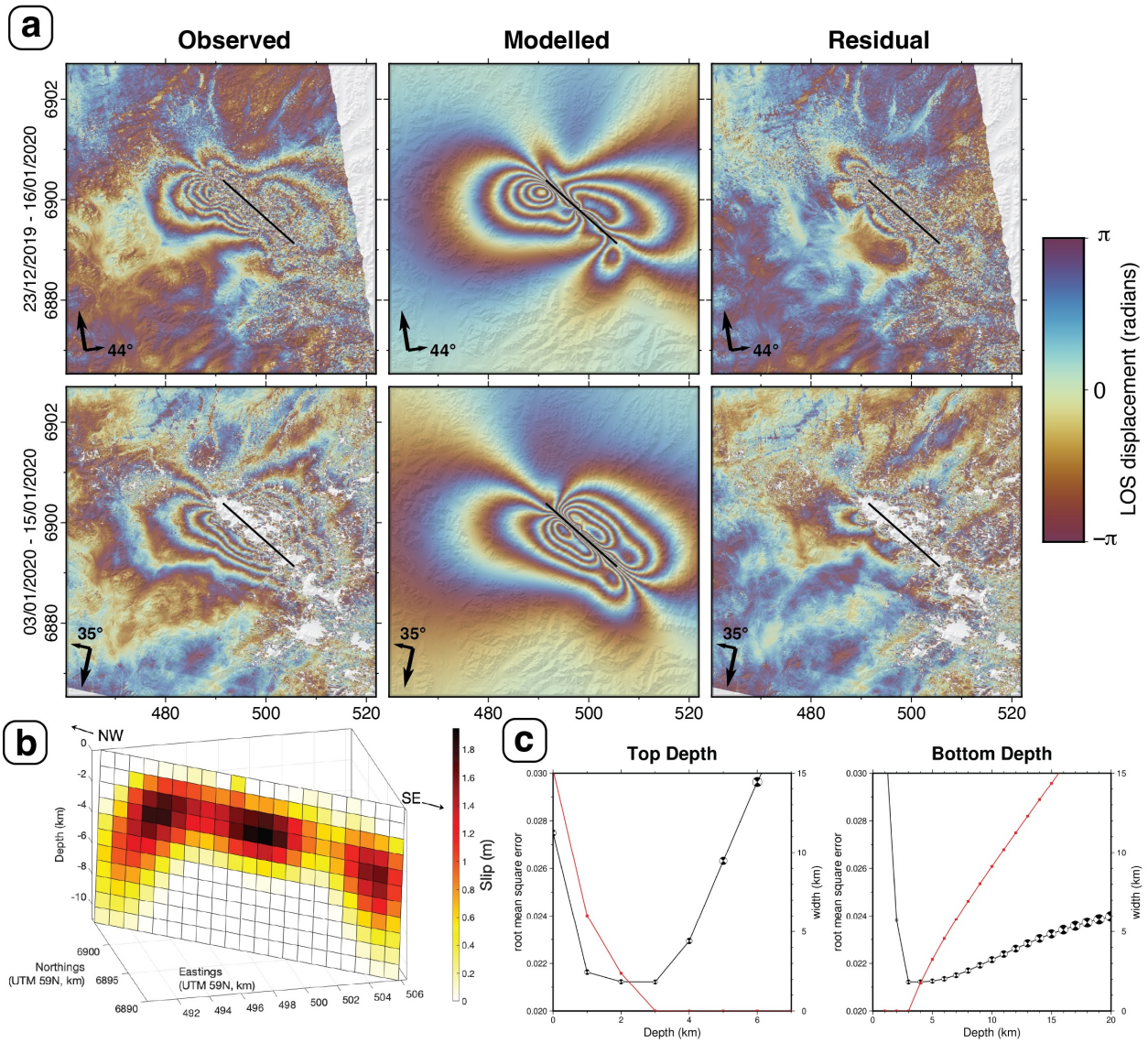

Figure 2.2: (a) Top row: (left) observed 24 day, (middle) model and (right) residual interferograms for Sentinel 1 ascending track 125. Bottom row: (left) observed 12 day, (middle) model and (right) residual interferograms for descending track 118. To better visualize the shape of the displacement field, all interferograms are left wrapped, with 2π radians equivalent to 2.77 cm line-of-sight (LOS) displacement. Large and small arrows show satellite track and LOS azimuths, along with the incidence angle measured from the vertical at the earthquake. The black line is the surface trace of our InSAR model fault. Coordinates are in UTM kilometres (Zone 59N). (B) Modelled slip distribution on 1 km $\times$ 1 km fault patches. (C) Uniform slip parameter sensitivity tests for (left) model fault top depth and (right) bottom depth, with root mean square error (black line) calculated at fixed 1 km increments and the inversion re-run with all other parameters free to vary. Focal mechanisms show how strike, dip, rake and magnitude parameters varied for each run. The red line is the implied rupture width for each inversion.

deformation lobes at either end of the faulting, which is as expected since its look vector is more oblique to fault strike than the descending one.

Inversion of downsampled InSAR data for uniform slip on a rectangular model fault can reproduce the observed deformation well, with root-mean-square residual LOS displacements of 2.17 cm (Appendix A.2 & A.3). The best fitting fault is 19.2 km long, trends NW-SE along the decorrelation zone (strike 132°), dips steeply SW (86°), and has left-lateral slip (rake 4°). Given elastic rigidity of 3.2×10^{10} Pa, this gives rise to a moment of 3.88×10^{18} Nm (equivalent to M_w 6.3), in the middle of the range of available seismological estimates (3.1–4.6×10^{18} Nm, Table 2.1). Our results are in reasonable agreement with those of Svigkas et al. (2023), with discrepancies of <15% in uniform slip, fault length, and width, and of 8° in strike, <1° in dip (which they fixed), and 7° in rake. However, our InSAR model fault geometry has closer consistency than Svigkas et al.'s with the NW-striking seismological nodal planes, with discrepancies in strike, dip and rake ranging from just 2–4° for the GEOFON model to 4–15° for those of the USGS and GCMT catalogues (Table 2.1). To explore the possibility of along-strike rupture segmentation, we also tried inversions with two rectangular uniform slip fault planes (Elliott et al., 2012), but found that these did not visually improve the fit to the data despite double the number of free parameters (Appendix A.4 & A.5). This result is consistent with the unusually high percentage (96–98%) double couple components of the reported USGS moment tensors, which imply a simple, planar earthquake source (e.g. Zaccagnino and Doglioni, 2022).

We tested the sensitivity of our uniform slip model to fault top and bottom depths by incrementally altering these parameters and assessing the effects on model misfit. When the top depth is reduced to zero, the misfit rises markedly, suggesting that the rupture did not reach the surface (Figure 2.2c). When the top depth is increased to 2–3 km, the misfit remains low but the fault width becomes unreasonably narrow. The bottom depth is less well constrained, with the misfit rising only gradually as the bottom depth is lowered from ∼5 km.

Our distributed slip InSAR inversion provides a more refined indication of the depth limits of coseismic slip as well as its variation along strike. In our preferred model, root-mean-square residual displacements are reduced by about a quarter from those of the uniform slip model to 1.66 cm, and the visual fit to the data is also improved (Figures 2.2a & A.6), with removal of some residual fringes present in the uniform slip model interferograms (Figures S1 & S2). Model slip peaks at 1.9 m at a depth of ∼3.5 km along the middle portion of the fault, with two distinct slip asperities near the NW and SE fault ends (Figure 2.2b). Only a small proportion of the slip reaches the shallowest row of model fault patches, supporting our earlier inference of a substantial shallow slip deficit. At the base of the model slip patch, slip tails off abruptly at 5–6 km depth beneath the central slip asperity and more gradually at 7–10 km beneath the distal ones. The InSAR moment of 3.71×10^{18} Nm (equal to M_w 6.3) is in agreement with the equivalent seismological values of 3.1–4.6 $\times 10^{18}$ Nm (Table 2.1). Our slip model with its three asperities and pronounced shallow slip deficit qualitatively resembles

Table 2.1: Source parameters of the 9 January 2020 Koryak Highlands mainshock, from the Global Centroid Moment Tensor (GCMT), United States Geological Survey (USGS) ANSS Comprehensive Earthquake Catalog, GEOFON, Svigkas et al.'s (2023) InSAR model, and from our own modelling. Location refers to the GCMT and GEOFON centroids, the USGS epicentre, and the peak slip patch of our InSAR model (surface projection coordinates of our InSAR model fault planes are listed separately in Appendix Table A.1). Depth refers to the centroid depth for all of the seismological solutions, and the depth of peak slip for the InSAR solutions. The asterisks caution that automated centroid depths of the GCMT, USGS, and GEOFON catalogs are unreliable for shallow continental earthquakes and are often assigned fixed values (e.g. Wimpenny and Watson, 2021).

Source	Location	Strike	Dip	Rake	Depth	Moment (Nm)	M_w
GCMT	62.27°, 171.00°	316°	86°	−11°	12 km*	4.38×10^{18}	6.4
USGS W-phase	62.358°, 171.061°	317°	88°	−13°	19.5 km*	4.60×10^{18}	6.4
USGS body wave	62.358°, 171.061°	320°	85°	−3°	13 km*	3.09×10^{18}	6.3
GEOFON	62.33°, 170.94°	135°	85°	0°	10 km*	3.60×10^{18}	6.3
Svigkas et al. (2023)	62.214°, 170.931°	304°	86°	−3.2°	2.5 km	3.87×10^{18}	6.3
This study (InSAR)	62.203°, 170.986°	132°	86°	4°	3.5 km	3.71×10^{18}	6.3
This study (body waves)	-	317°	85°	0°	9 km	3.22×10^{18}	6.3

the pattern resolved by Svigkas et al. (2023), though a direct comparison is impossible since their model is not tabulated.

Our body waveform modeling can reproduce observed teleseismic *P* and *SH* waveforms well with purely double couple motion lasting 12 seconds (Figure 2.3a), further confirmation of a simple, planar fault source. The best solution has a NW-trending nodal plane with strike 317°, dip 85° NE, and rake 0° (Table 2.1). This geometry is closely consistent with our InSAR model fault plane, with differences of just 4–9° in strike, dip and rake, accounting for the opposing dip direction and application of the right-hand rule. The minimum misfit centroid depth of 9 km is somewhat deeper than our InSAR model fault centre and peak slip depths of ∼4–5 km. However, centroid depth sensitivity tests (Figure 2.3b) reveal similarly low misfits for depths ranging from 3–10 km with relatively small consequences to model strike, dip, rake and magnitude. Only below 10 km do body-waveform model misfits increase markedly, while above 3 km, the misfit remains low but the NW-striking nodal plane inclines to an anomalously shallow angle. This result is within agreement with the focal depth of 13 km calculated during relocation in *mloc*, assuming that slip propagated upwards after nucleating near the base of the rupture plane (e.g. Karasözen et al., 2016; Wei et al., 2015).

To investigate discrepancies in fault plane geometry between the various available mainshock focal mechanisms (Table 2.1), which are important for understanding regional kinematics, we tested the sensitivities to strike and dip direction of our InSAR and teleseismic body waveform models. We repeated our InSAR uniform slip and body waveform inversions with strike values kept fixed at small (2–5°) increments either side of the minimum misfit values, and recorded the root mean square error or normalized error for each model run

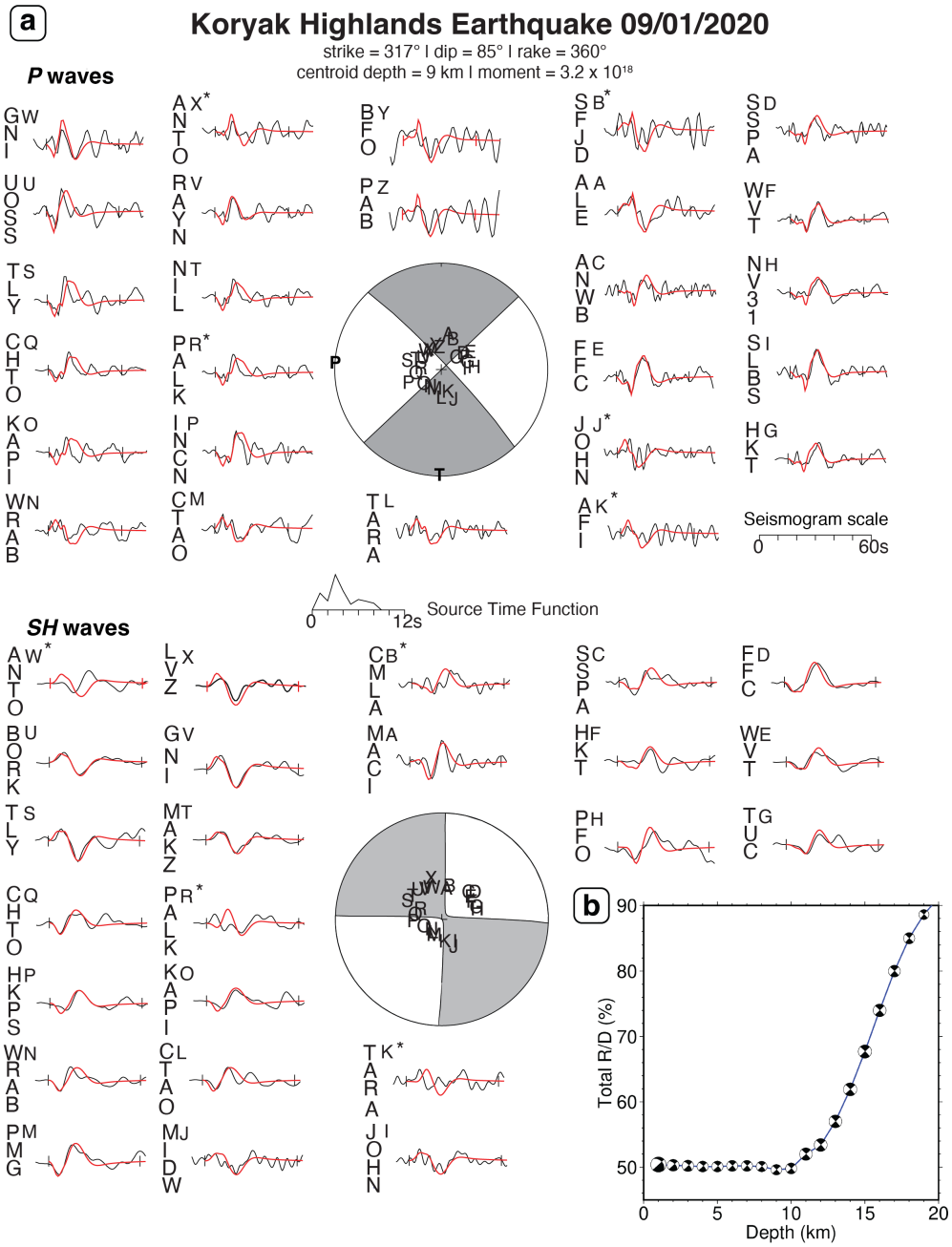

Figure 2.3: (a) Teleseismic body waveform model of the 9^{th} January 2020 earthquake. The stereoplots show the (top) *P* and (bottom) *SH* focal spheres, with stations marked by capital letters and P and T axes in bold. Surrounding each focal sphere are the observed (black) and synthetic (red) vertical (*P*) and transverse component (*SH*) seismograms, with station codes written vertically beside the stereoplot characters, and vertical ticks marking the inversion window with the time scale shown middle right. The source time function is in the centre of the figure. (b) Results of our centroid depth uncertainty tests, with the percent of weighted residual variance (R/D) plotted along with model strike, dip and rake at 1 km increments of fixed depth.

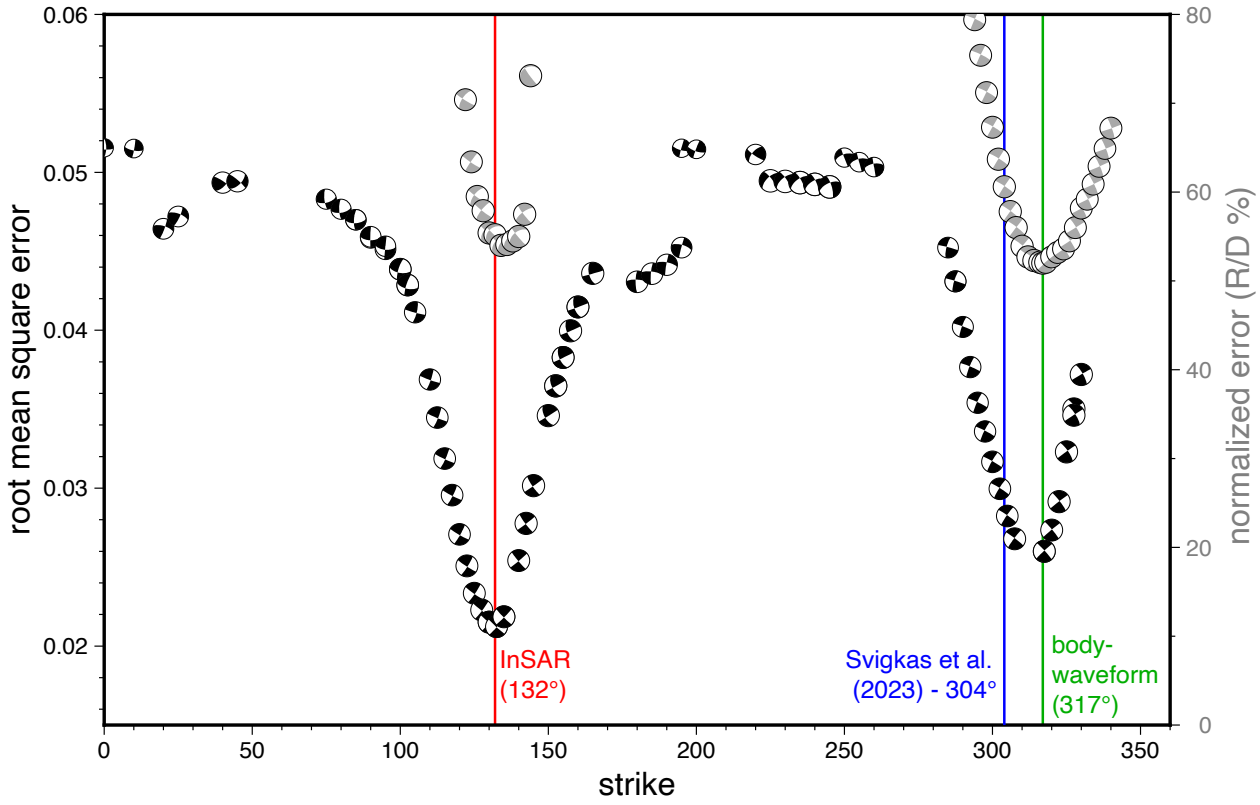

Figure 2.4: Strike sensitivity tests for InSAR and teleseismic body-waveform modelling of the 9 January 2020 Koryak Highlands mainshock. InSAR (black) and waveform (grey) focal mechanisms are plotted as a function of their fixed strike values and root mean square error or normalized error (defined as the percentage ratio of the weighted residual variance to the weighted data variance, or R/D %). Red, blue and green lines shows strike values of our own InSAR model, the InSAR model of Svigkas et al. (2023), and our body waveform model, respectively.

(Figure 2.4). When the waveform model is assigned our preferred InSAR model strike of 132° (Figure 2.4, red line), the resulting normalized error is only marginally greater than the minimum misfit value, whereas when the InSAR model is assigned our preferred waveform model strike of 317° (green line), the resulting root mean square error is conspicuously larger than the minimum misfit value. This leads us to favour the strike and south-westward dip direction yielded by our InSAR modelling. The broader minima in the waveform modelling misfit curve may reflect the large azimuthal gap to the SE (Figure 2.3), though uncertainties in the order of ±5–15° are common for this procedure (Molnar and Lyon-Caen, 1989). Notably, the strike of the InSAR model of Svigkas et al. (2023), which at 304° is 12–16° different from any of the other available solutions, falls outside of the minima in either of our misfit curves (Figure 2.4, green line).

Our back projection provides an independent check on the fault orientation and our best indication of the rupture kinematics, though we acknowledge that the earthquake is close to

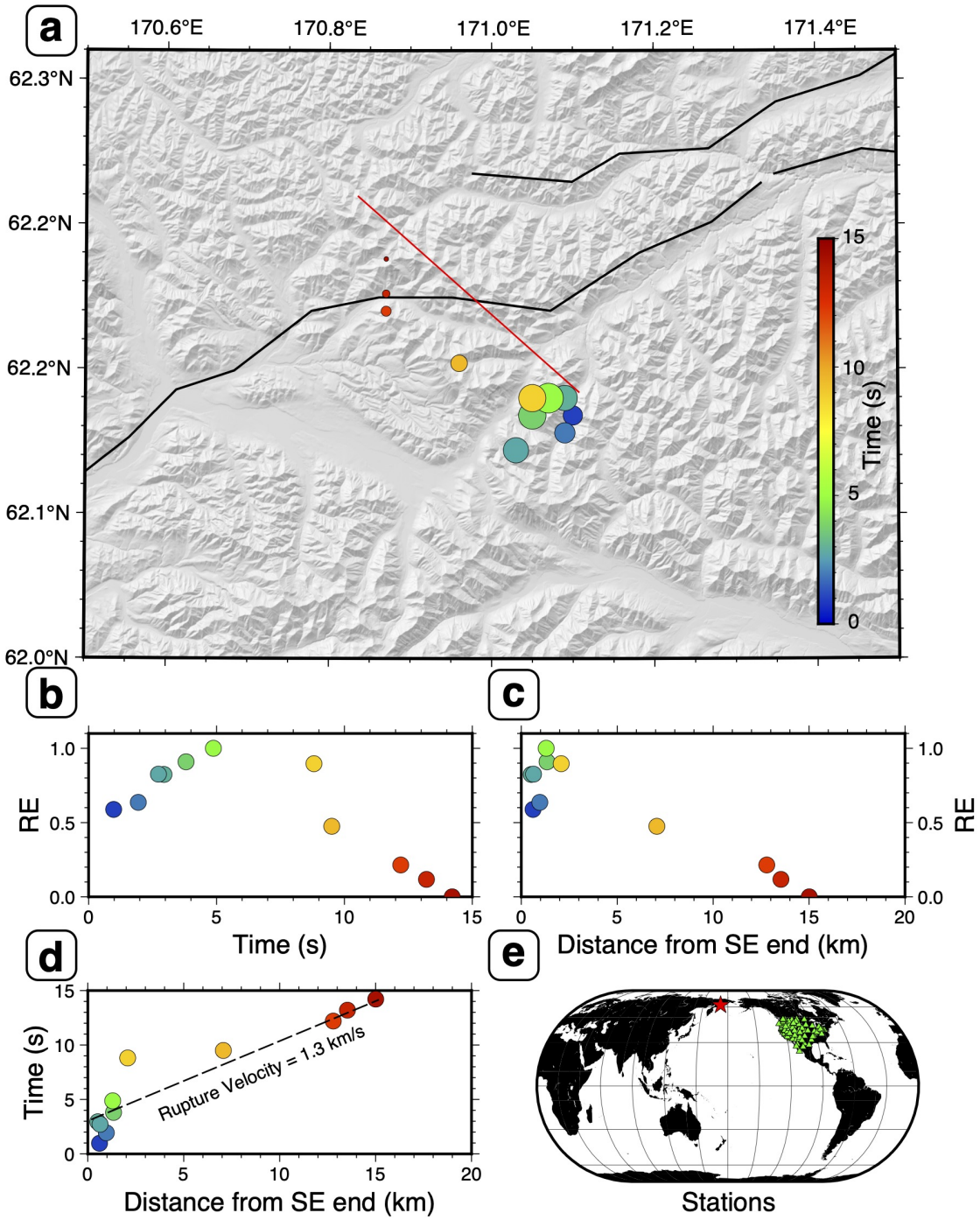

Figure 2.5: (a) Results of a phase-weighted back-projection using a contiguous US-based array. Colour scale shows the time since onset of the event while size shows the relative energy (RE). Red line marks the InSAR modelled fault, black lines are mapped faults (Zelenin et al., 2022). (b) Relative energy (RE) release versus time, where the relative energy has been normalized to 1. (c) Relative energy and projected distance along the InSAR modelled fault. (d) Time versus the projected distance along the InSAR fault. (e) Stations (green triangles) used in the back projection.

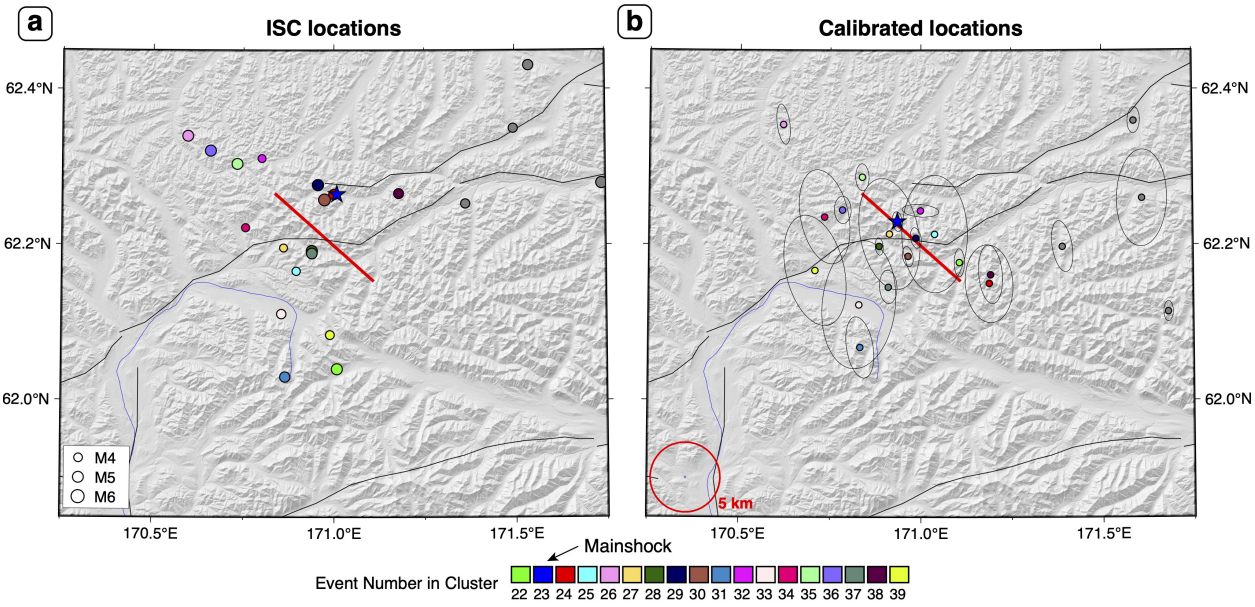

Figure 2.6: (a) Reported International Seismological Centre (ISC) epicentres and (b) relocated epicentres of the 2020 sequence, scaled by magnitude and numbered and coloured chronologically. These include one foreshock, the mainshock (blue star), 11 aftershocks, and a few other regional events (grey). The red line is our InSAR modelled fault and black lines are other regional faults (Zelenin et al., 2022). In (b), black ellipses are 90% confidence ellipses for individual cluster vectors (i.e. relative locations) and red circle of radius 5 km is for scale.

the M_w limit of 6.5 that this method can reliably resolve (Kiser and Ishii, 2017). Our results indicate that slip propagated unilaterally northwestwards at an average rupture velocity of ∼1.3 km/s (Figure 2.5a, d). Coherent back-projected energy is released over a duration of ∼14 sec (Figure 2.5b), consistent with the 12 sec source time function duration estimated from body waveform modelling (Figure 2.3), and over a distance of ∼15 km (Figure 2.5c), similar to the 22 km length of our InSAR model fault, with peak energy release at ∼6 s close to the epicentre.

2.5.2 Aftershock distribution

The original ISC epicentres for the 2020 sequence are highly scattered, but generally are located upon a step-over along the SW-trending Khatyrka-Vyvenka fault (Figure 2.6a). Relocation shifts and condenses the events southwards to between the mapped traces of the Khatyrka-Vyvenka and Vatyn-Vyvenka faults, but the aftershock cloud still lacks any obvious structure or preferred orientation (Figure 2.6b). Presumably, many of these aftershocks are rupturing unidentified faults secondary to both the mainshock and the main suture zones. Notably, there is no concentration of events in the inferred northwestward direction of main-

shock rupture propagation; in fact, the aftershock distribution is perhaps more favorably explained by a bilateral rupture. Additional maps, travel time curves and residual plots associated with the relocation can be found in the Appendix (A.7–A.11).

2.6 Discussion

2.6.1 Fault geomorphology, structural immaturity, and shallow slip deficit

Having located the mainshock fault with InSAR, we investigate whether its surface trace corresponds with any fault-related geomorphology such as scarps, shutter ridges or stream offsets. We used a section of the 2 m resolution ArcticDEM digital elevation model (DEM) (Porter et al., 2022), downloaded with a buffer of several km along the InSAR fault bounds (Figure 2.7). This was hillshaded from several different directions, in order to highlight potential tectonic features no matter their orientation or facing directions. We observed rugged topography, with the fault trace crossing several drainage systems and ridgelines, including several cirques and one large valley, mostly at high angles. After inspection, there are no clear, fault-related lineaments or landforms in this area, so it is likely that the 2020 M_w 6.4 earthquake ruptured a structurally-immature and/or slow slip-rate fault that has accumulated insufficient surface slip to imprint the post-glacial landscape. The Koryak Highlands were glaciated at least twice during the Pleistocene, although these were mostly valley glaciers with little evidence for large ice sheets and domes (Glushkova, 2011). This is consistent with the fault strike being orthogonal to the mature, terrane-bounding Khatyrka-Vyvenka fault (Zelenin et al., 2022), which by contrast is relatively well-expressed in the regional topography.

Other aspects of the 2020 earthquake sequence are also consistent with immature faulting. The propagation of the mainshock rupture front imaged by back projection is just $\sim$1.3 km/s, consistent with the slow rupture velocities expected along immature faults with many remaining asperities along the fault plane (Guo et al., 2023; Perrin et al., 2016). The scattered, off-fault aftershocks are another indication of structural immaturity, with seismic sequences along mature faults expected to cluster more narrowly along the principal shear zone (Perrin et al., 2021).

A final characteristic of the 2020 earthquake that may relate to fault structural immaturity is its pronounced shallow slip deficit (SSD), the reduction in slip towards the Earth surface commonly observed in geodetic slip models (e.g. Fialko et al., 2005; Simons et al., 2002). Understanding the causes of SSDs is important for seismic hazard assessment, and off-fault deformation in earthquakes on immature faults is one proposed mechanism (Dolan and Haravitch, 2014). By constructing a normalized slip profile from our distributed slip InSAR model (Figure 2.2b), we observe peak slip at 3–4 km depth diminishing by over 90%

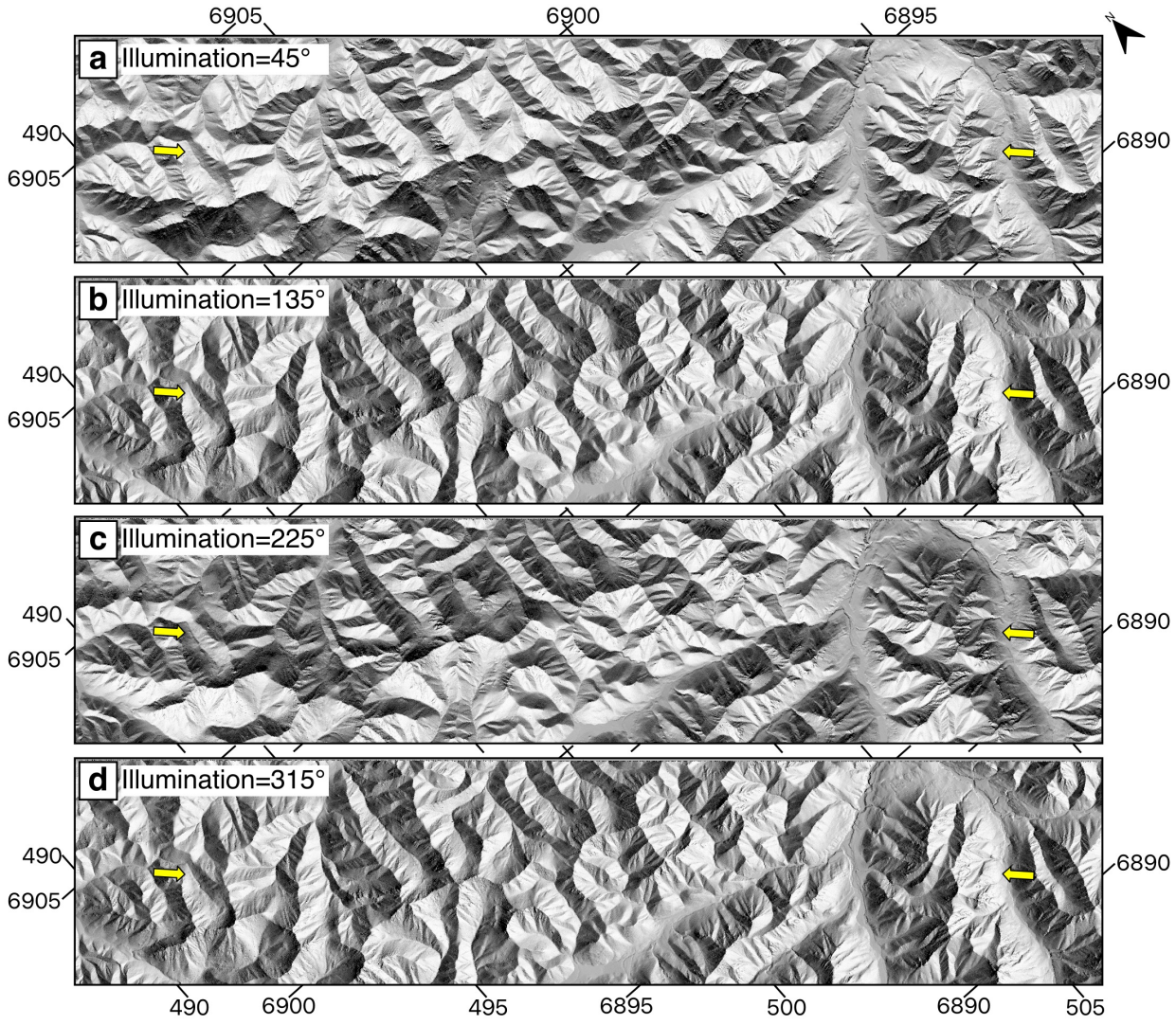

Figure 2.7: Hillshaded ArcticDEM topography (Porter et al., 2022) along our InSAR model fault (ends indicated by yellow arrows) with illumination from a) 45°, b) 135°, c) 225° and d) 315°. Coordinates are in UTM kilometres.

at the surface (Figure 2.8a, thick black line). Superimposing this onto a compilation of normalized slip profiles from 29 large strike-slip earthquakes with published InSAR slip models (Sethanant et al., 2023) highlights how a large subset of these earthquakes have similarly pronounced SSDs (Figure 2.8a). Following Sethanant et al. (2023), we further classify these earthquakes by the total offset of the host fault—a measure of structural maturity—and by magnitude (Figure 2.8b–c). This shows how those with pronounced SSDs are linked not by fault structural immaturity, but rather by their moderate magnitudes: strike-slip earthquakes only consistently rupture fully to the surface, no matter their nucleation depths, once they reach magnitudes greater than about 7.

2.6.2 Implications for active tectonics of the northern Pacific Cordillera

Due to the slow rates of deformation, sparse instrumentation, and limited exposure to earthquakes, active tectonics and seismic hazards in the northern Pacific Cordillera are poorly understood relative to other major continental orogenic systems such as the main North American Cordillera or the Alpine-Himalayan belt. As one of the best-recorded earthquakes in the region up till now, the 2020 Koryak Highlands event therefore offers an important new point of reference.

One important parameter in continental tectonics is the seismogenic layer thickness, which varies from about 10 km to 40 km across most orogenic belts (Maggi et al., 2000a). This parameter sets the lower depth limit for coseismic slip and thus helps control rupture area and magnitude. Routine earthquake catalogues are poor at resolving depths of crustal earthquakes and, outside of the most densely-instrumented regions, the best constraints on seismogenic layer thickness come from regional or teleseismic waveform modelling (Engdahl et al., 2006; Maggi et al., 2000b; Wimpenny and Watson, 2021). Unfortunately, only a handful of large earthquakes across the northern Pacific Cordillera have centroid depths resolved in this manner, and even fewer have slip distributions constrained by geodetic data (Figure 2.9), leaving the seismogenic thickness largely obscure.

Our InSAR analysis of the 2020 Koryak Highlands earthquake supports peak slip at 3–4 km depth, diminishing rapidly towards the base of the model fault plane at 11 km. Svigkas et al. (2023) yield a similar slip distribution but with small amounts of slip down to 14 km depth. Further SW within the Koryak Highlands, aftershocks of the 2006 M_w 7.6 Olyutorski earthquake recorded by three temporary local stations concentrate above about 18 km, but the mainshock itself, and the largest aftershock (M_w 6.6), are poorly constrained (Lander et al., 2010).

Constraints on seismogenic layer thickness in the Koryak Highlands therefore remain sparse, but earthquake studies from Alaska and Canada suggest that, inboard of active forearcs, much of the northern Pacific Cordillera may be characterized by shallow ($\sim$10–15 km) seismicity. In northern Alaska, InSAR modelling of the 2018 M_w 6.4 and 6.0 Kaktovik earthquakes reveals slip between about 2 km and 9 km depth, and centroid moment tensors of

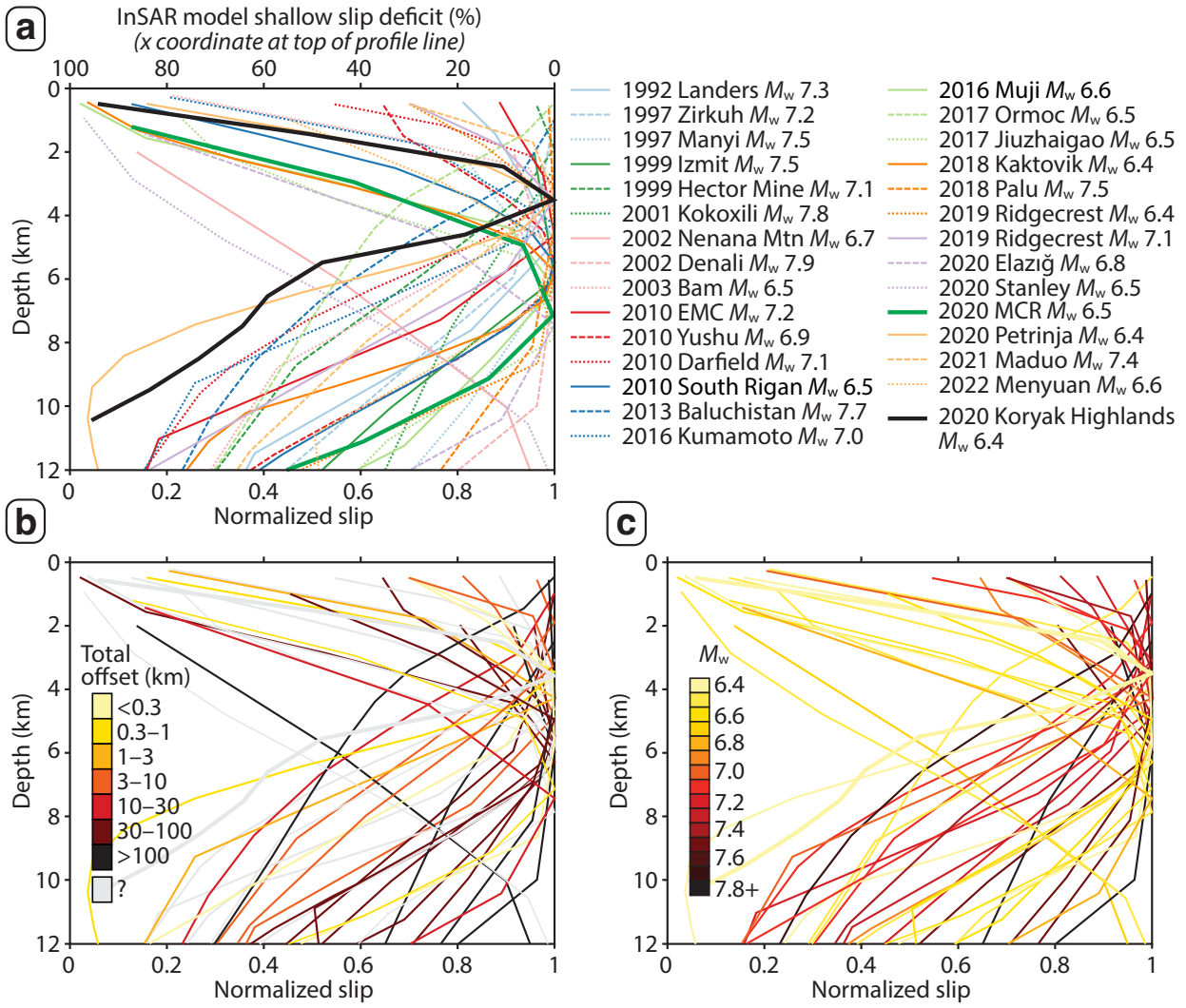

Figure 2.8: (a) Normalized slip profiles for the Koryak Highlands earthquake and 29 large (M_w6.4—7.9) continental earthquakes with predominantly strike-slip motion and InSAR-derived coseismic slip models, modified from Sethanant et al. (2023). Model slip along each row of slip patches was averaged, normalized by dividing it by the maximum value of average slip, and plotted against depth. SSD values plotted along the top of the graph refer to the shallowest data points of the profile, and are equal to one minus the normalized slip of the surficial row of model subfault patches expressed as a percentage (e.g. Fialko et al., 2005). (b) Normalized slip profiles coloured by total geological offset along the host fault and (c) by earthquake moment magnitude; see Sethanant et al. (2023) for details of the other earthquakes.

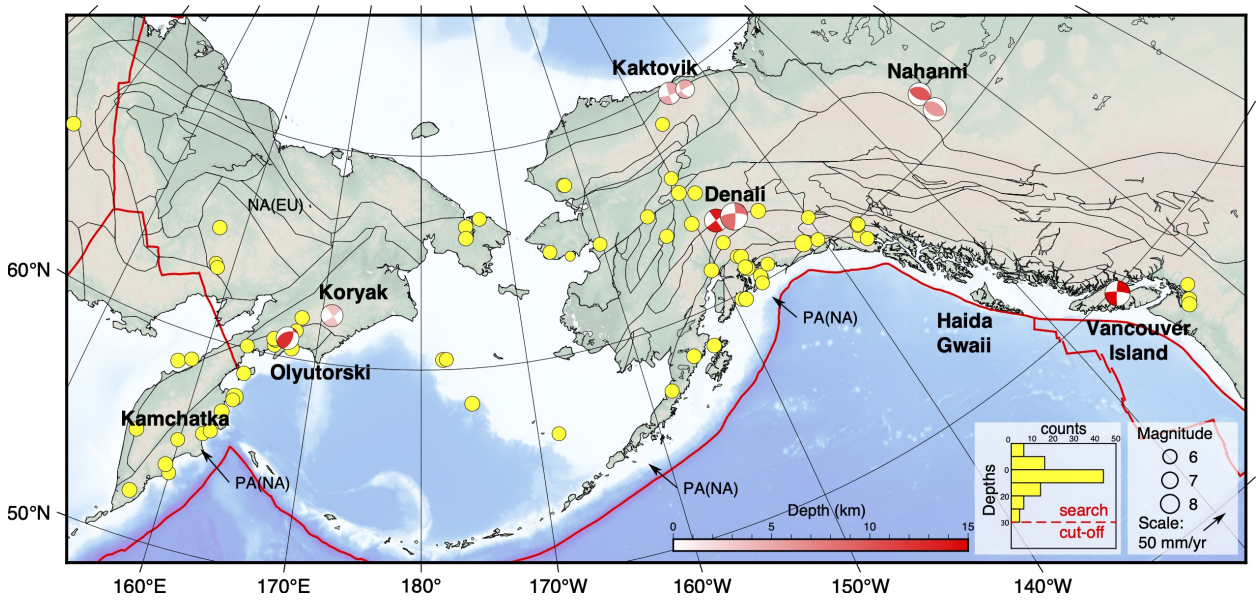

Figure 2.9: Terranes of the north Pacific Cordillera. Terrane boundaries, in black, are from a tectonic model of the Arctic (Shephard et al., 2013). Yellow circles indicate the location of large crustal earthquakes (M >6, with depths <30 km) within the north Pacific Cordillera. Many of these large events have occurred close to, or along, major structures. The histogram shows the depth distribution of these earthquakes. These events are from the ISC Bulletin for the period 1964-2024. Several notable events (discussed in the text) are labelled and coloured by the depth of maximum slip (Appendix Table A.3). Vectors show relative velocities of the Pacific (PA), North American (NA), Eurasia (EU) and Juan de Fuca (JF) plates from the ITRF2020 plate motion model (Altamimi et al., 2023).

aftershocks recorded by the USArray Transportable Array are similarly shallow (Estève et al., 2022; Gaudreau et al., 2019; Xu et al., 2020). In central Alaska, InSAR and GNSS models of the 2002 M_w 7.9 Denali earthquake exhibit peak slip within the upper ∼10 km, diminishing rapidly to about 18 km depth (Elliott et al., 2007; Hreinsdóttir et al., 2006; Wright et al., 2004), consistent with locally-recorded seismicity along the Denali fault (Biegel et al., 2024; Eberhart-Phillips et al., 2003; Ratchkovski et al., 2004; Choi et al., 2021). Older waveform-modelled earthquakes include the 1985 M_w 6.7 and 6.8 Nahanni doublet in the Mackenzie mountains of Canada, placed at 6–7 km centroid depth (Choy and Boatwright, 1988), consistent with local aftershock surveys that indicate focal depths mostly above ∼12 km (Horner et al., 1990). Additionally, the 1946 M_s 7.2 Vancouver Island earthquake was modelled by Rogers and Hasegawa (1978) to have a focal depth of 20–30 km. Subsequent geodetic (Slawson and Savage, 1979) and paleoseismic studies (Lynch et al., 2023) suggest that the peak slip of this event was shallow (<5km). The shallow seismicity across Alaska and northwestern Canada is likely the result of thinned back-arc lithosphere and high heat flow (Hyndman, 2023), and the limited results from the Koryak Highlands hint that the same may be true further west.

The regions that comprise the north Pacific Cordillera have undergone similar tectonic histories of terrane accretion, deformation, magmatism and batholith emplacement (Dickinson, 2004; Miller et al., 2002), and many of the major crustal earthquakes listed above are closely associated with terrane boundaries along which crustal fragments accreted to North America during the Mesozoic and early Cenozoic (Figure 2.9). For example, the 1991 M_w 6.7 and 2006 M_w 7.6 Olyutorski earthquakes ruptured the major Khatyrka–Vyvenka fault zone, the 2002 Denali rupture closely follows the Mesozoic suture of the Wrangellia and Yukon terranes (Fitzgerald et al., 2014), and the 2018 Kaktovik earthquakes may have partially reactivated terrane-bounding reverse faults associated with construction or reactivation of the Brooks Range (Gaudreau et al., 2019). This suggests that these first order geological boundaries form long-lasting zones of weakness along which seismic hazards remain elevated long after terrane accretion. However, in rupturing a fault in close proximity but orthogonal to a terrane boundary, the 2020 Koryak Highlands earthquake demonstrates that hazards are not restricted to the major terrane bounding faults, but encompass secondary faults with minimal geomorphic or geological signatures. Like many other parts of the northern Pacific Cordillera, the Koryak Highlands likely exhibits slow strain rates with faults that may have recurrence periods of thousands to tens of thousands of years (Li et al., 2018), such that Pleistocene glaciations may have eroded pre-existing geomorphic signals (e.g. Clague and James, 2002). This is one of many challenges to studying slowly deforming faults in high latitude, sub-Arctic regions, along with sparse seismic and geodetic instrumentation, GNSS strain signals that are masked by locking of the subducting Pacific plate and/or by glacio-isostatic rebound, and remote, mountainous, and densely forested terrain.

2.7 Conclusions

The 2020 M_w 6.4 Koryak Highlands earthquake ruptured a previously unknown, SE-striking, left-lateral strike-slip fault, orthogonal to the main sutures that bound the Khatyrka-Vyvenka zone. The earthquake likely propagated unilaterally northwestwards at approximately 1.3 km/s. This slow rupture speed, together with the lack of any clear fault-related geomorphology along the surface trace, indicates that the causative fault was structurally immature. The earthquake also exhibits a pronounced shallow slip deficit, though this may be related more to its moderate magnitude than to fault structural immaturity. The base of our slip model at 11 km depth hints at a relatively thin seismogenic layer thickness, consistent with other parts of the north Pacific Cordillera. Remote, mountainous, and recently glaciated areas like the Koryak Highlands are particularly challenging to study, but modern, remotely sensed or teleseismic data still allow us to characterize the geometry and kinematics of this earthquake fairly precisely. Our study highlights how unknown or uncharacterized faults may accommodate potentially damaging earthquakes along or near terrane boundaries within the northern North America plate.

2.8 Acknowledgements

This study is funded through grants from the Natural Sciences and Engineering Research Council of Canada (NSERC), the Canada Foundation for Innovation (CFI), and the BC Knowledge Development Fund (BCKDF), as well as a James A. & Laurette Agnew Memorial Award to Guy Salomon, and a Tier 2 Canada Research Chair to Edwin Nissen. The authors are grateful to Ezgi Karasözen, Lucinda Leonard, and Andrew Schaeffer for discussions of this work, and Jeffrey Freymueller and an anonymous reviewer for comments that improved the manuscript.

2.9 Data availability

The Appendix (A) comprises of 3 tables (A.1–A.3), 11 figures (A.1–A.11), and 2 data files.

The images used to produce the interferograms are freely available and were downloaded from the ESA's open access hub (European Space Agency, 2020). Several topography datasets were used in this study, including the Copernicus GLO-30 Digital Elevation Model (European Space Agency, Singergise, 2021), the GEBCO bathymetry dataset (GEBCO Compilation Group, 2023), and 2 m resolution ArcticDEM data along the InSAR fault (Porter et al., 2022), all of which are available on OpenTopography (https://opentopography.org/, last accessed July, 2024). Earthquake arrival times were collected from the International Seismological Centre (ISC) bulletin (DOI:10.31905/d808b825). Focal

mechanisms were downloaded from the Global Centroid-Moment-Tensor Project (Ekström et al., 2012). Figures were plotted using the Generic Mapping Tools, Version 6 (Wessel et al., 2019). Fault lines in figures were acquired from the Active Faults of Eurasia Database (AFEAD, Zelenin et al., 2022).

Chapter 3
Mapping fault geomorphology using drone lidar

3.1 Author names, affiliations and roles

Salomon, G.[1], Finley, T.[1], Nissen, E.[1], Stephen, R.[2], Menounos, B.[3,4]

[1] School of Earth and Ocean Sciences, University of Victoria, Victoria, BC, Canada
[2] Department of Geography, University of Victoria, Victoria, BC, Canada
[3] University of Northern British Columbia, Prince George, BC, Canada
[4] Geological Survey of Canada, PO Box 6000, Sidney, BC V8L 4B2, Canada

This chapter has been published in *Seismica* (https://doi.org/10.26443/seismica.v3i1.1186). I undertook the data processing (excluding Columbia Lake), analysis, figure creation, and wrote the manuscript. Dr Edwin Nissen supervised the project, provided manuscript edits and funding. Roger Stephen developed the processing workflow, and together with Theron Finley and myself, assisted with the data collection. Theron Finley provided manuscript edits and processed the Columbia Lake dataset. Brian Menounos provided airborne lidar for the Eastern Denali fault case study and manuscript edits.

3.2 Abstract

The advent of sub-metre resolution topographic surveying has revolutionized active fault mapping. Light detection and ranging (lidar) collected using crewed airborne laser scanning (ALS) can provide ground coverage of entire fault systems but is expensive, while Structure-from-Motion (SfM) photogrammetry from uncrewed aerial vehicles (UAVs) is popular for mapping smaller sites but cannot image beneath vegetation. Here, we present a new UAV laser scanning (ULS) system that overcomes these limitations to survey fault-related topography cost-effectively, at desirable spatial resolutions, and even beneath dense vegetation.

In describing our system, data acquisition and processing workflows, we provide a practical guide for other researchers interested in developing their own ULS capabilities. We showcase ULS data collected over faults from a variety of terrain and vegetation types across the Canadian Cordillera and compare them to conventional ALS and SfM data. Due to the lower, slower UAV flights, ULS offers improved ground return density (∼260 points/m^2 for the capture of a paleoseismic trenching site and ∼10–72 points/m^2 for larger, multi-kilometre fault surveys) over conventional ALS (∼3–9 points/m^2) as well as better vegetation penetration than both ALS and SfM. The resulting ∼20–50 cm-resolution ULS terrain models reveal fine-scale tectonic landforms that would otherwise be challenging to image.

3.3 Non-technical summary

Lidar remote sensing uses light pulses from a laser instrument to measure distances to objects and surfaces to create high precision, three-dimensional models. It is useful for mapping the ground surface where obscured by forest, because laser pulses that avoid foliage and branches will sample the ground surface while those that don't can be digitally removed, unlike in photogrammetry. Typically, lidar instruments are mounted on tripods (terrestrial laser scanning) or crewed aircraft (airborne laser scanning). Recently, lidar systems have become compact and light enough to be deployed from uncrewed aerial vehicles (UAVs, or drones) and this technology is being adopted across many disciplines. Here, we describe some of the first applications of a drone lidar system to study landforms generated by active faults, and illustrate its capabilities using surveys of a variety of faulted landscapes with different vegetation types across western Canada. Our system offers a cost-effective way of obtaining otherwise expensive lidar data, and compares favourably against established methods of topographic mapping, allowing us to survey the landscape in finer detail than was previously possible. The drone system is subject to practical and regulatory constraints and we discuss ways that these could be mitigated in the future.

3.4 Introduction

Lidar (light detection and ranging, see Table 3.1 for alternative capitalizations as well as other acronyms) is an increasingly popular terrestrial remote sensing method that combines the return times of reflected or back-scattered laser pulses with information on the location and orientation of the laser scanner to produce a dense 'point cloud' containing the Cartesian (x, y and z) co-ordinates of a geographic target (Xiaoye Liu, 2008; Glennie et al., 2013). The sub-metre point spacings characteristic of lidar data are finer than the ∼1–10 metre pixel dimensions typical of modern satellite-derived digital elevation models (DEMs) (e.g. Morin et al., 2016; Hodge et al., 2019; Wang et al., 2019; Benavente et al., 2021; Salomon et al., 2022). Furthermore, since multiple laser returns can be distinguished from the same

outgoing pulse, and since distinct canopy returns can be filtered out, lidar is able to penetrate vegetation to yield a bare Earth digital terrain model (DTM) of the ground surface. These unique attributes of lidar remote sensing have contributed to an explosion of interest across many geospatial fields, including tectonic geomorphology (Meigs, 2013). It is becoming common practice to acquire lidar along fault surface traces as it provides some of the best data for constraining fault offsets, kinematics, and scarp morphology (e.g. Cunningham et al., 2006; Hilley et al., 2010; Zielke et al., 2010, 2015; Elliott et al., 2012; Salisbury et al., 2012; Johnson et al., 2018; Wei et al., 2019), as well as a topographic baseline for mapping any future earthquake deformation (Diederichs et al., 2019; Glennie et al., 2014; Ishimura et al., 2019; Lajoie et al., 2019; Nissen et al., 2014b; Oskin et al., 2012; Scott et al., 2018; Wedmore et al., 2019) or aseismic fault creep (DeLong et al., 2015; Scott et al., 2020). Lidar is especially useful in regions such as northwestern North America, where widespread forest cover may otherwise obscure fault scarps or other earthquake-related landforms (e.g. Haugerud et al., 2003; Hunter et al., 2011; Morell et al., 2017; Nelson et al., 2017; Schermer et al., 2021; Witter et al., 2021).

Lidar data are typically collected through one of two established methods. In Terrestrial Laser Scanning (TLS), landscapes are mapped at low incidence angles from a laser instrument mounted on a stationary tripod (Telling et al., 2017). TLS can achieve very dense point clouds with 100s to 1000s of points per square metre (pts/m^2), but to avoid shadowing of features of interest behind objects like tree trunks or undulating topography, the scanner is typically deployed at several locations. Furthermore, due to the time taken to set up each new scanner position, TLS surveys are best suited for relatively small outcrop or landform-scale acquisitions (e.g. Jones et al., 2009; Haddad et al., 2012; Gold et al., 2013; Wiatr et al., 2013; Bubeck et al., 2015; DeLong et al., 2015; Wedmore et al., 2019). In rare instances, terrestrial lidar surveys have been expanded by mounting the scanner on motorized vehicles, backpacks, or tethered balloons, a configuration termed Mobile Laser Scanning (MLS) (Brooks et al., 2013; Brooks et al., 2017; Glennie et al., 2013; Nevitt et al., 2020; Zhu et al., 2022). The second, more prevalent method is Airborne Laser Scanning (ALS), where the laser scanner is mounted onto a crewed aircraft and flown over the target area (Glennie et al., 2013; Xiaoye Liu, 2008). This method is suitable for collecting much larger datasets, typically in 1–2 km wide swaths that can extend tens to hundreds of kilometres along linear targets such as fault traces, coastlines, or infrastructure corridors (e.g. Toth et al., 2007; Prentice et al., 2009; Hubbard et al., 2011; Oskin et al., 2012; Langridge et al., 2014; Clark et al., 2017; Johnson et al., 2018). ALS generally yields much lower point densities than TLS with typical values for modern acquisitions being 10–15 pts/m^2. Other limitations associated with ALS include the steep cost of deploying a crewed fixed-wing aircraft (10s to 100s of thousands of dollars per survey), restrictions on what altitudes and speeds they can fly at (which limits the raw point density), and constraints on scanning angles that can prevent penetration of the densest vegetation (Resop et al., 2019; VanValkenburgh et al., 2020). Rotary-wing aircraft (helicopters) are less constrained in terms of altitude and speed

and have been used to achieve higher point density in some lidar surveys (Chen et al., 2015), but are generally even more cost-prohibitive.

Recently, a proliferation of inexpensive uncrewed aerial vehicles (UAVs)—commonly referred to as 'drones' and formally as remotely piloted aircraft systems (RPAS)—have provided a more accessible means of terrain mapping, including for seismology and active tectonics (e.g. Bemis et al., 2014; Johnson et al., 2014; DuRoss et al., 2019). Until very recently, this has involved deploying cameras and using sophisticated photogrammetric algorithms to create Digital Surface Models (DSMs) (e.g. Harwin and Lucieer, 2012; James and Robson, 2012; Westoby et al., 2012), with consequently only very limited ability to map forested landscapes. However, the recent development of smaller, lighter laser scanners has opened up the possibility of collecting lidar datasets from UAV platforms, referred to from now on as drone lidar or UAV laser scanning (ULS) (Wieser et al., 2016). This new advancement has seen some early adoption in the fields of archaeology (Risbøl and Gustavsen, 2018; VanValkenburgh et al., 2020), forestry and ecology (Brede et al., 2017; Kellner et al., 2019; Tomsett and Leyland, 2021), and fluvial and landslide geomorphology (Resop et al., 2019; Pellicani et al., 2019), but its effectiveness for mapping active faulting has not yet been demonstrated.

This paper introduces a state-of-the-art ULS system (Figure 3.1) developed at the University of Victoria to study the geomorphology of putative active faults across the Canadian Cordillera. This is a region of widespread seismicity (Ristau et al., 2007) and elevated seismic hazard (Kolaj et al., 2020), but aside from the major plate boundary faults, only a few seismogenic faults have been conclusively identified and mapped owing to steep terrain, dense forest cover, and recent glaciation (e.g. Morell et al., 2017; Harrichhausen et al., 2023). We begin in Section 3.5 by describing the drone platform and instrumentation as well as our data collection, processing and analysis workflows. Our aim here is to provide a blueprint for other seismologists and geomorphologists interested in developing their ULS systems. In Sections 3.6–3.9, we then showcase examples of ULS lidar data collected using our drone platform along four faults with differing surface expressions in four unique types of vegetation cover from across western Canada (Figure 3.2 and Table 3.2). The spatial scales of these case studies vary from a paleoseismic trench site with dimensions of a few hundred metres surveyed in a few hours (Harrichhausen et al., 2023) to regional acquisitions along fault sections totalling several kilometres in length mapped over several days (Finley et al., 2022a). In each case study, we compare the ULS data both quantitatively and qualitatively with existing ALS data, as well as SfM data where available. Particular focus will be on vegetation penetration performance, achievable ground return densities, and their impacts on derived DTM resolutions for the different lidar acquisition modes. In Section 3.10, we assess the impact of UAV flight speed on survey duration, point density and data quality, before discussing the unique applications, advantages, and limitations of ULS in active tectonics research. One of the principal advantages is simplified and cheaper repeat observations, with the potential for imaging co-seismic rupture, off-fault deformation, and post-seismic afterslip

Table 3.1: Acronyms and initialisms used in this paper and/or common within the wider literature on drone-based and lidar remote sensing, with abbreviated definitions where helpful. Synonymous terms are within brackets.

Term	Description
AGL	Above ground level.
ALS	Airborne laser scanning—lidar from a crewed aircraft. (ALSM & airborne lidar).
ALSM	Airborne laser swath mapping—lidar from a crewed aircraft. (ALS & airborne lidar).
BVLOS	Beyond visual line-of-sight.
DEM	Digital Elevation Model—a 3-D representation of terrain heights. (DTM).
DoD	DEM of Difference—an elevation difference map between two DEMs.
DSM	Digital Surface Model—a 3-D representation of Earth surface heights, incl. natural or man-made objects.
DTM	Digital Terrain Model—a 3-D representation of terrain heights. (DEM).
GCP	Ground control point—an identifiable point on Earth's surface with known location used for geo-referencing.
GNSS	Global Navigation Satellite Systems—a system that uses satellites to provide autonomous geopositioning.
GPS	Global Positioning Systems—the world's most utilized GNSS, and sometimes used synonymously.
ICP	Iterative closest point—an algorithm used to co-register two point clouds.
IMU	Inertial Measurement Unit—a device that tracks orientation using magnetometer, accelerometer, and gyro.
INS	Inertial Navigation System—a device integrating an IMU and GNSS.
.LAS	Industry standard binary file format used for archiving of lidar data.
.LAZ	Compressed file format used for the interchange and archiving of lidar data.
lidar	Light detection and ranging, with varied capitalization (LiDAR, LIDAR, Lidar).
MLS	Mobile laser scanning—lidar from a roving scanner on or tethered to Earth's surface.
M3C2	Multiscale Model to Model Cloud Comparison— a method that measures differences between point clouds.
PPP	Precise Point Positioning—a GNSS method that calculates positions with errors of a few centimetres.
RINEX	Receiver Independent Exchange Format—a data format for raw GNSS data.
RPAS	Remotely Piloted Aircraft System. Synonymous with UAV and drone.
RTH	Return to Home—a feature of some UAS that allows the drone to return autonomously to its take-off point.
sbet	Smoothed best estimate of trajectory—relating to the processing of UAV flight paths.
SfM	Structure-from-Motion—an algorithm for estimating 3-D scene structure from a set of photographs.
sUAS	Small Unmanned Aircraft System—a UAV weighing less than 25 kg.
TLS	Terrestrial Laser Scanning—lidar from stationary location(s) on Earth's surface.
UAS	Uncrewed Aircraft System—a UAV and its accessories
UAV	Uncrewed Aerial Vehicle. (RPAS or drone).
ULS	UAV Laser Scanning—lidar from a UAV platform, also referred to as "drone lidar".
VLOS	Visual line-of-sight.

Table 3.2: Summary of case studies described in this paper. The drone lidar platform was tested in several different tectonic settings and climatic regions along faults of a variety of kinematic styles within the Canadian Cordillera in British Columbia and the Yukon. Canadian vegetation types are from Baldwin et al. (2019).

Section	Fault	Target and landscape description	Vegetation Type	Area (km^2)	Time to Collect
3.6	XEOLXELEK - Elk Lake fault, Vancouver Island	Reverse fault scarp within a suburban park	Pacific Dry Forest	0.01	5 hours (1 day)
3.7	San Juan fault, Cowichan Valley, Vancouver Island	Strike-slip fault within a steep-sided valley	Pacific Cool Temperate Forest	2.8	14 hours (2 days)
3.8	Southern Rocky Mountain Trench, East Kootenay	Suspected fault scarp crossing gently-sloping alluvial fans	Cordilleran Dry Forest	3.1	16 hours (3 days)
3.9	Eastern Denali, Kluane Lake	Major strike-slip fault in a broad glacial valley	Northwestern Boreal forest	10.4	12 days

at finer spatial (<50 cm) and temporal (<1 day) resolutions. Additionally, the higher spatial resolutions attainable with ULS allow for more confident measurement and interpretation of subtle fault scarp morphology. The limitations of ULS systems include spatial coverage, which is restricted by battery life, flight constraints imposed by civil aviation authorities, and the necessity of road access to launch sites with good visual sightlines, and we finish the paper by discussing ways in which these limitations might be mitigated in the future.

3.5 Methods

3.5.1 The ULS system

Our ULS platform was built using several commercially available and custom-built components (Figure 3.1). The former comprise a DJI Matrice 600 Pro hexacopter, a Riegl miniVUX-1UAV laser scanner, an Applanix APX-20 UAV Inertial Navigation System (INS), and a Trimble AV14 antenna. Custom-built elements include an interface board used to integrate the laser scanner and INS and a housing and mounting mechanism. The 2.75 kg payload is mounted to the drone with a dovetail-style connector, similar to those used in motion-stabilized gimbals for cinematography.

The DJI Matrice 600 Pro hexacopter has a payload capacity of 6 kg, more than double what we deploy. It uses one set of six TB47S Lithium-Ion Polymer batteries per flight (4500 mAh), enough power for ∼20 minutes of flying with our payload. Notably, these batteries are just below the 100 watt-hour rating restriction imposed by civil aviation authorities, allowing us to travel to field sites with the drone system via commercial airline. The drone is

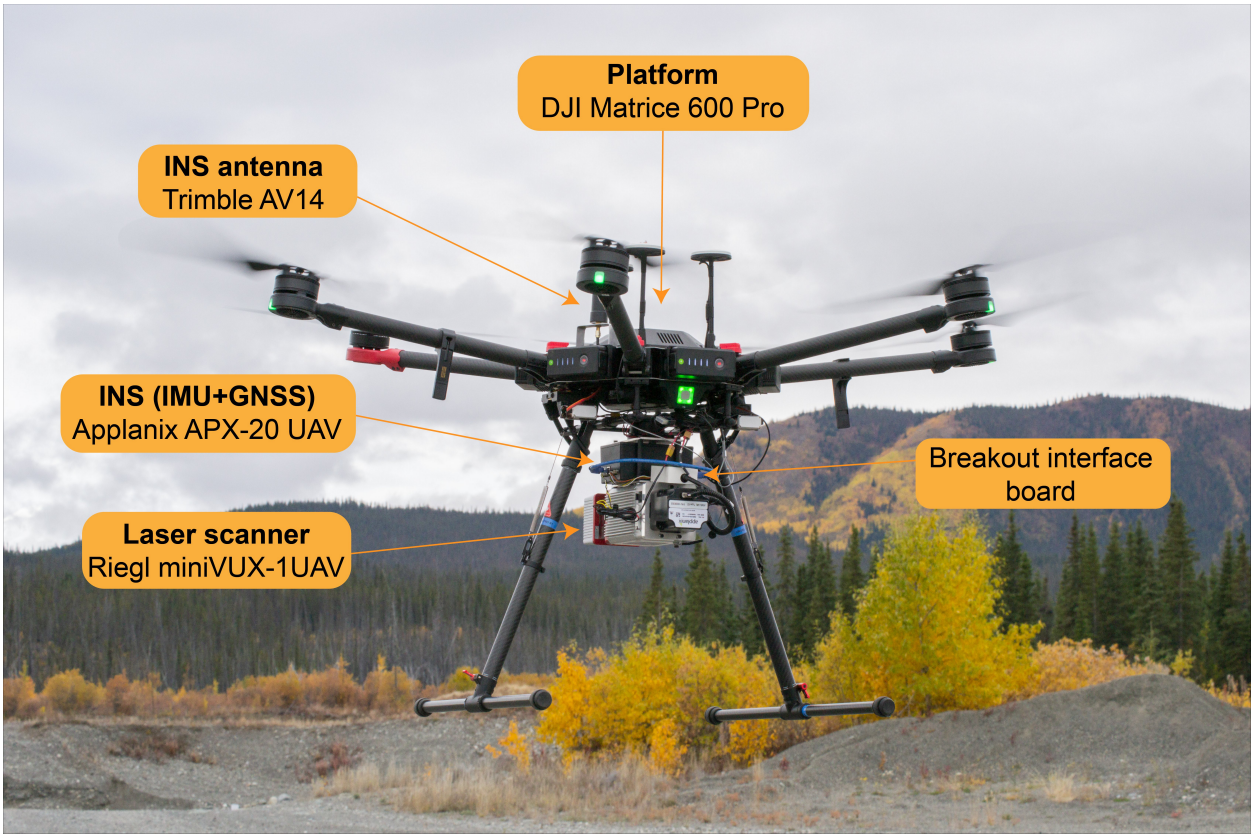

Figure 3.1: Annotated photograph of the drone platform and instrumentation used in this study. For scale, the full diameter of the drone, including rotor blades, is 1.66 m.

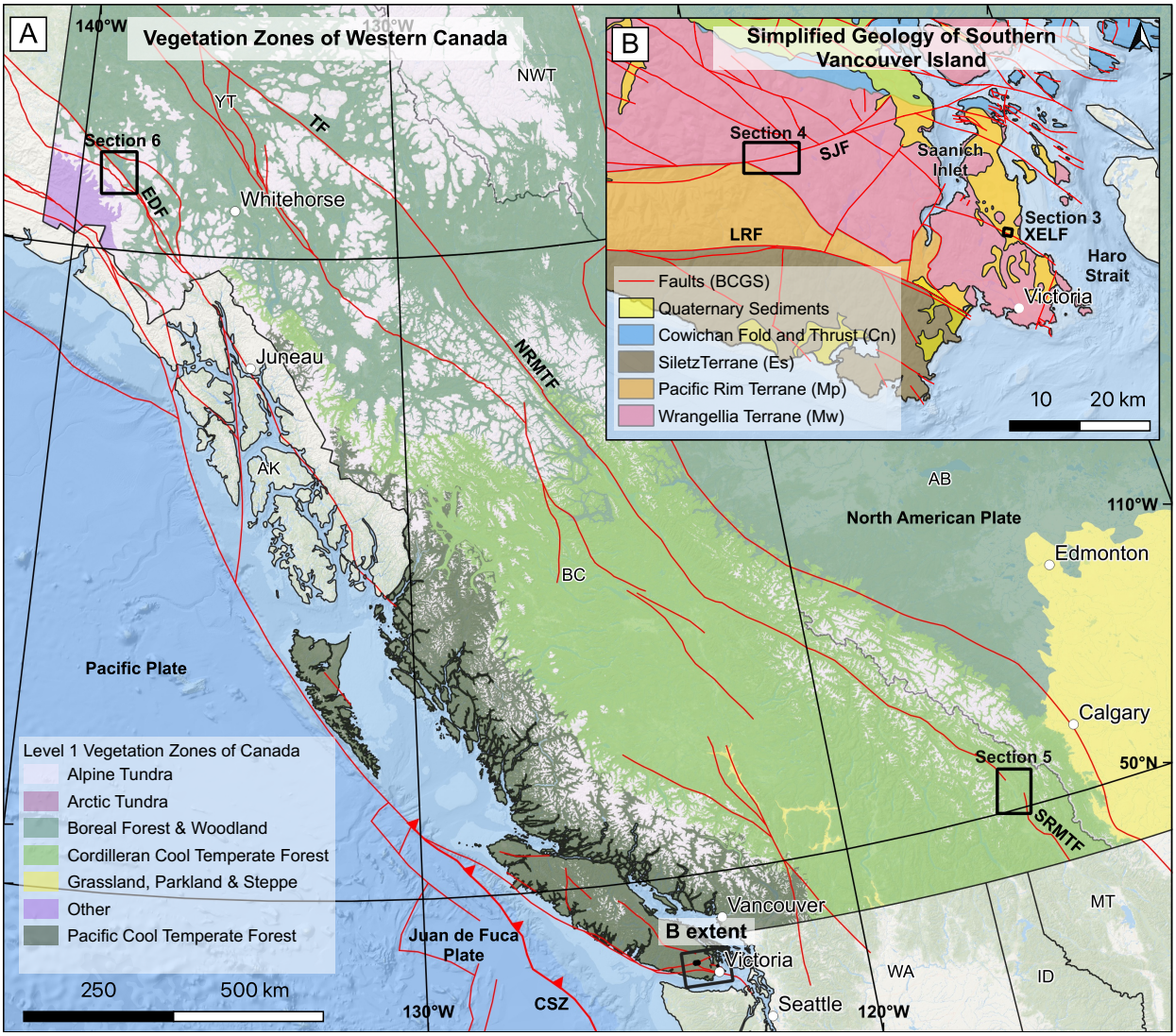

Figure 3.2: Location of case study sites (Table 3.2). (A) Level 1 Vegetation zones for Canada from Baldwin et al. (2019). Major faults are in red, some of which have been labelled. CSZ: Cascadia Subduction Zone, EDF: Eastern Denali fault, NRMTF: Northern Rocky Mountain Trench fault, SRMTF: Southern Rocky Mountain Trench fault, TF: Tintina fault. (B) Simplified geological map for southern Vancouver Island with major faults labelled, modified from the BC Geological Survey compilation by Cui et al. (2017). LRF: Leech River fault, SJF: San Juan fault, XELF: XEOLXELEK-Elk Lake fault. Abbreviations for states, provinces and territories are as follows; AB: Alberta, AK: Alaska, BC: British Columbia, ID: Idaho, MT: Montana, NWT: Northwest Territories, WA: Washington, YT: Yukon. Background imagery is from Esri (2022).

manoeuvred via a remote controller and transmitter with a manufacturer-stated maximum operating distance of 5 km, though in practice, we begin to encounter connectivity issues beyond ∼1.5 km in forested and mountainous terrain. The pilot must abide by flight constraints imposed by civil aviation authorities, including altitude limits of 400 ft (121.92 m) above ground level (AGL) in both Canada and the U.S., restrictions to flights over people, and maintenance of visual line-of-sight between the pilot (or a visual observer in constant radio contact with the pilot) and the drone. Many countries have similar UAV regulations, although exact parameters for flight height and horizontal distance do vary (Stöcker et al., 2017). In Canada, pilots must have obtained Advanced Operations drone pilot certification from Transport Canada (Transport Canada, 2022) through an online multiple-choice test and an in-person flight review. This certification allows the pilot to operate in controlled airspace with any drone weighing less than 25 kg. Many other national aviation authorities offer similar certifications (e.g. Federal Aviation Administration, 2023; UK Civil Aviation Authority, 2023; European Union Aviation Safety Authority, 2022; Civil Aviation Safety Authority, 2021).

Weighing 2 kg and with a manufacturer-stated optimum altitude of 80 m AGL, the miniVUX-1UAV laser scanner is specifically designed for deployment from a drone. It offers an eye-safe laser (at Laser Class 1) with a pulse repetition rate of 100 kHz and a 360° field of view. The laser footprint diameter at optimum altitude is 6.4 cm at nadir and 9 cm at 45° from nadir. The scanner can record up to 5 returns from a single laser pulse, making it suitable for application in densely vegetated areas where SfM terrain mapping would be unfeasible. The Applanix APX-20 UAV INS integrates a Global Navigation Satellite Systems (GNSS) device and an Inertial Measurement Unit (IMU), which together with the attached Trimble AV14 antenna track the precise location and orientation of the laser scanner. This allows the coordinates of points within the final point cloud to have sub-decimetre accuracies (3–5 cm). The breakout board interfaces with the laser scanner using a customized circuit board which allows communication and timing between components, streams data between the INS and the laser scanner, and distributes power to both of these systems.

Our ULS system also makes use of a range of auxiliary equipment (Figure 3.3A). This includes a Trimble R12 GNSS base station (and tripod) for post-processing the drone trajectory and—if the best possible absolute georeferencing is desired—a separate Trimble R12 GNSS rover unit, TSC7 handheld computer and monopod for surveying ground control points (GCPs). For these we use 120 cm × 120 cm fabric harlequin-iron cross targets, which we secure to the ground with hammer and nails. We also pack a field laptop with flight planning software installed, an iPad or cell phone to connect to the radio controller, walkie-talkies to allow constant communication between crew members, an inverter generator (minimum 2200 watts to support all charging needs), charging equipment and spare drone batteries to allow a quick succession of repeat flights, and field safety gear. All of the equipment fits inside our Jeep Wrangler field vehicle with room for three crew members and their personal gear.

3.5.2 Survey planning

Initial planning starts with consideration of three factors. Firstly, as our drone platform and auxiliary equipment (Figure 3.3) are too bulky to be carried easily by foot, launch sites must be accessible via vehicle. Existing coarse resolution DTMs, satellite imagery, and Google Streetview are great tools for identifying such spots. In areas with steep topography or forest cover, visual-line-of-sight is often impossible to maintain from the launch site and so we use one or more visual observers positioned in areas with good sight lines in constant communication with the drone pilot via walkie-talkie. Secondly, if the survey is located within classified airspace, approval must be applied for in advance. In Canada this can be done online through NAV Canada's NAV drone application. Thirdly, in the days leading up to the fieldwork we check the weather forecasts, as our drone cannot operate in any form of precipitation or in winds that are greater than 8 m s^{-1}.

Once these initial considerations are addressed, we use drone flight planning software to generate automated flight paths for our data collection. Map Pilot Pro by Maps Made Easy and Universal Ground Control Station (UgCS) by SPH Engineering have both been used successfully for this purpose, with the latter our current preference since it allows more control over survey design (custom base maps and images), flight parameters (e.g. altitude, speed), and laser parameters (e.g. field of view, swath overlap) such that a desired point density is achieved. There is a trade off between point density and areal coverage and the specific scientific goals of the survey need to be considered. These parameters are fine-tuned using Riegl's RiParameter software to ensure even point spacing, and set in the laser instrument using the RiAcquire tool. We discuss optimization of these parameters in section 3.10.1. Typical flight plans for fault-related studies consist of 2–8 strike parallel survey lines, and 2 cross-track lines for the purposes of track alignment in post-processing (Figure 3.3B). For larger surveys these will be undertaken in multiple flights in order to allow for battery replacement. Note that each individual flight must have a minimum of two overlapping lines, and it is best practice to design surveys that allow for the completion of full lines, rather than abandoning and resuming part-way along a line; overlapping data is critical for scanline alignment when merging flights in post-processing. In fault surveys when the desire is to achieve maximum coverage along-strike, the most efficient flight plans in our experience consume ∼35% battery on the outward track and ∼35% on the return track, allowing the drone to return to home safely at 30% battery, the depletion threshold recommended by the manufacturers. Survey extents are further limited by the need to maintain visual line-of-sight between the pilot, or one or more visual observers in constant radio contact with the pilot, and the drone. In the absence of obstacles we find this visual limit to be around ∼1.5 km, though it is often challenging in forested areas to find ideal sight lines. In practice, considering battery, radio controller connectivity, and line-of-sight requirements, we find that survey lengths from an individual launch site are limited to a maximum of ∼1.8 km even with visual observers present. Flight paths for the case studies presented in this study

are provided in the Appendix (B.1–B.11) to illustrate survey patterns required for different spatial extents and terrain.

3.5.3 Data acquisition

On the day of the survey, we drive to our launch site where we first set up the GNSS base station (Figure 3.3C). Getting the base recording started early ensures that there is a sufficiently long (minimum 3 hour) base observation for post processing the flight trajectories. The drone platform is assembled and the laser and IMU payload mounted onto it. Before uploading the automated flight plan, a short, manual test flight ensures that the controller is operating as expected and that the drone's gyroscope and magnetometer are calibrated. If desired, GCPs can be placed in 4–6 locations scattered across the survey footprint and clear of forest cover. These locations should ideally be situated beneath multiple overlapping and orthogonal flight lines. It is expedient to deploy GCPs before or during the drone setup and test flight, often by our visual observers as they move into position. In order to calibrate the IMU, the drone system is powered up and sits for 5 minutes of static calibration, followed by a dynamic calibration that involves accelerating, decelerating and strafing to the left and right. Finally, the flight plan is uploaded to the drone from our field laptop or tablet, after making any last minute adjustments as needed. The entire set-up period, from arriving at the launch site to the start of the first survey flights, typically takes an hour with two or three people present.

The drone is then launched and its automated flight pattern started, with pilot and visual observers in constant radio communication to ensure that it is always within sight and maintaining sufficient clearance of obstacles. Once the batteries approach the 30% depletion threshold, the drone is brought back to the landing spot, and the static calibration is repeated before the system can be powered down and the batteries changed for fresh ones. For larger surveys, it is necessary to bring several sets of batteries and generator to recharge depleted batteries and keep flying throughout the day. At our highest levels of operating efficiency, we find that 6 sets of 6 batteries (TB47S) and two DJI Hex Chargers, running simultaneously and continuously, are necessary to keep pace with surveying. Once the full survey has been successfully flown, the base station needs to remain running for a minimum of half an hour to ensure that its location is well constrained, as is recommended in both Riegl and Applanix documentation. If we are surveying GCPs with a GNSS rover, we usually do this after the final drone flight, and leave the base station running yet another half an hour as we pack up the remaining gear.

3.5.4 Data processing

After a successful survey, data from the laser scanner, the INS, and the GNSS base station and rover are copied to a workstation for processing. We follow the workflow summarized

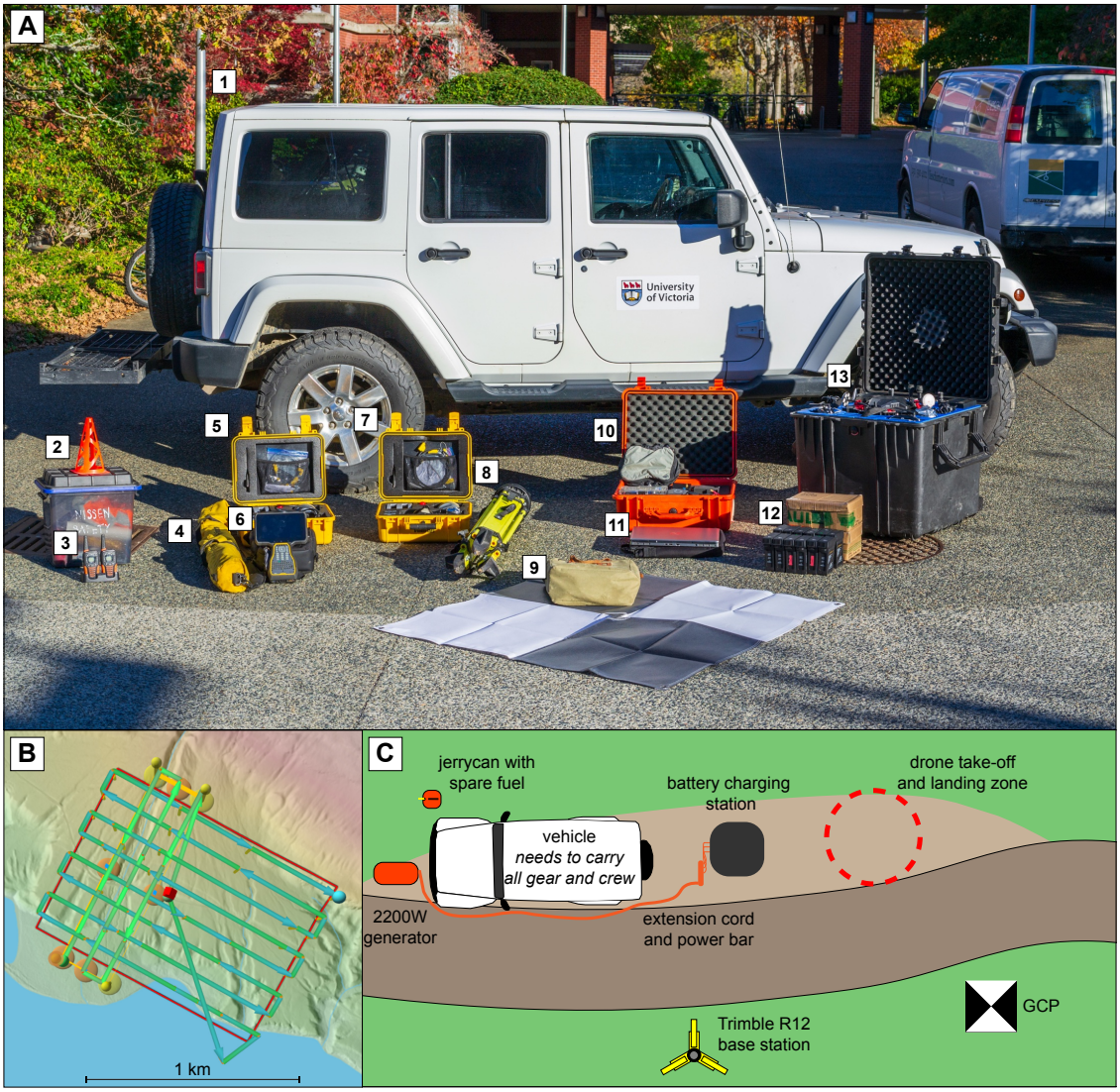

Figure 3.3: (A) Equipment needed for a typical acquisition. (1) Four-wheel drive vehicle. (2) Safety gear including first aid kit, traffic cones, high-visibility vests, and fire extinguisher. (3) Walkie-talkie radios for pilot and visual observers, plus chargers. (4) Trimble monopod for GNSS rover. (5) Trimble R12 GNSS rover in Pelican case. (6) TSC7 handheld computer for Trimble system. (7) Trimble R12 GNSS base station in Pelican case. (8) Trimble tripod for GNSS base station. (9) GCP targets, hammer and nails in carry bag. (10) Riegl miniVUX-1UAV laser scanner, Applanix APX-20 UAV INS, and assembly toolkit in Pelican case. (11) Windows laptop with UgCS flight planning and Riegl lidar processing software installed. (12) At least four but preferably six sets of batteries for the drone, plus two DJI Hex Chargers. (13) DJI Matrice 600 Professional hexa-copter in its customized carry-case (dimensions 68 cm $\times$ 53 cm $\times$ 49 cm). Not pictured: field iPad (to connect to the radio controller), generator (minimum 2200 W), extension cord, powerbar, and tarpaulin. (B) Flight line planning in UgCS for a segment of the Southern Rocky Mountain Trench acquisition (Section 3.8). The red pin is our launch site, the red box is our specified target area, and the blue-green lines are the drone flight lines. (C) Sketch-map showing a typical roadside survey set-up.

in Figure 3.4, which includes several pre-processing steps before the final point cloud is generated. The first step involves processing the GNSS data collected by the base station and rover. The base observation file is converted to RINEX format and uploaded to Natural Resource Canada's (NRCan) Precise Point Positioning (PPP) tool to post-process the GNSS observations and calculate an accurate base position using satellite orbit, clock and bias corrections. GCP locations surveyed with the rover can then be adjusted using the corrections to the base location from the PPP processing. The revised GCP locations are uploaded to the NRCan GPS-H tool to convert their ellipsoidal heights into orthometric heights, and the final coordinates exported as a csv file. The NRCan tools are free for use within the Canadian landmass, but other free online PPP options are available for use outside of Canada including; the National Geodetic Survey's Online Positioning User Service (OPUS, https://geodesy.noaa.gov/OPUS/index.jsp), GNSS Analysis and Positioning Software (GAPS) (Leandro et al., 2011), magicGNSS (Piriz et al., 2008), and the Automatic Precise Positioning Service (APPS) which uses JPL's GipsyX/RTGx software (Bertiger et al., 2020). The next pre-processing step involves refining the drone trajectory using INS data from the Applanix APX-20 UAV and converting this to orthometric heights. Working in Applanix's POSPac UAV software, the INS data are imported into a project and the base station observation added. The inertial processing tool is run to produce a smoothed best estimate of the trajectory (sbet), which is then exported in orthometric heights for import into the proprietary laser processing software (RiWorld).

We process the MiniVUX-1UAV lidar data in Riegl's proprietary RiProcess software. Each flight produces an individual laser file and associated trajectory. These are imported into the laser project and used to create an initial point cloud. The trajectories can be edited to remove unwanted data collected during turns or transits of the drone, leaving only data collected along the main survey lines. This is an important step as accelerations, decelerations, and rotations during turns and transits can negatively impact the final point cloud, creating sections with an uneven spacing of points. Once the point cloud has been sufficiently cleaned in this way, the individual flights can be merged into a single project. GCP coordinates can then be added by importing the csv file from GPS-H processing, and used to adjust and align the point clouds. In order to select the corresponding points in the laser file, we find that the cloud is best visualized using the reflectivity option. We select several points nearest the centre of each GCP target and average their elevations to account for centimetric vertical scatter. Once target centrepoints have been added for several flight lines, the flight line point clouds can be precisely georeferenced, aligned, and adjusted using the RiPrecision tool. Flat hard surfaces can be used to check the amount of scatter present within the point cloud. Many of our field sites are in remote regions with limited options for additional, independent ground control, and we have therefore not performed testing of georeferencing uncertainties of our system against geodetic control monuments. However, we estimate uncertainties in the order of ∼20 cm, based on random scatter observed in our point clouds (∼15 cm) as well as expected accuracies of our GNSS ground control. We ac-

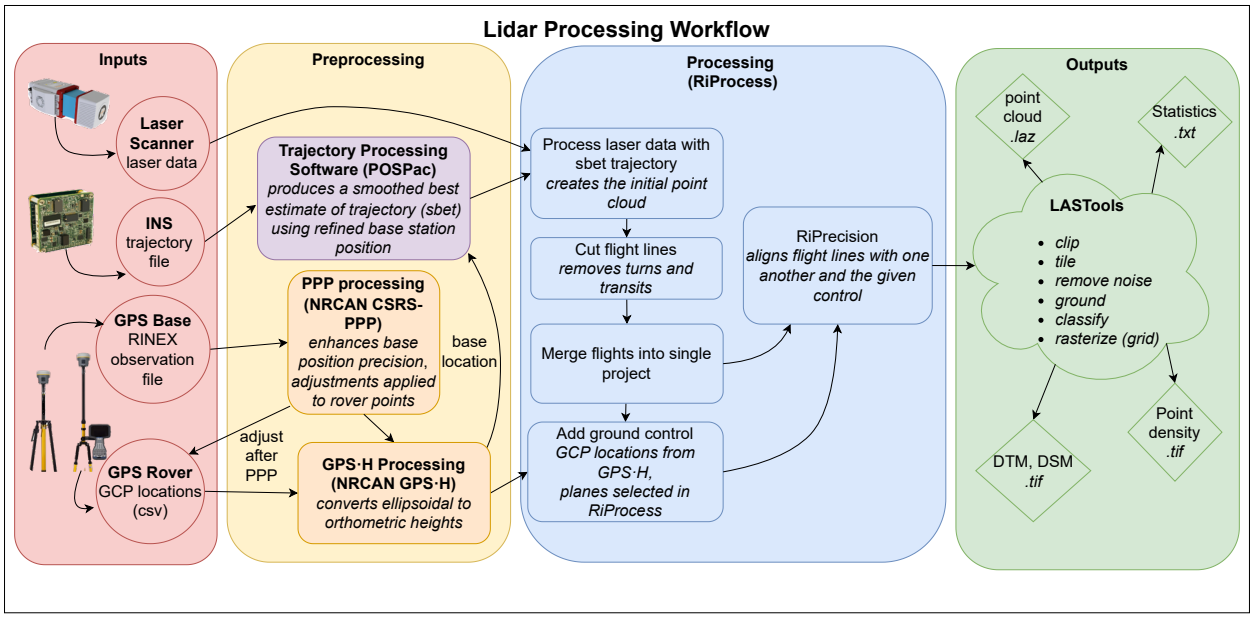

Figure 3.4: Flow diagram summarizing our ULS data processing workflow. Abbreviations used in this figure; DSM: Digital Surface Model, DTM: Digital Terrain Model, GPS: Global Positioning Systems, INS: Inertial Navigational System, NRCAN: Natural Resources Canada, PPP: Precise Point Positioning, sbet: smoothed best estimate of trajectory.

knowledge that constraining these errors is important, especially for applications involving change detection between multiple acquisitions. However, our ∼20 cm estimate compares favourably with uncertainties associated with ALS datasets, such as errors of ∼21 cm observed by Hodgson and Bresnahan (2004) over a range of land cover types, and horizontal and vertical errors of ∼29 cm and ∼9 cm observed by Glennie et al. (2013) in helicopter lidar acquisitions.

Once the flight lines have been aligned and geo-referenced, an unclassified point cloud can be exported for final classification, cleaning and gridding, for which we use a variety of programs within the licensed LAStools package (Isenburg, 2021). A copy of the shell script for classifying and rasterizing the raw lidar point cloud can be found in the Appendix (Script B1). To determine ground points we use lasground_new, a progressive morphological filter (Zhang et al., 2003). There are alternate options for ground classification, such as simple morphological filtering (Pingel et al., 2013) or cloth simulation filtering (Zhang et al., 2016), both of which can be freely used with the Point Data Abstraction Library (PDAL), an open-source library for processing and analysing point clouds (Butler et al., 2021). However, we prefer lasground_new because it has several parameters such as step, spike and bulge that can be adjusted to best find ground points according to the environment in which the data were collected, and which works well on steep, forested slopes (Cățeanu et al., 2017) that are prevalent in western Canada. Once the ground returns have been determined, we classify the remaining points using lasclassify. Other, optional steps at this stage of processing include

tiling the point cloud to allow for efficient multi-threaded processing and clipping it to a polygon of interest. Isolated noise points within the cloud are then removed using lasnoise before a DTM can be generated by rasterizing the ground points with lasgrid. Lasgrid can also be used to export other desired parameters such as point density per pixel, intensity, scan angle, and (if available) RGB values. The same LAStools parameters were used to process each dataset, with the only differences being the cell size for the resultant raster products, listed in Table 3.3.

3.5.5 Data comparisons and differencing

In Sections 3.6–3.9, we compare our fully processed drone lidar data with overlapping airborne lidar and SfM surveys in order to assess their consistency and to determine from any differences whether drone lidar offers advantages over the more established methods. For these analyses, we first used the iterative closest point (ICP) algorithm available within free CloudCompare software (http://www.danielgm.net/cc/) to perform a final registration of the drone and comparison point clouds. The ICP algorithm finds a rigid body transformation (translation and rotation) that iteratively minimizes the closest point pair distances between two point clouds. This step was taken in order to account for several sources of error, including random scatter within each point cloud, potential differences in the global registration of the two datasets including use of different vertical datums, and/or uncertainties within the control used to georeference either dataset. Consequently, remaining differences between the datasets (see below) will largely represent differences in the way each method characterizes the ground surface, coupled with (likely minor or localized) natural or anthropogenic landscape change that may occurred between each pair of surveys.

We used CloudCompare's M3C2 (Multiscale Model to Model Cloud Comparison) plugin (Lague et al., 2013) to calculate the distance between ground points within the compared datasets. The M3C2 algorithm computes the local distance between two point clouds along a normal surface direction. This calculation is performed upon the point clouds, without any meshing or gridding, providing a signed 3-D distance as opposed to alternative techniques which only offer either 2-D differences (e.g. vertical difference maps) or unsigned 3-D differences (CloudCompare's cloud-to-cloud distance tool). Additionally, the M3C2 method is designed for application to datasets of contrasting point spacings (DiFrancesco et al., 2020; Lague et al., 2013), and is thus well-suited for comparing dense drone lidar datasets with coarser airborne datasets. Within CloudCompare, the drone lidar dataset was selected to be cloud #1 and the airborne lidar or SfM dataset as cloud #2. The sign of the distance reflects where the reference point cloud was along the direction of the normal for each core point. For example, a negative M3C2 value indicates an area where the drone lidar data are located underneath the airborne lidar. The cloud distances were calculated with the 'multi-scale' option, meaning that the normal distances could be in any combination of horizontal and vertical. The coarser of the two datasets was used to determine the core points as its

wider point spacing reduces the number of computations required. The plugin produces a point cloud containing the M3C2 distances and areas with significant change as additional attributes. This was saved and rasterized, highlighting internal differences between the point clouds.

We further quantified disparities in the raster models produced for the drone lidar and comparison datasets by calculating their DEMs of Difference (DoD). For this, the drone lidar was first re-gridded (post point cloud alignment) at the same resolution as the airborne lidar DTM or SfM DSM, before the vertical topographic differencing was performed using the Geospatial Data Abstraction Library's gdal_warp tool (GDAL/OGR contributors, 2023). Following the methodology and conventions of Scott et al. (2021), the compare dataset (the newer drone lidar DTM) was subtracted from the reference dataset (the older airborne lidar DTM or SfM DSM). As such, negative DoD values represent areas in which the drone lidar DTM is lower than the reference ALS or SfM model, and vice versa. Note that this distance is purely vertical, unlike the M3C2 distances which are normal to the sparser of the point clouds. A shell script for differencing DTMs and generating histograms is provided in the Appendix (Script B2).

3.6 The X̲EOLX̲ELEK̶–Elk Lake fault: a local survey of a paleoseismic trench site

3.6.1 Background and motivations

The X̲EOLX̲ELEK̶–Elk Lake fault (XELF) is a newly-recognized active crustal fault within the forearc of the northern Cascadia subduction zone on southern Vancouver Island, BC (Harrichhausen et al., 2023). The fault is named after X̲EOLX̲ELEK̶ (pronounced *hul-lakl-lik*), the name given to Elk Lake by the W̲SÁNEĆ people. The XELF was first identified from provincial airborne lidar imagery (LidarBC, 2023) crossing Saanich peninsula between Saanich Inlet in the NW and Haro Strait in the SE (Figure 3.2B). The lidar data revealed several ∼N-facing fault lineaments including a 1-2.5 m high scarp displacing the surface of a Pleistocene glacial landform—a large, N–S drumlinoid ridge—between X̲EOLX̲ELEK̶ (Elk Lake) and Haro Strait. A site was chosen for paleoseismic trenching between the eastern lake shoreline and the Patricia Bay Highway, where the scarp passes through Elk-Beaver Lake Regional Park. The trench, excavated in August 2021, contained evidence that indicated the XELF has ruptured in at least one large (M_w ∼6.1–7.6) thrust earthquake during the late Holocene (Harrichhausen et al., 2023).

The eastern X̲EOLX̲ELEK̶ (Elk Lake) shoreline site (Figure 3.5A–B) provided an early and relatively simple test of our new ULS system, acquired prior to the planned trench and providing the best possible data for measuring the local scarp height. The survey area has dimensions of just ∼100 m and exhibits gentle relief other than a steep bank up to

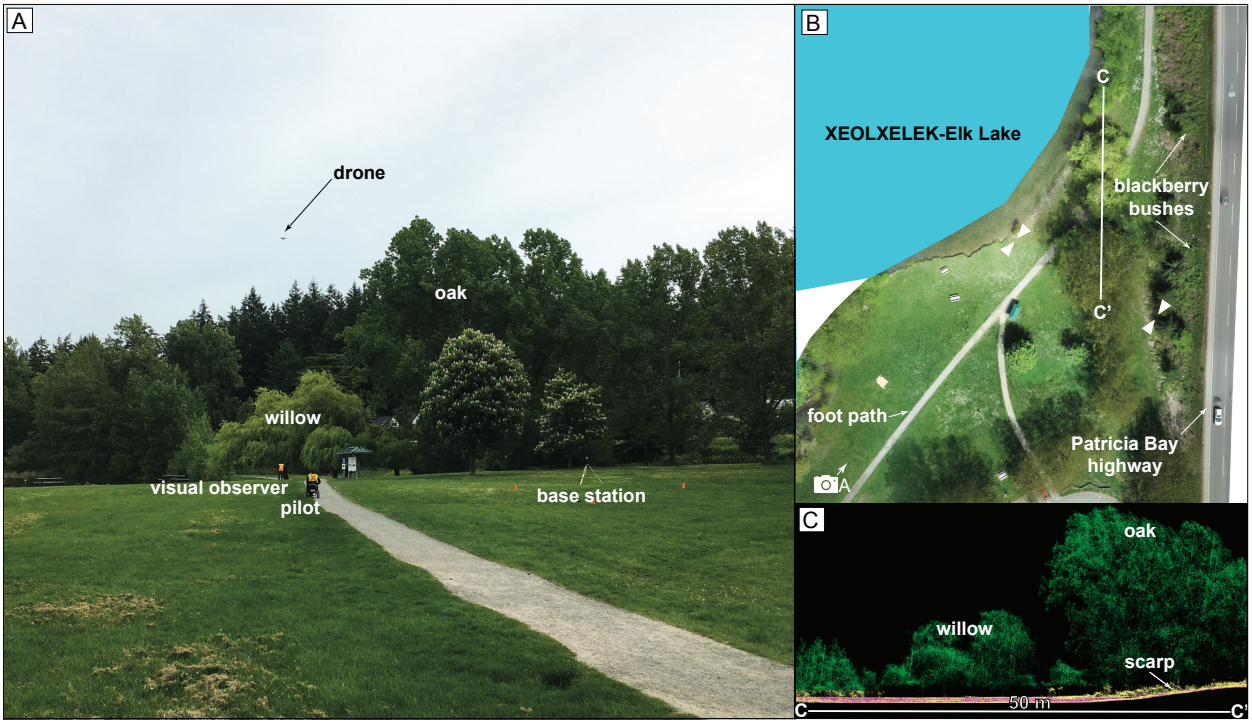

Figure 3.5: (A) Field photo showing ULS data collection at the eastern XEOLXELEK (Elk Lake) shoreline site. The photo location and orientation are shown in (B). The visual observer stands at the top of the XELF scarp and at the approximate mid-point of the future, NE-trending paleoseismic trench (Harrichhausen et al., 2023). (B) SfM-derived orthophoto of the acquisition site. White triangles indicate the location of the fault scarp. (C) Cross section C—C' through part of the classified drone lidar point cloud. Green points are vegetation, pink are ground points, and yellow points are unclassified.

the Patricia Bay Highway along the eastern boundary. The ground cover is mostly mowed grass as well as scattered blackberry bushes, deciduous trees (willow and oak) and conifers (Douglas Fir and Western Red Cedar), the tallest of which are around 35 m. Since the site lies within the municipal Elk-Beaver Lake Regional Park and on traditional WSÁNEĆ territory, further permissions had to be obtained to conduct research and operate a drone within the park, in addition to the civil aviation approvals described in Section 3.5.2 (see Acknowledgements).

3.6.2 ULS data acquisition and results

We surveyed the eastern XEOLXELEK (Elk Lake) shoreline site with our drone lidar system in May 2021 (Figure 3.5A), three months prior to the paleoseismic trench excavation by Harrichhausen et al. (2023). Our 100 m × 110 m (∼11,000 m^2) drone lidar dataset took a total of 4 hours to collect, including set-up, with a crew of a pilot, two visual observers, and two assistants who helped avoid flying over pedestrians in the busy park (see Section 3.5.1).

The drone was flown at a height of 45 m AGL in a cross-hatch pattern of N-S and E-W flight lines (Appendix B.1) and at a relatively slow speed of 2 m s^{-1}. These parameters were chosen in order to collect as high a resolution dataset as possible, with an expectation of >100 pts/m^2. At 45 m AGL the laser footprint is 3.6 cm at the centre of each 90 m-wide swath and 5 cm at the edges of the swath. Three GCPs were deployed and used to georeference the dataset.

Processing and classifying the drone lidar data using the workflow described in Section 3.5.4 yielded an average point density of 543 pts/m^2 and an average classified ground return density of 260 pts/m^2, leading to an average ground return spacing of ∼6 cm (Figure 3.6A–B, middle column, and Table 3.3). Classified ground returns constitute ∼48% of all points in the cloud. As expected, ground returns are densest away from the trees over areas of open, mowed grass, reaching values as high as ∼700 pts/m^2 where swaths from several flight paths overlap. However, a visual inspection of the classified point cloud in cross section also reveals successful imaging of the ground surface through tree and shrub foliage (Figure 3.5C). We find that a cell size of 20 cm optimizes the ULS raster DTM, minimizing its pixel dimensions without introducing widespread data gaps (Figure 3.6C, middle column). The cross-hatched point density pattern (Figure 3.6B, middle column) results from the perpendicular orientations of the survey flight lines.

3.6.3 Comparisons and differencing with ALS and SfM data

Our first comparison dataset is the provincial airborne lidar survey, flown in 2019 and available from the LidarBC (2023) portal. Within the ULS survey footprint, the ALS point cloud yields an average point density of 14 pts/m^2, an average ground return density of 9 pts/m^2 for a spacing of ∼33 cm, and a maximum ground return density of 10 pts/m^2 (Figure 3.6A–B, left column, and Table 3.3). The ALS point cloud also contains more, and larger, data gaps than the ULS cloud, indicating greater difficulty in imaging beneath vegetation. The ALS DTM has a cell resolution of 1 m, 25 times coarser than our ULS DTM (Figure 3.6C, left column). The fault scarp can be made out in both raster datasets as a gentle NNE-facing slope trending WNW-ESE across the centre of the target area, but the finer resolvability of the ULS dataset is evident in a small linear depression along one of the park footpaths, which is not visible in the ALS DTM. Though not a tectonic feature, this does highlight the potential for ULS to identify subtler fault offsets than are evident in traditional airborne lidar data.

Because much of the eastern XEOLXELEK (Elk Lake) shoreline site is covered by mowed grass, it provides our best opportunity out of all of our case studies to compare our drone lidar with SfM data. With this in mind, we surveyed the site with SfM two weeks before our drone lidar flights. Using a DJI Phantom 4 Professional V2 drone with the built-in camera, we captured 749 photographs which were then processed using the Agisoft Metashape Professional software package, with 15 GCPs deployed across the scene for georeferencing

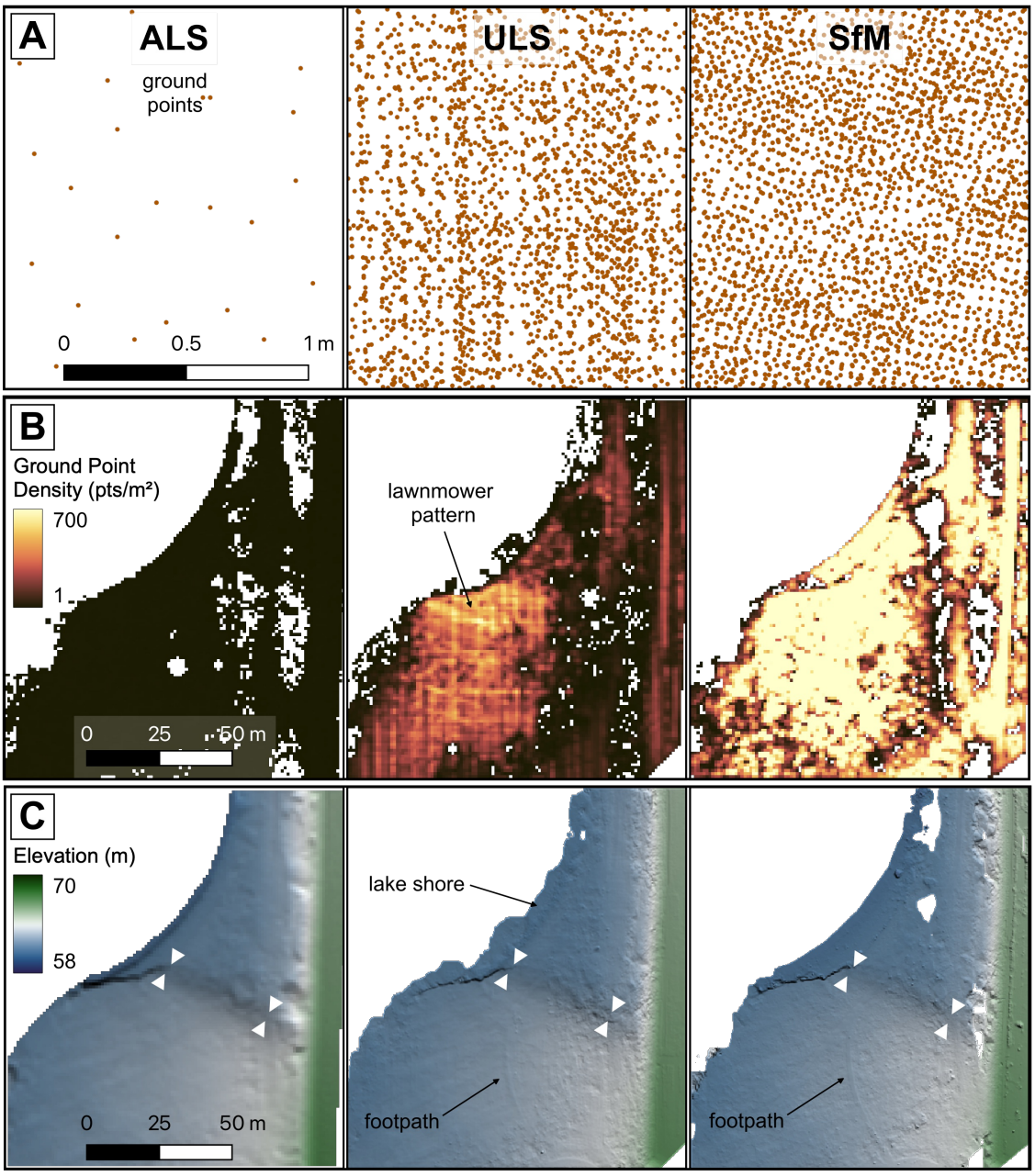

Figure 3.6: Comparison of topographic datasets at the eastern XEOLXELEK (Elk Lake) shoreline site: (left column) LidarBC ALS data, (middle) our ULS data, and (right) our SfM data. (A) Representative ground point clouds viewed at a roughly metric scale in order to contrast point spacings. (B) Survey-wide classified ground point densities. The same colour palette is used for each plot, and white spaces indicate areas without ground coverage (mostly trees and dense blackberry bushes). (C) Hillshaded DTMs illuminated from the SSW (210°) in order to highlight the NNE-facing fault scarp, further delineated by white arrows. The DTMs were constructed with an interpolation of 5 pixels in order to minimize holes.

(e.g. Johnson et al., 2014). After classifying the SfM point cloud with the LAStools LASclassify program, we yielded an average point density of 1,906 pts/m^2 and average classified ground point density of 554 pts/m^2 and spacing of 0.04 m (Figure 3.6A–B, right column, and Table 3.3). However, the SfM is strikingly less uniform than either lidar point clouds, containing far more, and larger, data gaps, reflecting its inability to image beneath vegetation (Figure 3.6B). As a consequence, we find that the optimal resolution of the SfM DTM is 20 cm (Figure 3.6C, right column), no finer than the ULS DTM despite their differing underlying ground point densities.

The ICP rigid body transformation that most closely aligns the ULS point cloud to the ALS point cloud involved a translation vector of 28 cm and rotations of $<$0.001 radians (Table 3.3). These values reflect small differences, within the expected error, of the global registration of the two surveys, with minimal tilting of one relative to the other. The mean M3C2 distance between the airborne and drone lidar point clouds was 5 cm with a standard deviation of 19 cm (Figure 3.7A, left panel). The equivalent DEM of Difference (DoD) exhibits a mean of -0.32 m and a standard deviation of 26 cm (Figure 3.7B, left panel). Positive values (blue colours) reflect areas where the ULS DTM is higher than the ALS DTM, and negative values (red colours) reflect those where the ULS DTM is lower. These non-zero values reflect a combination of factors, including residual misalignment of the point clouds (even after ICP co-registration) and internal vertical scatter, estimated from hard, flat, non-vegetated surfaces (e.g. roads, parking lots) at $\pm$6.7 cm in the ALS point cloud and $\pm$7.5 cm in our ULS point cloud. However, careful analysis of the DoD and M3C2 maps also supports a third cause of vertical differences. The largest differences (-2.6 m) were negative and are most likely the result some areas where returns off of dense vegetation were misclassified as ground in either of the datasets. These highest values are approximately in the same area that is covered by dense blackberry bushes (Figure 3.5). This also coincides with areas in the airborne lidar that have few to no points (Figure 3.6C). It is likely that the airborne dataset has its lowermost returns from within the blackberry bush rather than the ground surface, while the drone lidar, with its denser point cloud has managed to capture a better ground surface beneath these dense bushes. This also explains why the M3C2 distances are largest in the very same areas.

The ICP rigid body transformation that aligns the ULS and SfM point clouds involved rotations of $<$0.01 radians and a translation vector of 33 cm, again indicating consistency to within a few decimetres in global registration of the two datasets. The mean M3C2 distance

Table 3.3: Statistics of our ULS and comparison datasets (upper part of the table) and of the ICP alignments and subsequent M3C2 and DoD differencing (lower part of the table). ALS statistics are calculated from within the footprints of the corresponding ULS surveys, allowing a like-for-like comparison. % pts ground is the percentage of all lidar returns classified as ground.) Table on next page.

General Acquisition Information

Section	*Fault (site)*	*Data type*	*Provider*	*Area (km^2)*	*Point density (pts/m^2)*	*Ground return density (pts/m^2)*	*Ground return spacing (m)*	*% pts ground*	*DTM cell size (m)*
3.6	XELF	ULS	This study	0.01	543.39	260.11	0.06	48	0.2
	XELF	ALS	LidarBC		13.97	9.00	0.33	64	1.0
	XELF	SfM	This study		1906.16	554.04	0.04	29	0.2
3.7	SJF	ULS	This study	2.81	130.28	13.38	0.29	10	
	east			1.21	141.70	10.80	0.30	7	0.5
	west			1.59	121.59	17.24	0.24	13	0.5
	SJF	ALS	Mosaic		*(ground only)*	5.70	0.43	-	1.0
3.8	SRMT	ULS	This study	3.14	101.57	35.62	0.17	35	0.3
	SRMT	ALS	LidarBC		17.71	7.00	0.38	41	1.0
3.9	EDF	ULS	This study	10.42	97.54	45.47	0.21	47	
	BURW			0.37	92.75	25.95	0.20	28	0.3
	COPJ			1.02	79.60	25.46	0.20	32	0.3
	DUKE			4.86	112.33	71.78	0.19	64	0.3
	NINE			0.82	90.33	21.43	0.22	24	0.3
	QUIL			1.34	96.96	21.45	0.22	22	0.3
	SLIM			0.52	82.25	29.00	0.29	35	0.3
	TELL			1.49	81.61	19.69	0.23	24	0.3
	EDF	ALS	This study		7.85	3.45	0.54	44	1.0

			ICP transformation		**Differencing**			
					M3C2		*DoD*	
Section	*Fault (site)*	*Data comparison*	*Max rotation (°)*	*Translation vector (m)*	*Mean (m)*	*SD (m)*	*Mean (m)*	*SD (m)*
3.6	XELF	ULS–ALS	0.0008	0.28	−0.05	0.19	−0.32	0.26
	XELF	ULS–SfM	0.0005	0.33	−0.03	0.14	−0.27	0.27
3.7	SJF (east)	ULS–ALS	0.0001	0.07	0.22	0.42	0.21	0.62
	SJF (west)	ULS–ALS	0.0002	0.32	0.13	0.31	0.15	0.53
3.8	SRMT	ULS–ALS	0.0001	0.54	−0.01	0.09	−0.02	0.29
3.9	EDF (BURW)	ULS–ALS	0.0004	0.82	−0.01	0.14	0.01	0.26
	EDF (COPJ)	ULS–ALS	0.0002	0.87	−0.01	0.17	0.00	0.25
	EDF (DUKE)	ULS–ALS	0.0003	0.54	0.00	0.18	0.00	0.28
	EDF (NINE)	ULS–ALS	0.0002	0.99	0.01	0.18	0.01	0.23

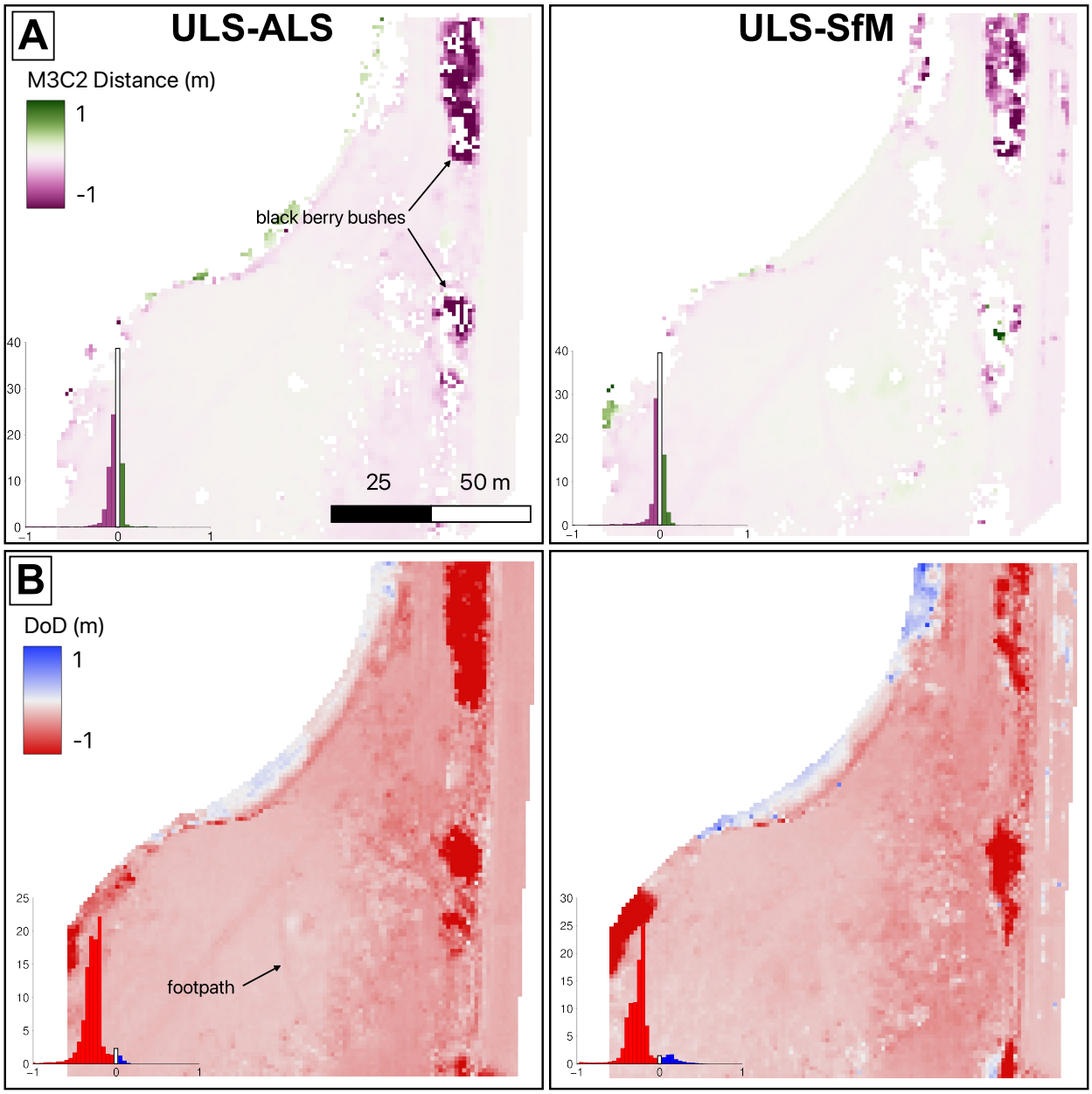

Figure 3.7: Differencing of the ULS and ALS datasets (left hand column) and of the ULS and SfM datasets (right hand column) at the eastern XEOLXELE~~K~~ (Elk Lake) shoreline site, shown as (A) M3C2 distances calculated in CloudCompare and (B) a DEM of Difference. Positive values indicate where the ULS dataset was higher than the comparison dataset. Histograms show distributions of raster values.

was −0.03 m with a standard deviation of 27 cm (Figure 3.7A, right column), while the DoD had a higher mean value of −0.27 m and a standard deviation of 27 cm (Figure 3.7A, right column). Given the stark contrast in vegetation penetration capability, it is difficult to interpret these centimetric-to-decimetric differences between the ULS and SfM surveys. Similar to the airborne lidar comparison, the greatest discrepancies are in areas that are covered in dense bushes, where the ULS alone seems to penetrate to ground level.

3.7 The San Juan fault: a kilometric survey of a fault scarp in steep, forested terrain

3.7.1 Background and motivations

The San Juan fault (SJF) is a major crustal fault on southern Vancouver Island, located north-west of the XELF (Figure 3.2B). The SJF transects the island west to east for ∼80 km across densely forested hills of the southern Vancouver Island ranges. In our area of interest, the fault separates the intrusive West Coast Crystalline Complex from the extrusive Jurassic Bonanza Group of the Wrangellia terrane (Harrichhausen et al., 2022). There have been numerous interpretations, inferred from regional geology, of the roles that the SJF has played throughout its evolution (Brandon, 1989; England and Calon, 1991; Johnson, 1984; Rusmore and Cowan, 1985). Most recently, its kinematics have been constrained to have been left-lateral during Eocene accretion of the Crescent-Siletz terrane (Harrichhausen et al., 2022). The position of the SJF in the forearc of the active Cascadia subduction zone, its favourable orientation relative to the regional stress field, and its conspicuously linear trace motivate a close examination of its current activity, but no convincing evidence of recent earthquake rupture has yet been found. If the SJF is active, it may pose a considerable risk to Victoria, Nanaimo, and other towns and infrastructure along Vancouver Island's Highway 1 corridor.

For our drone lidar surveying of the SJF, we targeted a ∼4 km section of the fault accessed via logging roads west of Shawnigan Lake (Figure 3.8A). The SJF trace is locally defined by a N-facing scarp that appears to cross-cut a glacially scoured surface as well as a number of small tributaries of the Koksilah River. The presence (or absence) of faulted offsets to these glacial and fluvial features could help determine whether this section of the SJF has been active in the late Quaternary. The area of interest includes some steep slopes with a topographic variation of 300 m. Vegetation cover includes stands of second growth Pacific cool temperate forest (Baldwin et al., 2019), with Douglas firs, Western Red Cedars, Western Hemlock and Sitka Spruce trees that are up to 50 m tall. Additionally, some of the area includes recent clearcuts with some small trees and shrubs. Our surveying of the SJF therefore provides good tests both of mapping at kilometric lengthscales over rugged terrain and of the vegetation penetration capability of the drone lidar system.

3.7.2 ULS data acquisition and results

We surveyed the SJF with our lidar drone in September 2022. For logistical reasons, we split the target area into two sections separated along strike of the SJF by a gap of ∼1 km (Figure 3.8A). The SJF West section is ∼2 km along strike by ∼700 m wide and the SJF East section is ∼1.7 km along strike by ∼700 m wide, with a total surveyed area of 2.9 km^2. The two sites took a total of 2 days to survey (14 hours of field work excluding travel) with a crew of three people (a pilot and two visual observers). The drone was flown at 5 m s^{-1} at a height of 80 m AGL along flight lines oriented parallel to the mapped fault scarp, that were merged with the help of orthogonal calibration lines (Appendix B.2 and B.3). For the SJF-East section, two launch points were required to maintain VLOS around high topography in the centre of the survey area. At 80 m AGL the laser footprint is 6.4 cm at the centre and 9 cm at the edges of each ∼160 m wide swath. At each site we deployed 5 GCPs to assist with georeferencing the point clouds.

Our SJF East and SJF West ULS surveys have average point densities of 121 pts/m^2 and 142 pts/m^2 and average classified ground return densities of 11 pts/m^2 (0.3 m spacing) and 17 pts/m^2 (0.24 m spacing), respectively (Table 3.3). The point clouds are therefore an order of magnitude sparser than those at XEOLXELEK (Elk Lake), reflecting the greater platform heights and speeds and reduced swath overlap used in our deployments along the SJF. Additionally, only ∼10% of the laser returns along the SJF are classified as ground compared to ∼48% at XEOLXELEK (Elk Lake), reflecting the stark differences in vegetation between the two target areas. Nevertheless, the drone lidar still captures an abundance of ground surface returns along the SJF, from beneath both mature forest and new growth within clear cuts (Figure 3.8C). The optimized 0.5 m-pixel hillshaded ULS DTM captures clearly both the ∼E–W-striking fault scarp and several ∼NNE–SSW-trending glacial flutes at the SJF West site, as well as the ∼NE-trending tributary channels at the SJF East site, one of which exhibits an apparent right-lateral offset at the fault (Figure 3.8A). Further analysis and interpretation of this rich dataset will form the basis of future study.

3.7.3 Comparison and differencing with ALS data

We can compare our ULS data with regional airborne lidar flown for Mosaic Forestry Management in 2021. In the year between the two surveys there appears to have been little forestry activity in the area (and no new cut blocks), allowing a like-for-like comparison. Within the footprint of the ULS surveys, the ALS yields an average ground point density of 6 pts/m^2 and average spacing of 0.43 m, somewhat coarser than the ULS data. A visual comparison of the 0.5 m-pixel ULS DTM with the 1 m-pixel ALS DTM demonstrates how the drone lidar allows for finer scale (<1 m) features to be identified (Figure 3.8B). For example, tree stumps and vehicle tracks on clear-cut slopes are clearly visible on the drone lidar hillshade but are only vaguely delineated in the airborne lidar.

The ICP rigid body transformations that best aligned the ALS and ULS point clouds

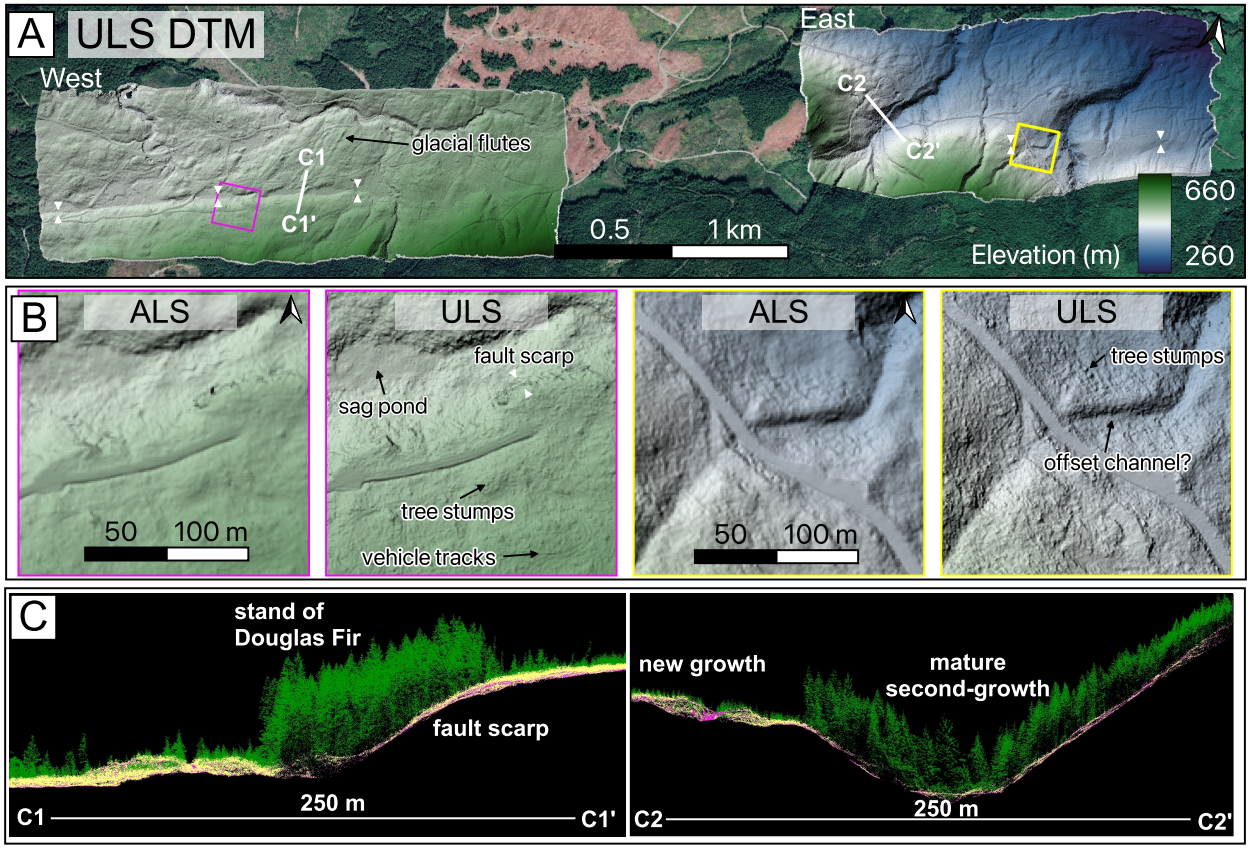

Figure 3.8: (A) Hillshaded UAV lidar DTM (illuminated from 315°) for the San Juan fault study area, overlain on satellite photograph. White triangles indicate the approximate location of the SJF. Coloured squares indicate the areas shown in the DTM comparisons below. (B) Comparisons between ALS and ULS DTM hillshades at the SJF West site (left hand panels) and the SJF East site (right hand panels). (C) Cross sections C1–C1' and C2–C2' through the ULS classified point cloud. Green points are vegetation, pink are ground points, and yellow points are unclassified.

involved rotations of <0.001 radians and translation vectors of 0.07–0.32 m. Post alignment, the average M3C2 distances were 0.22 m for SJF East and 0.13 m for SJF West, with standard deviations of 0.42 m and 0.31 m, respectively, while the equivalent DoDs have mean elevation discrepancies of 0.21 m and 0.15 m with standard deviations of 0.62 m and 0.53 m, respectively (Figure 3.9 and Table 3.3). These results indicate internal consistency of the two datasets to within a few decimetres.

The largest M3C2 distances in the SJF West dataset occur along the northern edge of the ULS survey within a steep valley (Figure 3.9A). Our point cloud is sparsest in this area, as it was covered fully by just one flight line. Other small areas with large M3C2 distances highlight where excavations for road maintenance were made between acquisitions (Figure 3.9A). There are also small channels that show up as negative values in the M3C2 distance and DoD plots, as a result of improved penetration through dense riparian vegetation in the ULS dataset. The strip of high M3C2 distances in the eastern part of the SJF East dataset results from a mis-aligned ULS flight line, which we discuss further in Section 3.10.2. In general, the raster differences are a lot noisier than the M3C2 point cloud comparison (Figure 3.9B). The largest raster differences are concentrated at the bottom of valleys, areas with both steep slopes and dense vegetation. It is likely that fewer true ground returns were obtained in these areas, but particularly in the ALS dataset, as the ULS dataset generally places the valley floors lower. Similar to the data comparisons undertaken in the previous section, this highlights the better vegetation penetration capability of the drone lidar system.

3.8 The Southern Rocky Mountain Trench: a kilometric survey of an alluvial fan scarp

3.8.1 Background and motivations

The Rocky Mountain Trench (RMT) is a conspicuously linear series of NW-trending valleys that crosses the Canadian Cordillera from northern Montana to southern Yukon, where it continues as the Tintina Trench into Alaska (Figure 3.2A). It demarcates the boundary between the Omineca and Foreland morphogeological belts and is defined by a series of major fault zones with distinct northern, central and southern segments (Clague, 1975; Gabrielse et al., 1991). The Southern RMT fault (SRMTF), in the East Kootenay region of southeastern BC is a steeply west-dipping normal fault active primarily in the Eocene (van der Velden and Cook, 1996). However, there is some evidence that the SRMTF may remain seismically active (Finley et al., 2022b; Purba et al., 2021), strongly motivating the acquisition and interpretation of lidar data. Our preliminary analysis of newly-released provincial airborne lidar (LidarBC, 2023) revealed a ∼3 km-long, W-facing scarp crossing a series of potentially Holocene-aged alluvial fans above the eastern shoreline of Columbia Lake, just south of the town of Fairmont Hot Springs (Figure 3.10A). The exact trace of

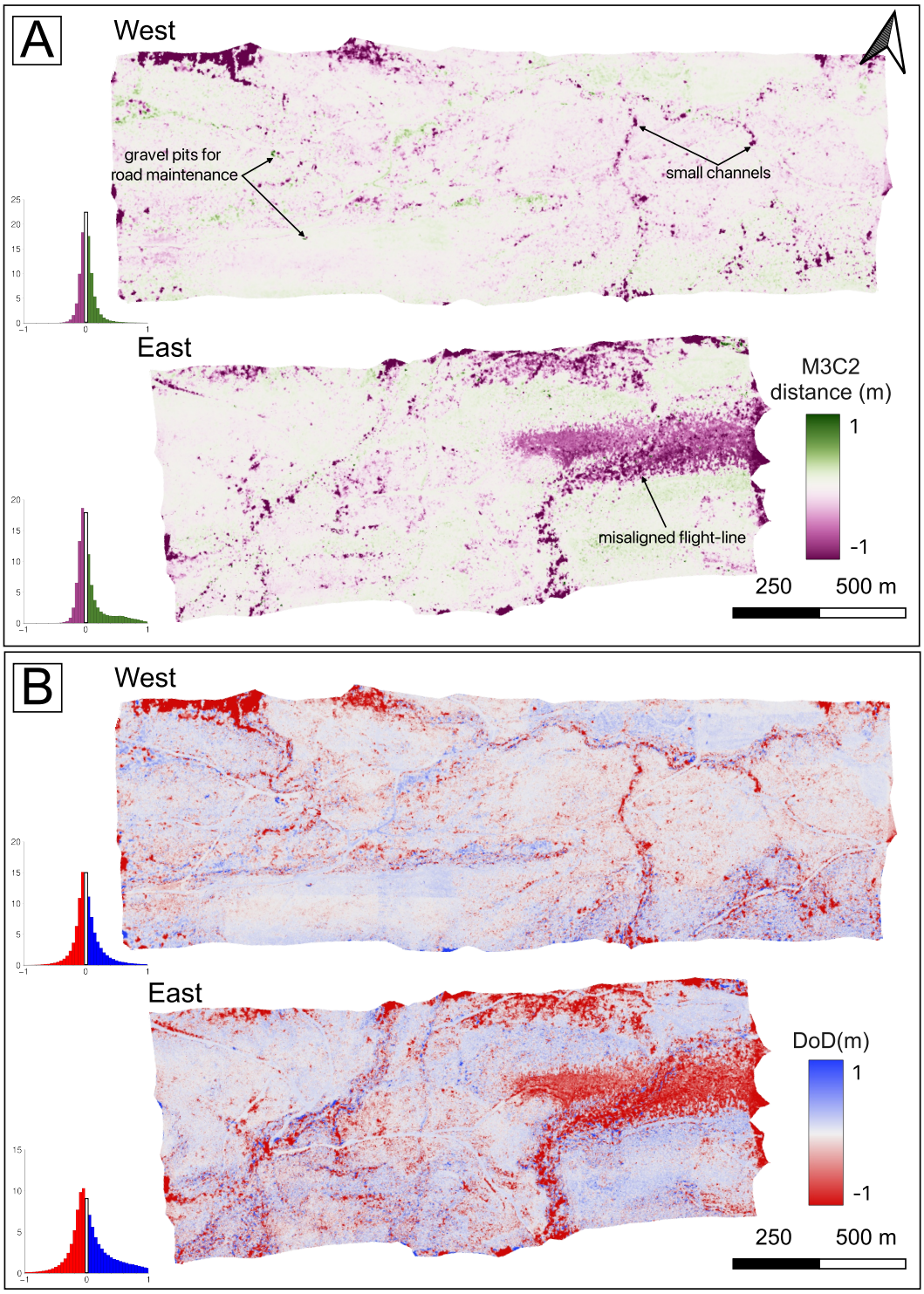

Figure 3.9: Differencing of the drone and airborne lidar datasets for the SJF study area, shown as (A) M3C2 distances calculated in CloudCompare and (B) a DEM of Difference. Positive values indicate where the ULS dataset was higher than the ALS dataset. Histograms show distributions of raster values.

the SRMTF is not well mapped at this location owing to the thick overburden in the valley floor. However, the scarp is parallel to and aligned with mapped strands of the SRMTF to the north and south, and could potentially indicate a neotectonic reactivation. Given that this part of the RMT was occupied by Glacial Lake Invermere during the late Pleistocene (Sawicki and Smith, 1992), other potential origins including wave-cut shorelines or slumping within weak glaciolacustrine sediments must also be considered.

Our goal in surveying the Columbia Lake scarp with our lidar drone was to help determine its true origin. This includes illuminating any lateral offsets to a series of small runnels that cross the scarp, and characterizing its detailed shape for the purpose of morphologic dating (e.g. Nash, 1980; Arrowsmith et al., 1998; Hilley et al., 2010) or to reveal any bevels that might indicate a compound, multi-earthquake origin (e.g. Zhang et al., 1986; Johnson et al., 2018; Wei et al., 2019). The alluvial fan that constitutes our principle target forms a gently-sloping surface from the western front of the Stanford Range at ∼900–1,000 m elevation to the lake shoreline at ∼809 m. This is covered by a mix of open grassland and groves of ponderosa pine, typical of Cordilleran dry forest (Baldwin et al., 2019). The Columbia Lake site therefore provides a test of our ULS system across a gentler relief and more sparsely-vegetated landscape than along the SJF. Since the survey area lies within traditional territories of the Ktunaxa and Secwépemc First Nations as well as within the Columbia Lake Provincial Park and Nature Conservancy of Canada land, extra research and drone use permissions had to be obtained in addition to the civil aviation approvals described in Section 3.5.2 (see Acknowledgements).

3.8.2 ULS data acquisition and results

We surveyed the Columbia Lake site over a period of three days in October 2022 with a crew of two people (the pilot and one visual observer). Our survey covers ∼3.22 km^2, with a length of ∼4 km along strike of the scarp and a width of ∼0.8 km, enough to capture most of the fan surfaces between the mountain rangefront and the Columbia Lake shoreline. The target area was flown in several segments, with orthogonal calibration lines that tie the flights together (Appendix B.4). Launch sites were located along the park access road that conveniently runs N–S down the middle of the fan surfaces, often adjacent to the scarp itself. The drone was flown at a height of 80 m AGL and a speed of 4 m s^{-1}, with the gentle relief and mix of grassland and scattered ponderosa pine allowing for excellent sight lines. The ULS data were georeferenced using ten harlequin-iron-cross GCPs.

Our ULS system yielded an average point density of 102 pts/m^2 and was easily able to image beneath the scattered ponderosa pine trees (inset, Figure 3.10), producing an average classified ground return density of 36 pts/m^2 at an average spacing of 0.17 m (Table 3.3). Overall, ∼35% of all laser returns are classified as ground, lower than the ∼48% at XEOLXELEK (Elk Lake) but substantially higher than the ∼9% along the SJF, reflecting the differing vegetation densities of the three areas. We optimally gridded the classified

ground returns at a pixel resolution of 30 cm (Figure 3.10A). The hillshaded DTM clearly reveals the primary scarp striking N–S across the largest, northern alluvial fan (af1), as well as some secondary splays just east of it (Figure 3.10D, right panel). It also reveals a lineament within the southernmost alluvial fan (af4) that may represent an along strike continuation of the scarp. We encountered difficulties aligning some of the flight lines due to poor INS calibration, which may explain some N-S linear corduroy artefacts visible in the centre of the hillshaded DTM (Figure 3.10D, right panel). However, to the trained eye, these minor and localized artefacts are easily distinguished from genuine tectonic landforms.

3.8.3 Comparison and differencing with ALS data

Our comparison data are provincial airborne lidar collected over a two year period (2015–2017) using multiple sensor platforms with unknown acquisition parameters (LidarBC, 2023). The sparse metadata owe to the fact that these surveys were flown by a third party and later acquired for LidarBC, without the control needed for them to verify accuracies. This captures $\sim 80\%$ of our ULS dataset, but misses the southernmost alluvial fan (af4) surveyed with the drone, where we observe an additional scarp along strike. Within the footprint of overlap, the ALS data have an average ground return density of 7 pts/m^2, five times coarser than the ULS survey, and an average ground return spacing of 0.38 m, twice that of the ULS survey (Table 3.3). Despite these differences in spatial resolution, there is little visual contrast between the ALS and ULS hillshaded DTMs (Figure 3.10D). However, fault-perpendicular topographic profiles reveal that the shape of the scarp is captured by ULS at greater detail than by ALS (inset to Figure 3.10D).

The ICP rigid body transformation that most closely aligns the two point clouds has a translation vector of 0.54 m and a rotation of $<0.001°$ (Table 3.3). After this global registration, the mean M3C2 distance between the aligned point clouds is -0.01 m with a standard deviation of 0.09 m, while the DoD has an average elevation difference of -0.02 m with a standard deviation of 0.29 m. These results show that despite some artefacts (described below), our ULS dataset is still both aligned to within a few decimetres and internally consistent to within a few centimetres with the ALS survey.

The greatest differences between the two point clouds as revealed by M3C2 and DoD maps (Figure 3.10 B–C) are along the park access road: a gravel pit in the south and a parking lot in the north, both of which we suspect were excavated or re-graded between surveys. There are also negative M3C2 and DoD values along the Columbia Lake shoreline, which likely represent changing water levels between acquisitions. However, the M3C2 distance and DoD plots also highlight alternating N–S strips of negative and positive values ($\pm$15 cm), clearest in the northern half of the survey. We interpret these as errors in the ULS point cloud due to a poorly calibrated INS on some of our flights.

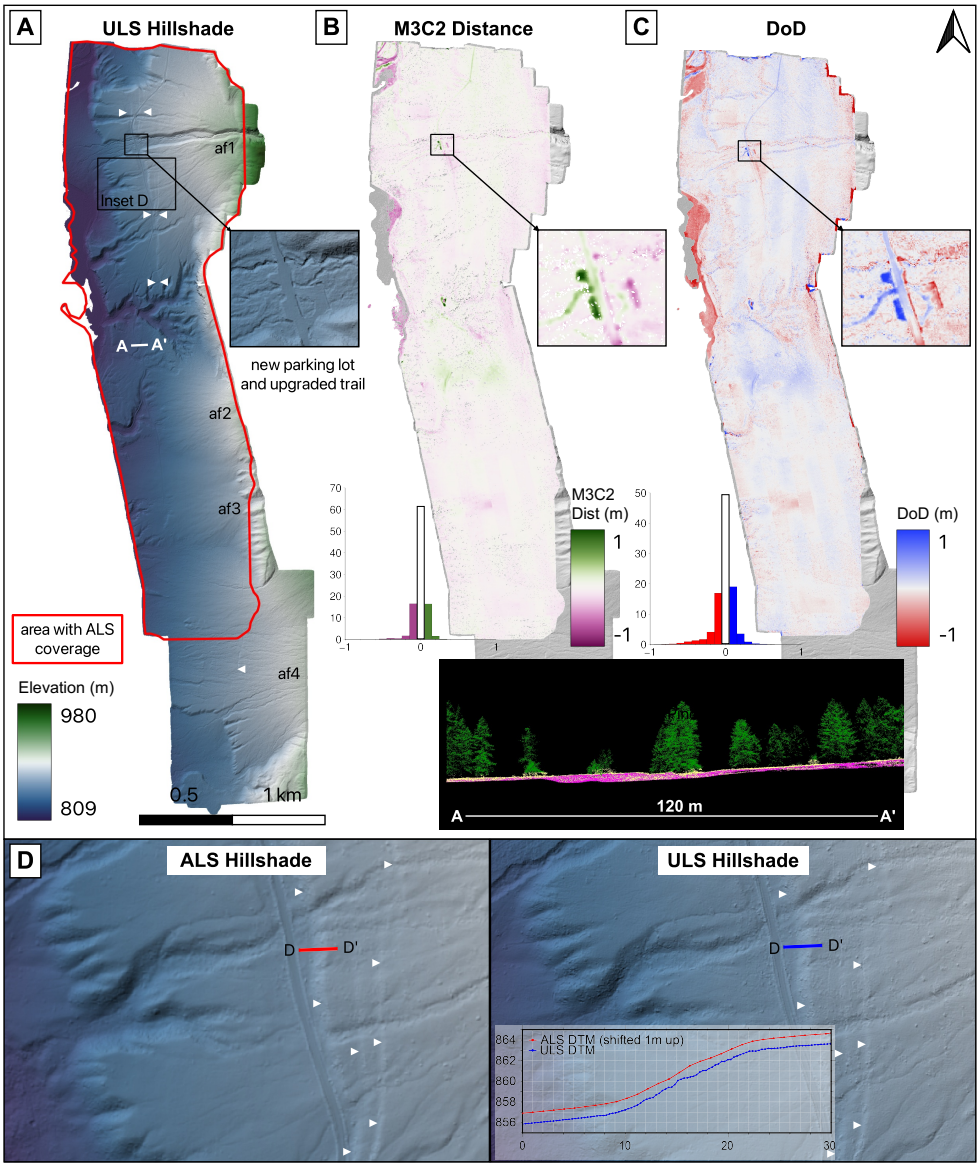

Figure 3.10: (A) Hillshaded ULS DTM for the Columbia Lake site along the SRMTF. The red polygon shows the area of the ULS survey overlapped by LidarBC ALS coverage. Inset shows the location of a new parking lot and upgraded trail to the lake shore that was not developed when the provincial lidar was collected. Alluvial fans (af) are numbered from northernmost (af1) to southernmost (af4). White triangles indicate the approximate location of the SRMTF. (B) M3C2 distances between the ULS and ALS point clouds, with an inset showing changes over the new parking lot and trail. Positive values indicate where the ULS dataset was higher than the ALS dataset. (C) DoD (ULS-ALS), with an inset showing changes over the new parking lot and trail. The inset below (C) and (D) shows cross section A—A' through the classified drone lidar point cloud, with green points for vegetation, pink for ground points, and yellow for unclassified returns. (D) Comparison between ALS and ULS hillshaded DTMs. Cross section D-D' shows the increased level-of-detail in the ULS DTM along the main scarp. Note that the ALS profile has been shifted upwards by 1 m in order to aid comparison.

3.9 The Eastern Denali fault: maximal coverage of a major strike-slip fault

3.9.1 Background and motivations

The Denali fault hosted North America's largest and longest onshore earthquake of the modern instrumental period. The M_w 7.9 earthquake of November 3 2002 ruptured for ~340 km west to east across central Alaska, producing mostly right-lateral surface offsets of up to ~9 m (Eberhart-Phillips et al., 2003). Though the Denali fault continues southeastwards into Yukon and northwestern BC (Figure 3.2A), the 2002 earthquake stopped short of the Canadian border, branching instead onto the Totshunda splay fault, where it terminated. This rupture pattern has elicited investigations into the current activity and kinematics of the Denali fault east of the Totshunda junction (Blais-Stevens et al., 2020; Bostock, 1952; Choi et al., 2021; Clague, 1975; Haeussler et al., 2017; Marechal et al., 2018), usually referred to as the Eastern Denali fault (EDF). The EDF has been active in the Holocene since it lacks a glacial overprint and displays several push-up or mole-track structures within till (Blais-Stevens et al., 2020; Bostock, 1952). Paleoseismic trenching of the fault and coring of lake sediments ponded against the scarp also revealed evidence for five strong earthquakes during the past ~6,800 years, leading Blais-Stevens et al. (2020) to call for the acquisition of lidar imagery to better illuminate the surface offsets, kinematic style, and other characteristics of these events.

We targeted a ~100 km stretch of the EDF centred upon Lù'àn Män (Kluane Lake) and paralleling the paved Alaska Highway (Figure 3.11D). This section of the fault occupies a broad glacial valley, surfacing up to a few kilometres NE of the frontal range of the St. Elias mountains and displays tectonic landforms including those targeted for paleoseismic trenching and coring by Blais-Stevens et al. (2020). The area is mostly covered by boreal forest (Figure 3.2A), consisting mainly of white spruce trees, aspen and balsam poplar. However, the EDF crosses several wide fluvial terraces deposited by rivers sourced in the St. Elias mountains, the youngest of which are only sparsely vegetated. Our work along the EDF therefore provides an example of surveying rugged (though not mountainous) topography containing both dense and sparse vegetation. Our surveying of the EDF also represents our closest attempt at a regional ULS survey. We sought to survey as much of the fault as possible, but sparse secondary road coverage off the main Alaska Highway prevented us from accessing long stretches of it. We therefore flew several separate sections of the EDF from launch sites located wherever a passable road crosses the fault, usually one that follows a major river sourced in the St. Elias mountains (Figure 3.11D). However, these river outlets are also where we expect to observe some of the best expressions of the fault in Quaternary deposits, such as deformed river terraces and offset terrace risers. Our drone coverage, though discontinuous, should therefore still capture many of the features of greatest

geomorphic interest.

3.9.2 ULS data acquisition and results

We collected ∼10 km^2 of drone lidar data at seven individual survey sites—from NW to SE, Quill Creek, Burwash Creek, Duke River, Copper Joe Creek, Nines Creek, Slims River/Topham Creek, and Telluride Creek—that together capture a ∼15 km length of the EDF (Figure 3.11D). Data were acquired during two, week-long field campaigns in September 2021 and August 2022, each involving three crew members (a pilot and two visual observers); the largest site, at Duke River, was flown over multiple days (Figure 3.11A). Flight paths for each site are plotted in the Appendix (B.5–B.11). The drone was flown at 80 m AGL and speeds of 5 m s^{-1} in 2021 and 4 m s^{-1} in 2022. Since large portions of each target area were difficult to access on foot, we were unable to deploy as many GCPs as we did at the study sites described in previous sections. The number of GCPs range from 2 at the Nines and Quill Creek sites to 20 at the Duke River site (cumulative across several days of surveying).

The seven ULS surveys yielded average point densities of 80–112 pts/m^2 with a mean of 98 pts/m^2, average classified ground return densities of 20–72 pts/m^2 with a mean of 45 pts/m^2, and average ground return spacings of 0.19–0.23 m with a mean of 0.21 m (see Table 3.3 for results of each individual survey). Generally, the ULS does an excellent job of imaging beneath the boreal forest canopy (inset, Figure 3.11A), with ∼47% of all laser returns classified as ground. We did encounter some misalignment of flight lines in some of the datasets—particularly at Quill Creek—again, potentially due to a poor INS calibration. This can produce some striping in the M3C2 and DoD results (Figure 3.12), with separations of ±15 cm in places. However, these linear artifacts are easily distinguished from genuine tectonic landforms. The ground returns were rasterized at an optimal pixel resolution of 0.3 m for each of the seven individual surveys.

We focus our further analysis in this paper on the Duke River site, which is the largest and densest of our EDF ULS surveys (Figure 3.11 and Table 3.3). Results from the other EDF drone lidar surveys are presented in the Appendix (B.12–B.14); some of them were also interpreted in an earlier technical report of ours (Finley et al., 2022a) and a full tectonic analysis of all of the EDF lidar topography will be the subject of a future paper. The 0.3 m-resolution Duke River DTM showcases several interesting tectonic landforms along the principal trace of the EDF (Figure 3.11A). From NW to SE, these include en-echelon push up structures indicative of dextral strike-slip, a pair of clear, right-lateral offsets to terrace risers south of the active Duke River, an abrupt, 7° bend in fault strike, and a large, SW-facing scarp with a vertical separation of ∼5 m. The lidar DTM also reveals a previously unmapped, secondary strand of the EDF, expressed as a SW-facing scarp crossing the widest, southern terrace of the Duke River (Figure 3.11B). This highlights the potential for drone lidar to capture subtle, off-fault tectonic landforms away from principal fault traces.

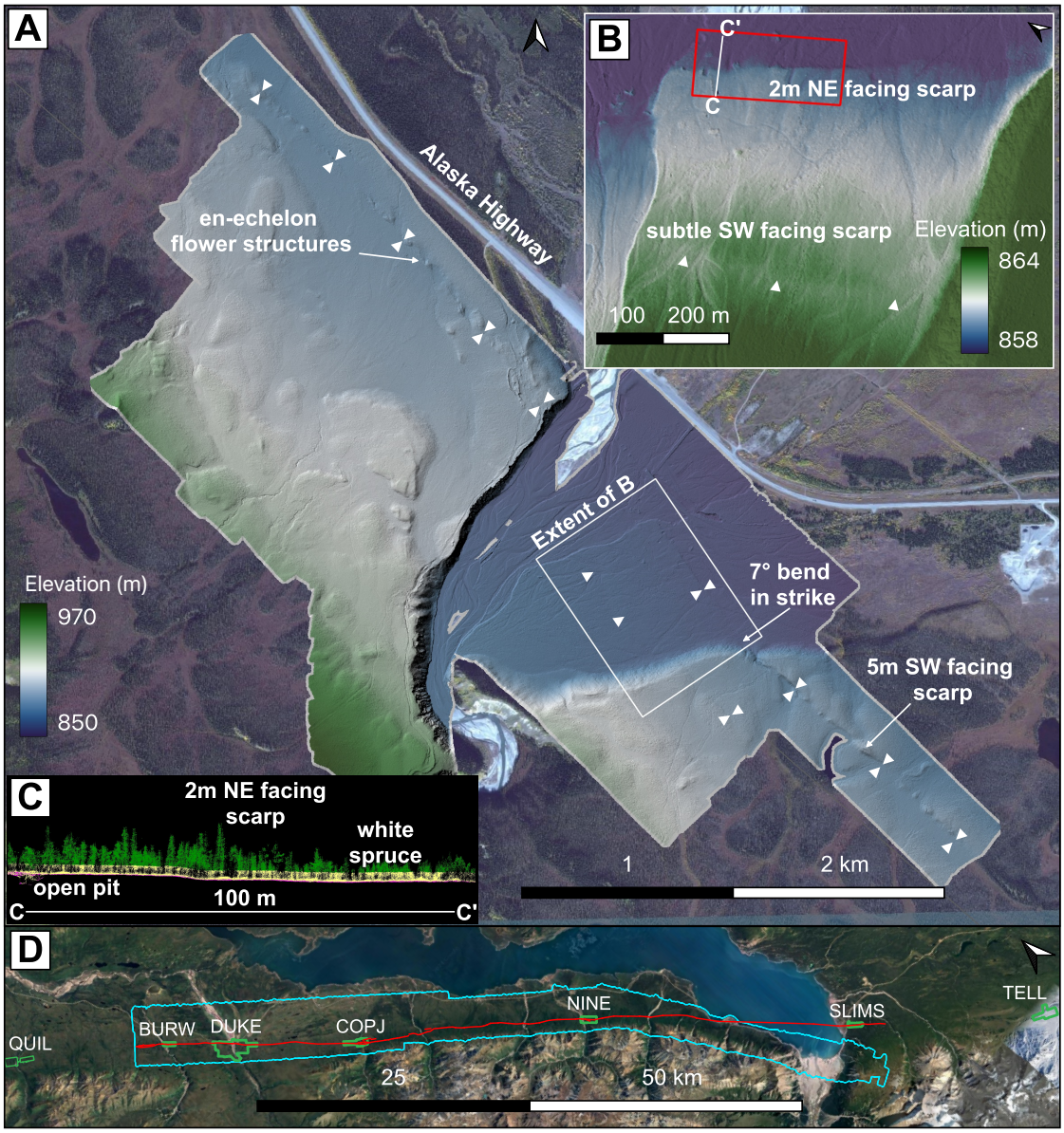

Figure 3.11: (A) Hillshaded drone lidar DTM of the Duke River site on the Eastern Denali fault (EDF). The extent of panel B is marked by the white rectangle. White triangles indicate the approximate location of the EDF. Underlying satellite imagery is from Bing. (B) Inset showing a 2 m high northeast facing scarp along a river terrace. The red polygon shows the bounds of the flight parameter testing discussed in Section 3.10.1. White line shows the location of cross section C–C'. (C) Cross section C–C' through the classified ULS point cloud, with green for vegetation, pink for ground returns, and yellow for unclassified points. (D) Locations of all ULS collection sites (green polygons) along the trace of the EDF as identified with lidar data (red line). The cyan polygon outlines the comparison ALS dataset. Satellite imagery is from Google. QUIL = Quill Creek, BURW = Burwash Creek, DUKE = Duke River, COPJ = Copper Joe Creek, NINE = Nines Creek, SLIMs = Slims River/Topham Creek, TELL = Telluride Creek.

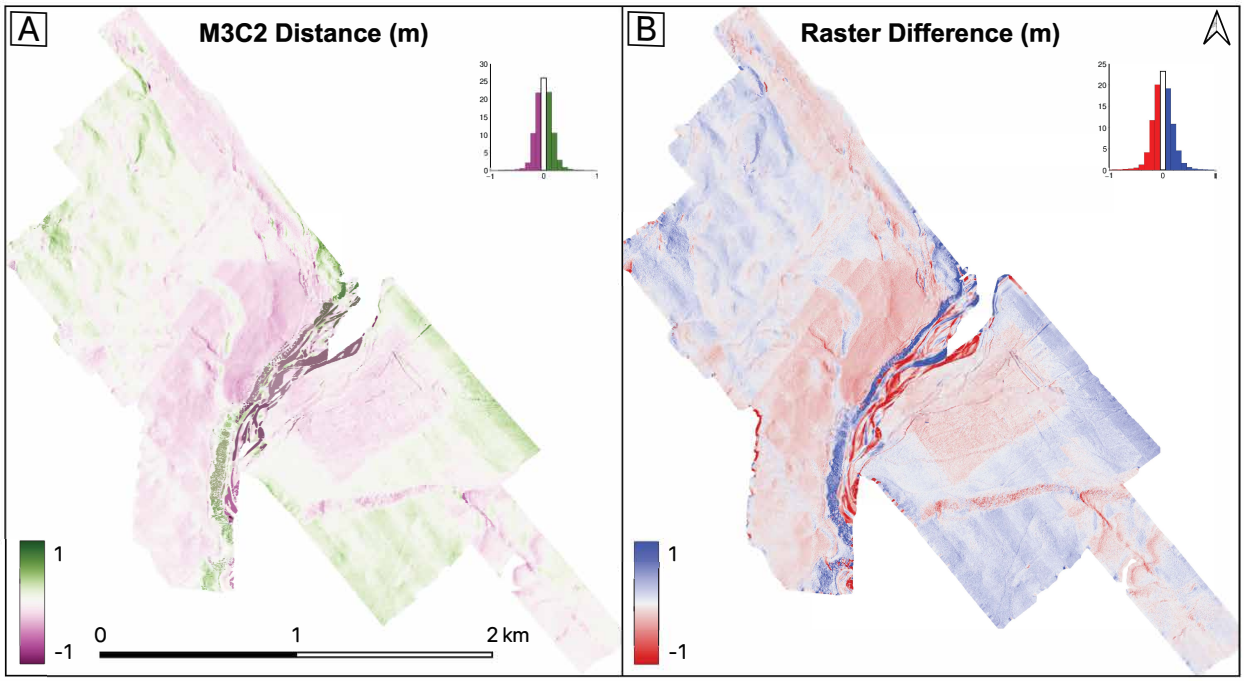

Figure 3.12: Differencing of the drone and airborne lidar datasets for the Duke River site along the EDF, shown as (A) M3C2 distances calculated in CloudCompare and (B) a DEM of Difference. Positive values indicate where the ULS dataset was higher than the ALS dataset. Histograms show distributions of raster values.

3.9.3 Comparison and differencing with ALS data

Until this study, the Canadian portion of the Denali fault had not been flown systematically with lidar, with the best freely-available topographic data coverage being the 2 m-resolution, satellite photogrammetry-derived ArcticDEM (Morin et al., 2016) and a bespoke 4 m-resolution DTM constructed from legacy airphotos using SfM (Bender and Haeussler, 2017). In addition to our drone lidar surveying described above, one of us (B.M.) also collected a ~295 km^2, ~70 km-long airborne lidar swath on 19 August 2018 that captures ~50 km of the EDF between Burwash Creek and south of Nines Creek (Figure 3.11D), which for the purposes of this study we use as our comparison dataset. The ALS survey covers four of our seven drone lidar sites, including the largest at Duke River. The airborne lidar yields an average point density of ~8 pts/m^2 and an average ground return density of ~3.5 pts/m^2, less than 10% of the equivalent ULS values, and the average ALS ground return spacing is 0.54 m, more than double that of the ULS (Table 3.3). Consequently, the ULS DTM exhibits noticeably finer detail than is discernible in the ALS DTM.

For the Duke River dataset, the ICP rigid body transformation that optimally aligns the ULS and ALS point clouds has a translation vector of 0.54 m and a maximum rotation of 0.0003°, indicating global registration to within a few decimetres and negligible tilting (Table 3.3). The mean M3C2 distance between the aligned point clouds is 0.00 m with a

standard deviation of 0.18 m, while the DoD has an average elevation difference of 0.00 m with a standard deviation of 0.28 m, indicating excellent internal consistency between the two lidar surveys. The other survey sites with paired coverage have slightly higher global ICP translations (of up to 0.99 m), but had similarly low mean M3C2 and DoD values (of up to 0.01 m) and standard deviations (of up to 0.28 m).

After ICP alignment of the ULS and ALS ground returns, the largest M3C2 distances between the two clouds are along the active braided channels of the Duke River, with some showing erosion and others deposition such as from the formation of sandbars (Figure 3.12A). There are also some large M3C2 distances found along the bluffs on the northern bank of the Duke River. These steep slopes are mostly composed of unconsolidated glacial till and are very unstable, with several small failures occurring while we were working in the area. Thus, it is unsurprising that there are differences in these surfaces between the ALS and ULS acquisitions. Other areas with non-negligible M3C2 values may result from slight misalignments between the individual, day-to-day acquisitions at the Duke River site, which were georeferenced using separately-surveyed GCP deployments. The raster DoD highlights similar areas of difference (Figure 3.12B), although it does appear a little noisier than the M3C2 distances due to small misalignments in the rasterization of roads, small channels and other linear features.

3.10 Discussion

3.10.1 Flight parameter trade-offs

The four case studies described in Sections 3.6–3.9 highlight not only the usual trade-off in remote sensing between data spatial resolution and coverage, but also the flexibility in drone surveying to adjust flight parameters for the job at hand in a way that would be difficult with a crewed aircraft platform. For example, for our local survey of the eastern XEOLXELE~~K~~ (Elk Lake) shoreline site, we flew the drone at a substantially slower speed and a lower height than in the other, kilometric-scale surveys, resulting in a point cloud that was around five times denser but also smaller in scale (Table 3.3). In practice, however, the trade-off between platform speed and point cloud density is complicated by the limited battery life of the drone, which restricts the area that can be collected in a single flight.

We therefore conducted an explicit test of the trade-offs between platform speed, flight duration, and lidar point density, with the aim of determining the ideal flight parameters for collecting high-density data as efficiently as possible. We did so during our surveying along the EDF in 2022, choosing for the test a small ($\sim$2500m^2) area of the Duke River site centred along a segment of the EDF that offsets an abandoned, forested river terrace (Figure 3.11B). We surveyed this area nine times over the course of a single day, at 1 m s^{-1} increments in speed from 1 m s^{-1} to 10 m s^{-1}, using the same optimal flight height (80 m AGL) and the same flight pattern (Figure 3.13B, left panel). The nine flights yielded order

Table 3.4: Results of our testing of platform speed trade-offs. The survey time does not include the static IMU calibrations (∼5 minutes per flight), nor the time taken to transit the drone between the launch site and the start of the first data collection flight line. The minimum DTM resolution is based on a recommendation that at least 3 ground points should be averaged per raster cell.

Speed ($m\ s^{-1}$)	*Survey time* (*min*)	*Point density* (pts/m^2)	*Ground point density* (pts/m^2)	*%pts ground*	*Minimum DTM resolution* (*m*)
1	23.50	495.63	68.36	14	0.21
2	11.75	242.49	28.16	12	0.33
3	7.83	155.68	23.80	15	0.36
4	5.88	122.87	20.10	16	0.39
5	5.37	99.83	19.20	19	0.40
6	4.47	84.98	15.58	18	0.44
7	3.83	72.70	12.12	17	0.50
8	3.35	65.17	14.19	22	0.46
9	2.98	57.93	9.70	17	0.56
10	2.68	50.52	10.05	20	0.55

of magnitude ranges in both point densities, from ∼51–496 pts/m^2, and classified ground return densities, from ∼10–68 pts/m^2 (Table 3.4). We observe the expected trade-off between platform speed and ground return density, with the slowest flight yielding more than double the point density of the next slowest flight but taking double the time (Figure 3.13A). The resulting DTMs all looked similar to the eye (Figure 3.13B), although the data from faster collections were slightly noisier. The faster collections had a greater variation in the DTM surface, potentially as a result of small bushes and other low vegetation being classified as ground.

Ultimately, the most efficient speed for a given survey depends on the desired point density and should be determined on a case-by-case basis accounting for both the scale of the features being targeted and the vegetation cover type. In our general case, we strive for sub-metre pixel DTMs in order to identify fine-scale fault geomorphology that might not be visible in existing airborne datasets. Ideally, each raster cell value should be based on the average of at least 3 ground returns. Thus, for a 50 cm DTM, 12 ground returns per square metre are desirable, allowing each raster cell to be calculated using a minimum of 3 ground points. The minimum DTM resolution in Table 3.4 was calculated using this rule of thumb. Using Figure 3.13A as a guide, an appropriate maximum acquisition speed would therefore be about 6 m s^{-1}. Anecdotally, this agrees well with our experience gleaned from many drone lidar campaigns.

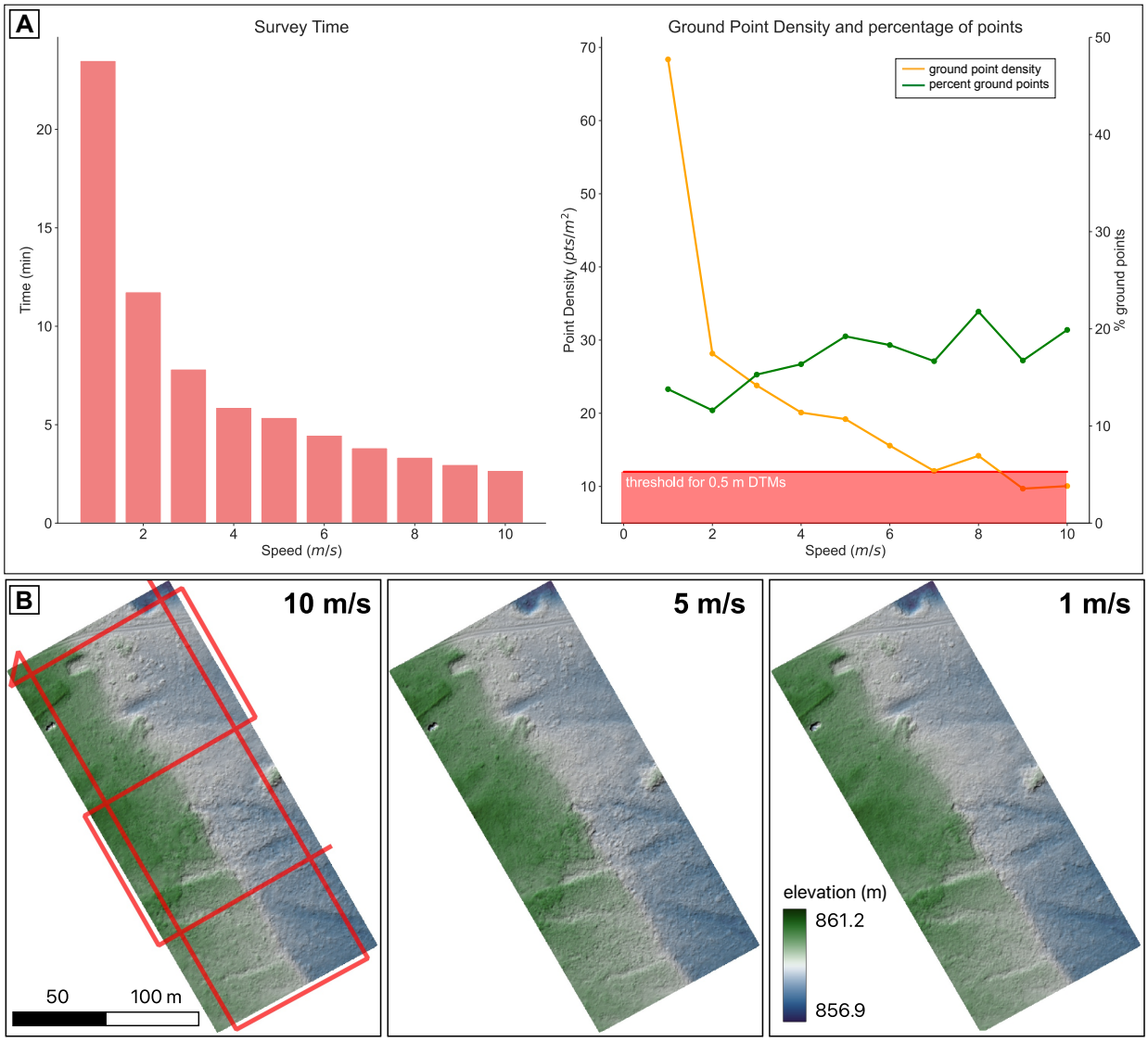

Figure 3.13: Results of platform speed trade off tests. (A) Relationships between acquisition time, platform speed, and the resulting ground return density. The 12 points per square metre threshold illustrates that 0.5 cm DTMs can only reliably be obtained at speeds of 6 m s^{-1} or less. (B) 30 cm-resolution DTMs for the fastest (10 m s^{-1}), intermediate (5 m s^{-1}) and slowest (1 m s^{-1}) flights. The red line on the 10 m s^{-1} panel shows the acquisition path used for all flights.

3.10.2 Drone lidar performance

Our four case studies described in Sections 3.6–3.9, as well as the additional testing at the Duke River site described above, demonstrate the wide range of ground return densities attainable with drone lidar, governed principally by the platform height and speed, swath overlap, and vegetation type. At its densest—our local survey of a planned paleoseismic site along the XELF with only scattered tree cover (Section 3.6)—we obtained a ground point density of 260 pts/m^2 at an average spacing of 6 cm, though of course further improvements would have been possible with additional, overlapping flight lines. In surveys undertaken at the kilometric length scales more generally of interest to tectonic geomorphologists, we obtained ground return densities ranging from ∼10 pts/m^2 (spacing of ∼30 cm) along the rugged, heavily forested SJF (Section 3.7) to ∼70 pts/m^2 (spacing of ∼20 cm) at the mixed-cover Duke River site on the EDF (Section 3.9). In all cases, the ULS densities were a marked improvement from those of the comparison ALS datasets, which ranged from 3.5–9 pts/m^2 with spacings of 0.33-0.54 m (Table 3.3). Of course, these differences trade off against aerial coverage; in our largest ULS survey along the EDF we collected a total of ∼10 km^2 of data in two week-long field campaigns, whereas our ALS survey collected 25 times that area in a single day. Our ULS surveying along the SJF, SRTM and EDF shows that coverage of 0.5–1.6 km^2 is achievable in a single day with the drone, including over rugged topography.

Our ICP alignments of ULS ground returns with corresponding ALS point clouds show that the two datasets are usually globally registered to within less than a metre of one another (Table 3.3), with the one exception, along the SJF, likely arising from differences in the geoid model used to calculate orthometric heights (Section 3.7.3). The Riegl MiniVUX-1UAV laser scanner has expected accuracy of 10 mm and precision of 5 mm and the Applanix APX20-UAV INS has a post-processed accuracy of 2–5 cm. Once the ULS and ALS ground return clouds are aligned using ICP, average M3C2 distances and DoD values on the order of a few centimetres are therefore within the expected noise, especially considering that the average is biased by localized occurrences of significant landscape alteration between surveys (e.g. road construction; Figure 3.10B–C). Generally, the M3C2 distances were very similar to the DoD values, implying that the local distances calculated on the point clouds were mainly in the vertical direction. We did encounter artifacts arising from misaligned flight lines within some of the ULS datasets (e.g. Figures 3.7B and 3.9), although further post-processing may have helped reduce these (Gu et al., 2023) and similar problems can occur in some ALS surveys, too (Scott et al., 2022). One main challenge for mobile lidar systems thus far has been in point accuracy, particularly as a result of the IMU trajectory (Glennie et al., 2013), and our ULS results bear this out.

Our detailed comparisons of data collected at the eastern XEOLXELEK (Elk Lake) shoreline site show how ULS penetrates low-lying vegetation (blackberry bushes) better than ALS does, with both lidar systems naturally outperforming SfM (Section 3.6.3). Counterintuitively, the ULS produces a lower fraction of ground returns (48%) than the ALS (64%),

which hints that in densely-vegetated areas, some laser returns off shrubs and bushes might be misclassified as ground in ALS datasets, to a greater extent than they are in ULS datasets. This would explain why the ground surface modelled from ULS data is often slightly lower than that from ALS data (Figures 3.7 and 3.9). It is important to note that many ground classification algorithms, such as progressive morphological filters (Zhang et al., 2003) and cloth simulation functions (Zhang et al., 2016), were developed using and for ALS data. Thus to effectively determine ground points within ULS data, the default algorithm parameters may need to be adjusted.

The relative vegetation penetration capabilities of ULS and ALS are further showcased in Figure 3.14. In the left-hand column, we plot 5 m wide point cloud swath cross-sections for typical vegetation present in each of the study sites. These demonstrates that the ULS is better at both capturing the vegetative structure and minimizing gaps in the ground returns. This may partly reflect that the ULS footprint is ∼6–9 cm in diameter at our optimal flight elevation of 80 m AGL, several times narrower than the ∼15–90 cm footprints typical of airborne systems (e.g. Lin et al., 2013; Fernandez-Diaz et al., 2014).

Tectonic geomorphologists generally analyze rasterized DTMs rather than point clouds and so it is important to consider ULS in this context. The ∼1–10 pts/m^2 ground return densities typical of ALS data (Figure 3.14, middle column) usually translate to ∼1 m raster resolutions, whereas the much the denser point clouds collected by our drone system (Figure 3.14, right-hand columns) allow for finer pixel dimensions of 0.2–0.5 m. Lin et al. (2013) proposed that 0.5 m was an optimal DTM resolution for detecting tectonic-geomorphic signals, with 0.25 cm pixels offering little improvement, but this may reflect the larger (0.41 m) footprint of their airborne laser scanner. Since ULS laser footprints are much smaller (6–9 cm), it enables us to produce sub-50 cm DTMs which aid the identification of many features obscured in typical 1 m resolution imagery, such as ruts in road-ways, footpaths, and individual tree stumps or logs (e.g. Figures 3.7 and 3.8B).

3.10.3 Limitations and future prospects of drone lidar

Based on our four case studies in Sections 3.6–3.9 and the performance metrics discussed above, we foresee a number of specific applications for drone lidar within the field of tectonic geomorphology. Because battery life, road access, and VLOS requirements limit us to kilometric fault length-scales (e.g. Figure 3.11D), we do not envisage ULS (or any other type of drone-based imaging) as a regional reconnaissance tool in the way that ALS has become. However, ULS may be a useful, relatively low-cost way of extending lidar coverage beyond the footprint of an existing ALS survey, such as we did along both the SRMT and EDF (Figures 3.10A and 3.11D). As demonstrated in Section 3.6 and 3.10.2, ULS also offers better and more even ground point coverage beneath trees and shrubs than ALS, making it possible to densify lidar coverage along known faults in vegetated landscapes. Faulted landforms targeted for paleoseismic trenching, slip rate studies, or morphologic dating may

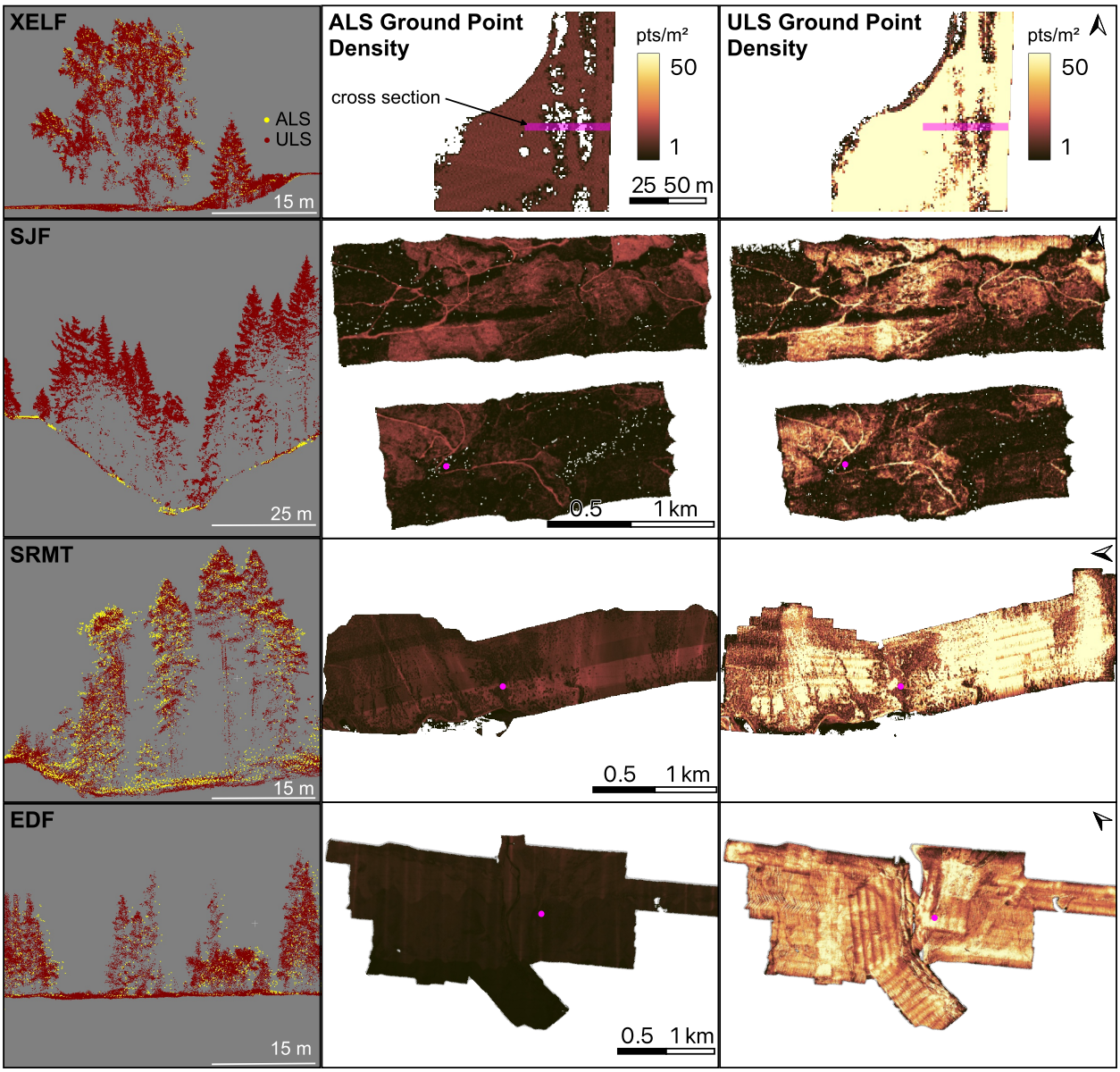

Figure 3.14: Left-hand column: representative 5 m-wide swath cross-sections through the ULS (red) and ALS (yellow) point clouds showing typical vegetation for the XELF (top row), SJF (second row), SRMT (third row) and EDF (bottom row) study sites. The point clouds are displayed concurrently, with ALS points enlarged to prevent them from being obscured behind ULS points. Note that for the SJF site, only ALS ground returns were provided to us. Middle column: ground point density maps for the ALS datasets at the four study sites. Pink polygons mark the cross-section locations of the left-hand column. Right-hand column: ground point density maps for the ULS datasets. Additional ULS point cloud profiles through stereotypical vegetation for each survey site are provided in the Appendix (Data files B1–B4).

benefit from the finer, decimetric spatial resolutions achievable with ULS. We have also shown how drone lidar can reveal subtle landforms associated with structural complexity and distributed deformation, such as the secondary scarps imaged on the Columbia Lake alluvial fans (Figure 3.10D) and at the Duke River site along the EDF (Figure 3.11). There is also scope for mapping landscapes and landforms associated with other natural hazards, such as landslides (Pellicani et al., 2019), volcanoes, tsunamis, and flooding. Finally, because drone deployments are both logistically easier and cheaper than procuring a crewed aircraft, there is rich potential for the use of ULS for rapid response (e.g. mapping of new earthquake surface ruptures) and in repeat mode (e.g. high temporal and spatial resolution time-series of postseismic afterslip). Building upon this study, the capability of repeat ULS surveying for mapping three-dimensional surface deformation will be tackled explicitly in a forthcoming paper of ours.

Just as ULS will complement rather than supplant ALS as a source of high-resolution topographic data, we do not see it replacing TLS or drone-based SfM systems for all applications. Firstly, the upfront costs of our ULS system (discussed further below) are higher than that of many TLS systems and much higher than those of drone-based SfM. Since many consumer drones come equipped with high-quality cameras (e.g. Pellicani et al., 2019), we envisage that SfM will remain the tool of choice for collecting high-resolution topography in arid, vegetation-sparse landscapes (e.g. Johnson et al., 2014). ULS would still offer certain advantages over SfM in such regions—for example its active source allows mapping in low light conditions, and the processing of the lidar point cloud is significantly less computationally intensive—but these would come at greatly increased cost. Similarly, ULS is unlikely to replace TLS for applications in which ground-based scanner vantage points suffice. However, ULS can capture a small target area quicker than TLS; for example, Brede et al. (2017) collected a 140 pts/m^2 ULS dataset in a single 9 minute flight, whereas it took two days to complete TLS coverage of the same 100 m $\times$ 180 m site.

The components of our ULS system cost more than CAD $100,000 when purchased in 2018–2019, though these costs are likely to decrease significantly as the technology matures (e.g. Van Tassel, 2021). As ULS is adopted for a broader range of scientific and commercial applications, an increasing variety of drones and miniaturized scanners and INS instruments are becoming available, including as part of integrated systems. In our experience, once the upfront costs of purchasing a ULS system is made, the year-on-year costs for insurance and software licensing are inexpensive. One of the biggest constraints on drone systems is their limited flight time, related to battery life. However, electric cars and a growing array of battery powered mobile devices are driving improvements in battery technology that will positively benefit drone surveying (Townsend et al., 2020; Liang et al., 2019; Rajashekara, 2013, e.g.). Alternatively, gasoline and hybrid-powered UAVs are becoming commercially available, offering much higher energy densities and ensuing improvements in both flight time and lifting capacity (e.g. Skyfront, 2023; Metcalf et al., 2022; Viswanathan et al., 2022; Harris Aerial, 2023). Another major constraint for ULS is imposed by aviation authorities,

which require specialist equipment and large amounts of permitting for beyond visual line-of-sight (BVLOS) flight in both Canada and the U.S. Flying BVLOS would allow for larger drone acquisitions with fewer crew and less time in the field. This will potentially change as drone software and collision avoidance systems mature and new RPAS-specific legislation emerges (Transport Canada, 2023).

3.11 Conclusions

We describe a state-of-the-art drone lidar system, provide a practical guide for other researchers interested in developing their own, and showcase its performance using four case studies from a range of terrain and vegetation types found within the Canadian Cordillera. These range from a local (∼100 m × 100 m) survey of a paleoseismic trenching site with scattered tree cover, captured at a ground return density of 260 pts/m^2, to multi-kilometre mapping of faults in remote, forested regions, captured with ground return densities of ∼10–72 pts/m^2. Our ULS point clouds are gridded into bare Earth DTMs with ∼20–50 cm pixel dimensions, substantially finer than the ∼1 m dimensions typical of airborne lidar DTMs. In most cases, the drone lidar ground returns are globally registered to overlapping airborne lidar data to within ∼0.3–1.0 m, and once aligned, point-to-point distances and DEMs of difference indicate internal consistency to within a few centimetres. Distinct advantages of terrain mapping using ULS include better imaging beneath vegetation, the flexibility to adjust flight parameters to achieve a desired ground return density, and relatively straightforward platform deployment logistics. In practice, ULS mapping is currently limited to kilometric lengthscales by battery life, road access requirements, and regulatory constraints, so it is unlikely to replace ALS for regional fault reconnaissance. However, we envisage rich potential of drone lidar for (1) cost-effectively mapping faults beyond the edges of existing ALS surveys; (2) detailed surveying of known faults for paleoseismic trenching, fault slip rate estimations, or morphologic dating; (3) revealing subtle landforms arising from off-fault deformation; (4) rapid collection of perishable data such as along earthquake surface ruptures; and (5) for repeat deployments along surface ruptures for capturing afterslip.

3.12 Acknowledgements

We are grateful to have conducted this work on the traditional territories of the W̱SÁNEĆ people (XELF), the Hul'q'umi'num speaking people (SJF), the Ktunaxa and Secwépemc (SRMT), and the Lù'àn Män Dän (Kluane Lake People, EDF). Our ULS system was supported through the Canada Foundation for Innovation John Evans Leadership Fund (CFI JELF) and the Government of British Columbia Knowledge Development Fund (BCKDF), and we also acknowledge generous educational discounts and in-kind contributions from Riegl, Applanix, Candrone, and Cansel. Fieldwork in BC was primarily supported by the

Natural Sciences and Engineering Research Council of Canada (NSERC) through Discovery Grants #2017-04029 and #2019-05639 (to E.N. and B.M. respectively) and fieldwork in the Yukon by the Yukon Geological Survey. G.S. was supported in part through an Agnew Memorial Scholarship from the University of Victoria, T.F. through an NSERC Alexander Graham Bell Canada Graduate Scholarship, and E.N. and B.M. through Canada Research Chairs. We thank Chris Bone at University of Victoria's Department of Geography for sharing lab space, equipment, and running costs so generously. We are grateful to Chris Crosby for facilitating the hosting of our drone lidar data on the OpenTopography web portal, which is supported by the National Science Foundation under NSF Award Numbers 1948997, 1948994 and 1948857. We thank the Capital Region District (in particular April Mitchell, Jeannette Mollin and Marc Solomon) for allowing us to work within the Elk/Beaver Lake Regional Park, BC Parks for granting us access to Columbia Lake Park, the Yukon Geological Survey (in particular Maurice Colpron, Carolyn Relf and Sarah Sternbergh) and the Arctic Institute of North America's Kluane Lake Research Station for facilitating fieldwork along the EDF, and Mosaic Forest Management for sharing airborne lidar data along the SJF and for granting us access to field sites there. We also thank our University of Victoria colleagues Israporn Sethanant, Élyse Gaudreau, Jinrui Liu, and Braeden Clark for their assistance as visual observers during our drone surveys, as well as Andrew Schaeffer, Lucinda Leonard, Eva Kwoll and John Cassidy for their suggestions and support of the project. Finally, we are grateful to Nadine Reitman, Randy Williams, and an anonymous reviewer for their thoughtful comments that improved the manuscript.

3.13 Data and code availability

Supplemental material can be found on Zenodo (https://doi.org/10.5281/zenodo.10092585) and in Appendix B. This includes shell scripts for the classification and rasterization of point cloud data collected by a UAV laser scanning (ULS) system. The Appendix B and the Zenodo folder includes visualizations of flight paths for each survey and data comparisons made at the BURW, COPJ and NINE sites along the Eastern Denali fault that were not included within the publication, as well as ULS point cloud cross sections that showcase stereotypical vegetation for each case study. All drone lidar data are available on the OpenTopography portal at the following links: XELF (https://doi.org/10.5069/G92V2DBC), SJF (https://doi.org/10.5069/G9TB1542), SRMT (https://doi.org/10.5069/G9PK0DCW), EDF (https://doi.org/10.5069/G998857Q). Airborne lidar data for the XELF (Section 3.6) and SRMT (Section 3.8) sites are available on the LidarBC (2023) portal.

Chapter 4
The San Juan fault, Vancouver Island, BC — late Quaternary surface ruptures in a newly deglaciated, forested landscape

4.1 Author names, affiliations and roles

Guy Salomon[1], Theron Finley[1], Edwin Nissen[1,2], Lucinda Leonard[1], Nicolas Harrichhausen[3]

[1] *School of Earth and Ocean Science, University of Victoria, British Columbia, Canada*
[2] *College of Earth, Ocean and Atmospheric Sciences, Oregon State University, OR, Corvallis, USA*
[3] *Department of Geological Sciences, University of Alaska Anchorage, AK, USA*

I took the lead on the project, planned the fieldwork, obtained permits, and created a set of research objectives. I processed the data and wrote the manuscript. Dr Edwin Nissen supervised the project, provided funding, assistance in the field, and manuscript edits. Theron Finley and Lucinda Leonard assisted with the field data collection. Nicolas Harrichhausen shared field observations and offered advice.

Note: this manuscript has been submitted for publication to *Seismica* – the Cascadia Special Issue. The title of the submitted article is "Probable surface ruptures along the San Juan fault in the recently-deglaciated northern Cascadia forearc". The title of this chapter has not been changed in order to keep the submitted article title unique.

4.2 Abstract

Crustal faults pose significant risks within the Cascadia subduction zone, and a wealth of new lidar data allow for their identification and characterization. In the northern Cascadia fore-arc, the E-W striking, terrane-bounding, San Juan fault (SJF) displays a topographic lineament that is more conspicuous in lidar imagery than other known active faults in the region, but it remains

unresolved whether the fault has ruptured in large prehistoric earthquakes and poses a risk to the ∼600,000 people living on southern Vancouver Island. We map a relatively continuous and linear set of 2–150 m high, north-facing scarps along the fault trace, but find limited evidence of clear offset of Quaternary sediment that would be diagnostic of neotectonic activity. An alternative hypothesis is that the scarp formed due to differential glacial erosion of the distinct bedrock units juxtaposed by the fault. We disprove this hypothesis using Schmidt hammer measurements, which reveal harder rocks on the lower (north) side of the scarp compared to the higher (south) side, suggesting south-side-up motion is tectonically driven. In combination with the vertical scarp, offset channels indicate a right-lateral sense of motion. We also use electrical resistivity tomography to investigate one prominent, uphill-facing scarp. Disruption to otherwise continuous subsurface structure beneath the scarp is further evidence of a late Quaternary rupture. These results, though somewhat equivocal, strongly motivate future paleoseismic investigations along the SJF.

4.3 Introduction

Crustal faults within subduction zone forearcs can host moderate to large earthquakes that pose significant risks to nearby populations. The damaging April 2016 Kumamoto, Japan and November 2016 Kaikoura, New Zealand earthquakes are recent examples of these types of events (Hata et al., 2016; Hamling, 2020). Characterizing crustal faults within the northern Cascadia subduction zone forearc is challenging, as loading of the megathrust dominates Global Navigation Satellite System (GNSS) velocities (Figure 4.1a), there are only low rates of seismicity (Figure 4.1b, Balfour et al. (2011); Li et al. (2018)), and dense vegetation often obscures fault-related geomorphology (Morell et al., 2018). Recently, records of late Quaternary surface rupturing earthquakes along several Vancouver Island faults (Figure 4.1b) including the terrane-bounding Leech River fault (Morell et al., 2017, 2018), the XEOLXELEK–Elk Lake fault (pronounced *hul-lakl-lik*, Harrichhausen et al., 2023), and the Beaufort Range fault (Lynch et al., 2023), have been facilitated by paleoseismic trenching guided by newly available airborne lidar imagery. Late Quaternary earthquakes have been similarly identified in neighbouring Washington State, along faults such as the Darrington–Devil's Mountain fault (Personius et al., 2014), the Upsalady Point fault (Johnson et al., 2004), the Birch Bay and Sandy Point faults (Kelsey et al., 2012), the southern Whidbey Island fault (Johnson et al., 1996), and the Lake Creek–Boundary Creek fault (Nelson et al., 2017) (Figure 4.1a) . These northern Cascadia crustal faults share common ∼E–W and ∼SE–NW trends and right-lateral strike-slip to transpressional kinematics.

Another difficulty in studying active faulting in this region is that late Quaternary glacial scouring acted to reset the landscape, potentially removing previously existing geomorphic features related to fault activity. Southern Vancouver Island has been affected by several glaciations throughout the Quaternary, though evidence of antecedent ice cover has largely been scoured from the landscape by the most recent late Wisconsinan (Fraser) glaciation (Jackson et al., 2024). This most recent glacial maximum began around 19,000 yr BP (Alley and Chatwin, 1979) as the Cordilleran ice sheet spread southwards, reaching a maximum at ∼14,000 ^{14}C yr BP (Clague and James, 2002; Clague and Ward, 2011). This maximum was followed by a rapid period of de-glaciation, where the ice sheet diminished into a series of valley glaciers, which produced streamlines, drumlins, and

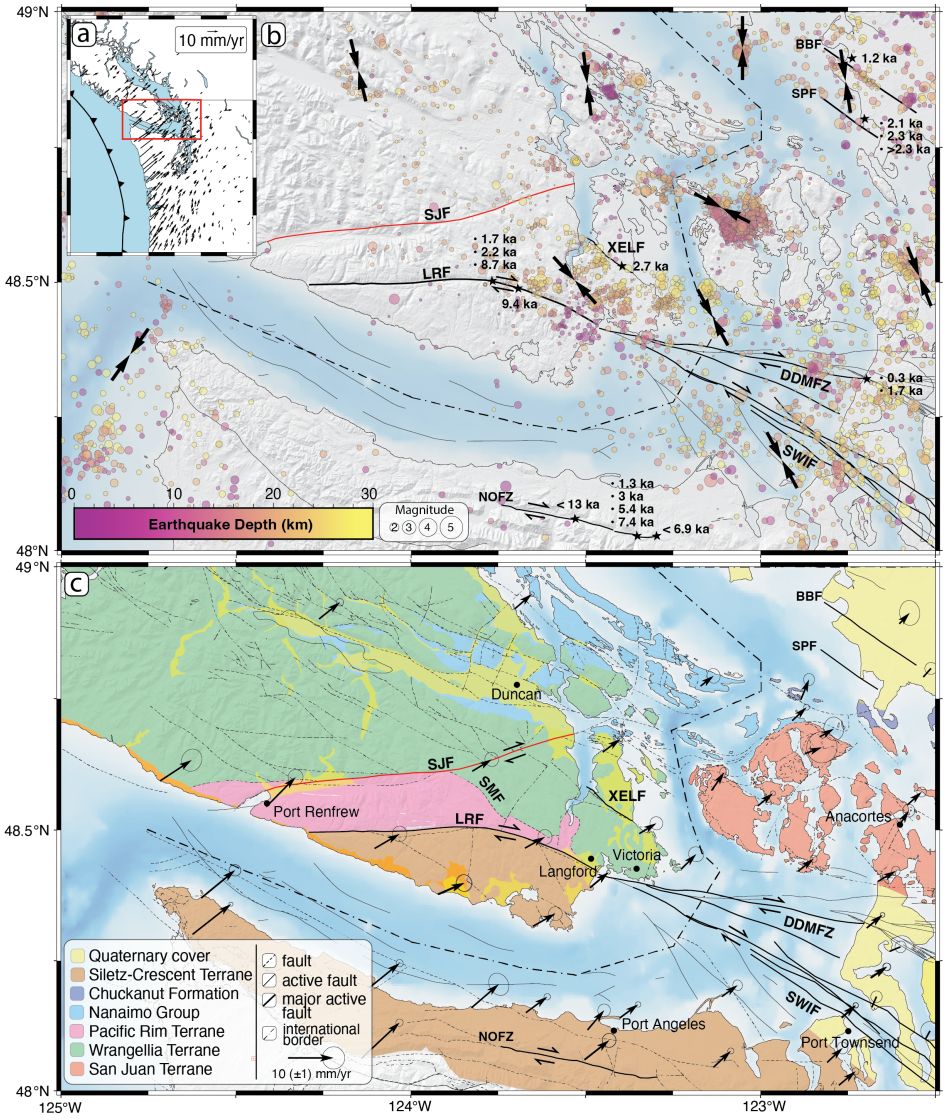

Figure 4.1: a) GNSS velocities for northern Cascadia relative to stable North America from McCaffrey et al. (2013). Red box shows extent of panels b and c. b) Crustal seismicity, stresses, and active faults of southern Vancouver Island, with the San Juan fault (SJF) marked in red. Circles are shallow (0–30 km) earthquakes for the period 1985–2024 (Natural Resources Canada, 1985), coloured by focal depth. Black arrows are regional S_{Hmax} directions (Balfour et al., 2011). Stars are paleoseismic study sites with earthquake ages from the cited literature. Other active faults are labelled as follows: BBF = Birch Bay Fault (Kelsey et al., 2012), DDMFZ = Darrington-Devil's Mountain Fault Zone (Johnson et al., 2004; Personius et al., 2014), NOFZ = North Olympic Fault Zone (Nelson et al., 2017; Schermer et al., 2021), LRF = Leech River Fault (Harrichhausen et al., 2021; Morell et al., 2018), SPF = Sandy Point Fault (Kelsey et al., 2012), SWIF = Southern Whidbey Island Fault, XELF = XEOLXELEK–Elk Lake Fault (Harrichhausen et al., 2023). c) Simplified geology of southern Vancouver Island, adapted from (Cui et al., 2017). GNSS velocities (black arrows) relative to stable North America are as in (a).

scours before fully retreating from the area by ∼12,000 ^{14}C yr BP (Clague and James, 2002). Such features are evident in our study area in the San Juan and Koksilah River valleys, both along and across the trace of the San Juan fault.

The San Juan fault (SJF) is one of several major crustal faults on southern Vancouver Island (Figure 4.1c), transecting the island from Port Renfrew on the west coast to Saanich Inlet ∼80 km to the ENE. It can be subdivided into two sections, either side of its intersection with the NW–SE-trending Survey Mountain fault (SMF). The longer (∼50 km), ∼E–W-trending western section of the SJF brings the Wrangellia terrane into contact with accretionary prism and mélange rocks of the Pacific Rim terrane. This western section occupies the prominent San Juan river valley and lies ∼10 km north of and subparallel to the relatively well-studied Leech River fault (Harrichhausen et al., 2021; Li et al., 2018; Morell et al., 2017). The shorter (∼30 km), ∼ENE–WSW-trending eastern section of the SJF separates the intrusive Mesozoic West Coast Crystalline Complex from the extrusive Jurassic Bonanza Group of the Wrangellia terrane (Harrichhausen et al., 2022). There are numerous interpretations of the timing and kinematics of slip along the SJF (Brandon, 1989; England and Calon, 1991; Johnson, 1984; Rusmore and Cowan, 1985). These include reverse faulting accommodating accretion of the Pacific Rim terrane to Wrangellia during the late Mesozoic to early Cenozoic (Brandon, 1989), oblique left-lateral faulting during the accretion of the Pacific Rim terrane (Rusmore and Cowan, 1985), and re-activated left-lateral faulting during the Eocene accretion of the Siletz terrane (England and Calon, 1991), as supported by 60 km of apparent left-lateral offset to Wrangellia terrane rocks (DeBari et al., 1999; Muller, 1977). Recent work by Harrichhausen et al. (2022) confirmed that the SJF accommodated left-lateral slip during the Eocene, which was temporally and kinematically consistent with the formation of the Cowichan fold and thrust belt and accretion of the Siletz ocean island plateau.

The proximity of the SJF to other known active faults in the northern Cascadia forearc, the observation that these active faults reactivate pre-existing crustal structures (Figure 4.1c), and its sharp, linear trace (Figure 4.2a), all support the hypothesis that it is active, but no convincing proof has yet been found. This is important to address because a large SJF earthquake would pose considerable risks to Victoria (∼400,000 inhabitants), Nanaimo (∼90,000), Cowichan Valley (∼84,000) and other towns along Vancouver Island's populous Trans-Canada Highway corridor. The community of Shawnigan Lake (population ∼10,000) lies directly along the fault trace.

Here, we test this hypothesis using airborne and drone lidar imagery recently acquired along the SJF. Such data have been proven highly effective at enabling the mapping of active faults in the densely vegetated northern Cascadia forearc, revealing numerous previously unrecognized surface ruptures across southern Vancouver Island, the Olympic Peninsula, and the Puget Sound (e.g. Harrichhausen et al. (2023); Haugerud et al. (2003); Morell et al. (2018); Sherrod et al. (2004)). Closest to the SJF, the Leech River fault was proven active on the basis of subtle geomorphic offsets (Morell et al., 2017)) and the XEOLXELE~~K~~–Elk Lake fault was first discovered using airborne lidar imagery (Harrichhausen et al., 2023).

Examination of lidar data along the mapped SJF trace reveals a sharp, continuous topographic lineation cutting through bedrock on the northern side of the upper San Juan valley. We do not observe the fault crossing any laterally-extensive, post-glacial, depositional landforms that would serve as unequivocal indicators of late Quaternary activity and help constrain the slip rate. However,

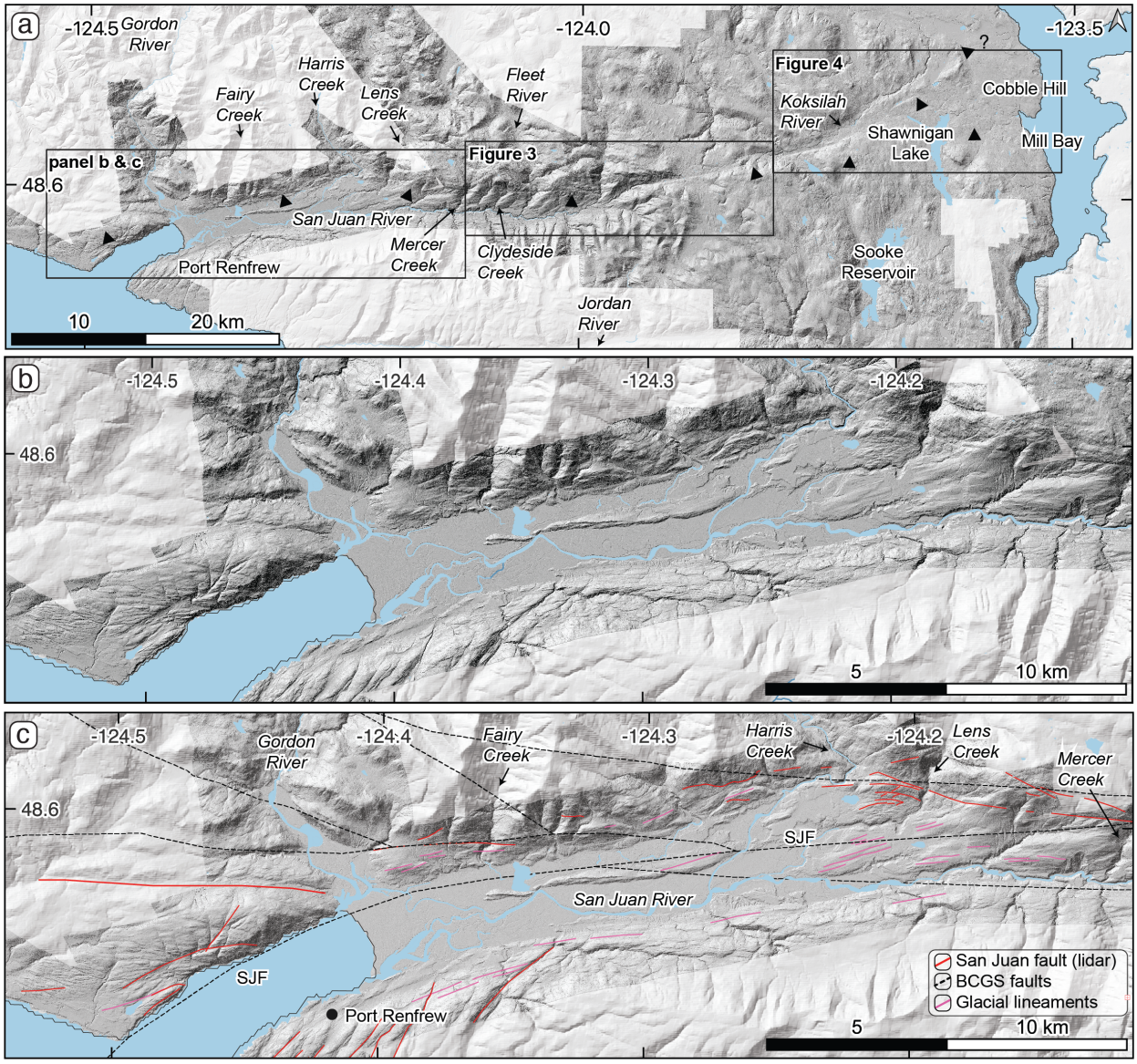

Figure 4.2: a) Overview of lidar coverage (darker hillshades) along the San Juan fault (black triangles). The western, central and eastern boxes show the extents of panels b and c, Figure 4.3, and Figure 4.4, respectively. b) Uninterpreted hillshaded lidar covering the western section of the San Juan Fault in the San Juan River valley. c) Interpretations of fault traces (red) and glacial lineaments (pink). Dashed black lines are geological faults as mapped by the British Columbia Geological Survey (BCGS).

we do map three sections of scarps that, with further testing, could be indicative of active faulting. The first of these is a N-facing scarp that crosses a glacially scoured surface 16 km west of Shawnigan Lake on the south side of the Koksilah River valley (Figures 4.2 & 4.3). The second is a smaller set of uphill-facing scarps that appear to offset colluvial sediments in the upper reaches of the San Juan valley. We further investigate the origin of these uphill facing scarps by imaging the shallow subsurface using Electrical Resistivity Tomography (ERT). On a more regional scale, we test whether these scarps could have been formed as a result of differential weathering or glacial scouring by using Schmidt hammer measurements of bedrock hardness on either side of the fault—a novel application within the Cascadia region.

4.4 Methods

4.4.1 High resolution topography

We collated all available airborne lidar datasets, from both the open access provincial LidarBC portal, the Capital Region District local government, and from the private collections of forestry companies (Mosaic, TimberWest, and Island Timber). Collectively, these airborne datasets cover an area of >1,000 km^2 along the fault with an average point density of ∼5 pts/m^2. We rasterized the ground returns to digital terrain models (DTMs) with a uniform cell resolution of 1 m for consistency. Hillshade, slope and topographic position index maps were derived from these DTMs using QGIS software v. 3.28 (QGIS Association, 2018). Together, the DTMs and secondary products were used as the basis for mapping topographic lineaments including fault scarps, sackungen, landslide scars, and glacial scours.

Additionally, where we thought higher resolution topographic data would augment the airborne lidar to allow for the analysis of particularly subtle tectonic landforms, we surveyed the fault with a novel drone lidar system (Figure 4.3b). For this, we used the instrumentation and methodology described in Salomon et al. (2024). The drone lidar data average ∼15 ground points per m^2, allowing us to produce DTMs with raster resolution of 0.5 m, four times finer than that of the airborne lidar (Supplemental Figures S1–S4). There are four discrete drone lidar surveys (Figure 4.3b), each targeting a feature identified in coarser imagery that is of potential tectonic origin. The UPSCARP site is centred on an isolated uphill-facing scarp along the mapped trace of the SJF and very near a significant outcrop of a bedrock shear zone. The SLIDE dataset covers a suite of uphill-facing scarps that we initially interpret as slope instabilities. The GSS dataset includes a glacially scoured surface which is cut by a ∼6 km long, 30 m high scarp. The EAST dataset includes several streams which appear offset in satellite images.

4.4.2 Fault scarp morphology

Scarps of suspected tectonic origin at the UPSCARP and GSS sites were further analyzed using the Monte Carlo Slip Statistics Toolkit (MCSST, Wolfe et al., 2020). Scarp-perpendicular topographic profiles were constructed at intervals along the fault trace (yellow, blue and green lines on

Figures 4.3 &4.4), and vertical separation was estimated by projecting the hanging and foot wall slopes to the fault and measuring their vertical offset. MCSST then uses a Monte Carlo approach to estimate dip slip and its uncertainty, through sampling allowable ranges in fault dip, fault position on the scarp, and the topographic surfaces of the hanging and footwalls. Fault dip and position are each assigned a trapezoidal uncertainty distribution, with the wide base of the trapezoid containing all possible values and the narrow top including the likeliest range. Because the fault trace cuts linearly across steep, undulating topography, we assigned a steep dip angle ranging between 70° N and 70° S with the highest probability between 80° N and 80° S. In the case of the UPSCARP location, we also used the dip from the ERT profile, but found no substantial difference in the dip slip calculated. For the position of the fault, we allowed its tip to sample the entire width of the scarp and assigned the highest probability to the middle third. Uncertainties in vertical separation are usually on the order of a few metres, but larger uncertainties occur in a few profiles in which hanging and foot wall slopes are markedly different.

4.4.3 Schmidt hammer rock hardness measurements

To explore whether observed scarps might have formed via differential erosion as opposed to recent earthquake activity, we used a Schmidt hammer to measure the hardness of bedrock exposures on either side of the fault. Initially developed for testing the strength of concrete, Schmidt hammers have since been been used in the Earth sciences to take in-situ, non-destructive measures of material hardness for use as a proxy for erosive resistance, degree of weathering, or exposure age (Matthews and Winkler, 2022; Stahl and Tye, 2020). Schmidt hammers may prove to be a useful tool for studying cryptic faults in recently glaciated terrain. We used an N-type hammer which, when pressed onto a surface, delivers a controlled blow of 2.207 Nm and bounces back. This rebound is recorded as the R-value, a unit-less measure of compressive strength (Matthews and Winkler, 2022).

There are limited natural bedrock outcrops within the study area, and most of our measurements are from near-vertical surfaces exposed in road cuts. We targeted each of the major geological units found along the San Juan fault in this area, namely the Leech River schist, the Survey Mountain volcanics, and the Bonanza Group. The Leech River schist is a metapelitic schist containing metapsammitic layers (Seyler et al., 2022), interpreted to have formed from a turbidite sequence near a continental margin and a spreading ridge (Fairchild and Cowan, 1982; Muller, 1977) with a maximum depositional age of 103 Ma (Groome et al., 2003). The Survey Mountain volcanics contain greenschist to amphibolite facies, green, weakly foliated, fine-grained volcanic flows with phenocrysts of epidote, chlorite and actinolite (Fairchild and Cowan, 1982). Both the Leech River schist and Survey Mountain volcanics make up the Leech River Complex of the Pacific Rim terrane (Harrichhausen et al., 2022). The Bonanza Group, of the Wrangellia terrane, is composed of volcanics (basaltic andesite–rhyolite) and interbedded sediments which contain early Jurassic fossils (Andrew and Godwin, 1989). Descriptions of the units observed during fieldwork can be found in Table 4.1. We only measured fresh, smooth surfaces without lichen cover, first cleaning them of soil or dust and orienting the hammer at a perpendicular angle. We also ensured that hammer tests were on solid, unfractured sections of outcrop, avoiding loose fragments that might respond differently to impact. In the case of testing schistose rocks, we measured rebound values in two orientations, both parallel and perpendicular to the foliation. We collected 5 rebound values for

each measurement site from which we calculated the mean. Control of potential instrument drift during the measurement period was constrained by calibrating the hammer on a steel test anvil (with a rebound value of 80) before and after use.

4.4.4 Electrical resistivity tomography

To investigate the origin of uphill facing scarps at the UPSCARP site, we used Electrical Resistivity Tomography (ERT) to profile the shallow subsurface resistivity structure (e.g. Harrichhausen et al., 2023; Improta et al., 2010; Mojica et al., 2017). Using an Advanced Geosciences Inc. (AGI) MiniSting^{TM} R1 resistivity meter with a 28 electrode cable and a dipole-dipole configuration, we collected two, partially co-located profiles perpendicular to and centred on the uphill facing scarp. Photographs of the ERT profiles and the MiniSting system can be found in Supplemental Figure S5. The first, coarser resolution profile is composed of two overlapping 81 m-long lines for a total length of ∼120 m with an electrode spacing of 3 m, which yielded a resolvable depth of approximately 15 m at the profile centre. The second, finer resolution line reoccupied the central part of the first, with an electrode spacing of 1.5 m and a total length of ∼40.5 m yielding a resolvable depth of ∼8 m. Electrode coordinates were surveyed using a Trimble R12 system set up in a base and rover configuration. The apparent resistivity data were inverted using a damped least-squares method within AGI's EarthImager 2D software (Advanced Geosciences Inc., 2009). The inversion was iteratively repeated for up to 15 times, or until the root-mean-square misfit between the modelled and measured values was lower than 5%. The resistivity data files are provided in the Appendix (Data Files C1–C4).

4.5 Results

4.5.1 Fault expression

We mapped >80 discrete fault scarps and topographic lineaments from Port Renfrew on the west coast to north of Mill Bay on the east coast (Figure 4.2a). Below, we summarize these observations, working from west to east.

West of Port Renfrew, field mapping by Harrichhausen et al. (2022) suggests that late Eocene–early Oligocene Carmanah Group marine clastic sediments unconformably overlie the SJF, implying minimal activity since the Eocene. The lidar data support this interpretation, with the western SJF trace first becoming clearly evident in the topography only east of Fairy Creek (Figure 4.2c). Some bedrock lineaments are mapped north and south of Port Renfrew. Between Fairy and Harris Creeks, we map a broad (<1 km) zone of deformation with short, discontinuous lineations. Between Harris Creek and Lens Creek, there are several large uphill-facing (N-facing) curvilinear fault scarps at an inflection point where the fault strike changes from ENE–WSW to E–W.

East of Mercer Creek, the main fault can be traced more continuously halfway up the northern side of the San Juan valley, with a prominent lineation and secondary faults forming a ∼250 m-wide deformation zone (Figure 4.3a, b). East of Clydeside Creek, the scarp becomes consistently N-facing, and the deformation zone broadens to 500 m east of Fleet River. Though this central SJF

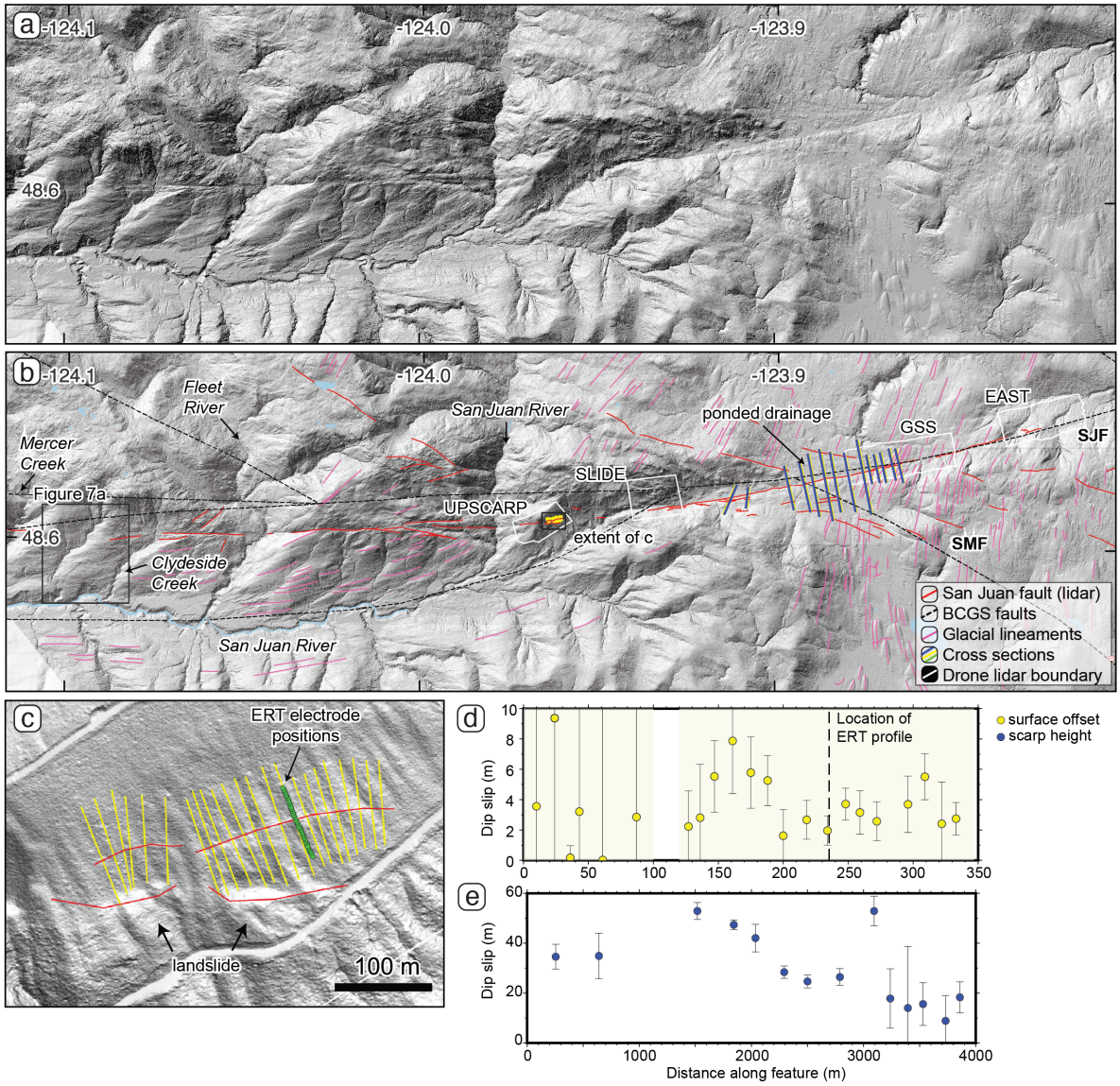

Figure 4.3: a) Uninterpreted hillshaded lidar in the central section of the San Juan Fault. Map extent shown in Figure 4.2 b) Interpretations of fault traces (red) and glacial lineaments (pink). White polygons indicate areas where finer-resolution drone lidar was collected, labelled UPSCARP (uphill facing scarp), SLIDE (several uphill facing features associated with some slope instabilities) GSS (glacially scoured surface), and EAST (several channels which appear offset in aerial imagery). Dashed black lines are geological faults from Cui et al. (2017)). Blue and yellow lines mark the locations of topographic profiles. c) Topographic profiles used to measure the surface offset on the uphill facing scarp. Green points show location of ERT electrodes d) Dip slip measurements for the uphill facing scarp, with ± 2 standard deviation error bars. The location of the ERT profiles is marked by the dashed line. e) Dip slip measurements for the glacially scoured surface, with ± 2 standard deviation error bars. Since there is a change in geology across this scarp, these measurements are merely of the scarp height and not surface offset.

section crosses numerous secondary channels and interfluves at high angles, we do not see any clear evidence of lateral offsets.

Of particular interest in this central SJF section is the isolated uphill facing scarp at the UPSCARP site, where a steep, S-facing slope overlooks the upper reaches of the San Juan valley (Figure 4.3). This feature is quite distinct from the swarms of uphill facing scarps found both to the east (the SLIDE site at the San Juan–Koksilah drainage divide) and west (between Mercer Creek and Clydeside Creek), which we interpret as sackungen caused by slope instability; the differing morphology of these uphill-facing scarp features is discussed further in Section 4.6). We constructed 26 densely-spaced topographic profiles of the UPSCARP feature (Figure 4.3c,d). After discarding the 6 westernmost profiles—which were drawn on a tentatively traced feature just west of the main scarp and which yielded large error bars—we estimated mean dip slip offset of 3.6 m (up to the south) with a range of 0.1–7.7 m. Individual topographic profiles are plotted in Supplemental Figures S6–S9. There are two landslides located south of the uphill facing scarp (Figure 4.3c), the potential relation of these to the fault is discussed in Section 4.6.

East of the UPSCARP site, the main fault can be traced continuously across the drainage divide with the upper Koksilah valley, where it forms a conspicuous N-facing scarp cutting across a glacially scoured surface (the GSS site), ∼15 km west of Shawnigan Lake. This is one of the prime locations for assessing whether late Quaternary landforms are offset by the SJF. For ∼4 km along strike, the N-facing fault scarp crosses a field of NNE-SSW-oriented scours and drumlins, their orientations indicative of southward ice flow (Figure 4.3). No single scour or drumlin can be correlated across the fault, depriving us of any means to estimate lateral offsets of features with known late Quaternary ages. A total of 14 topographic profiles were used to estimate the dip slip across the scarp, yielding a range of 8–52 m and a mean value of 30 m (Figure 4.3e; profiles are plotted in Supplemental Figures S10–S12). We discuss the significance of this offset in Section 4.6.

The fault trace then descends into the main Koksilah River valley, where it can be traced discontinuously in bedrock outcrops on the southern valley slopes (Figures 4.3 & 4.4). North of Grant Lake, the fault trace splits, with a large north-facing escarpment south of the river and a smaller south-facing bedrock scarp at the top of this escarpment. This morphology could be explained as a flower structure with primary and secondary faults facing in opposing directions. Thirteen profiles were drawn across the larger escarpments (Figures 4.4b, S13–14), yielding scarp heights of 21–165 m and a mean value of 92 m. However, due to the location of the Koksilah river, running parallel to the escarpment, it is difficult to determine if equivalent surfaces exist on either side of the fault, with the northern consisting of fluvial terraces and the southern portion being scoured bedrock. Additionally, ten profiles were drawn over the south-facing bedrock scarp (Figures 4.4c, S15–16) yield dip slip measurements of 4–22 m and a mean value of 10 m. Further east, where the scarp becomes more diffuse and potentially draped by some glacial drumlins, it becomes possible once again to measure an offset within a single surface (Figure 4.4b, S17–18). Nine profiles across this diffuse scarp yield dip slip values of 21–56 m with a mean value of 36 m. A plot of these dip slip measurements can be found on Figure 4.4d.

Just west of Shawnigan Lake, the fault zone widens further, with several mapped lineaments continuing eastward towards Mill Bay, and others curving northeastward towards Cobble Hill. There has been significant anthropogenic modification of the landscape east of Shawnigan Lake which

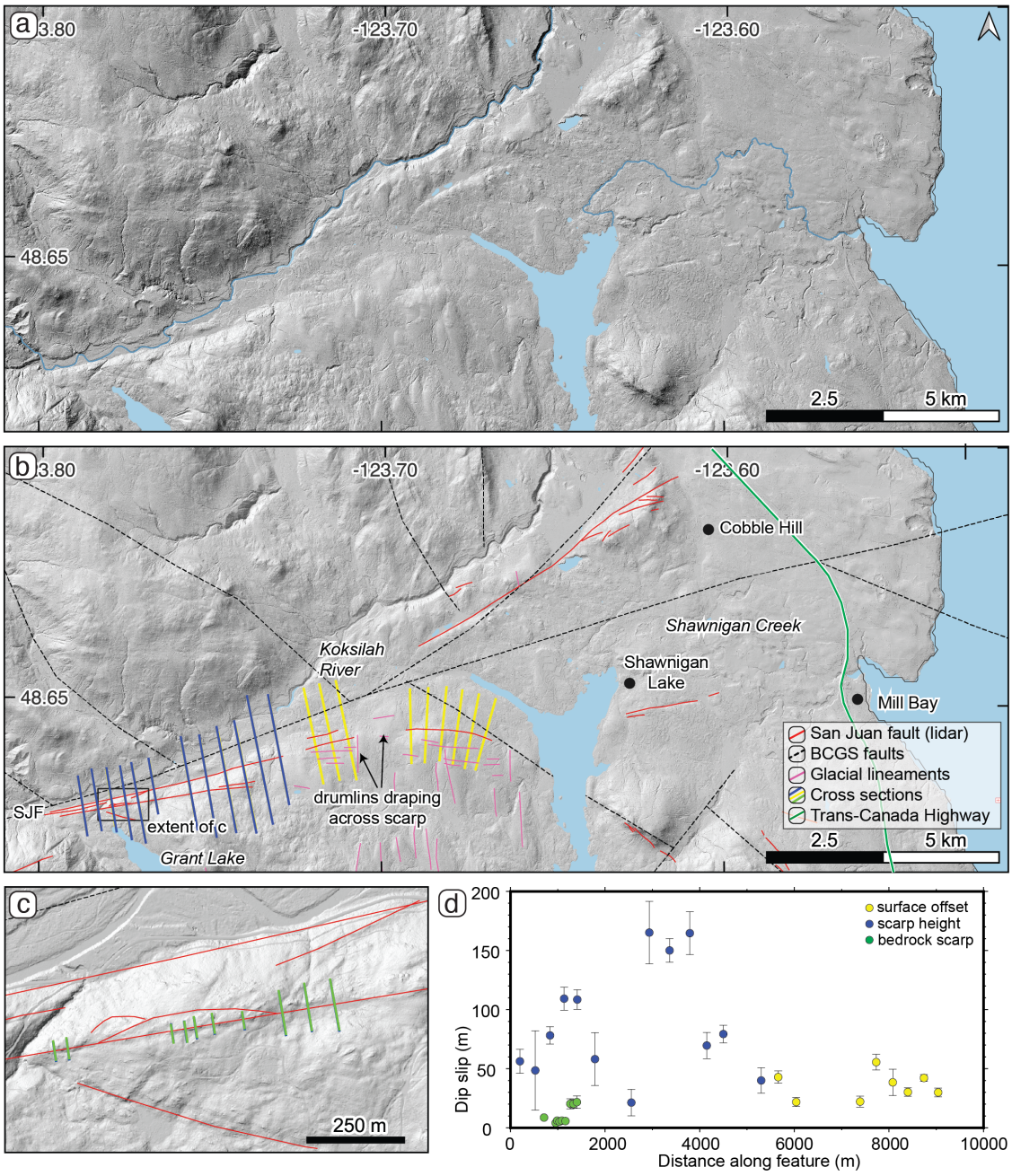

Figure 4.4: a) Uninterpreted hillshaded lidar in the eastern section of the San Juan Fault. b) Interpretations of fault traces (red) and glacial lineaments (pink). Dashed black lines are geological faults as mapped by the British Columbia Geological Survey (BCGS). Green line shows the location of the Trans-Canada Highway. Blue and yellow lines mark locations of topographic profiles. c) Inset showing locations of bedrock scarp measurements (green lines). d) Dip slip measurements with ±2 standard deviation error bars. Points are colored according to the type of measurement being recorded.

Terrane	Unit Name	Description
Pacific Rim	Leech River schist	Metamorphosed pelites; slate, phyllite, quartz-biotite schists, minor interbedded volcanics. Varied levels of weathering and friability. Foliation direction highly variable.
	Survey Mountain volcanics	Massive mafic volcanics, sometimes with minor lenses of limestone. Occasionally serpentinized in shear zones (scaly).
Wrangellia	Island Plutonic Group	Granodiorite.
	Bonanza Group	Massive basalts and rhyolites. Green and maroon tuffs, breccias.
	West Coast Crystalline Complex	Granodiorite, Quartz diorite.

Table 4.1: Description of lithologies sampled while collecting Schmidt hammer rebound values along the San Juan fault.

makes it difficult to trace subtle topographic lineaments in this area, and where visible, the fault trace is generally expressed as a linear furrow with neither side clearly uplifted. Some of these southeast trending lineaments are along strike of the active XELF (Harrichhausen et al., 2023).

Along the full length of the SJF, we identified 18 stream channels which cut across the fault trace, including several within the EAST drone lidar footprint. We attempted to measure strike-slip offsets across these channels by backslipping the DTMs, but none of them exhibit clear lateral offsets that could be quantified. At the GSS site, a field of linear glacial scours is present on either side of the fault, potentially capturing the amount of lateral slip since the last glaciation. However, none of the individual scours could be reliably traced across the fault. This may be because the scarp is at the foot of a change in slope, which likely affected the direction of ice flow (Figure 4.3c).

4.5.2 Schmidt hammer results

We focused our Schmidt hammer measurements on the central SJF because it has the clearest fault geomorphology and because of the relative ease of road access to suitable outcrops. We collected average rebound values at 81 sites from 405 individual measurements. Most of the sites are along two north-south (fault-perpendicular) transects, with the remainder distributed more broadly wherever outcrops were easily accessible by road (Figure 4.5a; see Supplemental Figure S19 for example photographs). Table 4.1 provides brief descriptions of the sampled lithologies. The most sampled lithologies were the Survey Mountain volcanics, with an average rebound value of 49 from 32 sites, followed by the Leech River schist, with an average rebound value of 33 from 27 sites. The Bonanza Volcanics and Island Plutonic Suite were measured in six and seven locations each and had average rebound values of 55 and 62 respectively. Lastly, we sampled the West Coast Crystalline complex in one locality, yielding an average rebound value of 55.

On the north side of the fault the geology is mostly composed of extrusive igneous rocks of Survey Mountain and the Bonanza Group, which yield an average rebound value of 54. South of the SJF, the most sampled lithology was the Leech River schist, with a few outcrops of Survey Mountain volcanics, together yielding an average rebound value of 36, significantly lower than on the

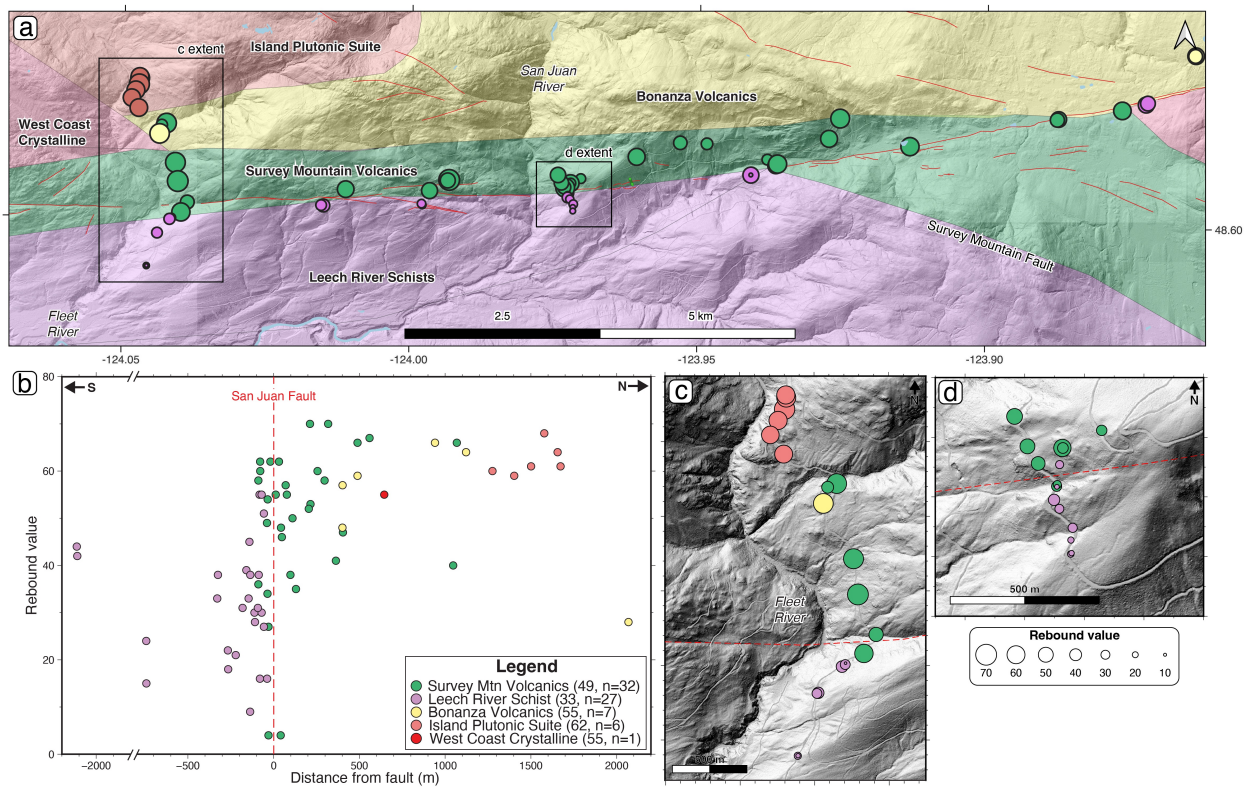

Figure 4.5: a) Geological map of study area (British Columbia Geological Survey digital collection), with the SJF trace in red and Schmidt hammer measurement locations marked by circles, coloured by sampled lithology. b) Schmidt hammer measurements plotted by distance from the fault (dashed red line) and coloured by lithology as in (a). Left is southwards. Legend shows average rebound values and number of measurements for each lithology. c) Transect 1 and d) transect 2 across the SJF, with measurements (circles) scaled by rebound value and coloured by lithology. Note how rebound values diminish rapidly along and south of the fault.

northern side. The difference between the harder rocks north of and softer rocks south of the fault is consistent with the regional geology, but inconsistent with the widespread north-facing scarps having formed through differential erosion. We return to this point in the Discussion.

4.5.3 Electrical resistivity tomography

The ERT profiles (Figure 4.6) confirm that the uphill facing scarp is not just a surface feature such as an old road bed. In the longer profile ((Figure 4.6a), a ∼2 m thick, surficial high-resistivity layer (HR1) is offset at the scarp by ∼1.4 m, south side up. The offset is best explained by a fault dipping approximately 73–82° to the north, making it normal slip sense. The high-resolution profile (Figure 4.6b) is consistent with these interpretations, showing a similar offset and fault dip angle. South of the uphill facing scarp, there is a slightly smaller offset (SF1), with the opposite sense of slip (reverse). This is evident in the lidar as a very subtle shallowing of the hillslope, followed by similarly subtle steepening (Figure 4.7c). There are additional offsets and discontinuities further downslope (SF2), near the southern end of the long profile. However, we are less confident that these are fault-related since several measurements in this area had to be discarded during the inversion and cleaning iterations, resulting in the profile being much shallower.

In addition to the ERT profiles, we dug a 0.5 m deep test pit on the uphill facing scarp to determine the composition of the surface layer (HR1). The test pit yielded a clast-supported assortment of sub-angular to sub-rounded clasts (5-10 cm) with a fine silty matrix. The clasts were of a variety of lithologies, but mainly volcanic in origin. This is consistent with colluvium in the area, as are the measured resistivity values of up to 50,000 ohm-m (Palacky, 1988). We interpret the lower resistivity unit below this to be weathered bedrock, with measured resistivities of 100-400 ohm-m being consistent with typical values for weathered volcanics (Palacky, 1988) as are expected at this location (Survey Mountain, Table 4.1).

4.6 Discussion

4.6.1 Cryptic evidence of Quaternary activity

The San Juan fault displays a remarkably clear surface trace in the hillshaded DTM (Figures 4.2–4.4), one that is more continuous than along other nearby active faults. By comparison, the Leech River fault (Morell et al., 2017), the XEOLXELEK–Elk Lake fault (Harrichhausen et al., 2023), and the Beaufort Range fault (Lynch et al., 2023) each exhibit subtle, discontinuous surface traces, but all three have been shown to have ruptured during the Holocene, largely because they fortuitously intersect and cross-cut late Quaternary-aged unconsolidated sediment, which provides an unequivocal record of recent activity. The San Juan fault presents a vexing challenge because, despite having such a clear geomorphic expression, it has no such age constraint. Below, we make the case for why the geomorphic, geomechanical, and geophysical evidence points towards Quaternary activity on the San Juan fault.

One possible explanation for the prominent scarp on the glacially scoured surface is that the rheological strength on either side of the fault is different; differential weathering could have lowered

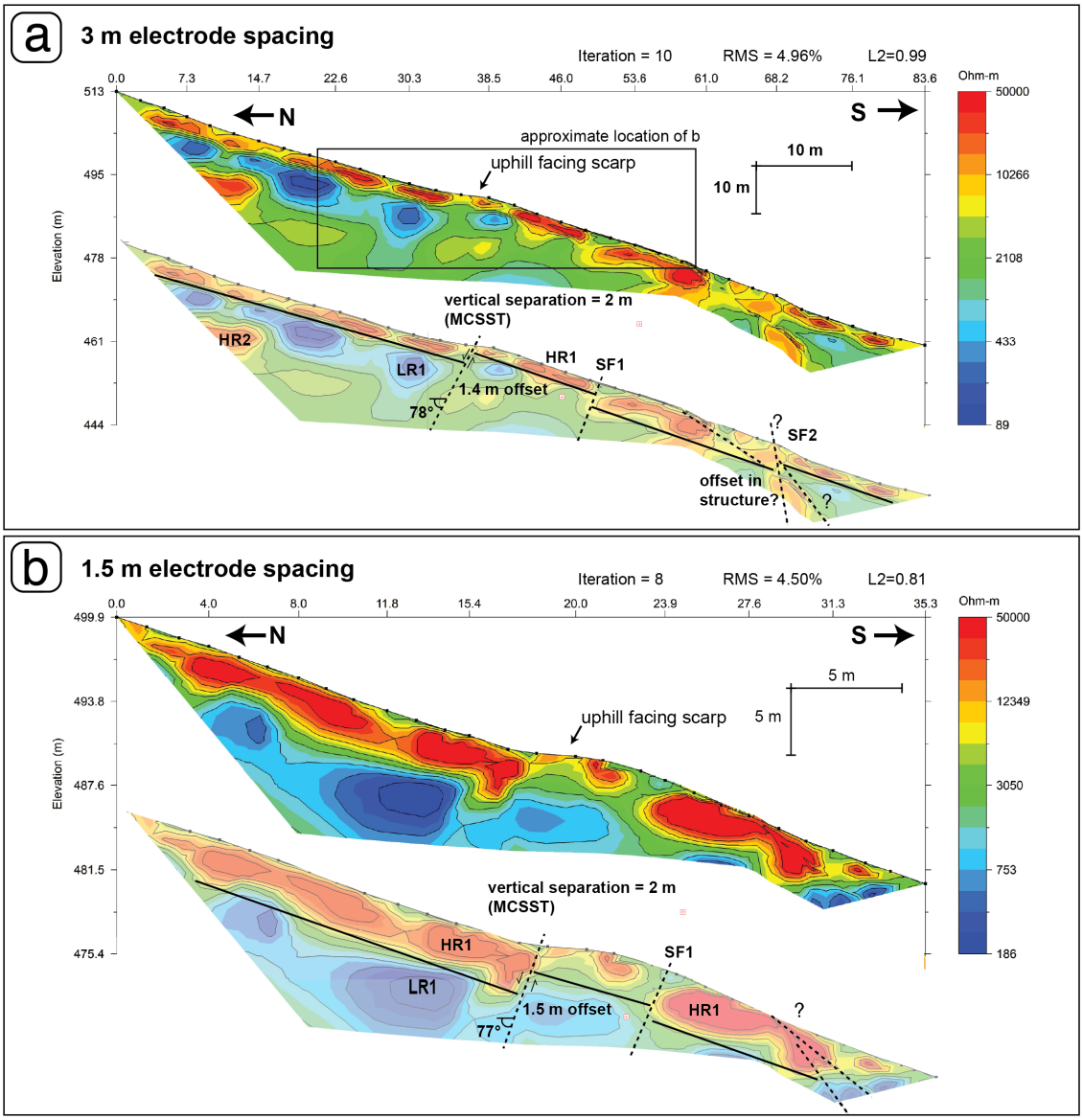

Figure 4.6: a) 3 m-spaced electrical resistivity tomography profile across the uphill facing scarp, with box showing approximate location of b. Lower transparent profile includes interpretations. Vertical separation of the HR1 unit is similar to the surface as measured using MCSST (Figure 4.3c,d). HR – high resistivity, LR – low resistivity, SF – secondary fault. b) 1.5 m-spaced high-resolution electrical resistivity tomography profile with interpretations below. Note that both profiles are horizontally stretched in order to highlight features in the resistivity structure (see "L"-shaped scale marker on the right).

the northern part, leaving the southern portion higher in the topography. However, this argument is inconsistent with the results from our Schmidt hammer measurements (Figure 4.5b), which show higher compressive strengths in the rocks north of the fault. Compressive strength is positively correlated with erosive resistance (Matthews and Winkler, 2022; Stahl and Tye, 2020) and we would therefore expect that, if subject to the same intensity of glacial scouring, the stronger rocks north of the fault should be less eroded. Furthermore, the lithologies south of the fault are mainly metamorphosed sediments and volcanics, which typically have erosion rates of 0.011–0.020 mm.yr^{-1}, while those north of the fault are mainly intrusive igneous rocks, which typically erode at slower rates of 0.009 mm.yr^{-1} (Portenga and Bierman, 2011). Another geomorphic process related to differential weathering that could potentially promote the development of a bedrock scarp feature is glacial plucking. However, the southward direction of ice-flow (as indicated by drumlins at the GSS site) is unlikely to have contributed to the formation of the scarp, as plucking generally occurs on the leeward side of a positive topographic feature (Alley et al., 2019). We therefore argue that differential weathering and glacial plucking cannot explain the prominence of the largely north-facing scarp.

Our preferred explanation is that the scarp was produced by oblique slip along a sub-vertical fault, with south-side-up motion counteracting and exceeding the effects of any differential erosion. However, at 30–36 m high at the GSS site and west of Shawnigan Lake (Figures 4.3 & 4.4), the scarp is in places too large to have been generated within the Holocene and since the end of the latest glaciation. Vertical slip rates would need to be > 2.5 mm.yr^{-1}, considerably higher than most other crustal faults in the Cascadia forearc (Kelsey et al., 2012; Morell et al., 2018; Schermer et al., 2021; Personius et al., 2014), and such a slip rate would imply numerous M 6–7 earthquakes in the Holocene, each with several meters of slip. We therefore suggest that the scarp is a product of a much longer period of tectonic activity extending before the Holocene, and that successive glacial cycles have not fully reset the landscape. Constraining glacial erosion is challenging, as rates can vary significantly both spatially and temporally (Alley et al., 2019; Patton et al., 2022). It is possible that the glaciers on southern Vancouver Island had high erosion rates (on the order of several mm.yr^{-1}) as warmer temperatures and higher precipitation are correlated to greater erosion (Cook et al., 2020). On the other hand, the Fraser glaciation was not particularly long-lived, and the Cordilleran Ice Sheet had a late onset and an early, rapid retreat from the Pacific coastal region (Alley and Chatwin, 1979; Clague and James, 2002; Clague and Ward, 2011). Pre-Holocene tectonic landforms may have been partially denuded, but not entirely removed from the landscape.

Although the prominent, continuous scarp is suggestive of pan-Quaternary fault activity, we must look to smaller, more subtle scarp features for evidence of more recent, post-glacial Holocene rupture. Along the San Juan River (e.g. Figure 4.7a), there are swarms of uphill facing scarps on hillsides with thick accumulations of sediment (mostly till), and landslide scars at the slope base. These features are likely sackungen, the result of gravitational slumping within the sediment in response to the San Juan River eroding the base of the slope.

However, we interpret that the uphill facing scarp at the UPSCARP site (Figure 4.7b) is not a sackung, since it is isolated, oblique to the ridgeline, but subparallel to the SJF trace and along strike from a significant bedrock shear zone. Furthermore, the normal offsets in our ERT profiles are inconsistent with the sackung model by Savage and Varnes (1987) which has compressive flow

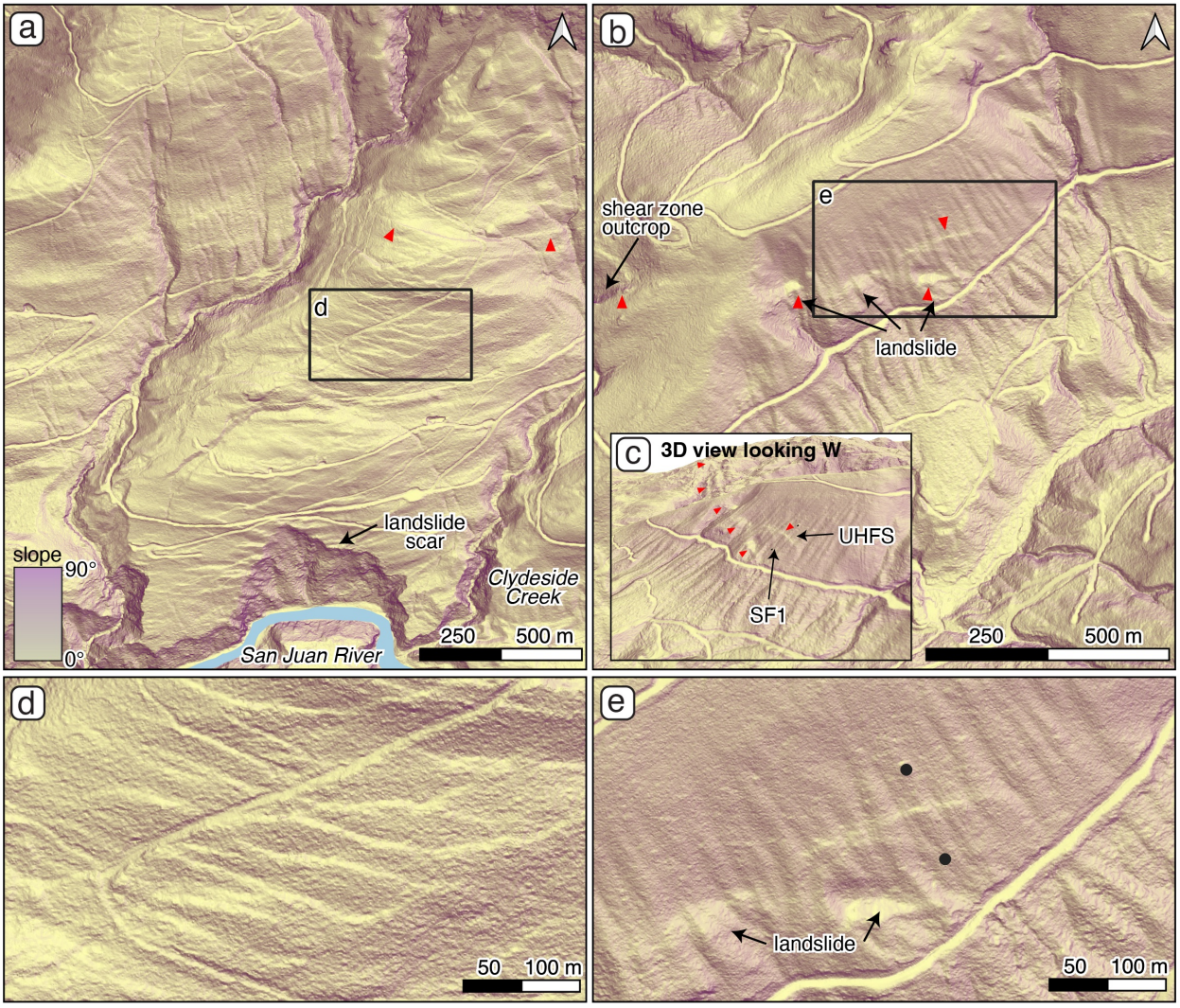

Figure 4.7: Lidar hillshades, coloured by slope angle, comparing (left) features interpreted as sackungen with (right) the uphill facing scarp interpreted as surface faulting. a) Sackungen west of Clydeside Creek (Figure 4.3b). Red triangles mark location of the San Juan fault. b) Uphill facing scarp (UHFS). c) 3D view of the uphill facing scarp, showing how it is located just off strike of the main fault trace. SF1 is the location of the secondary offset in Figure 4.6. d) Zoom in of the sackungen, which are generally parallel to topographic contours. e) Zoom in of the uphill facing scarp. Black points mark the ends of the ERT profile.

or thrust faults midway down the hillslope and normal features located at the ridgetop. The uphill facing scarp may provide evidence for a post-glacial Holocene earthquake along the SJF, as it offsets channels running across it, indicating that this offset was relatively recent and has not yet been removed by erosion. The offset colluvium (potentially till) could be a target for a future paleoseismic trench, though backhoe access would be challenging. The sackungen near Mercer Creek and the landslides south of the UPSCARP feature (Figure 4.7) could both be related to the fault, perhaps even triggered by strong coseismic ground accelerations, since similar features are not present on the other side of the valley. This is additional, circumstantial evidence for earthquake activity along the SJF.

4.6.2 Strike-slip offsets

Whether or not the SJF has a component of modern strike-slip motion remains unresolved. Throughout its history, the fault is interpreted by most authors to record left-lateral motion. The trace of the main scarp is highly linear even where it crosses variable topography, implying a steep dip consistent with predominantly strike-slip motion. Maximum horizontal compressive crustal stress orientations (Balfour et al., 2011) appear near fault normal, with perhaps a slight indication of right-lateral kinematics. Despite several channels and glacial flutes crossing the fault at high angles, we found no suitable locations with offset markers for lateral slip to be measured. Several factors can hinder interpretation of offset markers including: the palimpsestic nature of tectonic landscapes, transient variations in fault slip, and climate variability (Reitman et al., 2019). However, within the central section of the fault (Figure 4.3) we did observe deformed drainages and channels (including Mercer Creek, Clydeside Creek, and Fleet River) that have a right-lateral sense of motion (Figure 4.8). This subtle expression of right lateral slip might suggest distributed deformation (Duvall and Tucker, 2015; Gray et al., 2017), a long elapsed time since the latest earthquake (Reitman et al., 2019), or could be a result of poor preservation of lateral offsets in high precipitation climates (Reitman et al., 2022). For comparison, the Sadie Creek fault on the nearby Olympic peninsula (a branch fault of the NOFZ, Figure 4.1b) has notable channel offsets and a slip rate of around 1–2 mm/yr (Nelson et al., 2017) on very similar hillslopes to those found along the San Juan valley. As such, a slip rate of 1 mm/yr could be the upper bound for the SJF, although there are many other factors to consider as the underlying geology is different, being Siletz terrane basalts in the case of the Sadie Creek fault.

4.6.3 Implications for seismic hazard and risk

In spite of the lines of evidence discussed above, it is difficult to wholly and unequivocally prove that the SJF is an active fault. Similar observations have been made for studies along other active faults within northern Cascadia (e.g. Harrichhausen et al., 2023, 2021; Morell et al., 2018; Nelson et al., 2017). Dense vegetation, high precipitation rates and recent glaciations have resulted in many of the active structures in this region displaying discontinuous tectonic geomorphology, and instrumented seismicity does not align with the mapped faults. Including these structures in seismic hazard models is difficult since most models require that the slip rate is well-constrained. This brings into question the acceptable criteria for considering cryptic faults like the SJF in seismic hazard

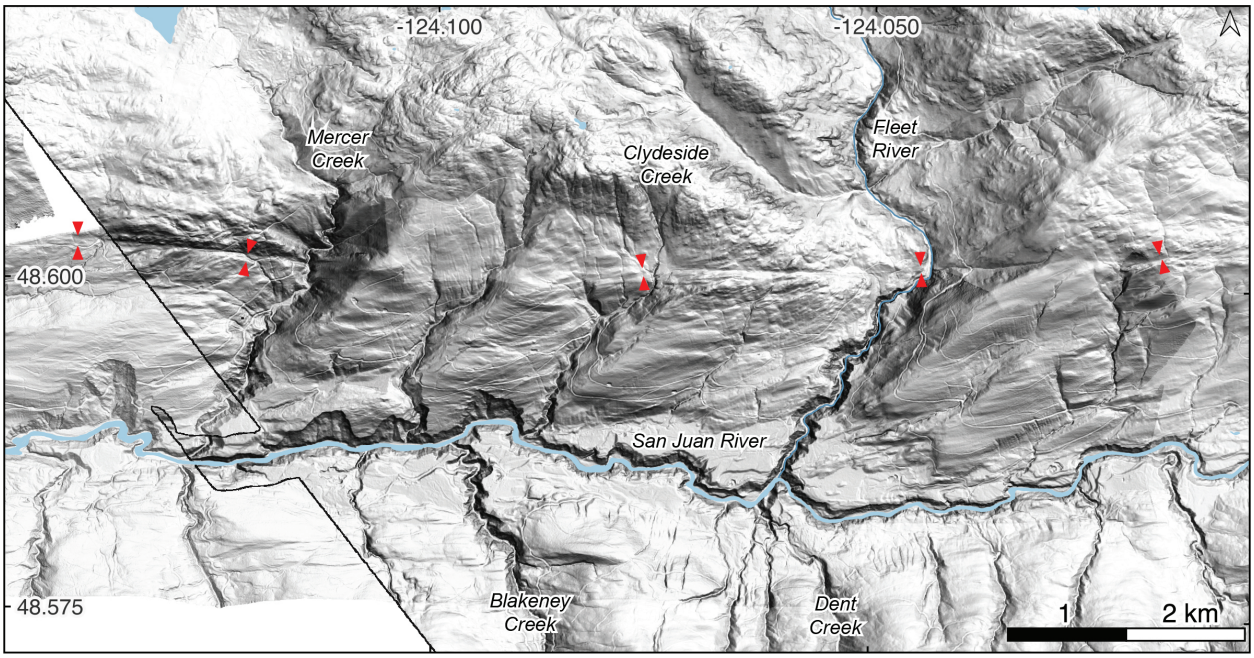

Figure 4.8: Hillshaded topography showing curved drainages crossing the San Juan Fault, deformation of these drainages is consistent with right-lateral motion along the fault. Red triangles indicate the fault location.

models: should they remain excluded until absolute evidence of rupture is found? Given the length of the fault trace (80 km), and conservative estimates for rupture width (10 km) and amount of slip (2 m), the SJF could potentially produce an earthquake of M_W >7, which would have consequential impacts for the nearby communities of Shawnigan Lake, Mill Bay, the Trans-Canada Highway and Greater Victoria.

Fault hazard assessments in such environments require a multi-faceted approach, combining seismological, geological and geophysical techniques. In our case, additional work is necessary to prove that the SJF is active, and provide dates of previous earthquakes for slip rate estimation and incorporation into seismic hazard models. The best option for this would be paleoseismic trenching. There are several potential trench sites, including the UPSCARP site discussed above or the drumlin crossing the fault west of Shawnigan Lake (Figure 4.4). Alternatively, sediment cores could be taken from nearby lakes and ponded sediment sites north of the scarp within the glacially scoured surface (Figure 4.3) in the hopes of finding earthquake related deposits.

4.7 Conclusions

The San Juan fault is one the major terrane-bounding faults on southern Vancouver Island in the northern Cascadia fore-arc. Several lines of evidence indicate that it has been active as a right-lateral reverse fault during the Quaternary, and likely as recently as the Holocene. For one, the surface expression of the SJF is remarkably clear and continuous, being preserved within numerous bedrock outcrops. Additionally, using our novel Schmidt Hammer approach, we were able to rule out

differential weathering as the formation mechanism of a prominent scarp in an otherwise glacially-scoured surface. To have built up to ∼30 m of vertical offset, we interpret that this scarp instead represents multiple earthquake cycles on a slow slip rate fault (<1 mm/yr), and that the scarp must partially predate the most recent glaciation. We also have identified a possible surface rupture from a recent (late Quaternary) event, which may be a suitable site for future paleoseismic trenching. In order to assign a slip rate to this fault and include it in seismic hazard models more work is required. Although currently poorly constrained, the potential for a large, surface-rupturing earthquake on the SJF has important implications for the nearby population centres of Greater Victoria, Shawnigan Lake, Mill Bay, and beyond.

4.8 Acknowledgements

We are grateful to have conducted this work on the traditional territories of the Pacheedaht First Nation and the Hul'q'umi'num speaking people (Cowichan Tribes). We thank Rishi Gupta and Bastien Lanusse for lending us their Schmidt hammer, Sophie Norris for discussing the glacial geomorphology, and Mosaic Forest Management and the Capital Regional District for granting field access and sharing lidar data. Our drone lidar system was developed with funding from the Canada Foundation for Innovation and the BC Knowledge Development Fund, and fieldwork costs were supported through an NSERC Discovery Grant to EN. GS was supported in part through the Agnew Memorial Scholarship from the University of Victoria, TF by an NSERC CGS-Doctoral Scholarship and a Dr. Margaret Perkins Hess Graduate Fellowship, and EN by a Canada Research Chair.

4.9 Data availability

While some of the lidar data used in this study was from private sources, comparable coverage has recently been made available on the British Columbia government's open lidar portal (LidarBC, 2023). The supplemental material (Appendix C) is comprised of 19 figures (Figures C1–C19), and 9 Data files. The figures show cross sections from the vertical separation measurements, hillshaded plots of the drone lidar collections, photographs from the schmidt hammer data collection, and photos from the ERT profile set-up. The data files include; a shapefile of the mapped lineaments, digital terrain models (DTMs) for the drone lidar sites, ERT measurement files, and terrain files (for the ERT profiles). They are available in the Zenodo repository (https://doi.org/10.5281/zenodo.15103480). Digital geology (faults and geological units) used in this study are from the British Columbia Geological Survey (Cui et al., 2017) and the Washington State Geological Survey (Washington Geological Survey, 2022). Earthquake locations are from the Canadian National Earthquake Database (Natural Resources Canada, 1985). GNSS velocities relative to stable North America are from McCaffrey et al. (2013). S_{Hmax} directions are from Balfour et al. (2011). River vector files and population centres are from OpenStreetMap (OpenStreetMap contributers, 2025). We used the MCSST toolkit (Wolfe et al., 2020) to measure vertical separation. Figures were prepared using QGIS (QGIS Association, 2018), GMT (Wessel et al., 2019) and Adobe Illustrator.

Chapter 5
Concluding remarks

The northern Pacific Cordillera is a vast region, with a rich and complicated geological history. The rugged topography, high precipitation rates, limited infrastructure, previous glaciations, and dense forest (lower latitudes) or periglacial tundra (higher latitudes) all contribute to the challenges of studying active tectonics within this environment. As such, a multi-faceted approach is required to understand the region's seismic hazard. Where possible, we can use observations from modern earthquakes, which may provide insights into previously misunderstood or uncharacterized risks, as was the case for the 2020 Koryak Highlands earthquake in Chapter 2. InSAR and seismological techniques were able to enhance our knowledge of tectonics within the otherwise poorly understood Koryak Highlands, without the need for boots-on-the-ground fieldwork. Notably, the fault that ruptured during the 2020 event was not in the expected orientation that geological maps would imply. This event showcases that while seismic hazards are elevated along Cordilleran suture zones, these are complicated regions, and it may not only be the main, mature faults that pose risks. The 2020 earthquake is the largest event to have occurred within the Koryak Highlands, providing an opportunity to estimate the seismogenic thickness of this area. Since modern crustal earthquakes are few and far between within the northern Pacific Cordillera, other techniques are required to extend the record of seismicity further back than the instrumental and historical records.

In Chapter 3, I introduce a UAV laser scanning platform that may further enable us to do just that. The platform is capable of collecting high-resolution topography, even in densely vegetated regions such as those in northern Cascadia. Not only is this chapter a practical guide for other researchers interested in using this technology for their own studies, but I show several ways that ULS can be used to study fault geomorphology, from the scale of a local (100 x 100 m) paleoseismic trench site to multi-kilometre mapping of faults in remote forested regions. While battery life and regulatory constraints prevent ULS from replacing ALS for regional fault reconnaissance, there remains an abundant potential for ULS data. This includes: cost-effectively mapping faults beyond the edges of existing ALS surveys; detailed surveying of known faults for paleoseismic trenching, fault slip rate estimations, or morphologic dating; revealing subtle landforms arising from off-fault deformation; rapid collection of perishable data such as along earthquake surface ruptures; and for repeat deployments along surface ruptures for capturing afterslip.

Chapter 4 makes use of several lidar datasets, ALS and ULS, to map the surface trace of the San Juan fault on southern Vancouver Island. A clear lineation is observed, prompting further investigation into whether the San Juan fault has been active during the Quaternary or not. Several

lines of evidence for geologically recent earthquakes along the SJF are found, including a right-lateral sense of offset across several channels; and a linear fault scarp cutting through a glacially scoured surface with an average vertical offset of 30 m, the up-thrown southern portion of which is rheologically weaker than the down-thrown northern side. This surface thus potentially records many Pleistocene earthquakes; the fault scarp remaining in the landscape despite glacial erosion. I also find an uphill facing scarp, which may represent one of the most recent ruptures along the SJF. Several potential sites for future paleoseismic work are identified, which would be necessary to assign an earthquake recurrence interval or fault slip rate for incorporation into seismic hazard models.

There remains a lot of work to be done in order to understand seismic hazard within the northern Pacific Cordillera. I believe that remote sensing observations are vital to identifying the main structures at play. Recent advances in this field include: satellite constellations which offer greatly reduced revisit periods expanding the capabilities of InSAR considerably, an increasing ubiquity of airborne lidar data (much of it publicly accessible), and commercially available drone platforms for collecting bespoke lidar datasets. Repeat observations (made easier by the aforementioned advancements) will allow us to observe these faults and systems at increasing resolution, both spatially and temporally. Combined with field observations and geophysical techniques, we will gain increased insights into the earthquake cycle.

Bibliography

Advanced Geosciences Inc. (2009). AGI EarthImager 2D. (version 2.4.0) [Software] AGIUSA. Retrieved from https://www.agiusa.com/agi-earthimager-2d.

Akinin, V. V., et al. (2020). Episodicity and the dance of late Mesozoic magmatism and deformation along the northern circum-Pacific margin: north-eastern Russia to the Cordillera. *Earth-Science Reviews*, *208*, 103272, https://doi.org/10.1016/j.earscirev.2020.103272.

Alley, N. F. & Chatwin, S. C. (1979). Late Pleistocene history and geomorphology, southwestern Vancouver Island, British Columbia. *Canadian Journal of Earth Sciences*, *16*(9), 1645–1657.

Alley, R. B., Cuffey, K. M., & Zoet, L. K. (2019). Glacial erosion: status and outlook. *Annals of Glaciology*, *60*(80), 1–13, https://doi.org/10.1017/aog.2019.38.

Altamimi, Z., Métivier, L., Rebischung, P., Collilieux, X., Chanard, K., & Barnéoud, J. (2023). ITRF2020 plate motion model. *Geophysical Research Letters*, *50*(24), e2023GL106373, https://doi.org/10.1029/2023GL106373.

Andrew, A. & Godwin, C. I. (1989). Lead- and strontium-isotope geochemistry of Paleozoic Sicker Group and Jurassic Bonanza Group volcanic rocks and Island Intrusions, Vancouver Island, British Columbia. *Canadian Journal of Earth Sciences*, *26*(5), 894–907, https://doi.org/10.1139/e89-072.

Angombe, M., Chien, J., Salomon, G., Liu, Y., Rowe, C., Sitali, M., & Shipena, S. (2025). Seismicity and surface deformation in Kamanjab Inlier, Northern Namibia. *Seismica*. (accepted with revisions).

Arrowsmith, J. R., Rhodes, D. D., & Pollard, D. D. (1998). Morphologic dating of scarps formed by repeated slip events along the San Andreas Fault, Carrizo Plain, California. *Journal of Geophysical Research (Solid Earth)*, *103*(B5), 10,141–10,160, https://doi.org/10.1029/98JB00505.

Bai, Y., Lay, T., Cheung, K. F., & Ye, L. (2017). Two regions of seafloor deformation generated the tsunami for the 13 November 2016, Kaikoura, New Zealand earthquake. *Geophysical Research Letters*, *44*(13), 6597–6606, https://doi.org/10.1002/2017GL073717.

Baldwin, K., et al. (2019). Vegetation Zones of Canada: A Biogeoclimate Perspective. https://open.canada.ca/data/en/dataset/22b0166b-9db3-46b7-9baf-6584a3acc7b1.

Balfour, N., Cassidy, J., Dosso, S., & Mazzotti, S. (2011). Mapping crustal stress and strain in southwest British Columbia. *Journal of Geophysical Research: Solid Earth*, *116*(B3), https://doi.org/10.1029/2010JB008003.

Bemis, S. P., Micklethwaite, S., Turner, D., James, M. R., Akciz, S., Thiele, S. T., & Bangash, H. A. (2014). Ground-based and UAV-Based photogrammetry: A multi-scale, high-resolution mapping tool for structural geology and paleoseismology. *Journal of Structural Geology*, *69*, 163–178, https://doi.org/10.1016/j.jsg.2014.10.007.

Benavente, C., et al. (2021). Paleoseismic evidence of an M_w 7 pre-Hispanic earthquake in the Peruvian forearc. *Tectonics*, *40*(6), e2020TC006479, e2020TC006479, https://doi.org/10.1029/2020TC006479.

Bender, A. M. & Haeussler, P. J. (2017). *Eastern Denali Fault surface trace map, eastern Alaska and Yukon, Canada*. USGS Numbered Series 2017-1049, U.S. Geological Survey, Reston, VA.

Bergman, E. A. & Solomon, S. C. (1990). Earthquake swarms on the Mid-Atlantic Ridge: Products of magmatism or extensional tectonics? *Journal of Geophysical Research: Solid Earth*, *95*(B4), 4943–4965, https://doi.org/10.1029/JB095iB04p04943.

Bertiger, W., et al. (2020). GipsyX/RTGx, a new tool set for space geodetic operations and research. *Advances in Space Research*, *66*(3), 469–489, https://doi.org/10.1016/j.asr.2020.04.015.

Biegel, K. M., Gosselin, J. M., Dettmer, J., Colpron, M., Enkelmann, E., & Caine, J. S. (2024). Earthquake relocations delineate a discrete fault network and deformation corridor throughout southeast Alaska and southwest Yukon. *Tectonics*, *43*(5), e2023TC008140, https://doi.org/10.1029/2023TC008140.

Biggs, J. & Wright, T. J. (2020). How satellite InSAR has grown from opportunistic science to routine monitoring over the last decade. *Nature Communications*, *11*(1), 3863, https://doi.org/10.1038/s41467-020-17587-6.

Bilek, S. L. & Lay, T. (2018). Subduction zone megathrust earthquakes. *Geosphere*, *14*(4), 1468–1500, https://doi.org/10.1130/GES01608.1.

Blais-Stevens, A., Clague, J. J., Brahney, J., Lipovsky, P., Haeussler, P. J., & Menounos, B. (2020). Evidence for Large Holocene Earthquakes along the Denali Fault in Southwest Yukon, Canada. *Environmental & Engineering Geoscience*, *26*(2), 149–166, https://doi.org/10.2113/EEG-2263.

Bostock, H. S. (1952). *Geology of northwest Shakwak Valley, Yukon Territory*. E. Cloutier, Queen's Printer.

Brandon, M. T. (1989). Origin of igneous rocks associated with melanges of the Pacific Rim Complex, western Vancouver Island, Canada. *Tectonics*, *8*(6), 1115–1136, https://doi.org/10.1029/TC008i006p01115.

Brede, B., Lau, A., Bartholomeus, H. M., & Kooistra, L. (2017). Comparing RIEGL RiCOPTER UAV LiDAR Derived Canopy Height and DBH with Terrestrial LiDAR. *Sensors*, *17*(10), https://doi.org/10.3390/s17102371.

Bro, R. & De Jong, S. (1997). A fast non-negativity-constrained least squares algorithm. *Journal of Chemometrics: A Journal of the Chemometrics Society*, *11*(5), 393–401.

Brooks, B. A., Glennie, C., Hudnut, K. W., Ericksen, T., & Hauser, D. (2013). Mobile Laser Scanning Applied to the Earth Sciences. *Eos, Transactions American Geophysical Union*, *94*(36), 313–315, https://doi.org/10.1002/2013EO360002.

Brooks, B. A., et al. (2017). Buried shallow fault slip from the South Napa earthquake revealed by near-field geodesy. *Science Advances*, *3*(7), e1700525, https://doi.org/10.1126/sciadv.1700525.

Bubeck, A., Wilkinson, M., Roberts, G. P., Cowie, P. A., McCaffrey, K. J. W., Phillips, R., & Sammonds, P. (2015). The tectonic geomorphology of bedrock scarps on active normal faults in the Italian Apennines mapped using combined ground penetrating radar and terrestrial laser scanning. *Geomorphology*, *237*, 38–51, https://doi.org/10.1016/j.geomorph.2014.03.011.

Butler, H., Chambers, B., Hartzell, P., & Glennie, C. (2021). PDAL: An open source library for the processing and analysis of point clouds. *Computers & Geosciences*, *148*, 104680, https://doi.org/10.1016/j.cageo.2020.104680.

Cățeanu, M., Arcadie, C., & others (2017). ALS for terrain mapping in forest environments: An analysis of LiDAR filtering algorithms. *EARSeL eProceedings*, *16*(1), 9–20, https://doi.org/10.12760/01-2017-1-02.

Chekhovich, V., Palandzhyan, S., Sukhov, A., Egorkin, A., & Ben'yamovsky, V. (2008). The Late Cretaceous-Paleogene active margin of Northeastern Asia: Geodynamic setting of terrigenous sedimentary basins in the Central Koryak terrane. *Geotectonics*, *42*(1), 48–63, https://doi.org/10.1134/S0016852108010056.

Chen, T., Akciz, S. O., Hudnut, K. W., Zhang, D. Z., & Stock, J. M. (2015). Fault-Slip Distribution of the 1999 Mw 7.1 Hector Mine Earthquake, California, Estimated from Postearthquake Airborne LiDAR Data. *Bulletin of the Seismological Society of America*, *105*(2A), 776–790, https://doi.org/10.1785/0120130108.

Choi, M., Eaton, D. W., & Enkelmann, E. (2021). Is the Eastern Denali fault still active? *Geology*, *49*(6), 662–666, https://doi.org/10.1130/G48461.1.

Choy, G. L. & Boatwright, J. (1988). Teleseismic and near-field analysis of the Nahanni earthquakes in the Northwest Territories, Canada. *Bulletin of the Seismological Society of America*, *78*(5), 1627–1652, https://doi.org/10.1785/BSSA0780051627.

Civil Aviation Safety Authority (2021). Remote pilot licence. (Accessed 23 October 2023) https://www.casa.gov.au/drones/get-your-operator-credentials/remote-pilot-licence.

Clague, J. J. (1975). Late Quaternary sediments and geomorphic history of the southern Rocky Mountain Trench, British Columbia. *Canadian Journal of Earth Sciences*, *12*(4), 595–605, https://doi.org/10.1139/e75-054.

Clague, J. J. & James, T. S. (2002). History and isostatic effects of the last ice sheet in southern British Columbia. *Quaternary Science Reviews*, *21*(1-3), 71–87, https://doi.org/10.1016/S0277-3791(01)00070-1.

Clague, J. J. & Ward, B. (2011). Chapter 44 - Pleistocene Glaciation of British Columbia. In J. Ehlers, P. L. Gibbard, & P. D. Hughes (Eds.), *Developments in Quaternary Sciences*, volume 15 (pp. 563–573). Elsevier.

Clark, K. J., et al. (2017). Highly variable coastal deformation in the 2016 M_W7.8 Kaikōura earthquake reflects rupture complexity along a transpressional plate boundary. *Earth and Planetary Science Letters*, *474*, 334–344, https://doi.org/10.1016/j.epsl.2017.06.048.

Coney, P. J. & Evenchick, C. A. (1994). Consolidation of the American Cordilleras. *Journal of South American Earth Sciences*, *7*(3), 241–262, https://doi.org/10.1016/0895-9811(94)90011-6.

Cook, S. J., Swift, D. A., Kirkbride, M. P., Knight, P. G., & Waller, R. I. (2020). The empirical basis for modelling glacial erosion rates. *Nature Communications*, *11*(1), 759, https://doi.org/10.1038/s41467-020-14583-8.

Cui, Y., Miller, D., Schiarizza, P., & Diakow, L. (2017). British Columbia digital geology. *British Columbia Ministry of Energy, Mines and Petroleum Resources, British Columbia Geological Survey Open File*, *8*(9). Data version 2019-12-19.

Cunningham, D., Grebby, S., Tansey, K., Gosar, A., & Kastelic, V. (2006). Application of airborne LiDAR to mapping seismogenic faults in forested mountainous terrain, southeastern Alps, Slovenia. *Geophysical Research Letters*, *33*(20), L20308, https://doi.org/10.1029/2006GL027014.

DeBari, S. M., Anderson, R. G., & Mortensen, J. K. (1999). Correlation among lower to upper crustal components in an island arc: the Jurassic Bonanza arc, Vancouver Island, Canada. *Canadian Journal of Earth Sciences*, *36*(8), 1371–1413, https://doi.org/10.1139/e99-029.

DeLong, S. B., Lienkaemper, J. J., Pickering, A. J., & Avdievitch, N. N. (2015). Rates and patterns of surface deformation from laser scanning following the South Napa earthquake, California. *Geosphere*, *11*(6), 2015–2030, https://doi.org/10.1130/GES01189.1.

Dickinson, W. R. (2004). Evolution of the North American cordillera. *Annu. Rev. Earth Planet. Sci.*, *32*, 13–45, https://doi.org/10.1146/annurev.earth.32.101802.120257.

Diederichs, A., et al. (2019). Unusual kinematics of the Papatea fault (2016 Kaikōura earthquake) suggest anelastic rupture. *Science Advances*, *5*(10), https://doi.org/10.1126/sciadv.aax5703.

DiFrancesco, P.-M., Bonneau, D., & Hutchinson, D. J. (2020). The implications of M3C2 projection diameter on 3D semi-automated rockfall extraction from sequential terrestrial laser scanning point clouds. *Remote Sensing*, *12*(11), 1885, https://doi.org/10.3390/rs12111885.

Dolan, J. F. & Haravitch, B. D. (2014). How well do surface slip measurements track slip at depth in large strike-slip earthquakes? The importance of fault structural maturity in controlling on-fault slip versus off-fault surface deformation. *Earth and Planetary Science Letters*, *388*, 38–47, https://doi.org/10.1016/j.epsl.2013.11.043.

Duckworth, W. C., Amos, C. B., Schermer, E. R., Loveless, J. P., & Rittenour, T. M. (2021). Slip and Strain accumulation along the Sadie Creek Fault, Olympic Peninsula, Washington. *Journal of Geophysical Research: Solid Earth*, *126*(3), https://doi.org/10.1029/2020JB020276.

DuRoss, C. B., Bunds, M. P., Gold, R. D., Briggs, R. W., Reitman, N. G., Personius, S. F., & Toké, N. A. (2019). Variable normal-fault rupture behavior, northern Lost River fault zone, Idaho, USA. *Geosphere*, *15*(6), 1869–1892, https://doi.org/10.1130/GES02096.1.

Duvall, A. R. & Tucker, G. E. (2015). Dynamic ridges and valleys in a strike-slip environment. *Journal of Geophysical Research: Earth Surface*, *120*(10), 2016–2026, https://doi.org/10.1002/2015JF003618.

Dziewonski, A. M., Chou, T.-A., & Woodhouse, J. H. (1981). Determination of earthquake source parameters from waveform data for studies of global and regional seismicity. *Journal of Geophysical Research: Solid Earth*, *86*(B4), 2825–2852.

Eberhart-Phillips, D., et al. (2003). The 2002 Denali Fault Earthquake, Alaska: A large magnitude, slip-partitioned event. *Science*, *300*(5622), 1113–1118, https://doi.org/10.1126/science.1082703.

Ebmeier, S. K., Biggs, J., Mather, T. A., & Amelung, F. (2013). Applicability of InSAR to tropical volcanoes: insights from Central America. *Geological Society, London, Special Publications*, *380*(1), 15–37, https://doi.org/10.1144/sp380.2.

Ekström, G., Nettles, M., & Dziewoński, A. (2012). The global CMT project 2004–2010: Centroid-moment tensors for 13,017 earthquakes. *Physics of the Earth and Planetary Interiors*, *200*, 1–9, https://doi.org/10.1016/j.pepi.2012.04.002.

Elliott, J., et al. (2012). Slip in the 2010–2011 Canterbury earthquakes, New Zealand. *Journal of Geophysical Research: Solid Earth*, *117*(B3), https://doi.org/10.1029/2011JB008868.

Elliott, J., Walters, R., & Wright, T. (2016). The role of space-based observation in understanding and responding to active tectonics and earthquakes. *Nature Communications*, *7*(1), 13844, https://doi.org/10.1038/ncomms13844.

Elliott, J. L., Freymueller, J. T., & Rabus, B. (2007). Coseismic deformation of the 2002 Denali fault earthquake: Contributions from synthetic aperture radar range offsets. *Journal of Geophysical Research (Solid Earth)*, *112*(B6), B06421, B06421, https://doi.org/10.1029/2006JB004428.

Engdahl, E. R., Jackson, J. A., Myers, S. C., Bergman, E. A., & Priestley, K. (2006). Relocation and assessment of seismicity in the Iran region. *Geophysical Journal International*, *167*(2), 761–778, https://doi.org/10.1111/j.1365-246X.2006.03127.x.

England, T. & Calon, T. (1991). The Cowichan fold and thrust system, Vancouver Island, southwestern British Columbia. *Geological Society of America Bulletin*, *103*(3), 336–362, https://doi.org/10.1130/0016-7606(1991)103<0336:TCFATS>2.3.CO;2.

Esri (2022). Ocean Basemap. (Assessed December 1, 2023) https://www.arcgis.com/home/item.html?id=6348e67824504fc9a62976434bf0d8d5.

Estève, C., Liu, Y., Koulakov, I., Schaeffer, A. J., & Audet, P. (2022). Seismic Evidence for a Weakened Thick Crust at the Beaufort Sea Continental Margin. *Geophysical Research Letters*, *49*(16), e00158, https://doi.org/10.1029/2022GL100158.

European Space Agency (2020). Copernicus Data Space Ecosystem. (Accessed 21 July 2022) https://dataspace.copernicus.eu/.

European Space Agency, Singergise (2021). Copernicus Global Digital Elevation Model. Distributed by OpenTopography. (Accesssed 22 May 2022).

European Union Aviation Safety Authority (2022). Drones - National Aviation Authorities. https://www.easa.europa.eu/en/domains/civil-drones/naa.

Fairchild, L. H. & Cowan, D. S. (1982). Structure, petrology, and tectonic history of the Leech River complex northwest of Victoria, Vancouver Island. *Canadian Journal of Earth Sciences*, *19*(9), 1817–1835, https://doi.org/10.1139/e82-161.

Federal Aviation Administration (2023). Become a Drone Pilot. https://www.faa.gov/uas/commercial_operators/become_a_drone_pilot.

Fernandez-Diaz, J., Carter, W., Shrestha, R., & Glennie, C. (2014). Now You See It... Now You Don't: Understanding Airborne Mapping LiDAR Collection and Data Product Generation for Archaeological Research in Mesoamerica. *Remote Sensing*, *6*(10), 9951–10001, https://doi.org/10.3390/rs6109951.

Fialko, Y., Sandwell, D., Simons, M., & Rosen, P. (2005). Three-dimensional deformation caused by the Bam, Iran, earthquake and the origin of shallow slip deficit. *Nature*, *435*(7040), 295–299.

Finley, T., Nissen, E., Cassidy, J., Salomon, G., Leonard, L., & Froese, D. (2025a). Large surface-rupturing earthquakes and a >12 kyr, open interseismic interval on the Tintina fault, Yukon. *Geophysical Research Letters*. (under review).

Finley, T., et al. (2025b). Dextral strike-slip rupture of the Eastern Denali Fault, a mature terrane bounding fault in a compressive setting. *Tectonics*. (in prep).

Finley, T., Salomon, G., Stephen, R., Nissen, E., Cassidy, J., & Menounos, B. (2022a). Preliminary results and structural interpretations from drone LiDAR surveys over the Eastern Denali fault, Yukon. In *Yukon Exploration and Geology* (pp. 83–105). MacFarlane, KE, (ed.), Yukon Geological Survey.

Finley, T. D., Johnston, S. T., Unsworth, M. J., Banks, J., & Pana, D.-I. (2022b). Modern dextral strain controls active hydrothermal systems in the southeastern Canadian Cordillera. *GSA Bulletin*, https://doi.org/10.1130/B36500.1.

Fitzgerald, P. G., Roeske, S. M., Benowitz, J. A., Riccio, S. J., Perry, S. E., & Armstrong, P. A. (2014). Alternating asymmetric topography of the Alaska range along the strike-slip Denali fault: Strain partitioning and lithospheric control across a terrane suture zone. *Tectonics*, *33*(8), 1519–1533, https://doi.org/10.1002/2013TC003432.

Funning, G. J., Parsons, B., Wright, T. J., Jackson, J. A., & Fielding, E. J. (2005). Surface displacements and source parameters of the 2003 Bam (Iran) earthquake from Envisat advanced synthetic aperture radar imagery. *Journal of Geophysical Research: Solid Earth*, *110*(B9), https://doi.org/10.1029/2004JB003338.

Gabrielse, H., Monger, J., Wheeler, J., & Yorath, C. (1991). Morphogeological Belts, Tectonic Assemblages and Terranes, Chapter 2, Part A, of Geology of the Cordilleran Orogen in Canada, Geology of Canada, no. 4. *Geological Survey of Canada*, (pp. 15–28)., https://doi.org/10.4095/134073.

Gaudreau, E., Nissen, E., Bergman, E. A., Benz, H. M., Tan, F., & Karasözen, E. (2019). The August 2018 Kaktovik earthquakes: Active tectonics in northeastern Alaska revealed with InSAR and seismology. *Geophysical Research Letters*, *46*(24), 14412–14420, https://doi.org/10.1029/2019GL085651.

GDAL/OGR contributors (2023). *GDAL/OGR Geospatial Data Abstraction software Library*. Open Source Geospatial Foundation. doi: 10.5281/zenodo.5884351.

GEBCO Compilation Group (2023). GEBCO 2023 Grid. Distributed by OpenTopography (Accessed 4 July 2024) https://doi.org/10.5069/G9D21VTT.

Ghayournajarkar, N. & Fukushima, Y. (2022). Using InSAR for evaluating the accuracy of locations and focal mechanism solutions of local earthquake catalogues. *Geophysical Journal International*, *230*(1), 607–622, https://doi.org/10.1093/gji/ggac072.

Ghods, A., Rezapour, M., Bergman, E., Mortezanejad, G., & Talebian, M. (2012). Relocation of the 2006 Mw 6.1 Silakhour, Iran, Earthquake Sequence: Details of Fault Segmentation on the Main Recent Fault. *Bulletin of the Seismological Society of America*, *102*(1), 398–416, https://doi.org/10.1785/0120110009.

Glennie, C., Brooks, B., Ericksen, T., Hauser, D., Hudnut, K., Foster, J., & Avery, J. (2013). Compact Multipurpose Mobile Laser Scanning System — Initial Tests and Results. *Remote Sensing*, *5*(2), 521–538, https://doi.org/10.3390/rs5020521.

Glennie, C. L., Carter, W. E., Shrestha, R. L., & Dietrich, W. E. (2013). Geodetic imaging with airborne LiDAR: the Earth's surface revealed. *Reports on Progress in Physics*, *76*(8), 086801, 086801, https://doi.org/10.1088/0034-4885/76/8/086801.

Glennie, C. L., Hinojosa-Corona, A., Nissen, E., Kusari, A., Oskin, M. E., Arrowsmith, J. R., & Borsa, A. (2014). Optimization of legacy lidar data sets for measuring near-field earthquake displacements. *Geophysical Research Letters*, *41*(10), 3494–3501, https://doi.org/10.1002/2014GL059919.

Glushkova, O. (2011). Late Pleistocene Glaciations in North-East Asia. In *Quaternary Glaciations - Extent and Chronology*, volume 15 (pp. 865–875). Elsevier.

Gold, P. O., Oskin, M. E., Elliott, A. J., Hinojosa-Corona, A., Taylor, M. H., Kreylos, O., & Cowgill, E. (2013). Coseismic slip variation assessed from terrestrial lidar scans of the El Mayor-Cucapah surface rupture. *Earth and Planetary Science Letters*, *366*, 151–162, https://doi.org/10.1016/j.epsl.2013.01.040.

Gray, H. J., Shobe, C. M., Hobley, D. E., Tucker, G. E., Duvall, A. R., Harbert, S. A., & Owen, L. A. (2017). Off-fault deformation rate along the southern San Andreas fault at Mecca Hills, southern California, inferred from landscape modeling of curved drainages. *Geology*, *46*(1), 59–62, https://doi.org/10.1130/G39820.1.

Groome, W. G., Thorkelson, D. J., Friedman, R. M., Mortensen, J. K., Massey, N. W. D., Marshall, D. D., & Layer, P. W. (2003). Magmatic and tectonic history of the Leech River Complex, Vancouver Island, British Columbia: Evidence for ridge-trench intersection and accretion of the Crescent Terrane. In V. B. Sisson, S. M. Roeske, & T. L. Pavlis (Eds.), *Geology of a transpressional orogen developed during ridge-trench interaction along the North Pacific margin* (pp. 327–354). Geological Society of America.

Gu, Y., Xiao, Z., & Li, X. (2023). A Spatial Alignment Method for UAV LiDAR Strip Adjustment in Nonurban Scenes. *IEEE Transactions on Geoscience and Remote Sensing*, *61*, 1–13, https://doi.org/10.1109/TGRS.2023.3281692.

Guo, H., Lay, T., & Brodsky, E. E. (2023). Seismological Indicators of Geologically Inferred Fault Maturity. *Journal of Geophysical Research: Solid Earth*, *128*(10), https://doi.org/10.1029/2023JB027096.

Haddad, D. E., et al. (2012). Applications of airborne and terrestrial laser scanning to paleoseismology. *Geosphere*, *8*(4), 771–786, https://doi.org/10.1130/GES00701.1.

Haeussler, P. J., Matmon, A., Schwartz, D. P., & Seitz, G. G. (2017). Neotectonics of interior Alaska and the late Quaternary slip rate along the Denali fault system. *Geosphere*, *13*(5), 1445–1463, https://doi.org/10.1130/GES01447.1.

Hamling, I. J. (2020). A review of the 2016 Kaikōura earthquake: insights from the first 3 years. *Journal of the Royal Society of New Zealand*, *50*(2), 226–244, https://doi.org/10.1080/03036758.2019.1701048.

Harrichhausen, N., et al. (2023). Discovery of an Active Forearc Fault in an Urban Region: Holocene Rupture on the XEOLXELEK-Elk Lake Fault, Victoria, British Columbia, Canada. *Tectonics*, *42*(12), https://doi.org/10.1029/2023TC008170.

Harrichhausen, N., Morell, K. D., Regalla, C., Bennett, S. E., Leonard, L. J., Lynch, E. M., & Nissen, E. (2021). Paleoseismic trenching reveals Late Quaternary kinematics of the Leech River fault: Implications for forearc strain accumulation in northern Cascadia. *Bulletin of the Seismological Society of America*, *111*(2), 1110–1138, https://doi.org/10.1785/0120200204.

Harrichhausen, N., Morell, K. D., Regalla, C., Lynch, E. M., & Leonard, L. J. (2022). Eocene Terrane Accretion in Northern Cascadia Recorded by Brittle Left-Lateral Slip on the San Juan Fault. *Tectonics*, *41*(10), https://doi.org/10.1029/2022TC007317.

Harris Aerial (2023). Carrier h6 hybrid - heavy lift drones. (Accessed July 2023) https://harrisaerial.com/carrier-drones/carrier-h6-hybrid/.

Harwin, S. & Lucieer, A. (2012). Assessing the Accuracy of Georeferenced Point Clouds Produced via Multi-View Stereopsis from Unmanned Aerial Vehicle (UAV) Imagery. *Remote Sensing*, *4*(6), 1573–1599, https://doi.org/10.3390/rs4061573.

Hasterok, D., Halpin, J. A., Collins, A. S., Hand, M., Kreemer, C., Gard, M. G., & Glorie, S. (2022). New Maps of Global Geological Provinces and Tectonic Plates. *Earth-Science Reviews*, *231*, https://doi.org/10.1016/j.earscirev.2022.104069.

Hata, Y., Goto, H., & Yoshimi, M. (2016). Preliminary analysis of strong ground motions in the heavily damaged zone in Mashiki town, Kumamoto, Japan, during the mainshock of the 2016 Kumamoto earthquake (Mw 7.0) observed by a dense seismic array. *Seismological Research Letters*, *87*(5), 1044–1049, https://doi.org/10.1785/0220160107.

Haugerud, R. A., Harding, D. J., Johnson, S. Y., Harless, J. L., Weaver, C. S., & Sherrod, B. L. (2003). High-resolution lidar topography of the Puget Lowland, Washington. *GSA Today*, *13*(6), 4–10, https://doi.org/10.1130/1052-5173(2003)13<0004:HLTOTP>2.0.CO;2.

Hilley, G. E., DeLong, S., Prentice, C., Blisniuk, K., & Arrowsmith, J. (2010). Morphologic dating of fault scarps using airborne laser swath mapping (ALSM) data. *Geophysical Research Letters*, *37*(4), L04301, https://doi.org/10.1029/2009GL042044.

Hodge, M., Biggs, J., Fagereng, Å., Elliott, A., Mdala, H., & Mphepo, F. (2019). A semi-automated algorithm to quantify scarp morphology (SPARTA): application to normal faults in southern Malawi. *Solid Earth*, *10*(1), 27–57, https://doi.org/10.5194/se-10-27-2019.

Hodgson, M. E. & Bresnahan, P. (2004). Accuracy of airborne lidar-derived elevation. *Photogrammetric Engineering & Remote Sensing*, *70*(3), 331–339, https://doi.org/10.14358/pers.70.3.331.

Horner, R. B., Wetmiller, R. J., Lamontagne, M., & Plouffe, M. (1990). A fault model for the nahanni earthquakes from aftershock studies. *Bulletin of the Seismological Society of America*, *80*(6A), 1553–1570.

Hreinsdóttir, S., Freymueller, J. T., Bürgmann, R., & Mitchell, J. (2006). Coseismic deformation of the 2002 Denali Fault earthquake: Insights from GPS measurements. *Journal of Geophysical Research (Solid Earth)*, *111*(B3), B03308, https://doi.org/10.1029/2005JB003676.

Hubbard, T. D., Koehler, R. D., & Combellick, R. A. (2011). High-resolution lidar data for Alaska infrastructure corridors. *Alaska Division of Geological and Geophysical Surveys: Fairbanks, AK, USA*, *3*, 291.

Hunter, L. E., Howle, J. F., Rose, R. S., & Bawden, G. W. (2011). LiDAR-Assisted Identification of an Active Fault near Truckee, California. *Bulletin of the Seismological Society of America*, *101*(3), 1162–1181, https://doi.org/10.1785/0120090261.

Hyndman, R. D. (2023). The Thermal Regime of NW Canada and Alaska, and Tectonic and Seismicity Consequences. *Geochemistry, Geophysics, Geosystems*, *24*(7), e2022GC010570, https://doi.org/10.1029/2022GC010570.

Imaeva, L. P., Gusev, G. S., Imaev, V. S., Ashurkov, S. V., Melnikova, V. I., & Seredkina, A. I. (2017). Geodynamic activity of modern structures and tectonic stress fields in northeast asia. *Geodynamics & Tectonophysics*, *8*(4), 737–768, https://doi.org/10.5800/GT-2017-8-4-0315.

Improta, L., et al. (2010). Detecting young, slow-slipping active faults by geologic and multidisciplinary high-resolution geophysical investigations: A case study from the Apennine seismic belt, Italy. *Journal of Geophysical Research: Solid Earth*, *115*(B11), https://doi.org/10.1029/2010JB000871.

International Seismological Centre (2024). On-line Bulletin. Place: Thatcham, United Kingdom http://www.isc.ac.uk.

Isenburg, M. (2021). LAStools-efficient LiDAR processing software (version 210418), obtained from https://lastools.github.io/.

Ishimura, D., Toda, S., Mukoyama, S., Homma, S., Yamaguchi, K., & Takahashi, N. (2019). 3D Surface Displacement and Surface Ruptures Associated with the 2014 Mw 6.2 Nagano Earthquake Using Differential Lidar. *Bulletin of the Seismological Society of America*, *109*(2), 780–796, https://doi.org/10.1785/0120180020.

Jackson, L. E., Ward, B. C., Hicock, S. R., Gromig, R., Clague, J. J., & Turner, D. G. (2024). New insights into the glacial and relative sea-level history of the western Fraser Lowland based on sediment cores from geotechnical drilling for the Evergreen Tunnel, British Columbia, Canada. *Quaternary Research*, *122*, 40–61, https://doi.org/10.1017/qua.2024.9.

James, M. R. & Robson, S. (2012). Straightforward reconstruction of 3D surfaces and topography with a camera: Accuracy and geoscience application. *Journal of Geophysical Research: Earth Surface*, *117*(F3), https://doi.org/10.1029/2011JF002289.

Johnson, K., et al. (2014). Rapid mapping of ultrafine fault zone topography with structure from motion. *Geosphere*, *10*(5), 969–986, https://doi.org/10.1130/GES01017.1.

Johnson, K. L., Nissen, E., & Lajoie, L. (2018). Surface Rupture Morphology and Vertical Slip Distribution of the 1959 M_w 7.2 Hebgen Lake (Montana) Earthquake From Airborne Lidar Topography. *Journal of Geophysical Research (Solid Earth)*, *123*(9), 8229–8248, https://doi.org/10.1029/2017JB015039.

Johnson, S. Y. (1984). Evidence for a margin-truncating transcurrent fault (pre-late Eocene) in western Washington. *Geology*, *12*(9), 538–541, https://doi.org/10.1130/0091-7613(1984)12<538:EFAMTF>2.0.CO;2.

Johnson, S. Y., et al. (2004). Evidence for Late Holocene Earthquakes on the Utsalady Point Fault, Northern Puget Lowland, Washington. *Bulletin of the Seismological Society of America*, *94*(6), 2299–2316, https://doi.org/10.1785/0120040050.

Johnson, S. Y., Potter, C. J., Miller, J. J., Armentrout, J. M., Finn, C., & Weaver, C. S. (1996). The southern Whidbey Island fault: An active structure in the Puget Lowland, Washington. *GSA Bulletin*, *108*(3), 334–354, https://doi.org/10.1130/0016-7606(1996)108<0334:TSWIFA>2.3.CO;2.

Jones, R. R., Kokkalas, S., & McCaffrey, K. J. W. (2009). Quantitative analysis and visualization of nonplanar fault surfaces using terrestrial laser scanning (LIDAR)–The Arkitsa fault, central Greece, as a case study. *Geosphere*, *5*(6), 465–482, https://doi.org/10.1130/GES00216.1.

Jónsson, S., Zebker, H., Segall, P., & Amelung, F. (2002). Fault slip distribution of the 1999 M w 7.1 Hector Mine, California, earthquake, estimated from satellite radar and GPS measurements. *Bulletin of the Seismological Society of America*, *92*(4), 1377–1389, https://doi.org/10.1785/0120000922.

Jordan, T. H. & Sverdrup, K. A. (1981). Teleseismic location techniques and their application to earthquake clusters in the south-central Pacific. *Bulletin of the Seismological Society of America*, *71*(4), 1105–1130, https://doi.org/10.1785/BSSA0710041105.

Kanamori, H. & Anderson, D. L. (1975). Theoretical basis of some empirical relations in seismology. *Bulletin of the Seismological Society of America*, *65*, 1073–1095, https://doi.org/10.1785/BSSA0650051073.

Karasözen, E., Nissen, E., Bergman, E. A., Johnson, K. L., & Walters, R. J. (2016). Normal faulting in the Simav graben of western Turkey reassessed with calibrated earthquake relocations. *Journal of Geophysical Research (Solid Earth)*, *121*(6), 4553–4574, https://doi.org/10.1002/2016JB012828.

Kellner, J. R., et al. (2019). New Opportunities for Forest Remote Sensing Through Ultra-High-Density Drone Lidar. *Surveys in Geophysics*, *40*(4), 959–977, https://doi.org/10.1007/s10712-019-09529-9.

Kelsey, H. M., Sherrod, B. L., Blakely, R. J., & Haugerud, R. A. (2012). Holocene faulting in the Bellingham forearc basin: Upper-plate deformation at the northern end of the Cascadia

subduction zone. *Journal of Geophysical Research: Solid Earth*, *117*(B3), https://doi.org/10.1029/2011JB008816.

Kennett, B. & Engdahl, E. (1991). Traveltimes for global earthquake location and phase identification. *Geophysical Journal International*, *105*(2), 429–465, https://doi.org/10.1111/j.1365-246X.1991.tb06724.x.

Kennett, B. L. N., Engdahl, E. R., & Buland, R. (1995). Constraints on seismic velocities in the Earth from traveltimes. *Geophysical Journal International*, *122*(1), 108–124, https://doi.org/10.1111/j.1365-246X.1995.tb03540.x.

Kiser, E. & Ishii, M. (2017). Back-Projection Imaging of Earthquakes. *Annual Review of Earth and Planetary Sciences*, *45*(Volume 45, 2017), 271–299, https://doi.org/10.1146/annurev-earth-063016-015801.

Kolaj, M., Adams, J., & Halchuk, S. (2020). The 6th generation seismic hazard model of canada. *Geological Survey of Canada, Open File 8630*, (pp. 1–12)., https://doi.org/https://doi.org/10.4095/327322.

Lague, D., Brodu, N., & Leroux, J. (2013). Accurate 3D comparison of complex topography with terrestrial laser scanner: Application to the Rangitikei canyon (N-Z). *ISPRS Journal of Photogrammetry and Remote Sensing*, *82*, 10–26, https://doi.org/10.1016/j.isprsjprs.2013.04.009.

Lajoie, L. J., Nissen, E., Johnson, K. L., Arrowsmith, J. R., Glennie, C. L., Hinojosa-Corona, A., & Oskin, M. E. (2019). Extent of Low-Angle Normal Slip in the 2010 El Mayor-Cucapah (Mexico) Earthquake From Differential Lidar. *Journal of Geophysical Research (Solid Earth)*, *124*(1), 943–956, https://doi.org/10.1029/2018JB016828.

Lander, A. V., Bukchin, B. G., Kiryushin, A. V., & Droznin, D. V. (1996). The Tectonic Environment and Source Parameters of the Khailino, Koryakiya Earthquake of March 8, 1991. In *Selected Papers from Volumes 26 and 27 of Vychislitel'naya Seysmologiya*, Computational Seismology and Geodynamics (pp. 80–96). Wiley Online Library.

Lander, A. V., Levina, V. I., & Ivanova, E. I. (2010). The earthquake history of the Koryak Upland and the aftershock process of the MW7.6 April 20(21), 2006 Olyutorskii earthquake. *Journal of Volcanology and Seismology*, *4*(2), 87–100, https://doi.org/10.1134/S074204631002003X.

Langridge, R. M., Ries, W. F., Farrier, T., Barth, N. C., Khajavi, N., & De Pascale, G. P. (2014). Developing sub 5-m LiDAR DEMs for forested sections of the Alpine and Hope faults, South Island, New Zealand: Implications for structural interpretations. *Journal of Structural Geology*, *64*, 53–66, https://doi.org/10.1016/j.jsg.2013.11.007.

Leandro, R. F., Santos, M. C., & Langley, R. B. (2011). Analyzing GNSS data in precise point positioning software. *GPS Solutions*, *15*(1), 1–13, https://doi.org/10.1007/s10291-010-0173-9.

Lee, H. & Liu, J. G. (2001). Analysis of topographic decorrelation in SAR interferometry using ratio coherence imagery. *IEEE Transactions on Geoscience and Remote Sensing*, *39*(2), 223–232, https://doi.org/10.1109/36.905230.

Li, G., Liu, Y., Regalla, C., & Morell, K. D. (2018). Seismicity relocation and fault structure near the Leech River fault zone, southern Vancouver Island. *Journal of Geophysical Research: Solid Earth*, *123*(4), 2841–2855, https://doi.org/10.1002/2017JB015021.

Liang, Y., et al. (2019). A review of rechargeable batteries for portable electronic devices. *InfoMat*, *1*(1), 6–32, https://doi.org/10.1002/inf2.12000.

LidarBC (2023). Open LiDAR Data Portal. https://lidar.gov.bc.ca/.

Lin, Z., Kaneda, H., Mukoyama, S., Asada, N., & Chiba, T. (2013). Detection of subtle tectonic–geomorphic features in densely forested mountains by very high-resolution airborne LiDAR survey. *Geomorphology*, *182*, 104–115, https://doi.org/10.1016/j.geomorph.2012.11.001.

Lynch, E. M., Regalla, C. A., Morell, K. D., Harrichhausen, N., & Leonard, L. J. (2023). Late Pleistocene to Holocene transtension in the northern Cascadia forearc: Evidence from surface ruptures along the Beaufort Range fault. *Authorea Preprints*, https://doi.org/10.22541/essoar.168614686.67638260/v1.

Maggi, A., Jackson, J. A., McKenzie, D., & Priestley, K. (2000a). Earthquake focal depths, effective elastic thickness, and the strength of the continental lithosphere. *Geology*, *28*(6), 495, https://doi.org/10.1130/0091-7613(2000)28<495:EFDEET>2.0.CO;2.

Maggi, A., Jackson, J. A., Priestley, K., & Baker, C. (2000b). A re-assessment of focal depth distributions in southern Iran, the Tien Shan and northern India: do earthquakes really occur in the continental mantle? *Geophysical Journal International*, *143*(3), 629–661, https://doi.org/10.1046/j.1365-246X.2000.00254.x.

Marechal, A., Ritz, J.-F., Ferry, M., Mazzotti, S., Blard, P.-H., Braucher, R., & Saint-Carlier, D. (2018). Active tectonics around the Yakutat indentor: New geomorphological constraints on the eastern Denali, Totschunda and Duke River Faults. *Earth and Planetary Science Letters*, *482*, 71–80, https://doi.org/10.1016/j.epsl.2017.10.051.

Massonnet, D., Rossi, M., Carmona, C., Adragna, F., Peltzer, G., Feigl, K., & Rabaute, T. (1993). The displacement field of the Landers earthquake mapped by radar interferometry. *Nature*, *364*(6433), 138–142, https://doi.org/10.1038/364138a0.

Matthews, J. A. & Winkler, S. (2022). Schmidt-hammer exposure-age dating: a review of principles and practice. *Earth-Science Reviews*, *230*, https://doi.org/10.1016/j.earscirev.2022.104038.

McCaffrey, R. & Abers, G. (1988). *SYN3: A Program for Inversion of Teleseismic Body Waveform on Microcomputers, Air Force Geophysics Laboratory Technical Report*. Technical report, AFGL-TR-88-0099.

McCaffrey, R., Abers, G., Zwick, P., & Lee, W. (1991). Inversion of teleseismic body waves. *IASPEI Software library*, *3*, 81–166.

McCaffrey, R., King, R. W., Payne, S. J., & Lancaster, M. (2013). Active tectonics of northwestern U.S. inferred from GPS-derived surface velocities. *Journal of Geophysical Research: Solid Earth*, *118*(2), 709–723, https://doi.org/10.1029/2012JB009473.

Meigs, A. (2013). Active tectonics and the LiDAR revolution. *Lithosphere*, *5*(2), 226–229, https://doi.org/10.1130/RF.L004.1.

Meng, L., Ampuero, J.-P., Luo, Y., Wu, W., & Ni, S. (2012). Mitigating artifacts in back-projection source imaging with implications for frequency-dependent properties of the Tohoku-Oki earthquake. *Earth, planets and space*, *64*(12), 1101–1109.

Metcalf, A., Welles, T., Murakami, Y., Nakamura, H., & Ahn, J. (2022). Unmanned Aerial Vehicle Solid Oxide Fuel Cell and Internal Combustion Engine Hybrid Powertrain: An Experimental and Simulation Centered Review. *American Society of Mechanical Engineers Digital Collection*, https://doi.org/10.1115/POWER2022-86357.

Mikhailov, V. O., Timoshkina, E. P., Diament, M., & Smirnov, V. B. (2023). Enigma of the Olyutorskii Earthquake Resolved by SAR Interferometry. *Pure and Applied Geophysics*, *180*(10), 3423–3433, https://doi.org/10.1007/s00024-023-03351-6.

Miller, E. L., Gelman, M., Parfenov, L., & Hourigan, J. (2002). Tectonic setting of Mesozoic magmatism: A comparison between northeastern Russia and the North American Cordillera. In E. L. Miller, A. Grantz, & S. L. Klemperer (Eds.), *Tectonic Evolution of the Bering Shelf-Chukchi Sea-Artic Margin and Adjacent Landmasses*, volume 360. Geological Society of America.

Mojica, A., Pérez, T., Toral, J., Miranda, R., Franceschi, P., Calderón, C., & Vergara, F. (2017). Shallow electrical resistivity imaging of the Limón fault, Chagres River Watershed, Panama Canal. *Journal of Applied Geophysics*, *138*, 135–142, https://doi.org/10.1016/j.jappgeo.2017.01.010.

Molnar, P. & Lyon-Caen, H. (1989). Fault plane solutions of earthquakes and active tectonics of the Tibetan Plateau and its margins. *Geophysical Journal International*, *99*(1), 123–153.

Monger, J. & Price, R. (2002). The Canadian Cordillera: Geology and Tectonic Evolution. *CSEG Recorder*, (pp. 17–36).

Monger, J. W. H. (1977). Upper Paleozoic rocks of the western Canadian Cordillera and their bearing on Cordilleran evolution. *Canadian Journal of Earth Sciences*, *14*(8), 1832–1859, https://doi.org/10.1139/e77-156.

Morell, K., et al. (2018). Holocene surface rupture history of an active forearc fault redefines seismic hazard in southwestern British Columbia, Canada. *Geophysical Research Letters*, *45*(21), 11–605.

Morell, K. D., Regalla, C., Leonard, L. J., Amos, C., & Levson, V. (2017). Quaternary rupture of a crustal fault beneath Victoria, British Columbia, Canada. *GSA Today*, *7*(3), https://doi.org/10.1130/GSATG291A.1.

Morin, P., et al. (2016). ArcticDEM; A Publically Available, High Resolution Elevation Model of the Arctic. In *EGU General Assembly Conference Abstracts*.

Muir, R. A., et al. (2023). Exceptional Scarp Preservation in SW Namibia Reveals Geological Controls on Large Magnitude Intraplate Seismicity in Southern Africa. *Tectonics*, *42*(4), https://doi.org/10.1029/2022TC007693.

Muller, J. E. (1977). Evolution of the Pacific Margin, Vancouver Island, and adjacent regions. *Canadian Journal of Earth Sciences*, *14*(9), 2062–2085, https://doi.org/10.1139/e77-176.

Nash, D. B. (1980). Morphologic Dating of Degraded Normal Fault Scarps. *Journal of Geology*, *88*(3), 353–360, https://doi.org/10.1086/628513.

Natural Resources Canada (1985). Canadian National Earthquake Database.

Nelson, A. R., Personius, S. F., Wells, R. E., Schermer, E. R., Bradley, L., Buck, J., & Reitman, N. (2017). Holocene Earthquakes of Magnitude 7 during Westward Escape of the Olympic Mountains, Washington. *Bulletin of the Seismological Society of America*, *107*(5), 2394–2415, https://doi.org/10.1785/0120160323.

Nelson, J., Colpron, M., & Goodfellow, W. (2007). Tectonics and metallogeny of the British Columbia, Yukon and Alaskan Cordillera, 1.8 Ga to the present. *Mineral deposits of Canada: a synthesis of major deposit-types, district metallogeny, the evolution of geological provinces, and exploration methods: Geological Association of Canada, Mineral Deposits Division, Special Publication*, *5*, 755–791.

Nevitt, J. M., Brooks, B. A., Catchings, R. D., Goldman, M. R., Ericksen, T. L., & Glennie, C. L. (2020). Mechanics of near-field deformation during co- and post-seismic shallow fault slip. *Scientific Reports*, *10*, 5031, https://doi.org/10.1038/s41598-020-61400-9.

Nissen, E., Jackson, J., Jahani, S., & Tatar, M. (2014a). Zagros "phantom earthquakes" reassessed—The interplay of seismicity and deep salt flow in the Simply Folded Belt? *Journal of Geophysical Research (Solid Earth)*, *119*(4), 3561–3583, https://doi.org/10.1002/2013JB010796.

Nissen, E., Maruyama, T., Ramon Arrowsmith, J., Elliott, J. R., Krishnan, A. K., Oskin, M. E., & Saripalli, S. (2014b). Coseismic fault zone deformation revealed with differential lidar: Examples from Japanese M_w ∼7 intraplate earthquakes. *Earth and Planetary Science Letters*, *405*, 244–256, https://doi.org/10.1016/j.epsl.2014.08.031.

Okada, Y. (1985). Surface deformation due to shear and tensile faults in a half-space. *Bulletin of the seismological society of America*, *75*(4), 1135–1154.

OpenStreetMap contributers (2025). OpenStreetMap. Available as open data under the Open Data Commons Open Database License (ODbL) http://openstreetmap.org/.

Oskin, M. E., et al. (2012). Near-Field Deformation from the El Mayor-Cucapah Earthquake Revealed by Differential LIDAR. *Science*, *335*(6069), https://doi.org/10.1126/science.1213778.

Palacky, G. (1988). Resistivity Characteristics of Geologic Targets. In *Electromagnetic Methods in Applied Geophysics: Voume 1, Theory* (pp. 52–129). Society of Exploration Geophysicists.

Patton, H., et al. (2022). The extreme yet transient nature of glacial erosion. *Nature Communications*, *13*(1), https://doi.org/10.1038/s41467-022-35072-0.

Pellicani, R., Argentiero, I., Manzari, P., Spilotro, G., Marzo, C., Ermini, R., & Apollonio, C. (2019). UAV and Airborne LiDAR Data for Interpreting Kinematic Evolution of Landslide Movements: The Case Study of the Montescaglioso Landslide (Southern Italy). *Geosciences*, *9*(6), https://doi.org/10.3390/geosciences9060248.

Perrin, C., Manighetti, I., Ampuero, J.-P., Cappa, F., & Gaudemer, Y. (2016). Location of largest earthquake slip and fast rupture controlled by along-strike change in fault structural maturity due to fault growth. *Journal of Geophysical Research: Solid Earth*, *121*(5), 3666–3685, https://doi.org/10.1002/2015JB012671.

Perrin, C., Waldhauser, F., & Scholz, C. H. (2021). The Shear Deformation Zone and the Smoothing of Faults With Displacement. *Journal of Geophysical Research (Solid Earth)*, *126*(5), e2020JB020447, https://doi.org/10.1029/2020JB02044710.1002/essoar.10503483.1.

Personius, S. F., et al. (2014). Holocene earthquakes and right-lateral slip on the left-lateral Darrington–Devils Mountain fault zone, northern Puget Sound, Washington. *Geosphere*, *10*(6), 1482–1500, https://doi.org/10.1130/GES01067.1.

Pingel, T. J., Clarke, K. C., & McBride, W. A. (2013). An improved simple morphological filter for the terrain classification of airborne LIDAR data. *ISPRS Journal of Photogrammetry and Remote Sensing*, *77*, 21–30, https://doi.org/10.1016/j.isprsjprs.2012.12.002.

Piriz, R., Mozo, A., Navarro, P., & Rodriguez, D. (2008). MagicGNSS: Precise GNSS products out of the box. In *Proceedings of the 21st International Technical Meeting of the Satellite Division of The Institute of Navigation (ION GNSS 2008)* (pp. 1242–1251).

Portenga, E. W. & Bierman, P. R. (2011). Understanding Earth's eroding surface with 10Be. *GSA Today*, *21*(8), 4–10, https://doi.org/10.1130/G111A.1.

Porter, C., et al. (2022). ArcticDEM - Strips, Version 4.1. Section: 2022-09-29 15:45:45.761.

Prentice, C. S., Crosby, C. J., Whitehill, C. S., Arrowsmith, J. R., Furlong, K. P., & Phillips, D. A. (2009). Illuminating Northern California's Active Faults. *EOS Transactions*, *90*(7), 55, https://doi.org/10.1029/2009EO070002.

Press, W. H., William, H., Teukolsky, S. A., Saul, A., Vetterling, W. T., & Flannery, B. P. (2007). *Numerical recipes 3rd edition: The art of scientific computing*. Cambridge University Press.

Purba, J. C. S., Gilbert, H., & Dettmer, J. (2021). Structure and Dynamics of the Southern Rocky Mountain Trench near Valemount, British Columbia, Inferred from Local Seismicity. *Seismological Research Letters*, *92*(5), 3087–3099, https://doi.org/10.1785/0220200350.

QGIS Association (2018). QGIS Geographic Information System. https://www.qgis.org/.

Rajashekara, K. (2013). Present Status and Future Trends in Electric Vehicle Propulsion Technologies. *IEEE Journal of Emerging and Selected Topics in Power Electronics*, *1*(1), 3–10, https://doi.org/10.1109/JESTPE.2013.2259614.

Ratchkovski, N. A., S., W., & A., H. R. (2004). Seismotectonics of the Central Denali Fault, Alaska, and the 2002 Denali Fault Earthquake Sequence. *Bulletin of the Seismological Society of America*, *94*(6B), S156–S174, https://doi.org/10.1785/0120040621.

Reitman, N. G., Klinger, Y., Briggs, R. W., & Gold, R. D. (2022). Climatic influence on the expression of strike-slip faulting. *Geology*, *51*(1), 18–22, https://doi.org/10.1130/G50393.1.

Reitman, N. G., Mueller, K. J., Tucker, G. E., Gold, R. D., Briggs, R. W., & Barnhart, K. R. (2019). Offset Channels May Not Accurately Record Strike-Slip Fault Displacement: Evidence From Landscape Evolution Models. *Journal of Geophysical Research: Solid Earth*, *124*(12), 13427–13451, https://doi.org/10.1029/2019JB018596.

Resop, J. P., Lehmann, L., & Hession, W. C. (2019). Drone laser scanning for modeling riverscape topography and vegetation: Comparison with traditional aerial lidar. *Drones*, *3*(2), 35, https://doi.org/10.3390/drones3020035.

Risbøl, O. & Gustavsen, L. (2018). LiDAR from drones employed for mapping archaeology–Potential, benefits and challenges. *Archaeological Prospection*, *25*(4), 329–338, https://doi.org/10.1002/arp.1712.

Ristau, J., Rogers, G. C., & Cassidy, J. F. (2007). Stress in western Canada from regional moment tensor analysis. *Canadian Journal of Earth Sciences*, *44*(2), 127–148, https://doi.org/10.1139/e06-057.

Rogers, G. C. & Hasegawa, H. S. (1978). A second look at the British Columbia earthquake of June 23, 1946. *Bulletin of the Seismological Society of America*, *68*(3), 653–676, https://doi.org/10.1785/BSSA0680030653.

Rogozhin, E. A., Gordeev, E. I., & Chebrov, V. N. (2007). The Koryak strong earthquake of April 20 (21), 2006: Preliminary results. *Izvestiya, Physics of the Solid Earth*, *43*(2), 103–110, https://doi.org/10.1134/S1069351307020012.

Rogozhin, E. A., Ovsyuchenko, A. N., Lutikov, A. I., Ruzaykin, A. I., Dontsova, G. Y., & Sysolin, A. I. (2021). The Koryak Earthquake: an Example of a Successfully Predicted Seismic Event. *Seismic Instruments*, *57*(1), 88–96, https://doi.org/10.3103/S0747923921010072.

Rosen, P., Hensley, S., Joughin, I., Li, F., Madsen, S., Rodriguez, E., & Goldstein, R. (2000). Synthetic aperture radar interferometry. *Proceedings of the IEEE*, *88*(3), 333–382, https://doi.org/10.1109/5.838084.

Rusmore, M. E. & Cowan, D. S. (1985). Jurassic–Cretaceous rock units along the southern edge of the Wrangellia terrane on Vancouver Island. *Canadian Journal of Earth Sciences*, *22*(8), 1223–1232, https://doi.org/10.1139/e85-124.

Salisbury, J. B., Rockwell, T. K., Middleton, T. J., & Hudnut, K. W. (2012). LiDAR and Field Observations of Slip Distribution for the Most Recent Surface Ruptures along the Central San Jacinto Fault. *Bulletin of the Seismological Society of America*, *102*(2), 598–619, https://doi.org/10.1785/0120110068.

Salomon, G. (2024). Supplemental material for Mapping fault geomorphology with drone-based lidar. https://doi.org/10.5281/zenodo.11081289.

Salomon, G., Finley, T., Nissen, E., Stephen, R., & Menounos, B. (2024). Mapping fault geomorphology with drone-based lidar. *Seismica*, *3*(1), https://doi.org/10.26443/seismica.v3i1.1186.

Salomon, G. W., et al. (2022). Geomorphological and geophysical analyses of the Hebron Fault, SW Namibia: implications for stable continental region seismic hazard. *Geophysical Journal International*, *229*(1), 235–254, https://doi.org/10.1093/gji/ggab466.

Satake, K., Shimazaki, K., Tsuji, Y., & Ueda, K. (1996). Time and size of a giant earthquake in Cascadia inferred from Japanese tsunami records of January 1700. *Nature*, *379*(6562), 246–249, https://doi.org/10.1038/379246a0.

Savage, W. Z. & Varnes, D. J. (1987). Mechanics of gravitational spreading of steep-sided ridges («sackung»). *Bulletin of the International Association of Engineering Geology - Bulletin de l'Association Internationale de Géologie de l'Ingénieur*, *35*(1), 31–36, https://doi.org/10.1007/BF02590474.

Sawicki, O. & Smith, D. G. (1992). Glacial Lake Invermere, upper Columbia River valley, British Columbia: a paleogeographic reconstruction. *Canadian Journal of Earth Sciences*, *29*(4), 687–692, https://doi.org/10.1139/e92-059.

Schermer, E. R., Amos, C. B., Duckworth, W. C., Nelson, A. R., Angster, S., Delano, J., & Sherrod, B. L. (2021). Postglacial Mw 7.0-7.5 Earthquakes on the North Olympic Fault Zone, Washington. *Bulletin of the Seismological Society of America*, *111*(1), 490–513, https://doi.org/10.1785/0120200176.

Schimmel, M. & Paulssen, H. (1997). Noise reduction and detection of weak, coherent signals through phase-weighted stacks. *Geophysical Journal International*, *130*(2), 497–505, https://doi.org/10.1111/j.1365-246X.1997.tb05664.x.

Scott, C., Phan, M., Nandigam, V., Crosby, C., & Arrowsmith, J. R. (2021). Measuring change at Earth's surface: On-demand vertical and three-dimensional topographic differencing implemented in OpenTopography. *Geosphere*, *17*(4), 1318–1332, https://doi.org/10.1130/GES02259.1.

Scott, C. P., Arrowsmith, J. R., Nissen, E., Lajoie, L., Maruyama, T., & Chiba, T. (2018). The M7 2016 Kumamoto, Japan, Earthquake: 3-D Deformation Along the Fault and Within the Damage Zone Constrained From Differential Lidar Topography. *Journal of Geophysical Research (Solid Earth)*, *123*(7), 6138–6155, https://doi.org/10.1029/2018JB015581.

Scott, C. P., Beckley, M., Phan, M., Zawacki, E., Crosby, C., Nandigam, V., & Arrowsmith, R. (2022). Statewide USGS 3DEP Lidar Topographic Differencing Applied to Indiana, USA. *Remote Sensing*, *14*(4), 847, https://doi.org/10.3390/rs14040847.

Scott, C. P., DeLong, S. B., & Arrowsmith, J. R. (2020). Distribution of Aseismic Deformation Along the Central San Andreas and Calaveras Faults From Differencing Repeat Airborne Lidar. *Geophysical Research Letters*, *47*(22), e90628, https://doi.org/10.1029/2020GL090628.

Sethanant, I., Nissen, E., Pousse-Beltran, L., Bergman, E., & Pierce, I. (2023). The 2020 Mw 6.5 Monte Cristo Range, Nevada, Earthquake: Anatomy of a Crossing-Fault Rupture through a Region of Highly Distributed Deformation. *Bulletin of the Seismological Society of America*, *113*(3), 948–975, https://doi.org/10.1785/0120220166.

Seyler, C. E., Kirkpatrick, J. D., Faber, C., Licht, A., Šilerová, D., & Regalla, C. (2022). Structural and Metamorphic History of the Leech River Shear Zone, Vancouver Island, British Columbia. *Tectonics*, *41*(11), https://doi.org/10.1029/2021TC007132.

Shephard, G. E., Müller, R. D., & Seton, M. (2013). The tectonic evolution of the Arctic since Pangea breakup: Integrating constraints from surface geology and geophysics with mantle structure. *Earth-Science Reviews*, *124*, 148–183, https://doi.org/10.1016/j.earscirev.2013.05.012.

Sherrod, B. L., et al. (2004). Holocene fault scarps near Tacoma, Washington, USA. *Geology*, *32*(1), 9–12, https://doi.org/10.1130/G19914.1.

Simons, M., Fialko, Y., & Rivera, L. (2002). Coseismic deformation from the 1999 M w 7.1 Hector Mine, California, earthquake as inferred from InSAR and GPS observations. *Bulletin of the Seismological Society of America*, *92*(4), 1390–1402.

Skyfront (2023). Perimeter 8 uas. https://skyfront.com/perimeter-8.

Slawson, W. F. & Savage, J. C. (1979). Geodetic deformation associated with the 1946 Vancouver Island, Canada, earthquake. *Bulletin of the Seismological Society of America*, *69*(5), 1487–1496, https://doi.org/10.1785/BSSA0690051487.

Stahl, T. & Tye, A. (2020). Schmidt hammer and terrestrial laser scanning (TLS) used to detect single-event displacements on the Pleasant Valley fault (Nevada, USA). *Earth Surface Processes and Landforms*, *45*(2), 473–483, https://doi.org/10.1002/esp.4748.

Stöcker, C., Bennett, R., Nex, F., Gerke, M., & Zevenbergen, J. (2017). Review of the Current State of UAV Regulations. *Remote Sensing*, *9*(5), https://doi.org/10.3390/rs9050459.

Svigkas, N., Atzori, S., Kozhurin, A., Tolomei, C., Antonioli, A., & Pezzo, G. (2023). Implications for the geometry of plate boundaries in NE Asia based on the geodetic analysis of the 2020 Mw 6.4 Koryak event. *Geophysical Journal International*, *234*(2), 1412–1421, https://doi.org/10.1093/gji/ggad142.

Tan, F., Ge, Z., Kao, H., & Nissen, E. (2019). Validation of the 3-D phase-weighted relative back projection technique and its application to the 2016 Mw 7.8 Kaikōura earthquake. *Geophysical Journal International*, *217*(1), 375–388, https://doi.org/10.1093/gji/ggz032.

Telling, J., Lyda, A., Hartzell, P., & Glennie, C. (2017). Review of Earth science research using terrestrial laser scanning. *Earth Science Reviews*, *169*, 35–68, https://doi.org/10.1016/j.earscirev.2017.04.007.

Tomsett, C. & Leyland, J. (2021). Development and Testing of a UAV Laser Scanner and Multispectral Camera System for Eco-Geomorphic Applications. *Sensors*, *21*(22), 7719, https://doi.org/10.3390/s21227719.

Toth, C., Brzezinska, D., Csanyi, N., Paska, E., & Yastikli, N. (2007). Lidar mapping supporting earthquake research of the san andreas fault. In *Proceedings of the ASPRS 2007 Annual Conference* (pp. 1–11).: American Society for Photogrammetry and Remote Sensing (ASPRS) Tampa, FL.

Townsend, A., Jiya, I. N., Martinson, C., Bessarabov, D., & Gouws, R. (2020). A comprehensive review of energy sources for unmanned aerial vehicles, their shortfalls and opportunities for improvements. *Heliyon*, *6*(11), e05285, https://doi.org/10.1016/j.heliyon.2020.e05285.

Tozer, B., Sandwell, D. T., Smith, W. H. F., Olson, C., Beale, J. R., & Wessel, P. (2019). Global Bathymetry and Topography at 15 Arc Sec: SRTM15+. *Earth and Space Science*, *6*(10), 1847–1864, https://doi.org/10.1029/2019EA000658.

Tralli, D. M., Blom, R. G., Zlotnicki, V., Donnellan, A., & Evans, D. L. (2005). Satellite remote sensing of earthquake, volcano, flood, landslide and coastal inundation hazards. *ISPRS Journal of Photogrammetry and Remote Sensing*, *59*(4), 185–198, https://doi.org/10.1016/j.isprsjprs.2005.02.002.

Transport Canada (2022). Getting a drone pilot certificate. https://tc.canada.ca/en/aviation/drone-safety/drone-pilot-licensing/getting-drone-pilot-certificate.

Transport Canada (2023). Minister of Transport announces Canada's first proposed drone safety regulations for beyond visual line-of-sight operations. https://www.canada.ca/en/transport-canada/news/2023/06/minister-of-transport-announces-canadas-first-proposed-drone-safety-regulations-for-beyond-vi
html.

UK Civil Aviation Authority (2023). Registering a drone or model aircraft. https://register-drones.caa.co.uk/individual.

van der Velden, A. J. & Cook, F. A. (1996). Structure and tectonic development of the southern Rocky Mountain trench. *Tectonics*, *15*(3), 517–544, https://doi.org/10.1029/95TC03288.

Van Tassel, C. (2021). Defining the true cost behind implementing lidar systems into your business. https://candrone.com/blogs/news/the-real-cost-of-starting-a-lidar-drone-business.

VanValkenburgh, P., Cushman, K., Butters, L. J. C., Vega, C. R., Roberts, C. B., Kepler, C., & Kellner, J. (2020). Lasers without lost cities: Using drone lidar to capture architectural complexity at Kuelap, Amazonas, Peru. *Journal of Field Archaeology*, *45*(sup1), S75–S88, https://doi.org/10.1080/00934690.2020.1713287.

Viswanathan, V., Epstein, A. H., Chiang, Y.-M., Takeuchi, E., Bradley, M., Langford, J., & Winter, M. (2022). The challenges and opportunities of battery-powered flight. *Nature*, *601*(7894), 519–525, https://doi.org/10.1038/s41586-021-04139-1.

Walker, R., Bergman, E., Szeliga, W., & Fielding, E. (2011). Insights into the 1968-1997 Dasht-e-Bayaz and Zirkuh earthquake sequences, eastern Iran, from calibrated relocations, InSAR and high-resolution satellite imagery. *Geophysical Journal International*, *187*(3), 1577–1603, https://doi.org/10.1111/j.1365-246X.2011.05213.x.

Wang, L., Marzahn, P., Bernier, M., & Ludwig, R. (2020). Sentinel-1 InSAR measurements of deformation over discontinuous permafrost terrain, Northern Quebec, Canada. *Remote Sensing of Environment*, *248*, https://doi.org/10.1016/j.rse.2020.111965.

Wang, S., et al. (2019). DEM generation from Worldview-2 stereo imagery and vertical accuracy assessment for its application in active tectonics. *Geomorphology*, *336*, 107–118, https://doi.org/10.1016/j.geomorph.2019.03.016.

Washington Geological Survey (2022). Surface geology, 1:500,000 scale-GIS data, February 2022: Washington Geological Survey Digital Data Series 25. previously released June 2010, https://fortress.wa.gov/dnr/geologydata/publications/data_download/ger_portal_surface_geology_500k.zip.

Wedmore, L. N. J., Gregory, L. C., McCaffrey, K. J. W., Goodall, H., & Walters, R. J. (2019). Partitioned Off-Fault Deformation in the 2016 Norcia Earthquake Captured by Differential Terrestrial Laser Scanning. *Geophysical Research Letters*, *46*(6), 3199–3205, https://doi.org/10.1029/2018GL080858.

Wei, S., et al. (2015). The 2014 Mw 6.1 South Napa Earthquake: A Unilateral Rupture with Shallow Asperity and Rapid Afterslip. *Seismological Research Letters*, *86*(2A), 344–354, https://doi.org/10.1785/0220140249.

Wei, Z., He, H., Su, P., Zhuang, Q., & Sun, W. (2019). Investigating paleoseismicity using fault scarp morphology of the Dushanzi Reverse Fault in the northern Tian Shan, China. *Geomorphology*, *327*, 542–553, https://doi.org/10.1016/j.geomorph.2018.11.025.

Werner, C., Wegmüller, U., Strozzi, T., & Wiesmann, A. (2000). Gamma SAR and interferometric processing software. In *Proceedings of the ERS-Envisat Symposium, Gothenburg, Sweden*, volume 1620 (pp. 1620).: Citeseer.

Werner, C., Wegmüller, U., Strozzi, T., & Wiesmann, A. (2002). Processing strategies for phase unwrapping for INSAR applications. In *Proceedings of the European Conference on Synthetic Aperture Radar EUSAR*.

Wessel, P., Luis, J. F., Uieda, L., Scharroo, R., Wobbe, F., Smith, W. H. F., & Tian, D. (2019). The Generic Mapping Tools Version 6. *Geochemistry, Geophysics, Geosystems*, *20*(11), 5556–5564, https://doi.org/10.1029/2019GC008515.

Westoby, M., Brasington, J., Glasser, N., Hambrey, M., & Reynolds, J. (2012). 'Structure-from-Motion' photogrammetry: A low-cost, effective tool for geoscience applications. *Geomorphology*, *179*, 300–314, https://doi.org/10.1016/j.geomorph.2012.08.021.

Wetmiller, R. J., Horner, R. B., Hasegawa, H. S., North, R. G., Lamontagne, M., Weichert, D. H., & Evans, S. G. (1988). An analysis of the 1985 Nahanni earthquakes. *Bulletin of the Seismological Society of America*, *78*(2), 590–616.

Wiatr, T., Reicherter, K., Papanikolaou, I., Fernández-Steeger, T., & Mason, J. (2013). Slip vector analysis with high resolution t-LiDAR scanning. *Tectonophysics*, *608*, 947–957, https://doi.org/10.1016/j.tecto.2013.07.024.

Wieser, M., Hollaus, M., Mandlburger, G., Glira, P., & Pfeifer, N. (2016). ULS LiDAR supported analyses of laser beam penetration from different ALS systems into vegetation. *ISPRS Annals of Photogrammetry, Remote Sensing & Spatial Information Sciences*, *3*(3), https://doi.org/10.5194/isprs-annals-III-3-233-2016.

Wimpenny, S. & Watson, C. S. (2021). gWFM: A Global Catalog of Moderate-Magnitude Earthquakes Studied Using Teleseismic Body Waves. *Seismological Research Letters*, *92*(1), 212–226.

Witter, R. C., Bender, A. M., Scharer, K. M., DuRoss, C. B., Haeussler, P. J., & Lease, R. O. (2021). Geomorphic expression and slip rate of the Fairweather fault, southeast Alaska, and evidence for predecessors of the 1958 rupture. *Geosphere*, *17*(3), 711–738, https://doi.org/10.1130/GES02299.1.

Wolfe, F. D., Stahl, T. A., Villamor, P., & Lukovic, B. (2020). Short communication: A semi-automated method for bulk fault slip analysis from topographic scarp profiles. *Earth Surface Dynamics*, *8*(1), 211–219, https://doi.org/10.5194/esurf-8-211-2020.

Wright, T., Parsons, B., Jackson, J., Haynes, M., Fielding, E., England, P., & Clarke, P. (1999). Source parameters of the 1 October 1995 Dinar (Turkey) earthquake from SAR interferometry and seismic bodywave modelling. *Earth and Planetary Science Letters*, *172*(1-2), 23–37, https://doi.org/10.1016/S0012-821X(99)00186-7.

Wright, T. J., Lu, Z., & Wicks, C. (2004). Constraining the slip distribution and fault geometry of the M w 7.9, 3 November 2002, Denali fault earthquake with interferometric synthetic aperture radar and global positioning system data. *Bulletin of the Seismological Society of America*, *94*(6B), S175–S189, https://doi.org/10.1785/0120040623.

Xiaoye Liu (2008). Airborne LiDAR for DEM generation: some critical issues. *Progress in Physical Geography: Earth and Environment*, *32*(1), 31–49, https://doi.org/10.1177/0309133308089496.

Xu, G., Xu, C., Wen, Y., Xiong, W., & Valkaniotis, S. (2020). The Complexity of the 2018 Kaktovik Earthquake Sequence in the Northeast of the Brooks Range, Alaska. *Geophysical Research Letters*, *47*(19), e88012, https://doi.org/10.1029/2020GL088012.

Yukon Geological Survey (2020). A digital atlas of terranes for the northern Cordillera. https://data.geology.gov.yk.ca/Compilation/2.

Zaccagnino, D. & Doglioni, C. (2022). The impact of faulting complexity and type on earthquake rupture dynamics. *Communications Earth and Environment*, *3*(1), 258, https://doi.org/10.1038/s43247-022-00593-5.

Zelenin, E., Bachmanov, D., Garipova, S., Trifonov, V., & Kozhurin, A. (2022). The Active Faults of Eurasia Database (AFEAD): the ontology and design behind the continental-scale dataset. *Earth System Science Data*, *14*(10), 4489–4503, https://doi.org/10.5194/essd-14-4489-2022.

Zhang, B., Liao, Y., Guo, S., Wallace, R. E., Bucknam, R. C., & Hanks, T. C. (1986). Fault scarps related to the 1739 earthquake and seismicity of the Yinchuan graben, Ningxia Huizu Zizhiqu, China. *Bulletin of the Seismological Society of America*, *76*(5), 1253–1287, https://doi.org/10.1785/BSSA0760051253.

Zhang, H. & Ge, Z. (2010). Tracking the Rupture of the 2008 Wenchuan Earthquake by Using the Relative Back-Projection Method. *Bulletin of the Seismological Society of America*, *100*(5B), 2551–2560, https://doi.org/10.1785/0120090243.

Zhang, K., Chen, S.-C., Whitman, D., Shyu, M.-L., Yan, J., & Zhang, C. (2003). A progressive morphological filter for removing nonground measurements from airborne LIDAR data. *IEEE Transactions on Geoscience and Remote Sensing*, *41*(4), 872–882, https://doi.org/10.1109/TGRS.2003.810682.

Zhang, W., Qi, J., Wan, P., Wang, H., Xie, D., Wang, X., & Yan, G. (2016). An Easy-to-Use Airborne LiDAR Data Filtering Method Based on Cloth Simulation. *Remote Sensing*, *8*(6), https://doi.org/10.3390/rs8060501.

Zhu, X., Glennie, C. L., & Brooks, B. A. (2022). Automated near-field deformation detection from mobile laser scanning for the 2014 M_w 6.0 South Napa earthquake. *Journal of Applied Geodesy*, *16*(1), 65–79, https://doi.org/10.1515/jag-2021-0023.

Zielke, O., Arrowsmith, J. R., Ludwig, L. G., & Akçiz, S. O. (2010). Slip in the 1857 and Earlier Large Earthquakes Along the Carrizo Plain, San Andreas Fault. *Science*, *327*(5969), 1119–1122, https://doi.org/10.1126/science.1182781.

Zielke, O., Klinger, Y., & Arrowsmith, J. R. (2015). Fault slip and earthquake recurrence along strike-slip faults - Contributions of high-resolution geomorphic data. *Tectonophysics*, *638*, 43–62, https://doi.org/10.1016/j.tecto.2014.11.004.

Zwick, P., McCaffrey, R., & Abers, G. (1994). MT5 program. *IASPEI software library*, *4*.

Appendix A
Supplemental Material for Chapter 2

This appendix is composed of 11 figures (Figures A1-A11), 3 tables (Tables A1-A3), and 2 Data files. The figures show satellite imagery for the region, additional results from the InSAR modelling, and additional plots from the *mloc* relocation. Tables include the fault parameters and their search bounds for the InSAR inverse and forward models and the normalized slip profile from the distributed slip model. Data files include the full distributed slip model and our relocated hypocentres. Descriptions of each data field (column) in the data files are included in this document.

List of Data Files

1. Data File A1: Distributed slip model (distributed_slip_model.csv)
2. Data File A2: *mloc* calibrated hypocentres (relocated_hypocenters.csv)

Parameter	**Range allowed in uniform slip modelling**
Strike (°)	127 — 137
Dip (°)	77 — 87
Rake (°)	-6 — 14
Slip (m)	*fixed at 0.9 m*
Easting (km, UTM Zone 59N)	498 ± 4
Northing (km, UTM Zone 59N)	6897 ± 4
Length (km)	15 — 25
Minimum depth (km)	0 — 4
Maximum depth (km)	6 — 14

Table A.1: Fault parameter search bounds used in uniform source modelling. We inverted the InSAR data 100 times with starting parameters picked at random from within the search bounds, using the downhill simplex algorithm to obtain 100 local misfit minima, from which the global minimum misfit was obtained.

Depth	Average Slip (m)	Normalized
0.5	0.09	0.07
1.5	0.64	0.51
2.5	1.14	0.9
3.5	1.27	1
4.5	1.05	0.83
5.5	0.67	0.52
6.5	0.53	0.42
7.5	0.46	0.36
8.5	0.33	0.26
9.5	0.22	0.17
10.5	0.09	0.07

Table A.2: Average slip profile, normalized to 1, calculated from the distributed slip model (Data file 1)

Date	Lat	Long	Depth peak slip	M	Fault type	Name	Reference
23/06/1946	49.76	-125.34	10	7.3	SS, RL	Vancouver Island	Slawson and Savage (1979)
5/10/1985	62.21	-124.22	6	6.6	RF	Nahanni	Wetmiller et al. (1988)
23/12/1985	62.19	-124.24	6	6.9	RF	Nahanni	Wetmiller et al. (1988)
23/10/2002	63.514	-147.912	14	6.6	SS - RL	Denali Foreshock	Wright et al. (2004)
03/11/2002	63.514	-147.453	8.5	7.9	SS - RL	Denali	Wright et al. (2004)
29/04/2006	60.949	167.089	12.5	7.6	T	Kamchatka	Mikhailov et al. (2023)
12/08/2018	69.576	-145.291	5	6.4	SS - RL	Kaktovik	Gaudreau et al. (2019)
12/08/2018	69.523	-144.339	5	6	SS - RL	Kaktovik	Gaudreau et al. (2019)
09/01/2020	62.2035	170.9869	3.5	6.4	SS - LL	Koryak	*this study*

Table A.3: Depth of peak slip for selected events plotted in Figure 2.9

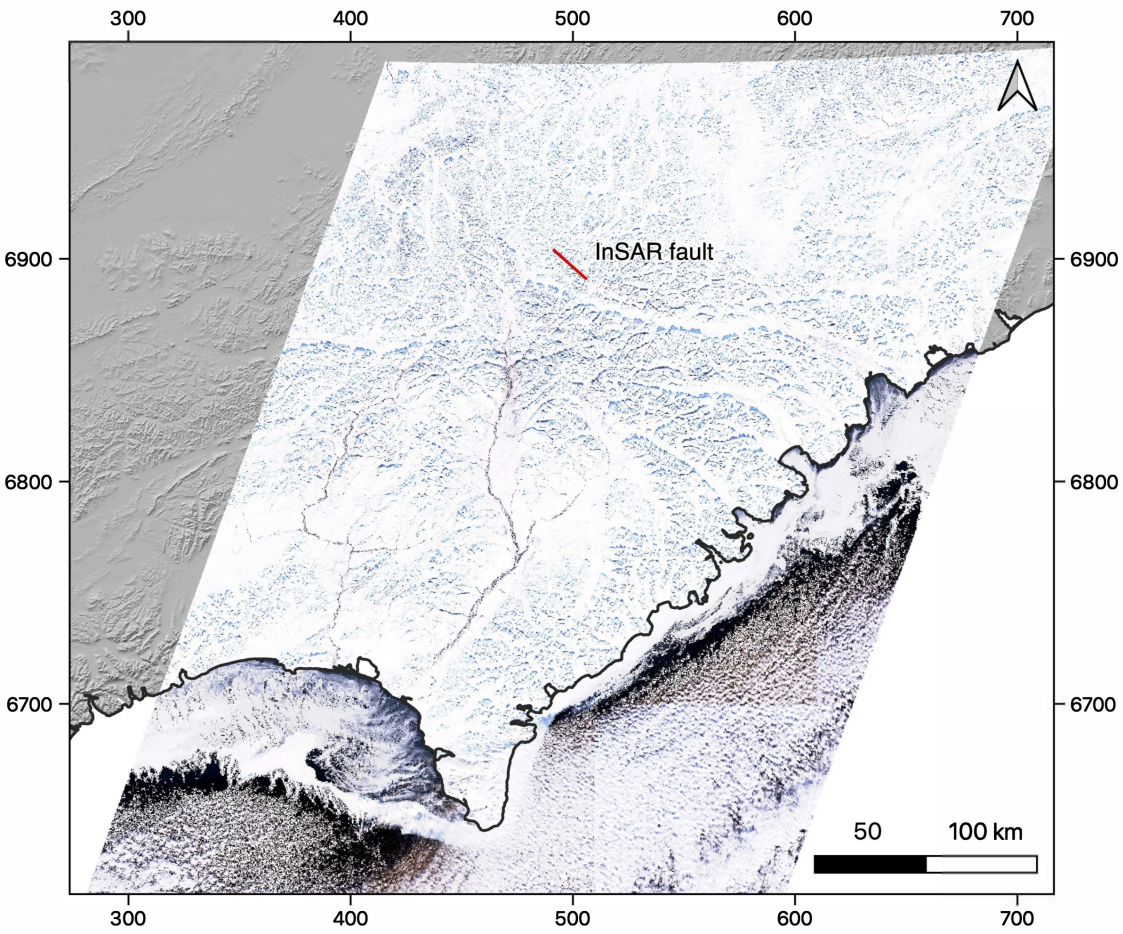

Figure A.1: Sentinel 2 imagery for the Koryak Highlands on 8 February 2020, showing that the region is snow-covered. Unfortunately the pre-earthquake imagery acquisitions during December and early January were cloud covered. Red line shows the location of the InSAR fault. Coordinates are in UTM kilometres (Zone 59N). Imagery was accessed using the Sentinel Hub (https://apps.sentinel-hub.com/eo-browser/).

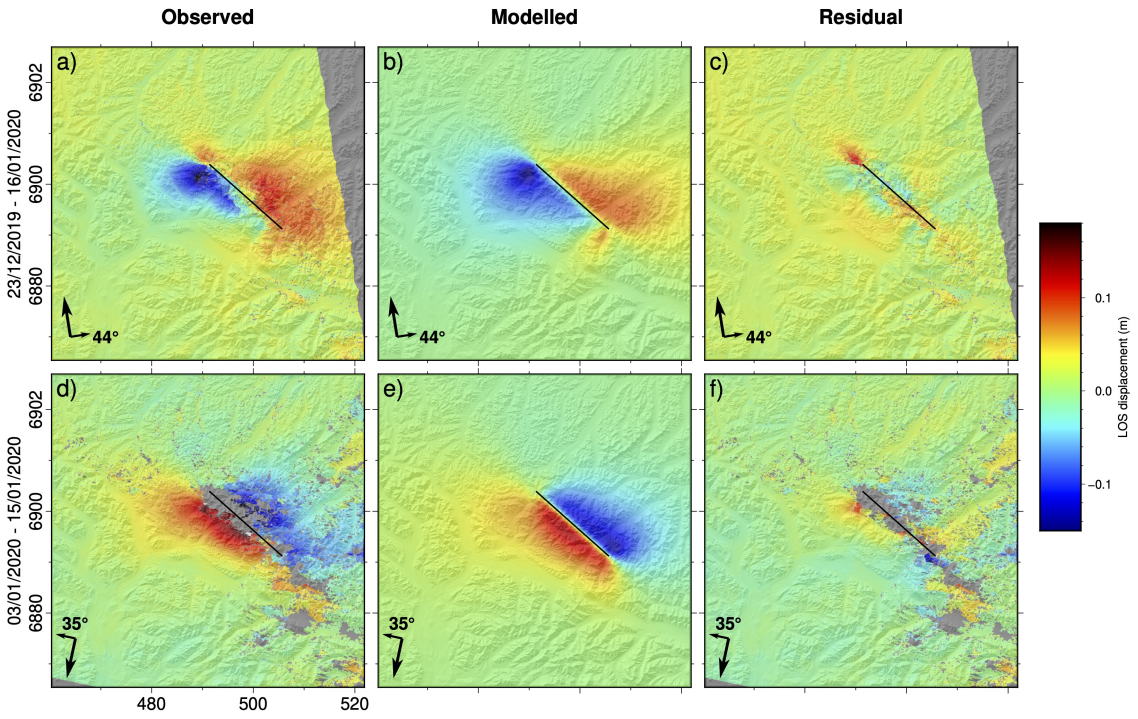

Figure A.2: InSAR results (uniform slip, unwrapped). Top row: (left) observed 24 day, (middle) model and (right) residual interferograms for Sentinel-1 ascending track 125. Bottom row: (left) observed 12 day, (middle) model and (right) residual interferograms for descending track 118. Large and small arrows show satellite track and LOS azimuths, along with the incidence angle measured from the vertical at the earthquake. The black line is the surface trace of the InSAR model fault. Coordinates are in UTM kilometres (Zone 59N).

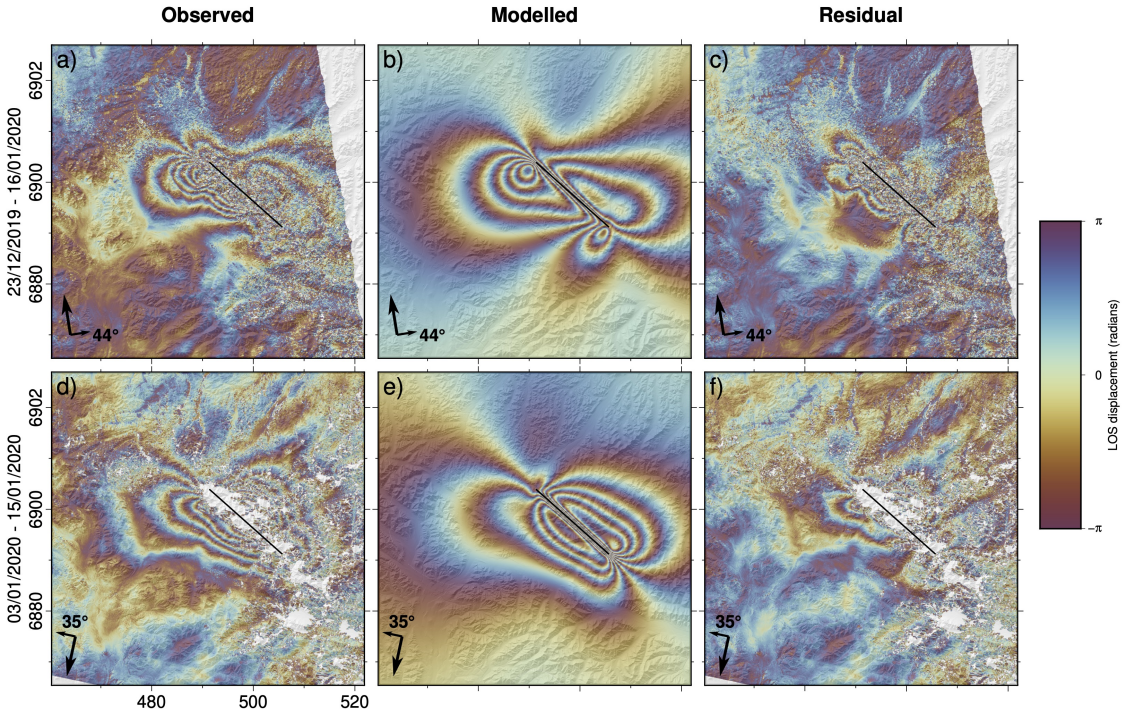

Figure A.3: InSAR results (uniform slip, wrapped). Top row: (left) observed 24 day, (middle) model and (right) residual interferograms for Sentinel-1 ascending track 125. Bottom row: (left) observed 12 day, (middle) model and (right) residual interferograms for descending track 118. Large and small arrows show satellite track and LOS azimuths, along with the incidence angle measured from the vertical at the earthquake. The black line is the surface trace of the InSAR model fault. Coordinates are in UTM kilometres (Zone 59N).

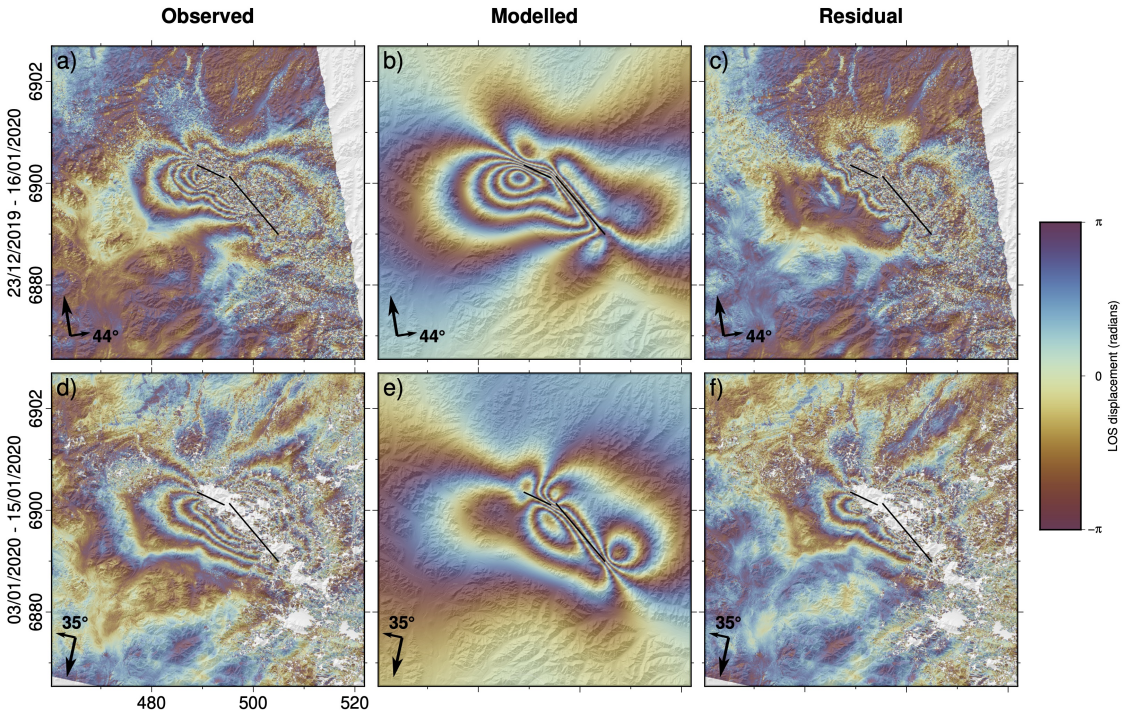

Figure A.4: InSAR results (two-fault model, uniform slip, wrapped). Top row: (left) observed 24 day, (middle) model and (right) residual interferograms for Sentinel-1 ascending track 125. Bottom row: (left) observed 12 day, (middle) model and (right) residual interferograms for descending track 118. Large and small arrows show satellite track and LOS azimuths, along with the incidence angle measured from the vertical at the earthquake. The black line is the surface trace of the InSAR model fault. Coordinates are in UTM kilometres (Zone 59N).Note that the two-fault model performed well for the ascending track interferogram, matching the shape and number of fringes, but does not perform as well on the descending track.

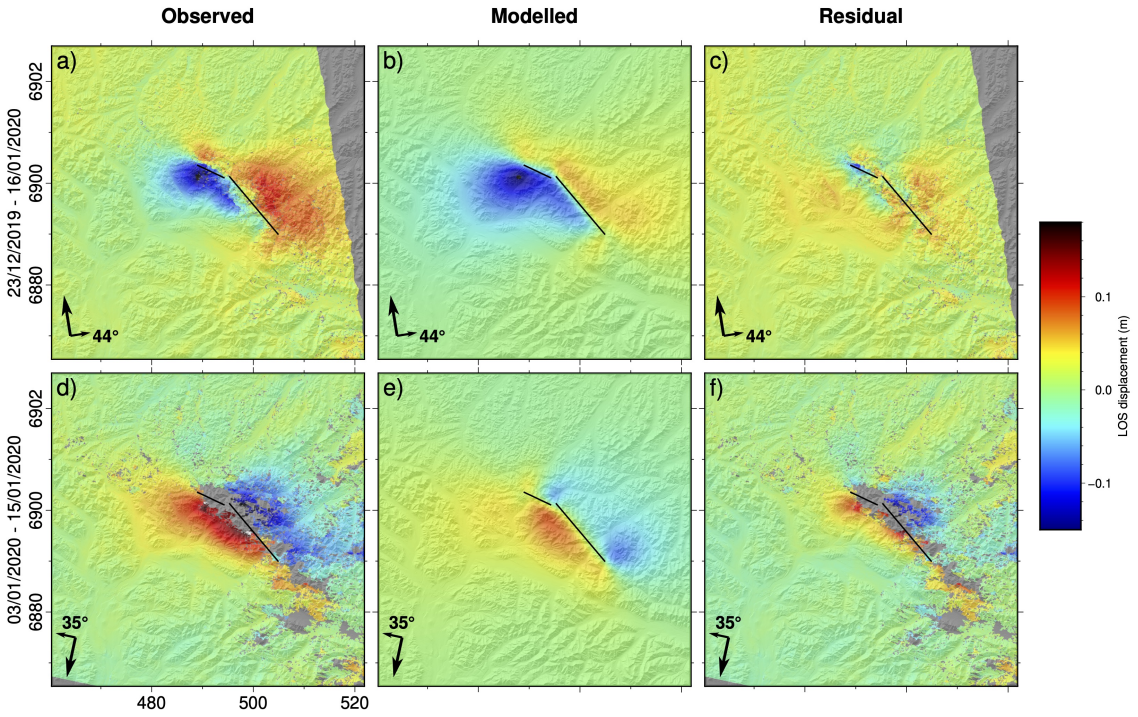

Figure A.5: InSAR results (two-fault model, uniform slip, unwrapped). Top row: (left) observed 24 day, (middle) model and (right) residual interferograms for Sentinel-1 ascending track 125. Bottom row: (left) observed 12 day, (middle) model and (right) residual interferograms for descending track 118. Large and small arrows show satellite track and LOS azimuths, along with the incidence angle measured from the vertical at the earthquake. The black line is the surface trace of the InSAR model fault. Coordinates are in UTM kilometres (Zone 59N).Note that the two-fault model performed well for the ascending track interferogram, with low residuals, but does not capture the deformation associated with the descending track.

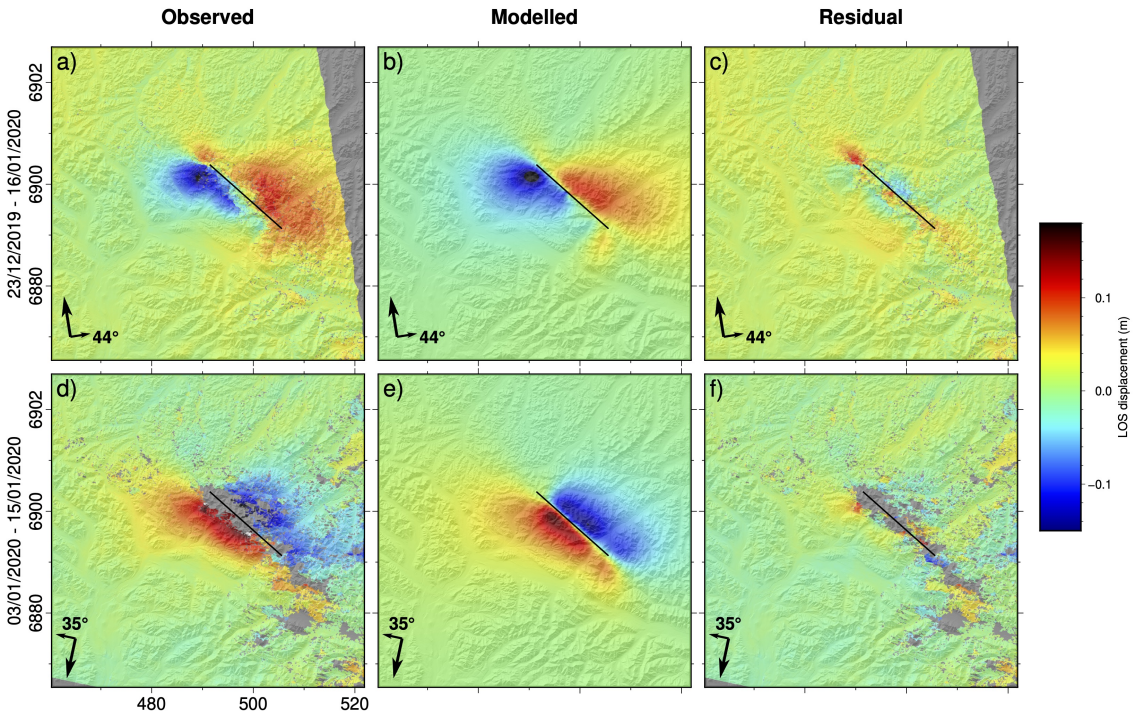

Figure A.6: InSAR results (distributed slip, unwrapped). Top row: (left) observed 24 day, (middle) model and (right) residual interferograms for Sentinel-1 ascending track 125. Bottom row: (left) observed 12 day, (middle) model and (right) residual interferograms for descending track 118. Large and small arrows show satellite track and LOS azimuths, along with the incidence angle measured from the vertical at the earthquake. The black line is the surface trace of the InSAR model fault. Coordinates are in UTM kilometres (Zone 59N).

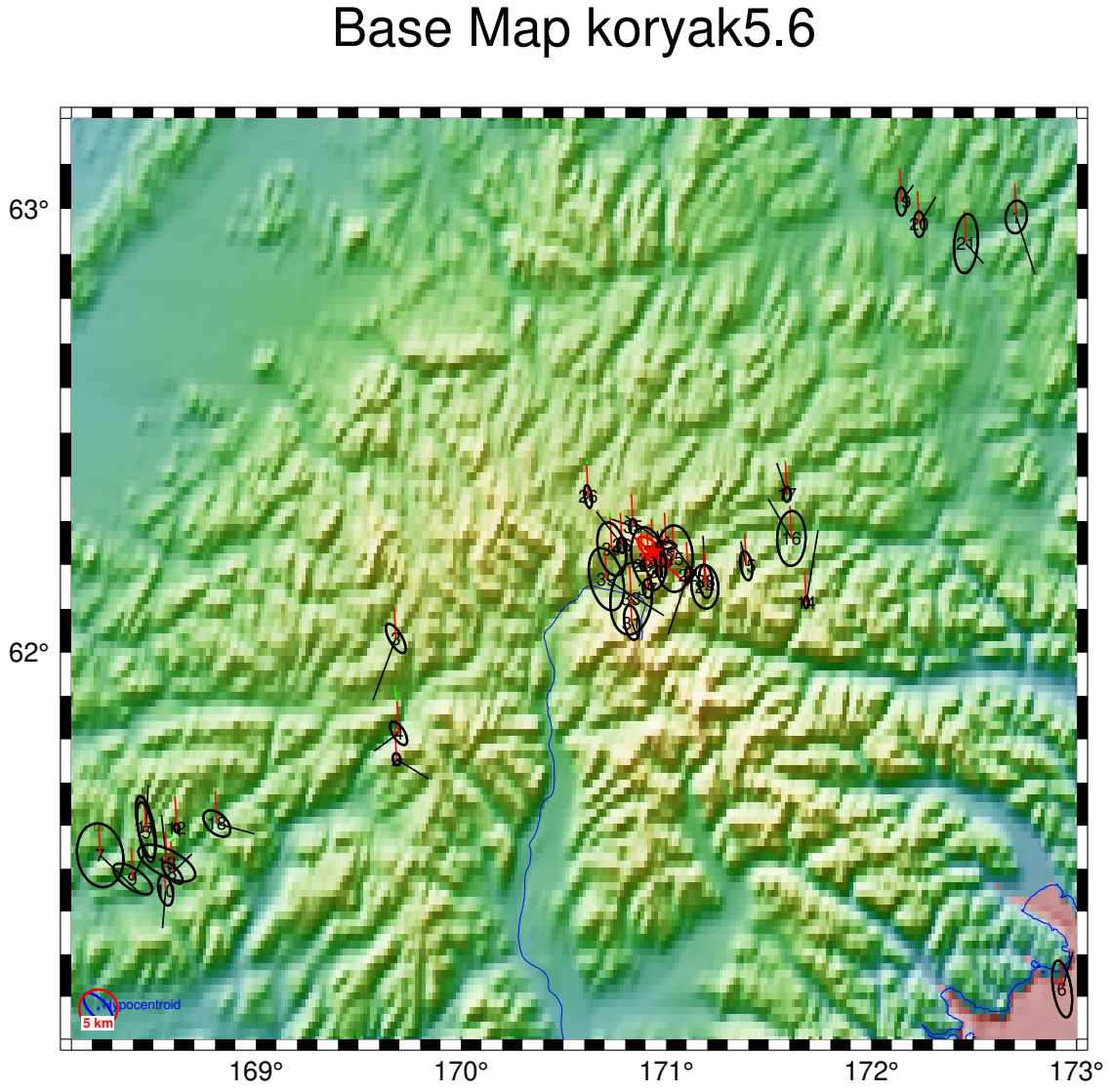

Figure A.7: Map of the relocated cluster epicentres with confidence ellipses for the cluster vectors. Green lines show change in location from the starting location for the current run of mloc, while black lines show change from the location given in the event data file. Each epicentre is numbered. The red circle in the lower left corner has a radius of 5 km for scale.

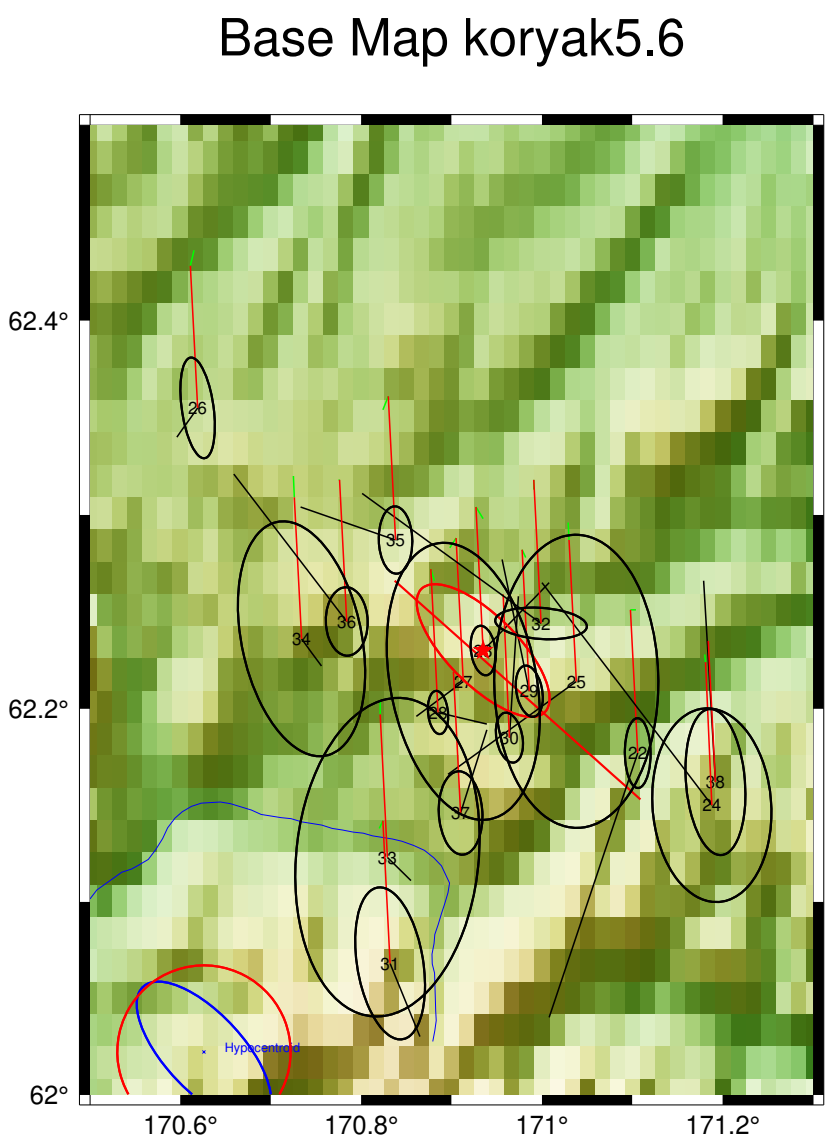

Figure A.8: Map of selected (2020 cluster) relocated epicentres with confidence ellipses for the cluster vectors. Green lines show change in location from the starting location for the current run of mloc, while black lines show change from the location given in the event data file. Each epicentre is numbered. The red circle in the lower left corner has a radius of 5 km for scale.

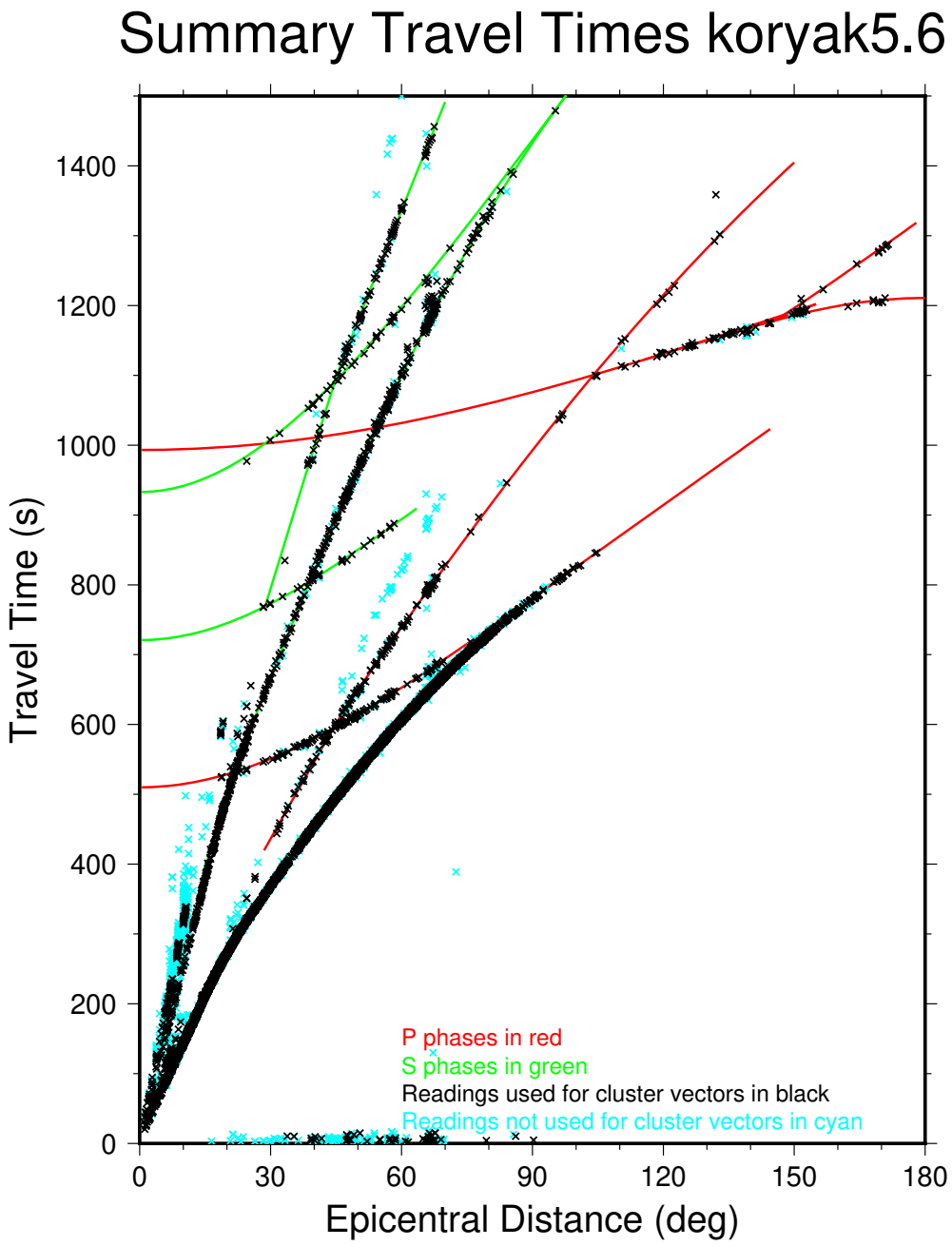

Figure A.9: This plot displays arrival time data and theoretical TT curves out to 180° and to a travel time of 1500 s. Theoretical curves are from ak135 (Kennett et al., 1995), with depth set to that of the hypocentroid. Curves are yellow for P, PP, Pdiff and core phases; cyan for S, SS, ScP and ScS.

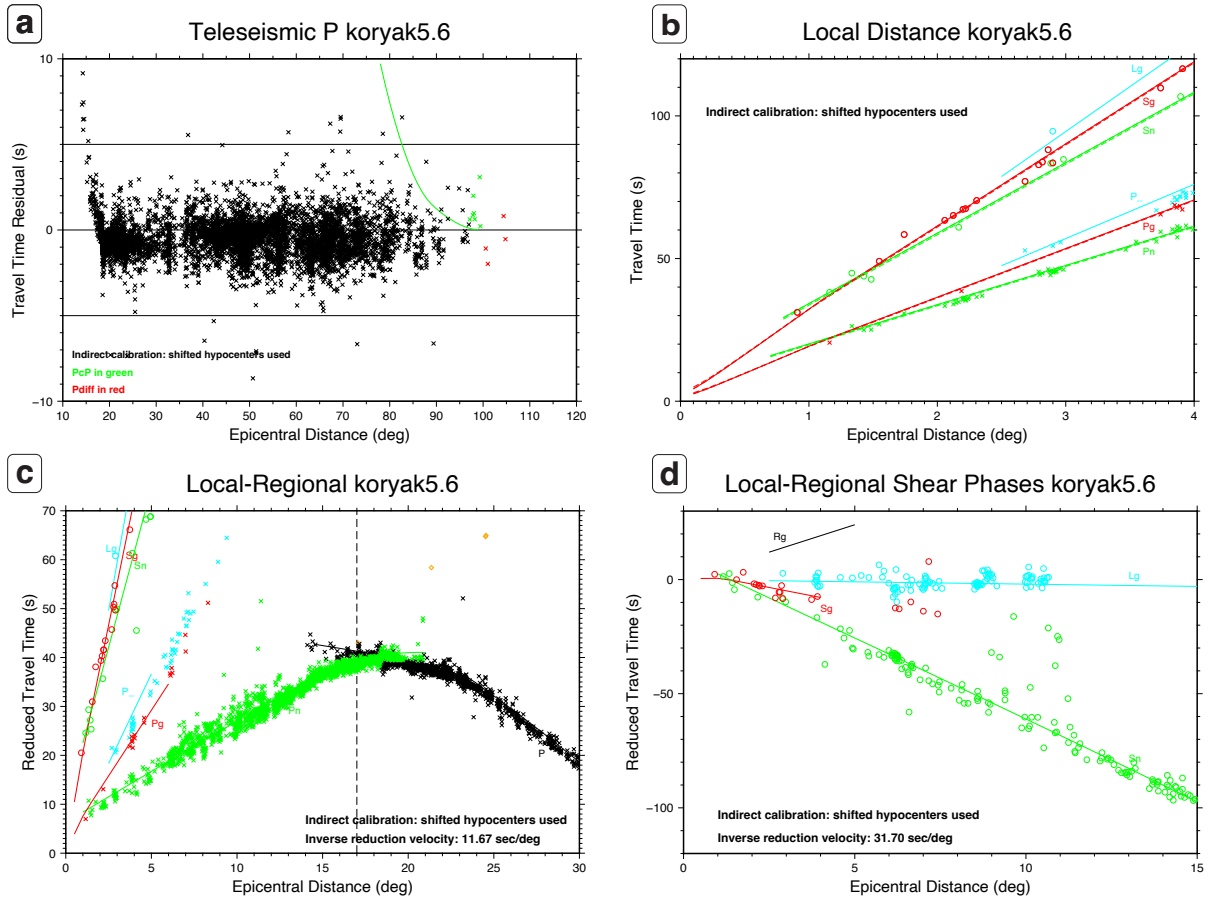

Figure A.10: Arrival times at various epicentral distance ranges. (a) P phase arrivals, (black crosses) from 10°–120°, reduced to the theoretical time (ak135, Kennett et al. (1995)). The green line denotes the theoretical arrival time of phase PcP. (b) Travel times over 0°–4° epicentral distances. The phases include: red crosses—Pg; blue crosses—Pb; green crosses—Pn; red circles—Sg; blue circles—Sb; green circles—Sn; cyan circles—any other phases. The vertical dashed line denotes the distance limit used to calculate the hypocentroid. (c) Travel times up to an epicentral distance of 30° and reduced for visual readability. (d) The residual for each arrival time within the epicentral distance used for estimating the hypocentroid, illustrated by the vertical dashed line at 0.7°. The solid and dashed red lines represent the average travel time residual for each phase. The green circles beyond the 0.7° mark is phase Sn.

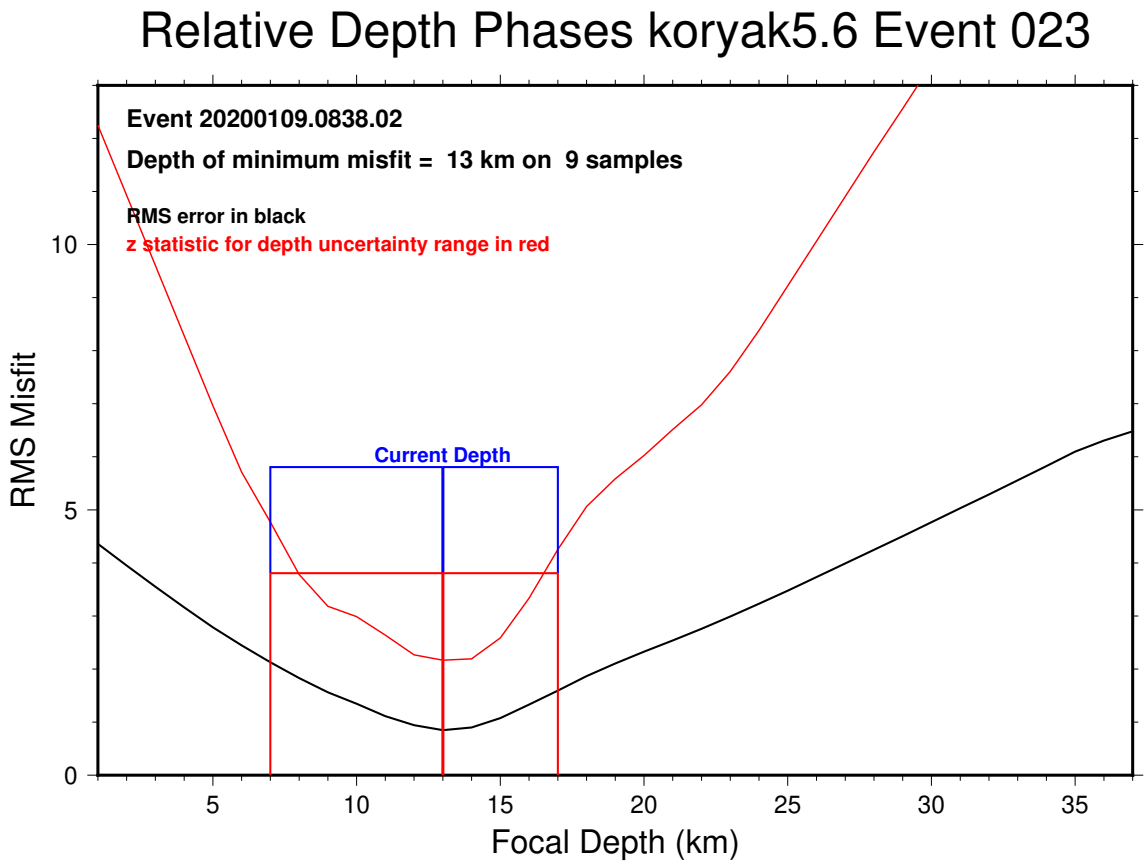

Figure A.11: Relative depth phase plot for the M_w 6.4 Koryak Highlands Earthquake. The black curve is the raw RMS error function. The red curve is a statistic (more sensitive than RMS) used to determine the optimal depth and the asymmetric uncertainty range of that depth. The current estimate of depth (in blue) is also shown.

Data File A1

distributed_slip_model.csv

```
"easting
UTM Zone 59N, m","northing
UTM Zone 59N, m","model slip
m","top depth
km","bottom depth
km"
491047.5,6904190.6,0.10,2.99,3.99
491047.5,6904190.6,0.36,3.99,4.99
491047.5,6904190.6,0.55,4.99,5.98
491047.5,6904190.6,0.61,5.98,6.98
491047.5,6904190.6,0.55,6.98,7.98
491047.5,6904190.6,0.43,7.98,8.98
491047.5,6904190.6,0.29,8.98,9.97
491047.5,6904190.6,0.15,9.97,10.97
491795.2,6903526.6,0.30,1.99,2.99
491795.2,6903526.6,0.63,2.99,3.99
491795.2,6903526.6,0.91,3.99,4.99
491795.2,6903526.6,1.03,4.99,5.98
491795.2,6903526.6,0.98,5.98,6.98
491795.2,6903526.6,0.81,6.98,7.98
491795.2,6903526.6,0.59,7.98,8.98
491795.2,6903526.6,0.37,8.98,9.97
491795.2,6903526.6,0.17,9.97,10.97
492542.9,6902862.6,0.44,1,1.99
492542.9,6902862.6,1.02,1.99,2.99
492542.9,6902862.6,1.36,2.99,3.99
492542.9,6902862.6,1.43,3.99,4.99
492542.9,6902862.6,1.29,4.99,5.98
492542.9,6902862.6,1.04,5.98,6.98
492542.9,6902862.6,0.75,6.98,7.98
492542.9,6902862.6,0.47,7.98,8.98
492542.9,6902862.6,0.25,8.98,9.97
492542.9,6902862.6,0.10,9.97,10.97
493290.7,6902198.6,0.02,0,1
493290.7,6902198.6,0.85,1,1.99
493290.7,6902198.6,1.57,1.99,2.99
493290.7,6902198.6,1.79,2.99,3.99
493290.7,6902198.6,1.61,3.99,4.99
493290.7,6902198.6,1.23,4.99,5.98
493290.7,6902198.6,0.82,5.98,6.98
493290.7,6902198.6,0.48,6.98,7.98
493290.7,6902198.6,0.23,7.98,8.98
493290.7,6902198.6,0.09,8.98,9.97
493290.7,6902198.6,0.02,9.97,10.97
494038.4,6901534.6,0.06,0,1
```

494038.4,6901534.6,1.05,1,1.99
494038.4,6901534.6,1.72,1.99,2.99
494038.4,6901534.6,1.78,2.99,3.99
494038.4,6901534.6,1.41,3.99,4.99
494038.4,6901534.6,0.90,4.99,5.98
494038.4,6901534.6,0.46,5.98,6.98
494038.4,6901534.6,0.17,6.98,7.98
494038.4,6901534.6,0.04,7.98,8.98
494786.1,6900870.6,0.08,0,1
494786.1,6900870.6,1.08,1,1.99
494786.1,6900870.6,1.61,1.99,2.99
494786.1,6900870.6,1.51,2.99,3.99
494786.1,6900870.6,1.03,3.99,4.99
494786.1,6900870.6,0.50,4.99,5.98
494786.1,6900870.6,0.14,5.98,6.98
494786.1,6900870.6,0.00,6.98,7.98
495533.9,6900206.6,0.14,0,1
495533.9,6900206.6,1.00,1,1.99
495533.9,6900206.6,1.42,1.99,2.99
495533.9,6900206.6,1.25,2.99,3.99
495533.9,6900206.6,0.73,3.99,4.99
495533.9,6900206.6,0.23,4.99,5.98
496281.6,6899542.6,0.14,0,1
496281.6,6899542.6,0.88,1,1.99
496281.6,6899542.6,1.33,1.99,2.99
496281.6,6899542.6,1.18,2.99,3.99
496281.6,6899542.6,0.65,3.99,4.99
496281.6,6899542.6,0.16,4.99,5.98
497029.3,6898878.6,0.01,0,1
497029.3,6898878.6,0.82,1,1.99
497029.3,6898878.6,1.41,1.99,2.99
497029.3,6898878.6,1.35,2.99,3.99
497029.3,6898878.6,0.81,3.99,4.99
497029.3,6898878.6,0.24,4.99,5.98
497777.1,6898214.6,0.42,0,1
497777.1,6898214.6,0.95,1,1.99
497777.1,6898214.6,1.60,1.99,2.99
497777.1,6898214.6,1.65,2.99,3.99
497777.1,6898214.6,1.09,3.99,4.99
497777.1,6898214.6,0.39,4.99,5.98
497777.1,6898214.6,0.00,5.98,6.98
498524.8,6897550.6,0.73,1,1.99
498524.8,6897550.6,1.67,1.99,2.99
498524.8,6897550.6,1.89,2.99,3.99
498524.8,6897550.6,1.33,3.99,4.99
498524.8,6897550.6,0.53,4.99,5.98
498524.8,6897550.6,0.04,5.98,6.98
499272.5,6896886.6,0.76,1,1.99

499272.5,6896886.6,1.73,1.99,2.99
499272.5,6896886.6,1.95,2.99,3.99
499272.5,6896886.6,1.39,3.99,4.99
499272.5,6896886.6,0.58,4.99,5.98
499272.5,6896886.6,0.06,5.98,6.98
500020.3,6896222.6,0.01,0,1
500020.3,6896222.6,0.69,1,1.99
500020.3,6896222.6,1.55,1.99,2.99
500020.3,6896222.6,1.74,2.99,3.99
500020.3,6896222.6,1.21,3.99,4.99
500020.3,6896222.6,0.48,4.99,5.98
500020.3,6896222.6,0.03,5.98,6.98
500768.0,6895558.6,0.03,0,1
500768.0,6895558.6,0.56,1,1.99
500768.0,6895558.6,1.20,1.99,2.99
500768.0,6895558.6,1.31,2.99,3.99
500768.0,6895558.6,0.87,3.99,4.99
500768.0,6895558.6,0.30,4.99,5.98
501515.7,6894894.6,0.09,0,1
501515.7,6894894.6,0.44,1,1.99
501515.7,6894894.6,0.85,1.99,2.99
501515.7,6894894.6,0.90,2.99,3.99
501515.7,6894894.6,0.57,3.99,4.99
501515.7,6894894.6,0.16,4.99,5.98
502263.5,6894230.6,0.07,0,1
502263.5,6894230.6,0.27,1,1.99
502263.5,6894230.6,0.60,1.99,2.99
502263.5,6894230.6,0.70,2.99,3.99
502263.5,6894230.6,0.47,3.99,4.99
502263.5,6894230.6,0.16,4.99,5.98
503011.2,6893566.6,0.11,1,1.99
503011.2,6893566.6,0.57,1.99,2.99
503011.2,6893566.6,0.81,2.99,3.99
503011.2,6893566.6,0.70,3.99,4.99
503011.2,6893566.6,0.41,4.99,5.98
503011.2,6893566.6,0.15,5.98,6.98
503011.2,6893566.6,0.02,6.98,7.98
503758.9,6892902.6,0.06,0,1
503758.9,6892902.6,0.20,1,1.99
503758.9,6892902.6,0.76,1.99,2.99
503758.9,6892902.6,1.15,2.99,3.99
503758.9,6892902.6,1.16,3.99,4.99
503758.9,6892902.6,0.89,4.99,5.98
503758.9,6892902.6,0.54,5.98,6.98
503758.9,6892902.6,0.25,6.98,7.98
503758.9,6892902.6,0.08,7.98,8.98
504506.7,6892238.6,0.13,1,1.99
504506.7,6892238.6,0.82,1.99,2.99

```
504506.7,6892238.6,1.40,2.99,3.99
504506.7,6892238.6,1.57,3.99,4.99
504506.7,6892238.6,1.37,4.99,5.98
504506.7,6892238.6,1.00,5.98,6.98
504506.7,6892238.6,0.60,6.98,7.98
504506.7,6892238.6,0.29,7.98,8.98
504506.7,6892238.6,0.10,8.98,9.97
504506.7,6892238.6,0.02,9.97,10.97
505254.4,6891574.6,0.69,1.99,2.99
505254.4,6891574.6,1.35,2.99,3.99
505254.4,6891574.6,1.63,3.99,4.99
505254.4,6891574.6,1.53,4.99,5.98
505254.4,6891574.6,1.20,5.98,6.98
505254.4,6891574.6,0.81,6.98,7.98
505254.4,6891574.6,0.47,7.98,8.98
505254.4,6891574.6,0.22,8.98,9.97
505254.4,6891574.6,0.08,9.97,10.97
506002.1,6890910.6,0.47,1.99,2.99
506002.1,6890910.6,0.92,2.99,3.99
506002.1,6890910.6,1.12,3.99,4.99
506002.1,6890910.6,1.08,4.99,5.98
506002.1,6890910.6,0.87,5.98,6.98
506002.1,6890910.6,0.62,6.98,7.98
506002.1,6890910.6,0.38,7.98,8.98
506002.1,6890910.6,0.20,8.98,9.97
506002.1,6890910.6,0.08,9.97,10.97
```

Data File A2

relocated_hypocenters.csv

```
Basic hypocenter list from indirect calibration,,,,,,,,,,,
Cluster #,Year,Month,Day,Hours,Minutes,Seconds,Latitude,Longitude,Depth,Magnitude,
1,1979,7,27,4,28,49.27,63.0554,172.7065,10,4.5mb,
2,1988,10,13,0,32,11.16,61.8276,169.6848,10,5.7mb,
3,1988,10,15,7,5,39.01,62.1054,169.6808,10,,
4,1992,1,21,18,7,37.93,61.8882,169.6952,10,4.6mb,
5,1994,6,11,16,44,56.31,61.6589,168.4636,10,4.7mb,
6,1998,4,1,0,12,13.53,61.2918,172.9299,10,4.3mb,
7,2006,4,21,0,47,40.75,61.6049,168.2396,10,4.0mb,
8,2006,4,24,7,42,19.17,61.5634,168.5922,10,4.0mb,
9,2006,5,6,12,42,15.72,61.5498,168.3986,10,4.0mb,
10,2006,7,22,4,16,47.8,61.5231,168.5588,10,4.3mb,
11,2006,7,22,8,31,50.7,61.6711,168.4632,10,4.2mb,
12,2006,9,6,5,0,28.49,61.6676,168.6129,10,5.5mb,
13,2006,9,9,17,48,2.48,61.5864,168.5654,10,4.2mb,
```

```
14,2007,5,24,12,39,29.87,62.1876,171.6817,10,5.2mb,
15,2007,5,24,22,18,58.19,62.2715,171.3901,10,4.2mb,
16,2007,6,4,2,36,23.16,62.3338,171.6104,10,4.2mb,
17,2007,10,4,14,6,15.05,62.4333,171.5885,10,4.7mb,
18,2009,7,4,18,21,33.73,61.6786,168.8093,10,4.1mb,
19,2014,10,5,23,11,9.83,63.0901,172.1459,10,4.6mb,
20,2014,10,6,1,7,41.15,63.0394,172.2332,10,4.5mb,
21,2014,10,6,1,44,22.67,62.9964,172.4612,10,4.2mb,
22,2020,1,9,8,17,59,62.251,171.1058,10,5.1Ml,
23,2020,1,9,8,38,9.09,62.3037,170.935,13,6.4Ml,
24,2020,1,9,8,47,1.73,62.2241,171.1885,10,4.7mb,
25,2020,1,9,8,52,27.81,62.2873,171.0377,10,3.8mb,
26,2020,1,9,9,0,50.66,62.4283,170.6192,10,5.0Ml,
27,2020,1,9,9,15,53.66,62.2876,170.9132,10,3.6mb,
28,2020,1,9,9,56,47.6,62.2717,170.8846,10,5.2Ml,
29,2020,1,9,10,11,11.6,62.2823,170.986,10,5.2Ml,
30,2020,1,9,10,47,20.05,62.2591,170.9645,10,5.4Ml,
31,2020,1,9,11,5,43.68,62.1417,170.832,10,4.7Ml,
32,2020,1,9,11,21,56.85,62.3176,170.9988,10,3.6mb,
33,2020,1,9,11,56,41.14,62.1965,170.8289,10,4.3Ml,
34,2020,1,9,14,19,13.45,62.3094,170.7339,10,3.7mb,
35,2020,1,9,16,6,50.5,62.3608,170.8382,10,5.0Ml,
36,2020,1,10,4,50,33.51,62.3185,170.7836,10,5.1Ml,
37,2020,1,10,12,10,31.93,62.2193,170.9101,10,4.9Ml,
38,2020,1,17,19,22,13.13,62.2353,171.1922,10,4.6Ml,
39,2022,3,31,1,30,3.62,62.2406,170.7076,10,4.1Ml,
```

Appendix B
Supplemental Material for Chapter 3

This appendix is composed of 14 figures (Figures B1-B14), 2 scripts and 4 Data files. The figures include flight lines for each study site and comparisons made along the Eastern Denali fault that were not included within the publication. The data files are point cloud profiles through typical vegetation types found within in each case study. All the appendix material is available on the Zenodo repository. Salomon (2024).

List of Scripts

1. Script B1: shell script to process point clouds (SM12_pointcloud_processing.sh)
2. Script B2: shell script to difference rasters (SM13_raster_difference.sh)

Script B1

SM12_pointcloud_processing.sh

```
#!/bin/bash

# This script takes a raw lidar file not yet classified as exported from RiProcess and creates several p
# Requires the following software: LASTools https://github.com/LAStools/LAStools and gdal https://gdal.o
#
#   Note: this script makes use of closed source tools within the LASTools suite, as such, a paid licen
#
#   To run LASTools executables on my macbook, I use Wine Crossover installed with Homebrew.
#   To make the executables accessible from any directory, I added the wine64 call and the path to the p
#       e.g. "alias lasgrid="wine64 ~/LAStools/bin/lasgrid.exe""
#
#   - Guy Salomon, April 2023, updated April 2024


# Recommended file structure
# Master project folder with .las or .laz files,
#   sub folder "control" with csv of control features x,y,z, etc. within the given point cloud.
#   subfolder with the polygon .shp that you want to clip the area to.
```

```
# Usage: . workflow.sh NAME

# Some useful variables to set
res=0.3             # resolution in meters for raster products
n1=7                # number of cores to use, usually use max n -1
fill=15             # number of pixels to fill while interpolating
tile=300            # size of tiles meters
buffer=25           # buffer for tiles meters
step=3              # for lasground
spike=0.25           # lasground spike typ 0.25
spikedown=0.25       # lasground spike_down typ 0.25
bulge=0.5          # lasground bulge typ 0.5
clip_polygon="path/to/clip_polygon.shp"

##### Explanation of lasground parameters below #####
# Initially lasground creates a ground estimate by using the lowest point in each cell of a coarse grid
# The '-wilderness' tag is just a short-hand for a step of 3 meter. '-town' is a short-hand for a step o

# http://rapidlasso.com/lasground
# http://lastools.org/download/lasground_README.txt
# http://lastools.org/download/lasground_new_README.txt

# The bulge parameter defines how "high" coarse triangles of the coarse TIN are allowed to "bulge up" wh
# considered last return into the slowly refining ground TIN or not. The lower you set it the less the T
# are potentially chopped off. Setting it to zero or asking for 'no_bulge' can be quite aggressive - esp

# The spike parameter is used between refinement passes. After each we refinement we check in the curren
# an up or a down "spike" with its immediate one-triangle-ring of other points. If the observed spike ex
# Hence, a larger '-spike' value is useful if you expect your ground TIN to have great variation or if y

# Finally there is also '-stddev'. That is a special option designed to, for example, get cleaner roads
# road near the two steep sides. In some cases this may have undesirable side-effects so try to set it t

# Clean up - can toggle this off.
rm -r 2_tiles 3_ground 4_classified 5_final_las 6_raster

# Clip the input
echo "Clipping the point cloud"
mkdir 1_clipped
lasclip -cpu64 -v -i
# Tile the input - NB for large datasets!
echo "Tiling the point cloud"
mkdir 2_tiles
lastile -cpu64 -v -i 1_clipped/
# Determine a ground surface
echo "Determining the ground surface"
mkdir 3_ground
lasground_new -cpu64 -v -i 2_tiles/
```

```
# Classify the remaining points
echo "Classifying the remaining points"
mkdir 4_classified
lasclassify -cpu64 -v -i 3_ground/lasclassify -cpu64 -v -i 3_ground/
# Remove some noisy points
echo "Cleaning up"
mkdir 5_final_las
lasnoise -cpu64 -v -i 4_classified/
# Index files and remove buffer
lasindex -i 5_final_las/lastile -cpu64 -v -i 5_final_las/lasinfo -cpu64 -v -i 8_final_all/
# Merge the files and grid
echo "Creating a DTM"
mkdir 6_raster
mkdir 6_raster/dtm
lasgrid -cpu64 -v -i 5_final_las/
mkdir 6_raster/dsm
las2dem -cpu64 -v -i 5_final_las/
mkdir 7_ground_only
las2las -cpu64 -v -i 5_final_las/lasinfo -cpu64 -v -i 7_ground_only/
mkdir 8_final_all
las2las -cpu64 -v -i 5_final_las/lasinfo -cpu64 -v -i 8_final_all/
# Make some more raster products
cd 6_raster/dtm
gdaldem hillshade -z 1.0 -s 1.0 -az 315.0 -alt 45.0 dtm.tif hillshade.tif
gdaldem slope -of GTiff -b 1 -s 1.0 dtm.tif slope.tif

echo "Calculating canopy height CHM"
cd ..
gdal_calc.py -A dsm/dsm.tif -B dtm/dtm.tif --outfile=$1"CHM.tif" --calc="A-B" --extent intersect
cd ..

echo "cleaning up - run: rm -r 2_tiles 3_ground 4_classified 5_final_las"

echo "done"
```

Script B2

SM13_raster_difference.sh

```
#!/bin/bash

# Create raster difference products difference, histogram and stats, M3C2 raster previously generated ir
# DoD [DEM of Difference] = newer DTM - older DTM erosion is negative, deposition is positive
# Requires the following software: gdal https://gdal.org/index.html and gmt https://www.generic-mapping-
#   Dependencies include: CMake >=3.16, netCDF >=4.0, curl, Ninja
#
# Guy Salomon - June 2023, updated January 2024
```

```
#
# Usage: ./raster_difference.sh [NAME]

new="path/to/drone/dtm.tif"
old="path/to/comparison/dtm.tif"

### Calculate the DoD ###
gdal_calc.py -A $new -B $old --outfile=difference_$1.tif --calc="A-B" --extent intersect --overwrite
### Calculate some stats for the final raster
gdalinfo difference_$1.tif -stats  tail > difference_stats_summary.txt
### Create a histogram for the DoD
diff="difference_"$1".tif"
bin_width=0.05                  # bin size for histogram
bounds="-1/1/0/0"               # xmin/max/ymin/ymax
cpt="SM13_AUX_diff.cpt"
font_size="30p"
# convert the geotiff
gmt grd2xyz difference_$1.tif > temp.xyz
# create the raster difference histogram
gmt begin $1'_diff_histogram' PNG
    awk '{print $3}' temp.xyz  gmt histogram -R$bounds -F -T$bin_width -W0.25p -BWS -Bxa1f0.2 -C$cpt -Z1
gmt end

rm temp.xyz

### M3C2 ###
# Calculate some stats for the M3C2 distance raster
gdalinfo ### create the M3C2 histogram
gmt grd2xyz cpt="SM13_AUX_bam.cpt"
gmt begin $1'_M3C2_histogram' PNG
    awk '{print $3}' temp.xyz  gmt histogram -R$bounds -F -T$bin_width -W0.25p -BWS -Bxa1f0.2 -C$cpt -Z1
gmt end

rm temp.xyz

echo "done"
```

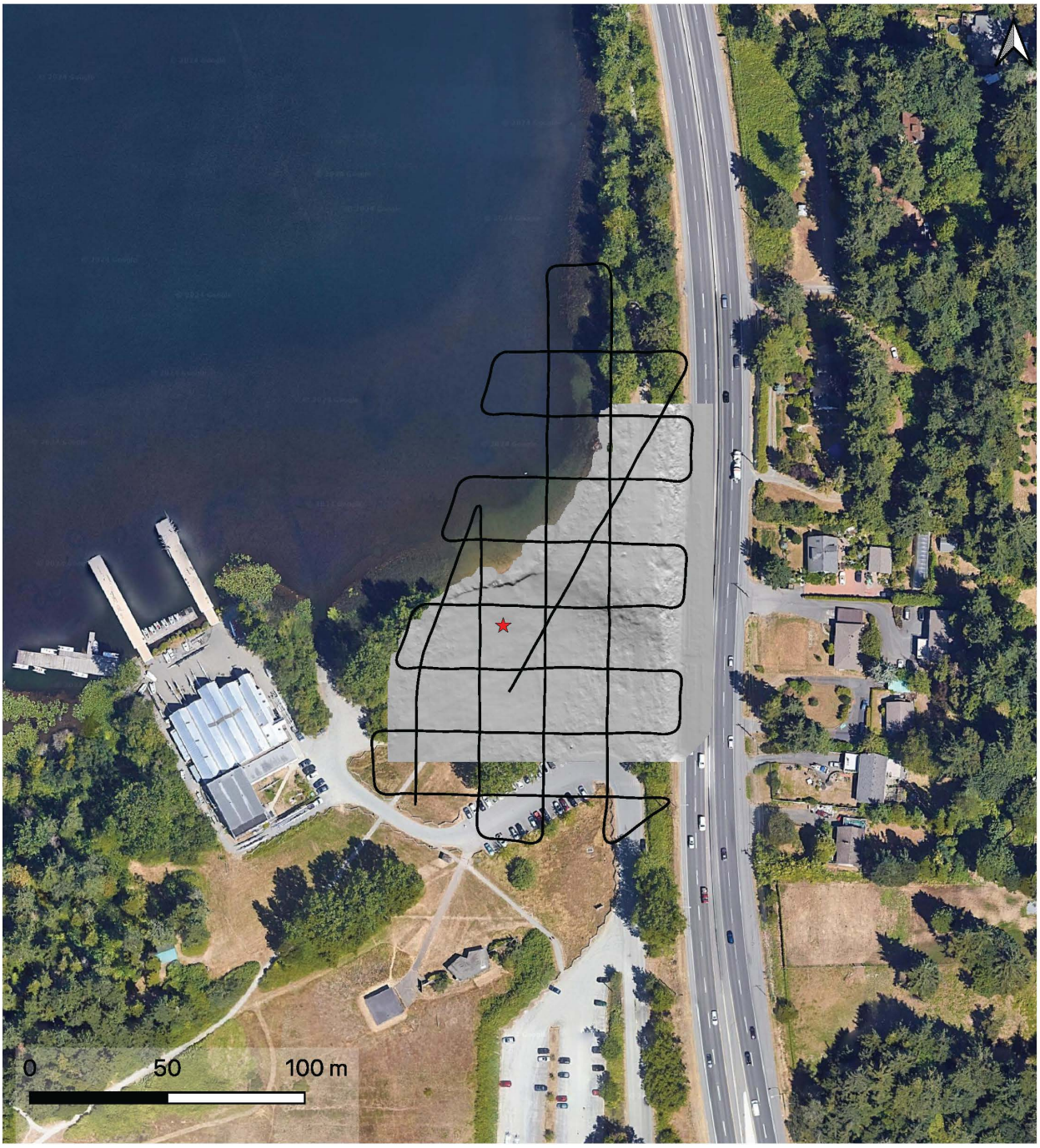

Figure B.1: Flightlines along the XEOLXELEK Elk Lake fault site. Black lines are flight lines superimposed on the resultant DTM. Red star indicates the takeoff and landing location for the collection. Satellite imagery from Google.

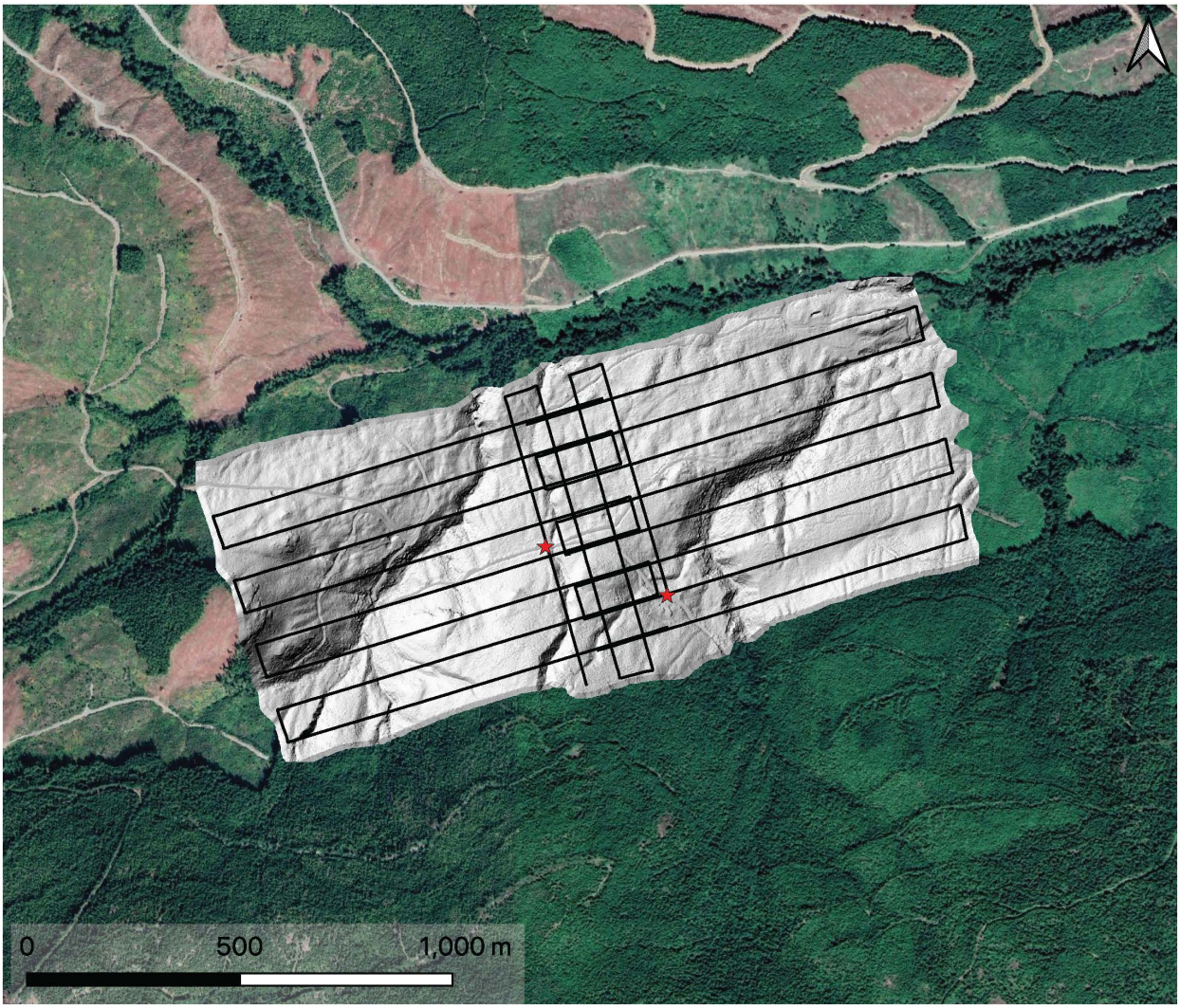

Figure B.2: Flightlines for the easternmost site — San Juan fault. Black lines are flight lines superimposed on the resultant DTM. Red star indicates the takeoff and landing location for the collection. Satellite imagery from Google.

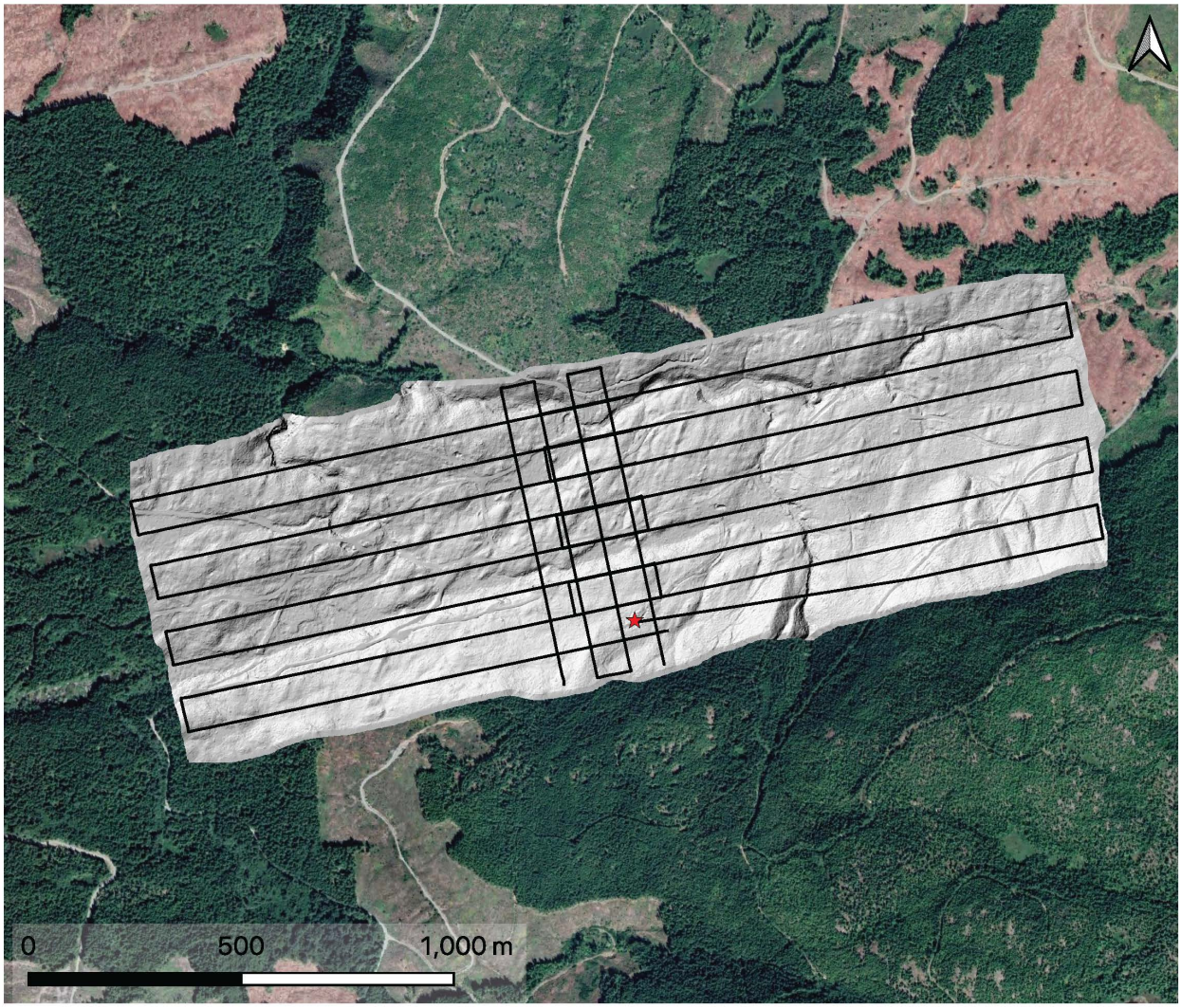

Figure B.3: Flightlines for the westernmost site — San Juan fault. Black lines are flight lines superimposed on the resultant DTM. Red star indicates the takeoff and landing location for the collection. Satellite imagery from Google.

Figure B.4: Flightlines for the Southern Rocky Mountain Trench site. Black lines are flight lines superimposed on the resultant DTM. Red star indicates the takeoff and landing location for the collection. Satellite imagery from Google.

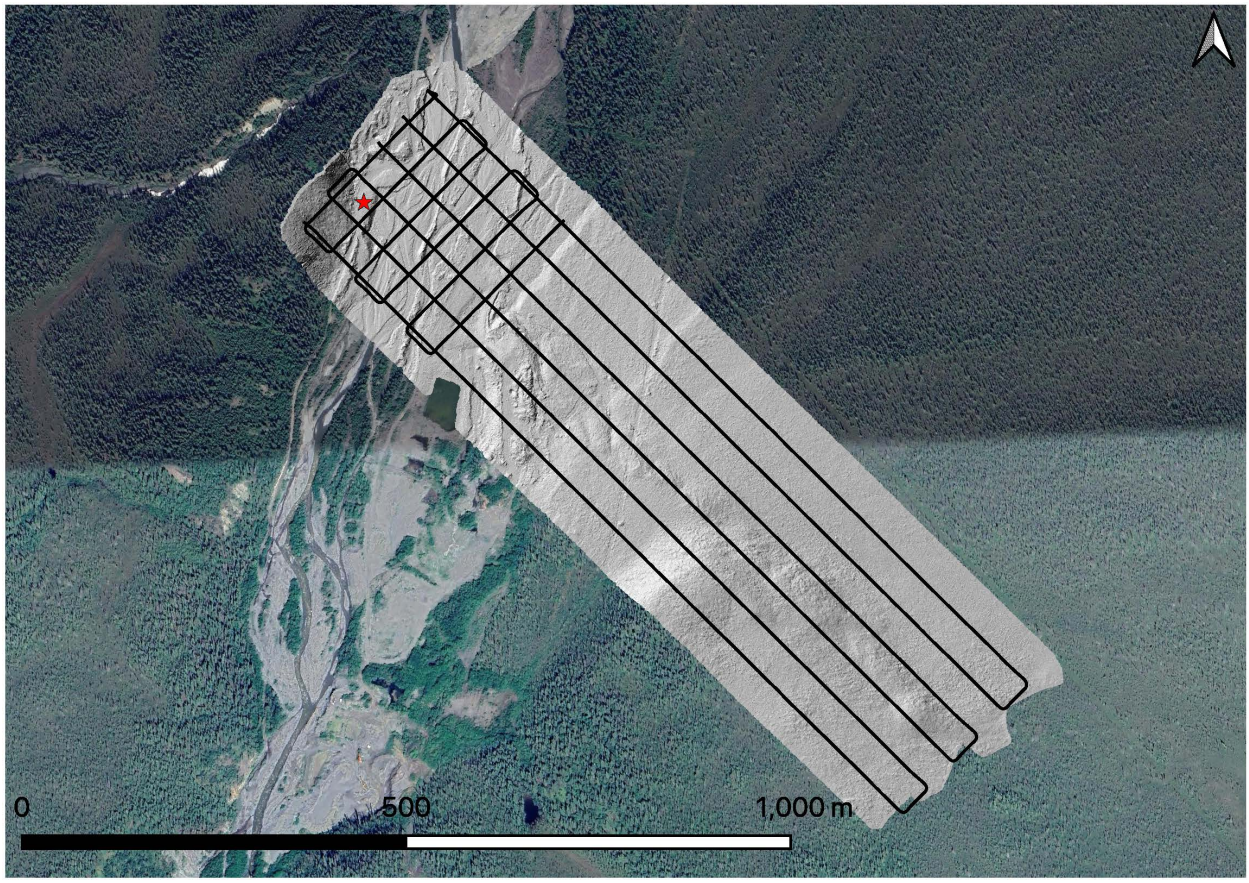

Figure B.5: Flightlines for the Burwash Creek site — Eastern Denali fault. Black lines are flight lines superimposed on the resultant DTM. Red star indicates the takeoff and landing location for the collection. Satellite imagery from Google.

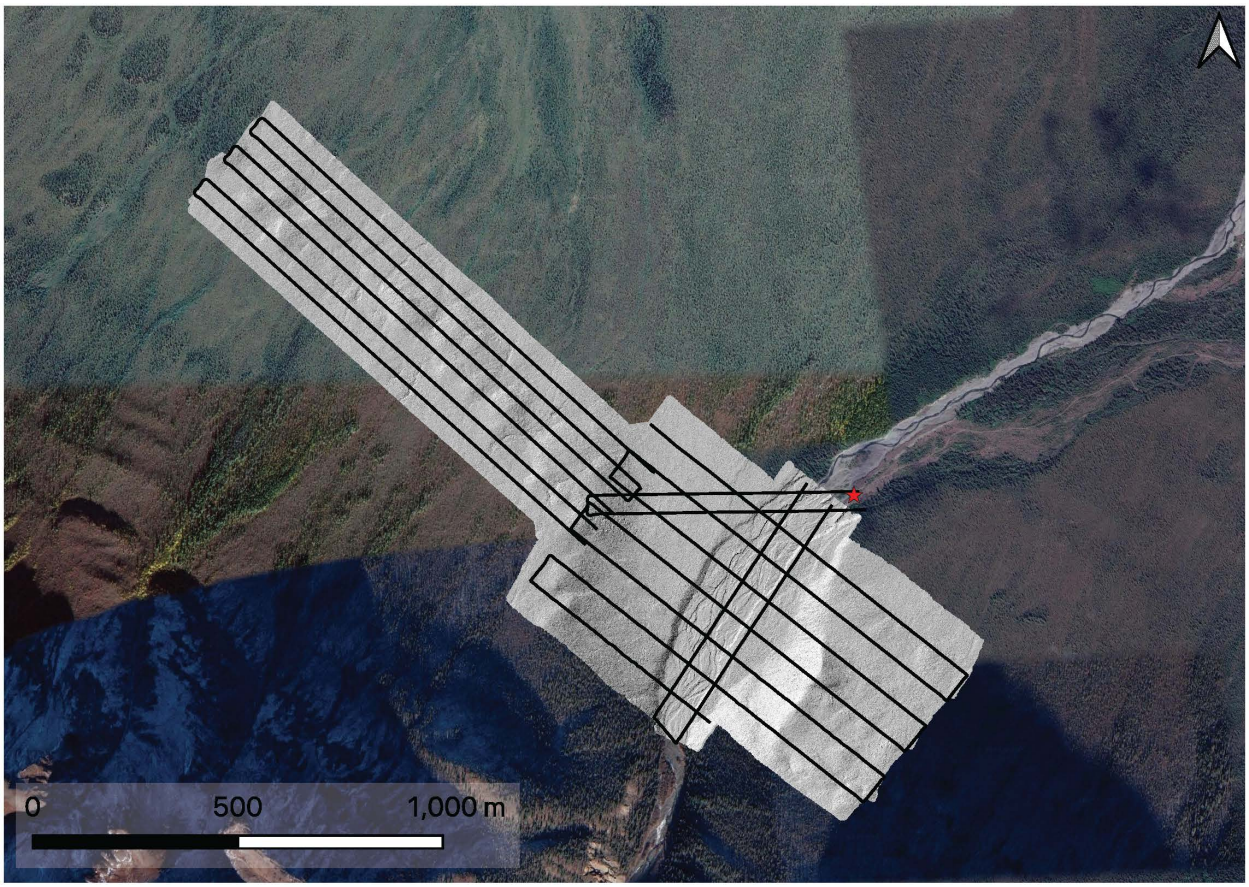

Figure B.6: Flightlines for the Copper Joe Creek site — Eastern Denali fault. Black lines are flight lines superimposed on the resultant DTM. Red star indicates the takeoff and landing location for the collection. Satellite imagery from Google.

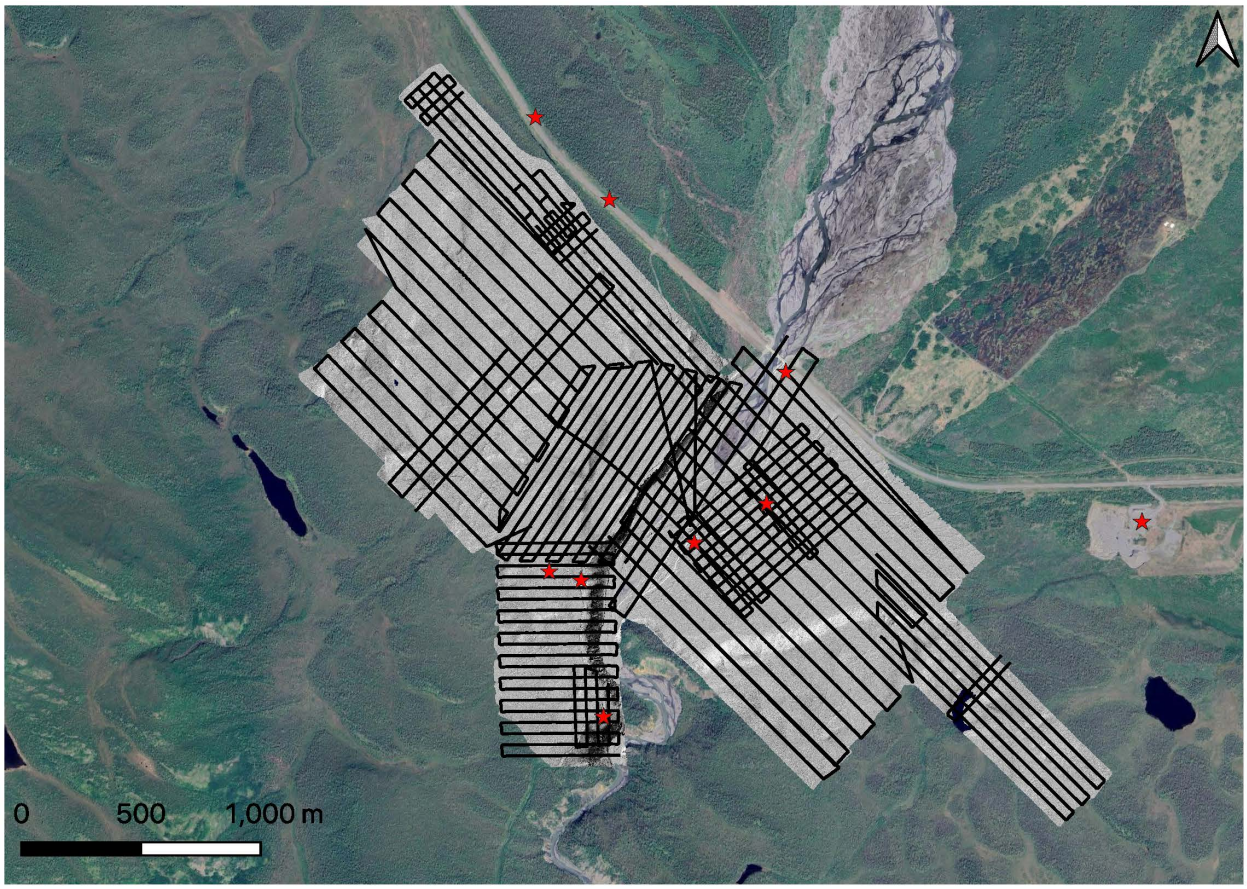

Figure B.7: Flightlines for the Duke River site — Eastern Denali fault. Black lines are flight lines superimposed on the resultant DTM. Red star indicates the takeoff and landing location for the collection. Satellite imagery from Google.

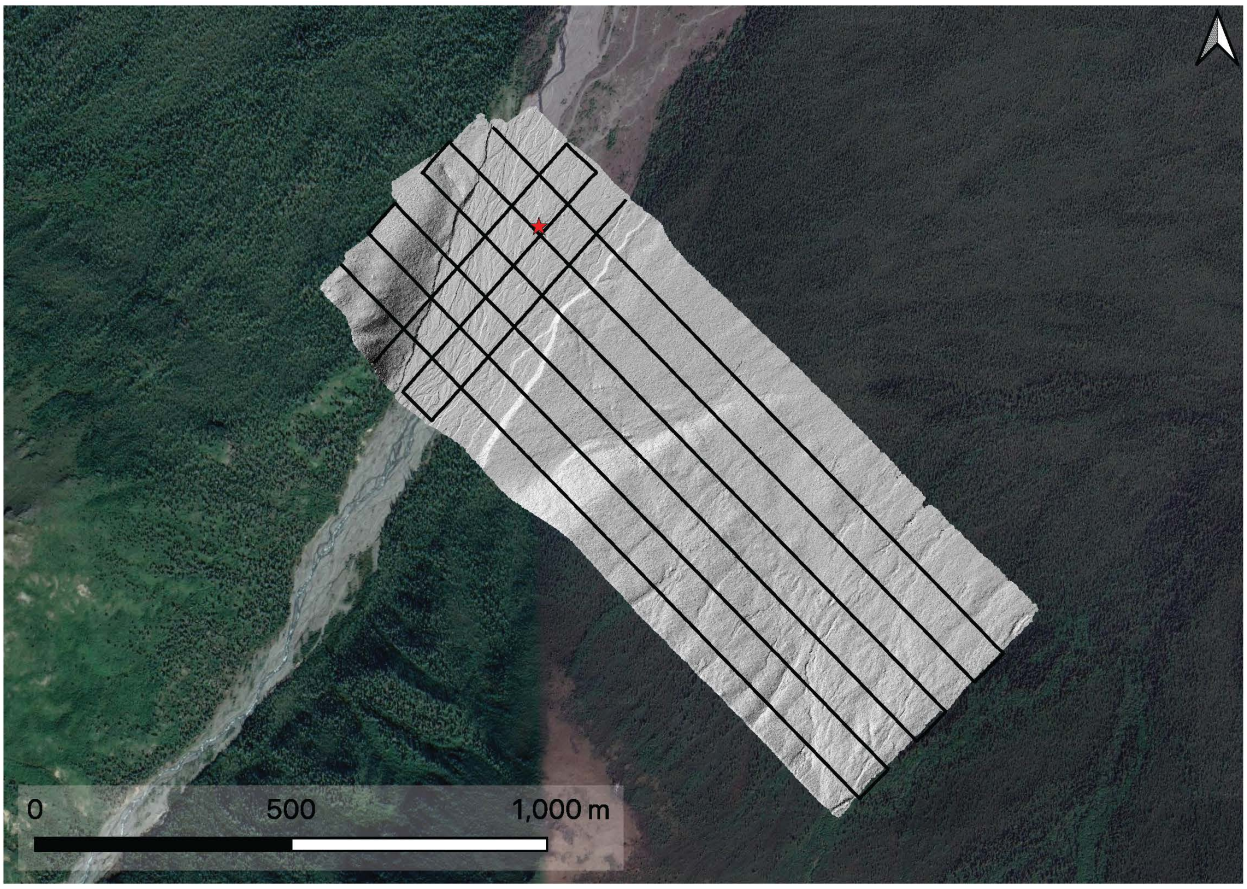

Figure B.8: Flightlines for the Nines Creek site — Eastern Denali fault. Black lines are flight lines superimposed on the resultant DTM. Red star indicates the takeoff and landing location for the collection. Satellite imagery from Google.

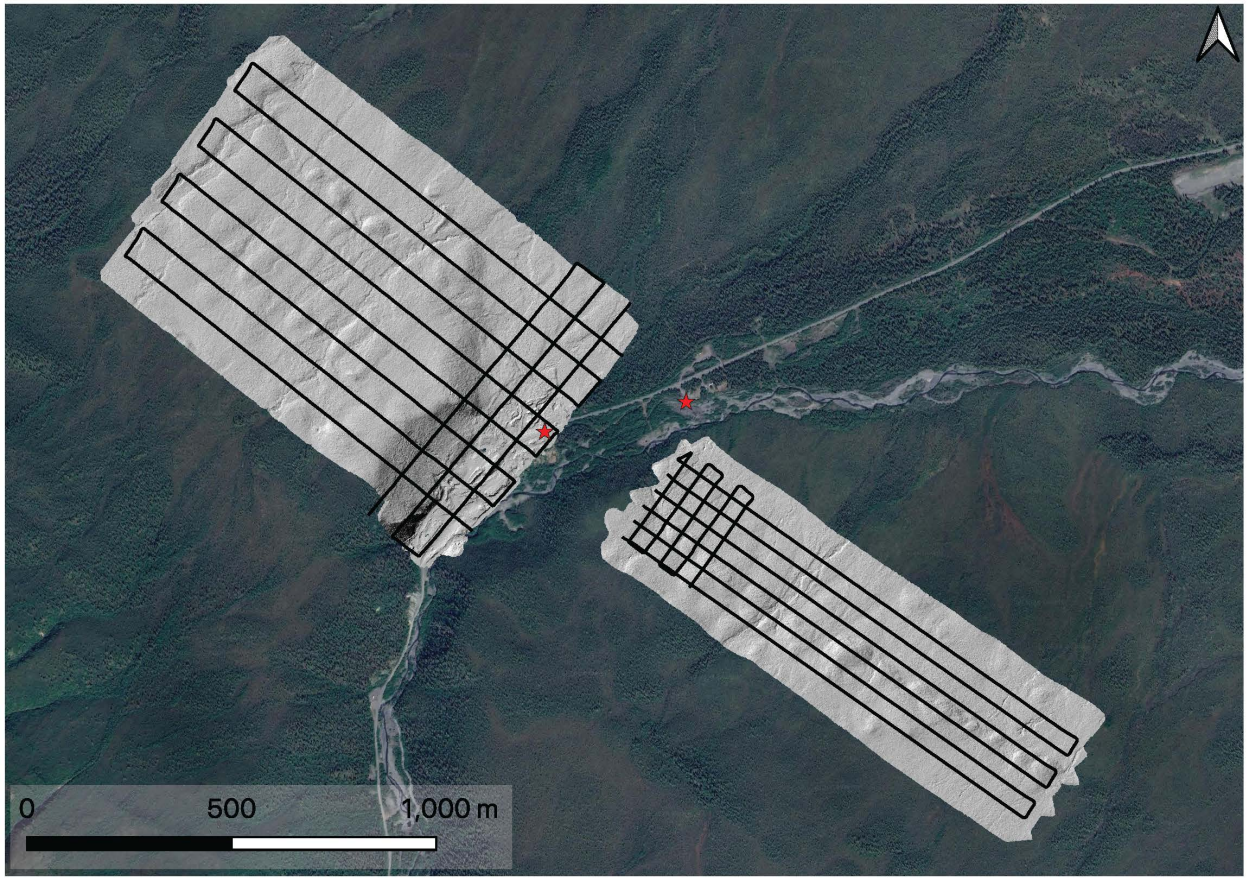

Figure B.9: Flightlines for the Quill Creek site — Eastern Denali fault. Black lines are flight lines superimposed on the resultant DTM. Red star indicates the takeoff and landing location for the collection. Satellite imagery from Google.

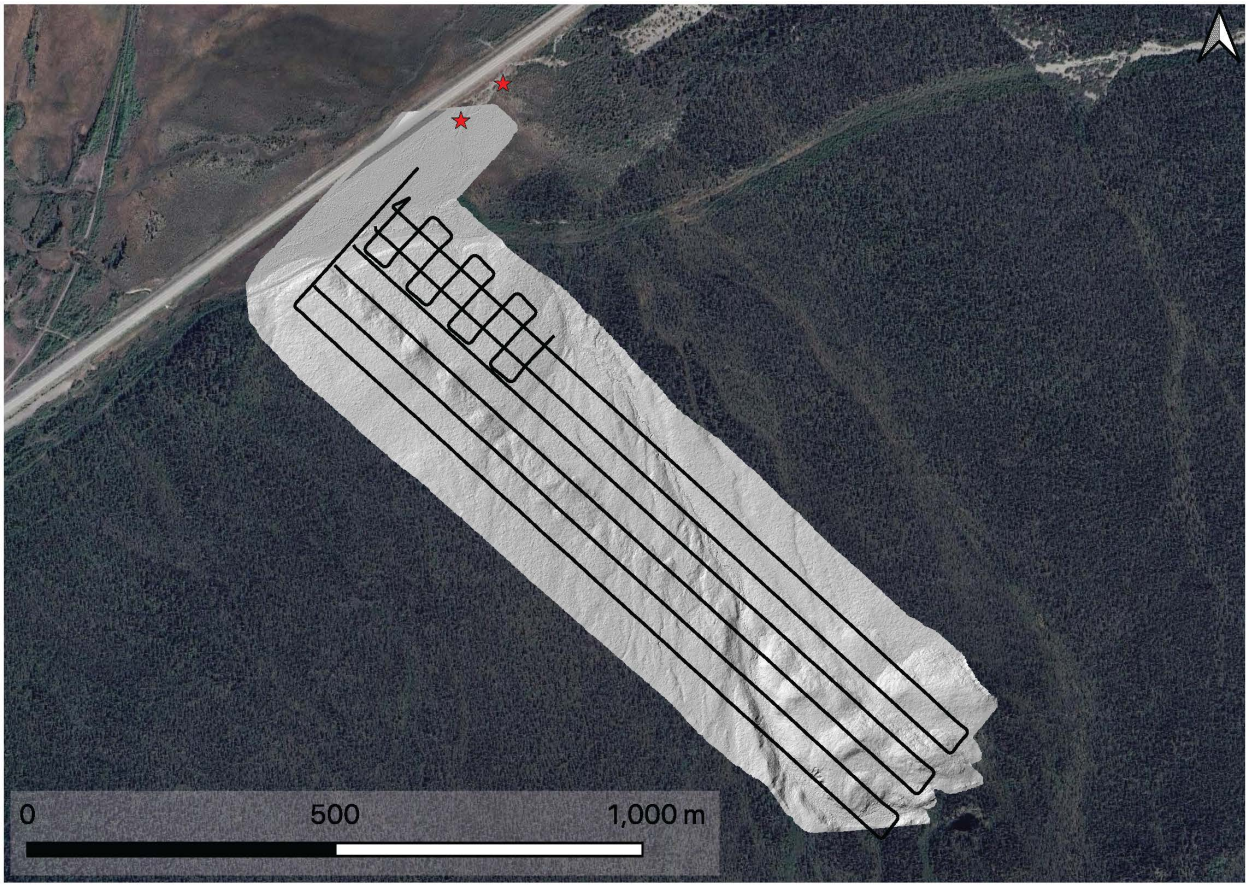

Figure B.10: Flightlines for the Slims River site — Eastern Denali fault. Black lines are flight lines superimposed on the resultant DTM. Red star indicates the takeoff and landing location for the collection. Satellite imagery from Google.

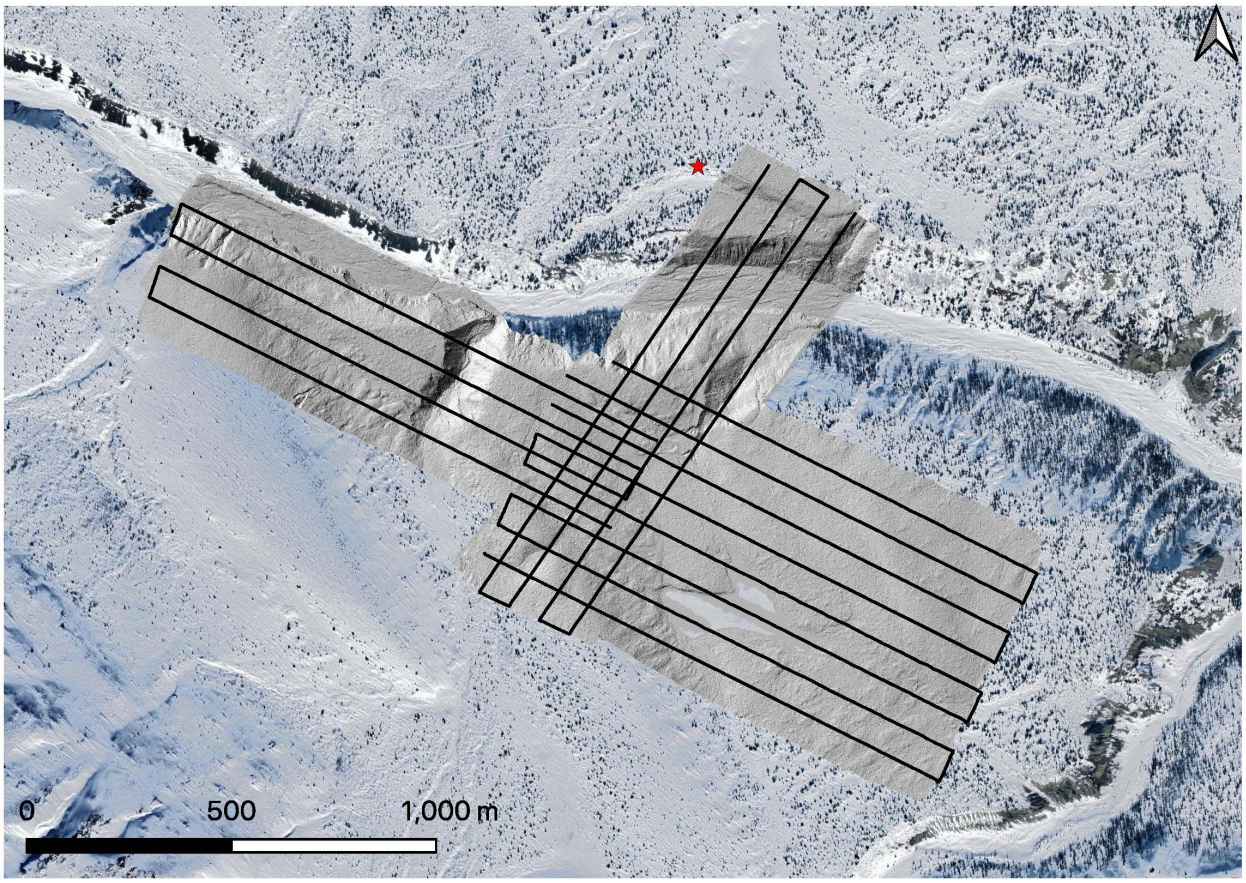

Figure B.11: Flightlines for the Telluride Creek — Eastern Denali fault. Black lines are flight lines superimposed on the resultant DTM. Red star indicates the takeoff and landing location for the collection. Satellite imagery from Google.

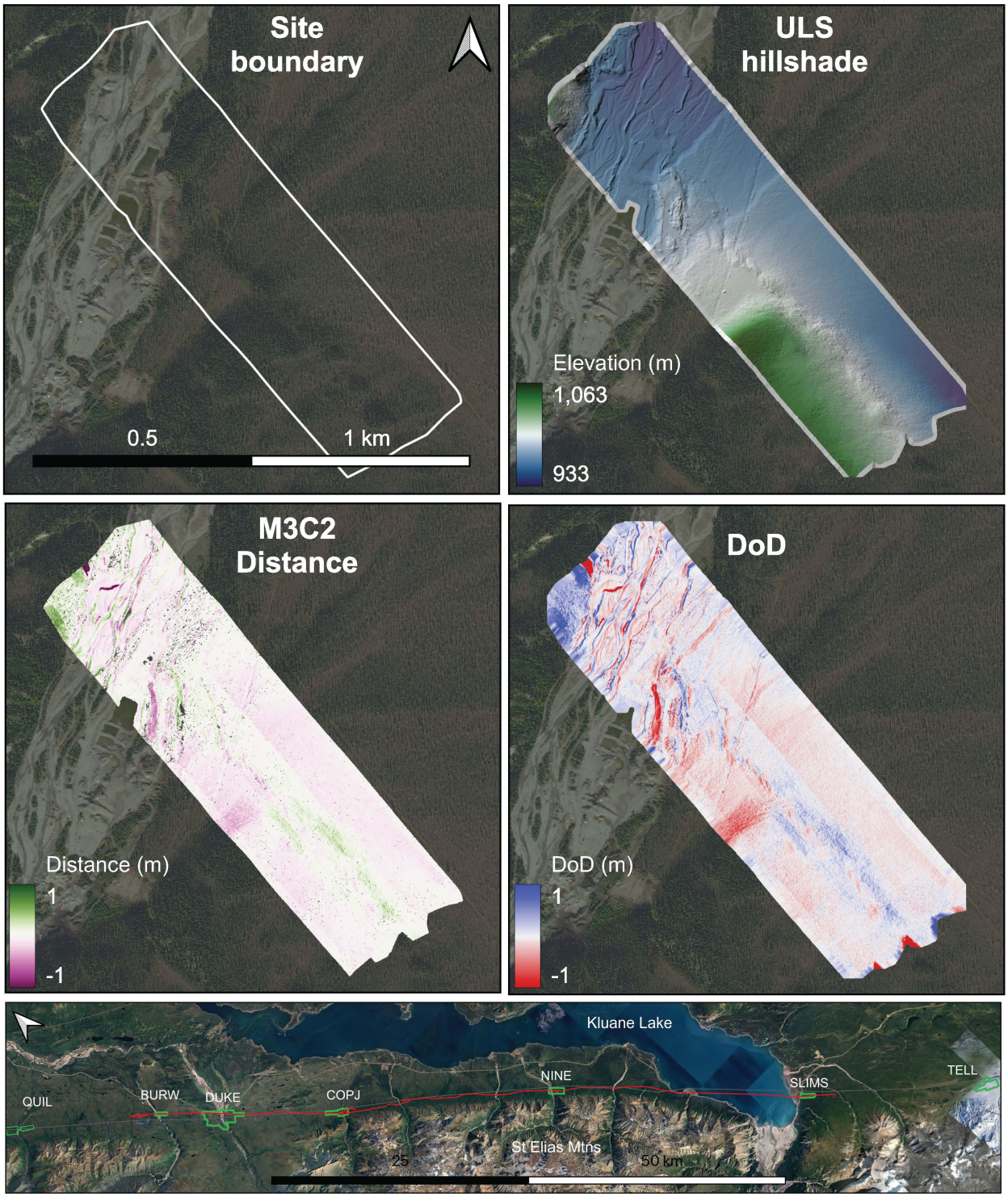

Figure B.12: Comparison visualization for the Burwash Creek site — Eastern Denali fault. See bottom panel for site location. There is a small placer mining operation in the creek bed. Comparison results are available in Table 3.3. Satellite imagery from Bing and Google.

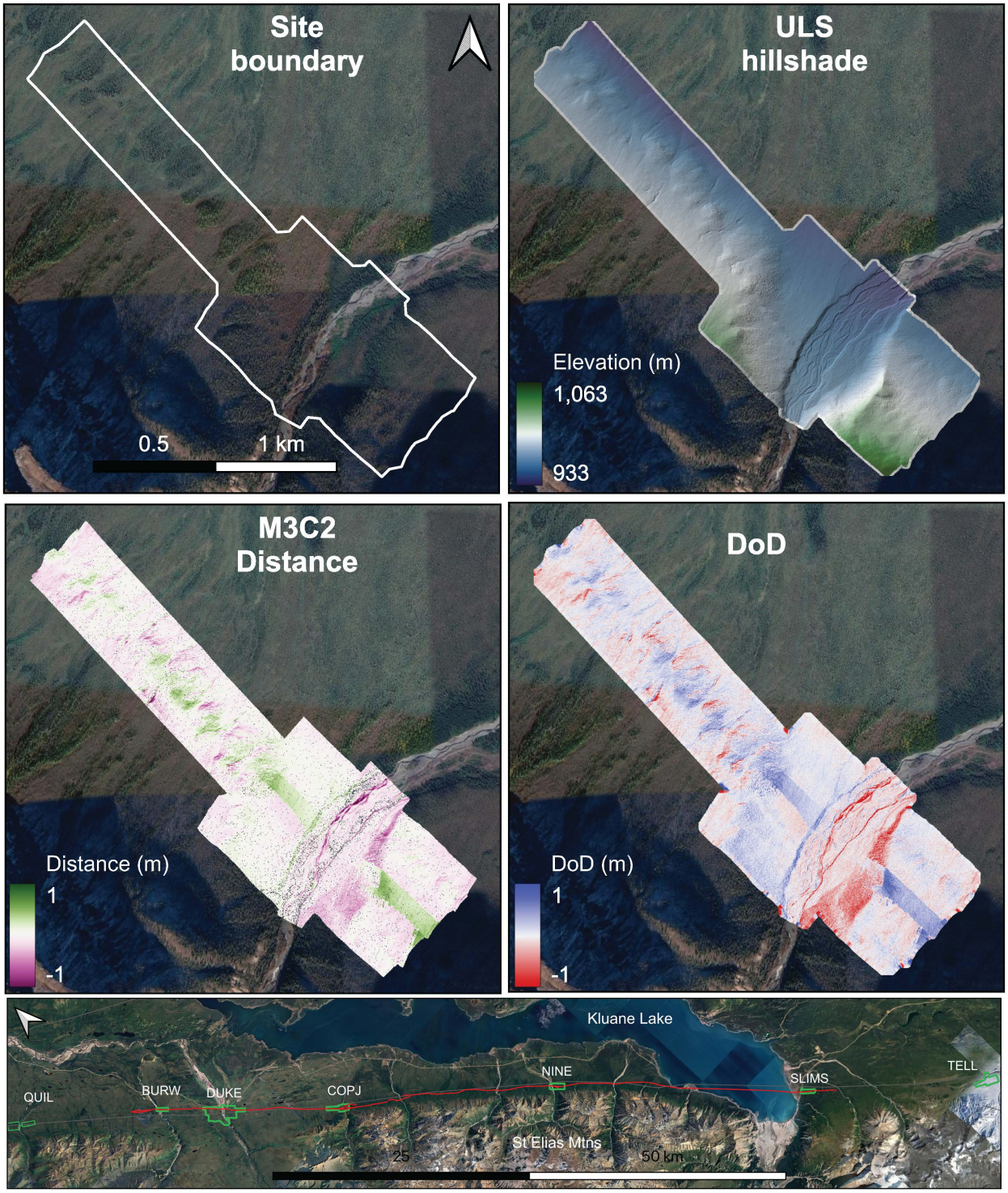

Figure B.13: Comparison visualization for the Copper Joe Creek site — Eastern Denali fault. See bottom panel for site location. Comparison results are available in Table 3.3. Satellite imagery from Bing and Google.

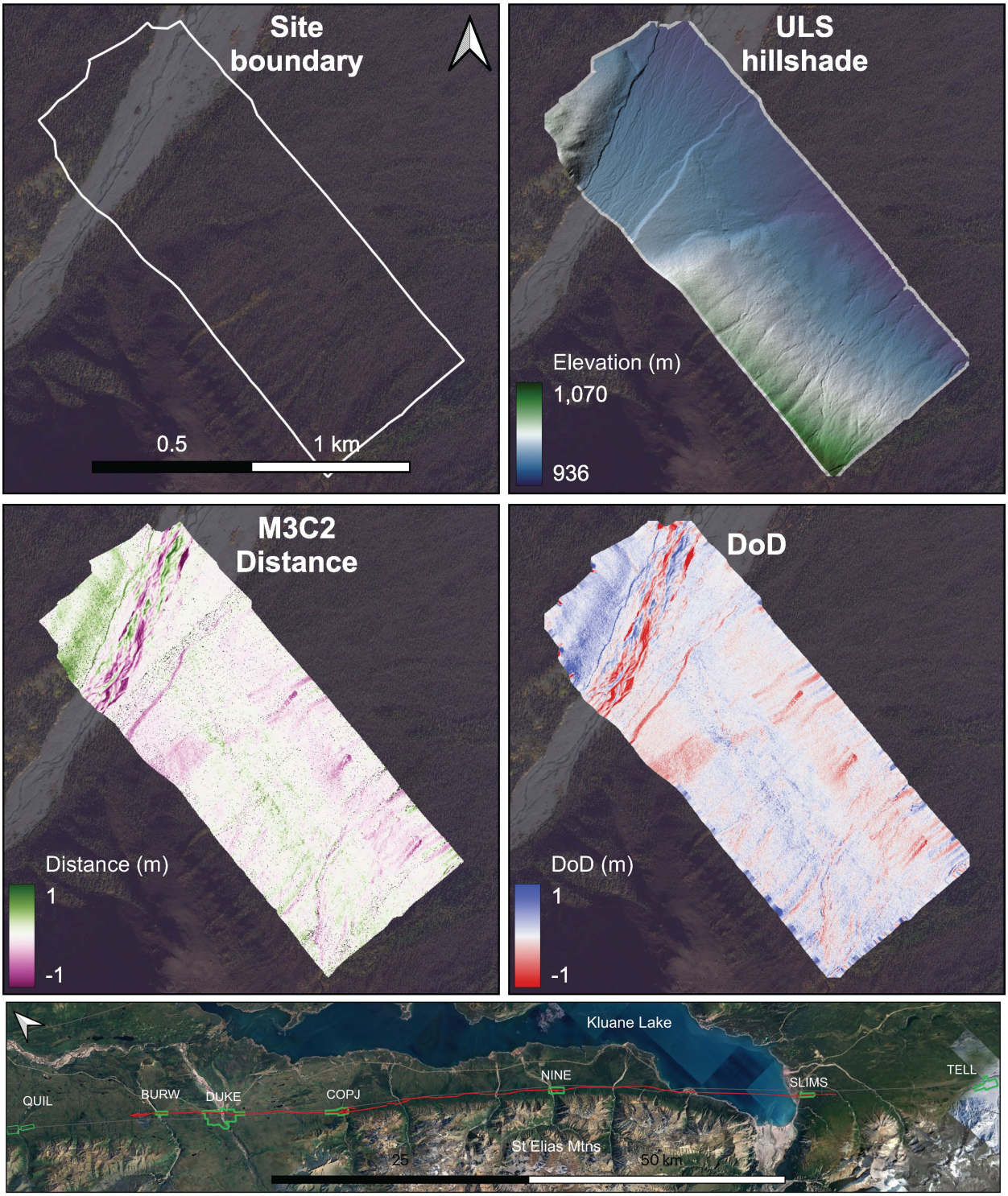

Figure B.14: Comparison visualization for the Nines Creek site — Eastern Denali fault. See bottom panel for site location. Comparison results are available in Table 3.3. Satellite imagery from Bing and Google.

Appendix C
Supplemental Material for Chapter 4

This appendix is composed of 19 figures (Figures C1–C19), and 9 Data files. The figures show cross sections from the vertical separation measurements, hillshaded plots of the drone lidar collections, photographs from the Schmidt hammer data collection, and photos from the ERT profile set-up. The data files include; a shapefile of the mapped lineaments, digital terrain models (DTMs) for the drone lidar sites, ERT measurement files, and terrain files (for the ERT profiles). The data files are available in a Zenodo repository (https://doi.org/10.5281/zenodo.15103481).

List of Data Files

1. Shape file for San Juan Fault (SanJuanFaultTrace.shp)
2. DTM for UPSCARP drone lidar (UPSCARP_dtm_drone.tif)
3. DTM for SLIDE drone lidar (SLIDE_dtm_drone.tif)
4. DTM for GSS drone lidar (GSS_dtm_drone.tif)
5. DTM for EAST drone lidar (EAST_dtm_drone.tif)
6. Data File S1: Resistivity measurements for 3 m spaced line (3m_SJF_merged_2024.stg)
7. Data File S2: Terrain file for 3 m spaced line (Terrain_3m_SJF_merged_2024.trn)
8. Data File S3: Resistivity measurements for 1.5 m spaced line (1.5m_SJF_July22_2024.stg)
9. Data File S4: Terrain file for 1.5 m spaced line (Terrain_1.5m_SJF_July22_2024.trn)

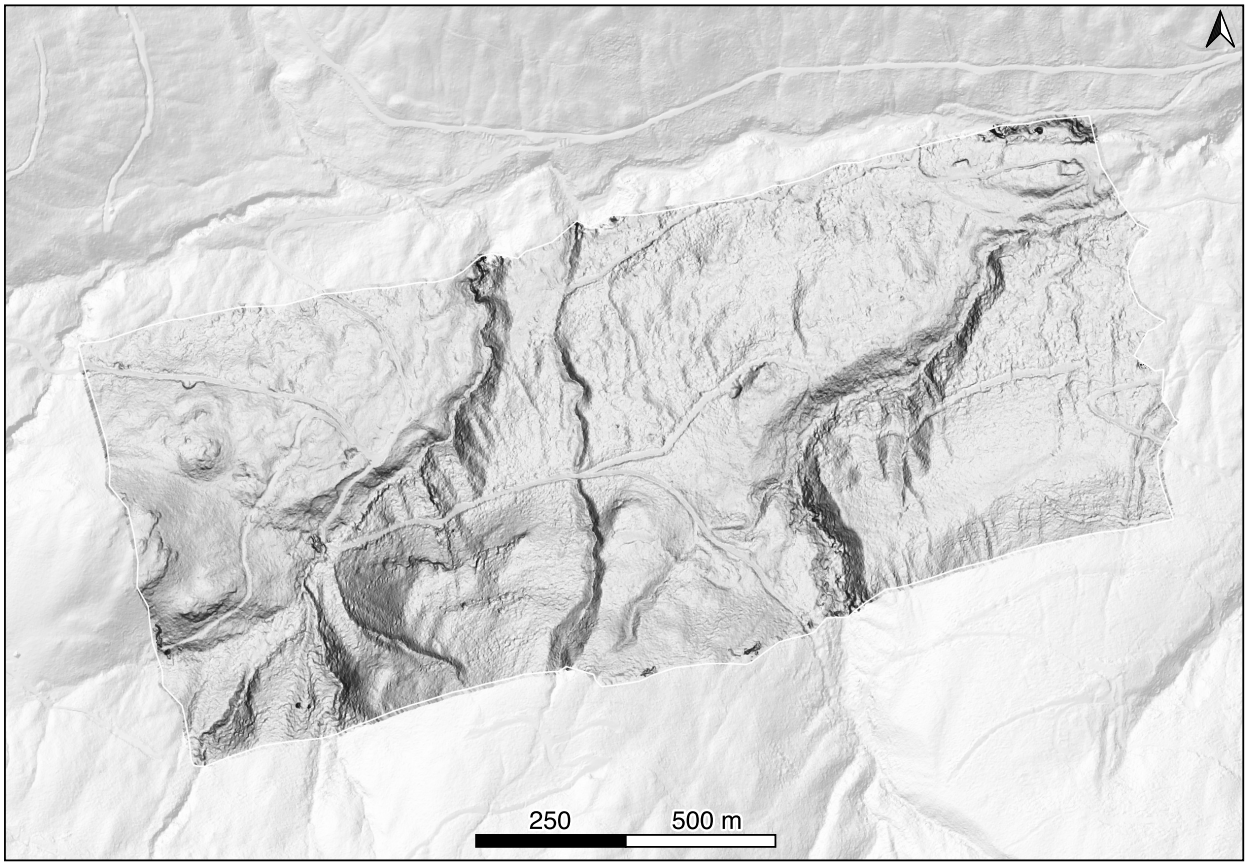

Figure C.1: Drone lidar hillshade for the EAST site

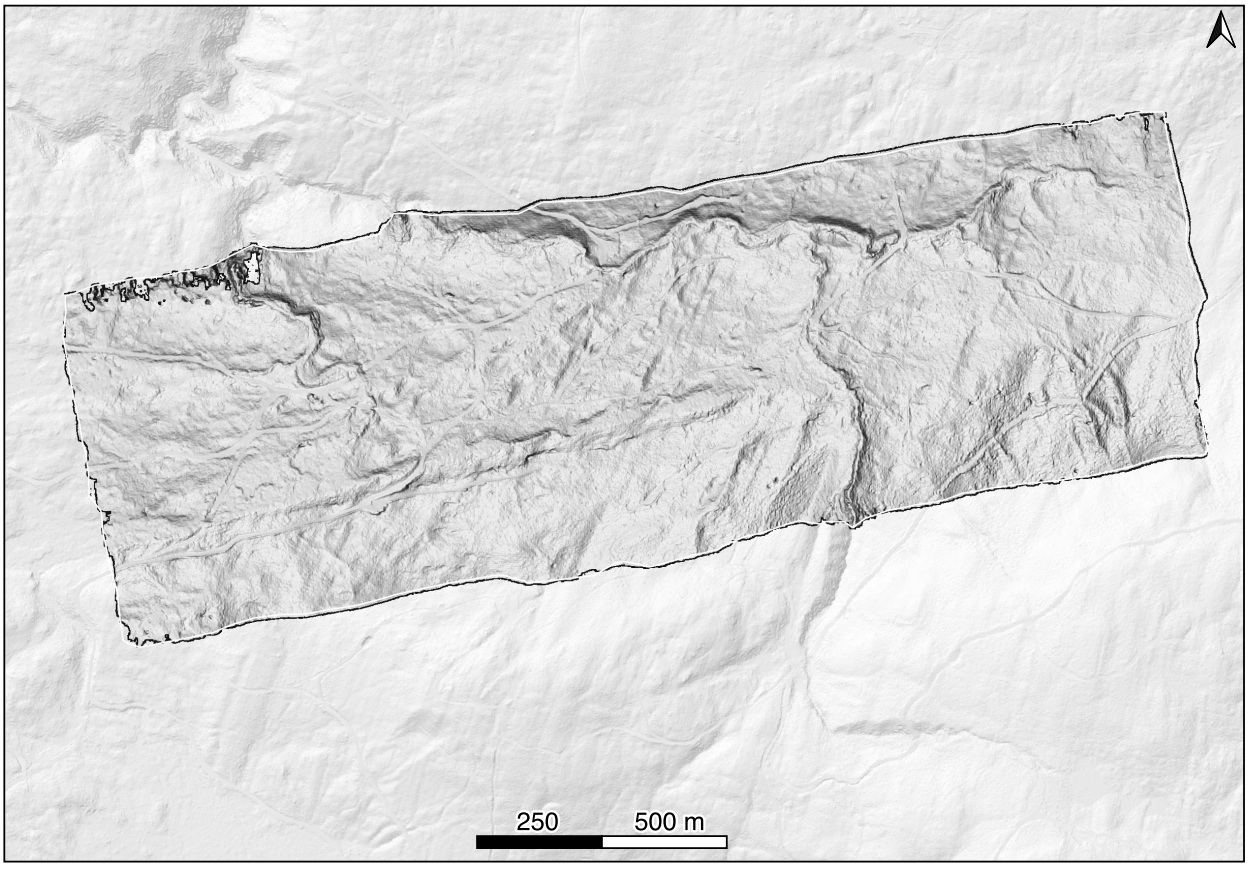

Figure C.2: Drone lidar hillshade for the GSS site

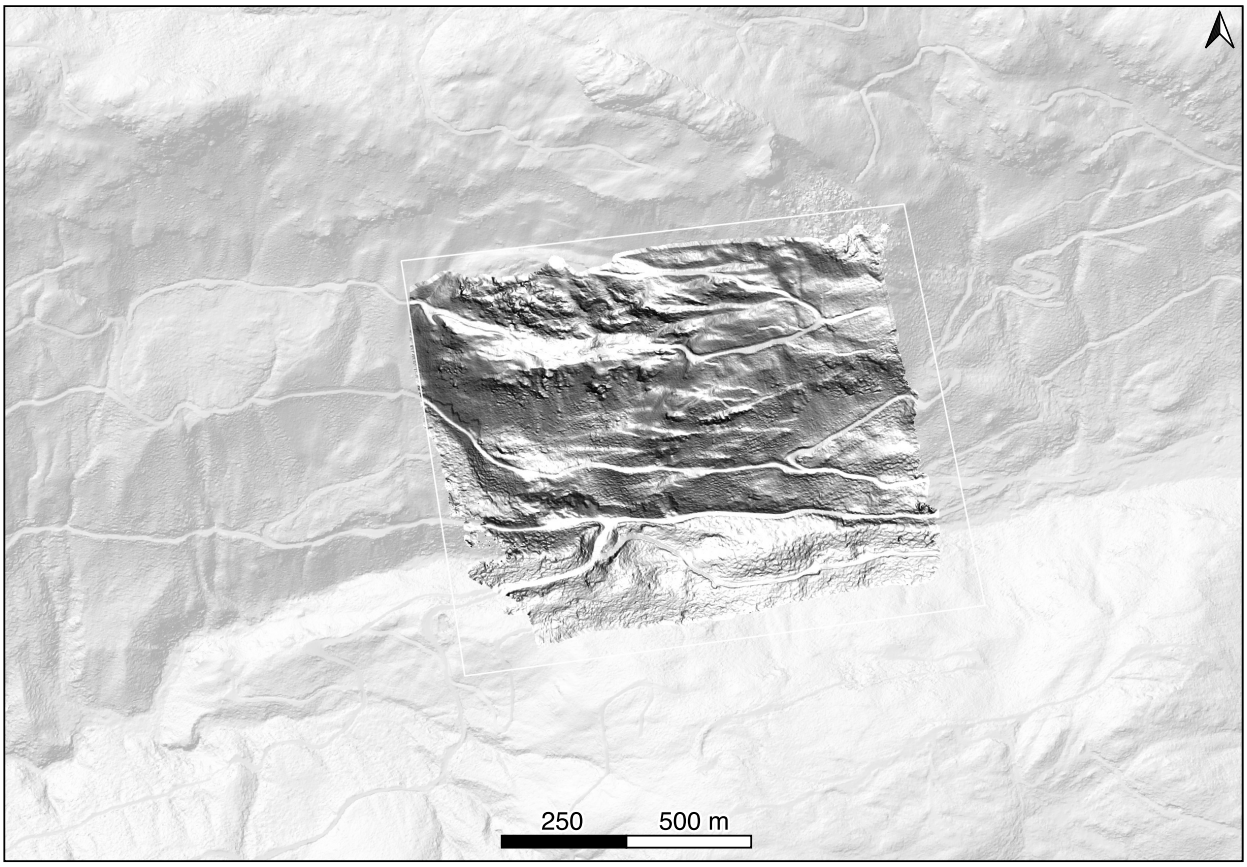

Figure C.3: Drone lidar hillshade for the SLIDE site

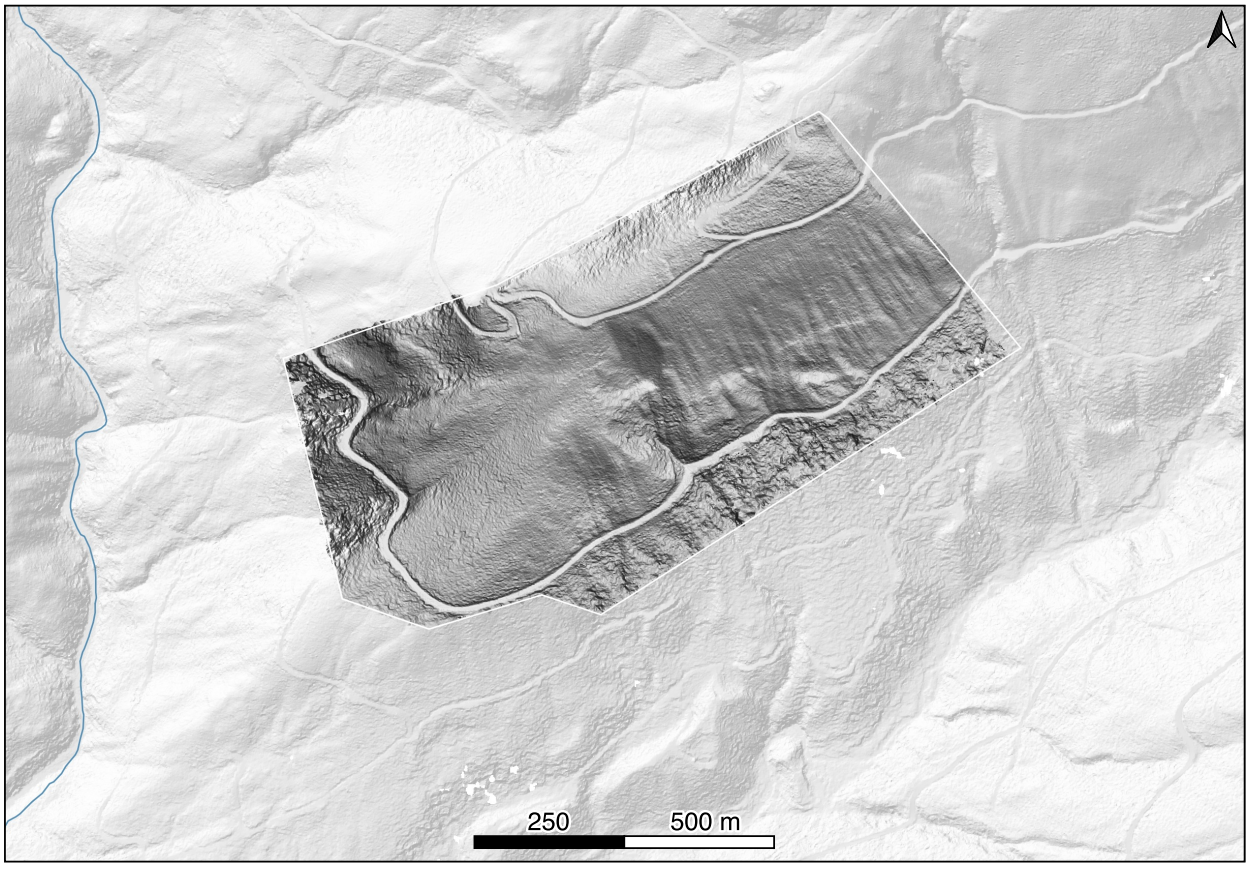

Figure C.4: Drone lidar hillshade for the UPSCARP site

Figure C.5: Photographs from the ERT data collection. a) View up the steep slope, top two figures are on the uphill facing scarp. Note that conditions were dry and dusty. b) View to the East, the fault should run through the valley in the distance. c) Luckily the slope was not densely vegetated — the area was clear cut in the last 5–6 years. d) AGI MiniSting R1 resistivity meter.

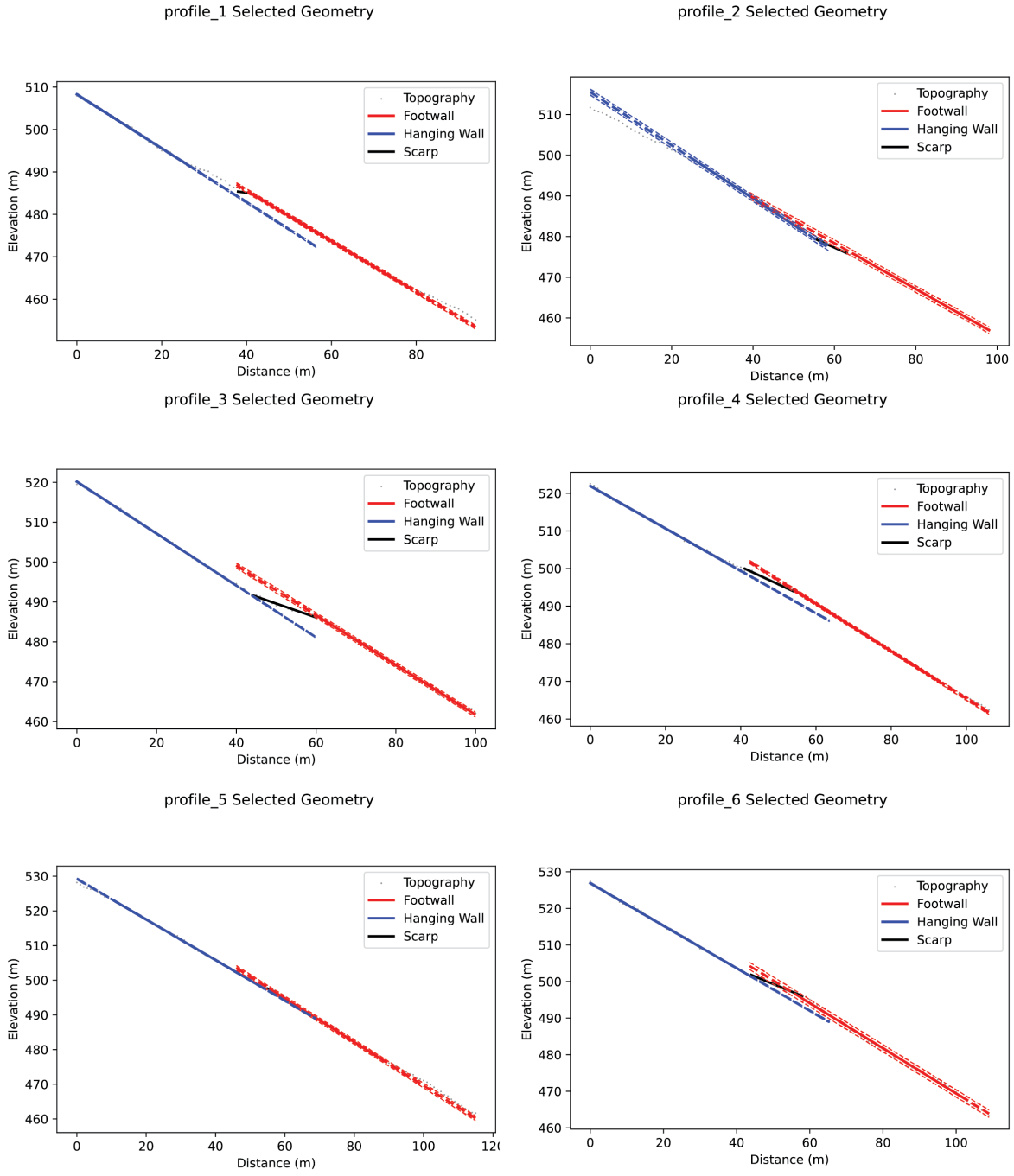

Figure C.6: Cross sections for profiles 1–6 from the uphill facing scarp (UPSCARP). Short dashed lines show 95% error in linear regression fit.

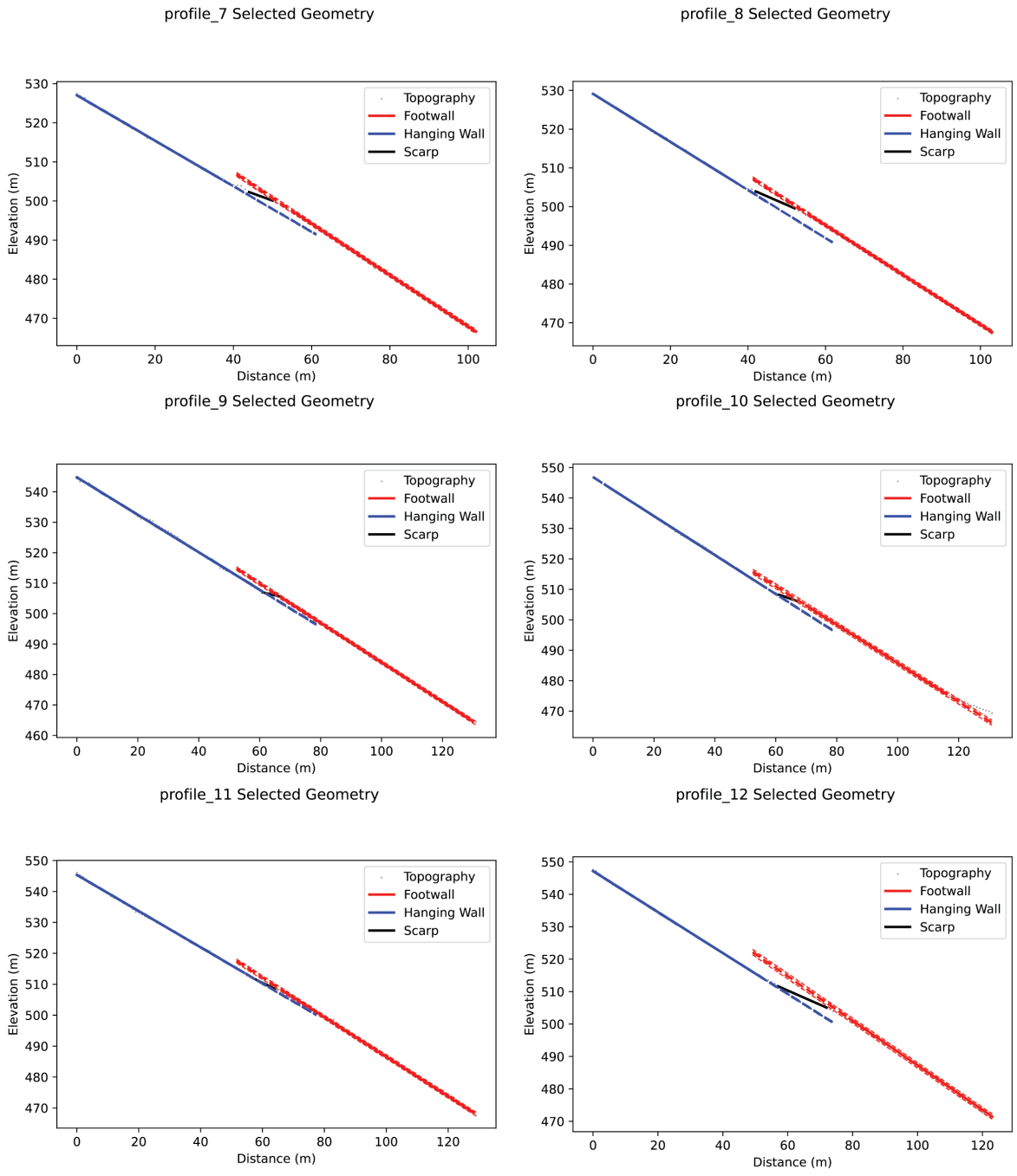

Figure C.7: Cross sections for profiles 7–12 from the uphill facing scarp (UPSCARP). Short dashed lines show 95% error in linear regression fit.

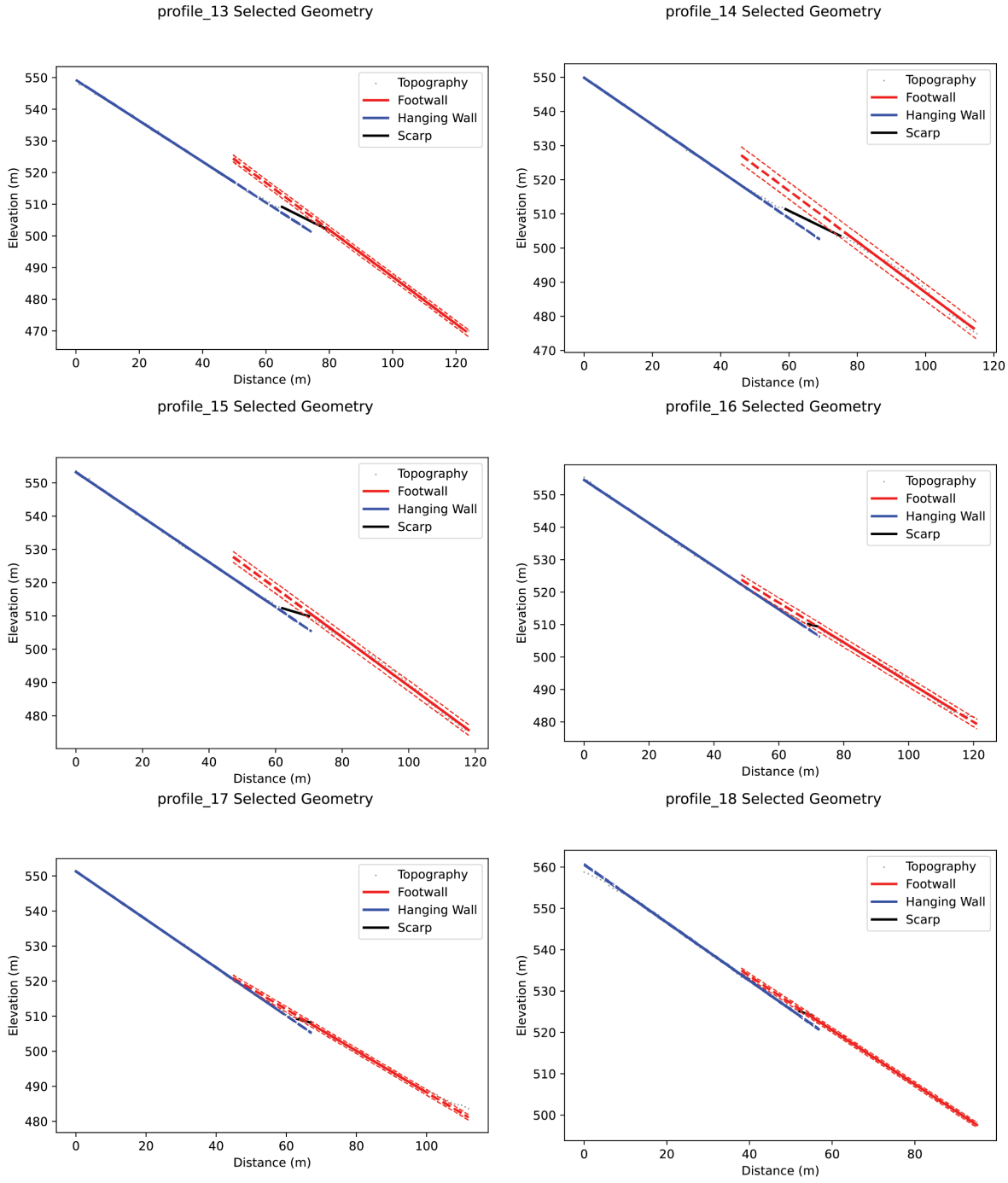

Figure C.8: Cross sections for profiles 13–18 from the uphill facing scarp (UPSCARP). Short dashed lines show 95% error in linear regression fit.

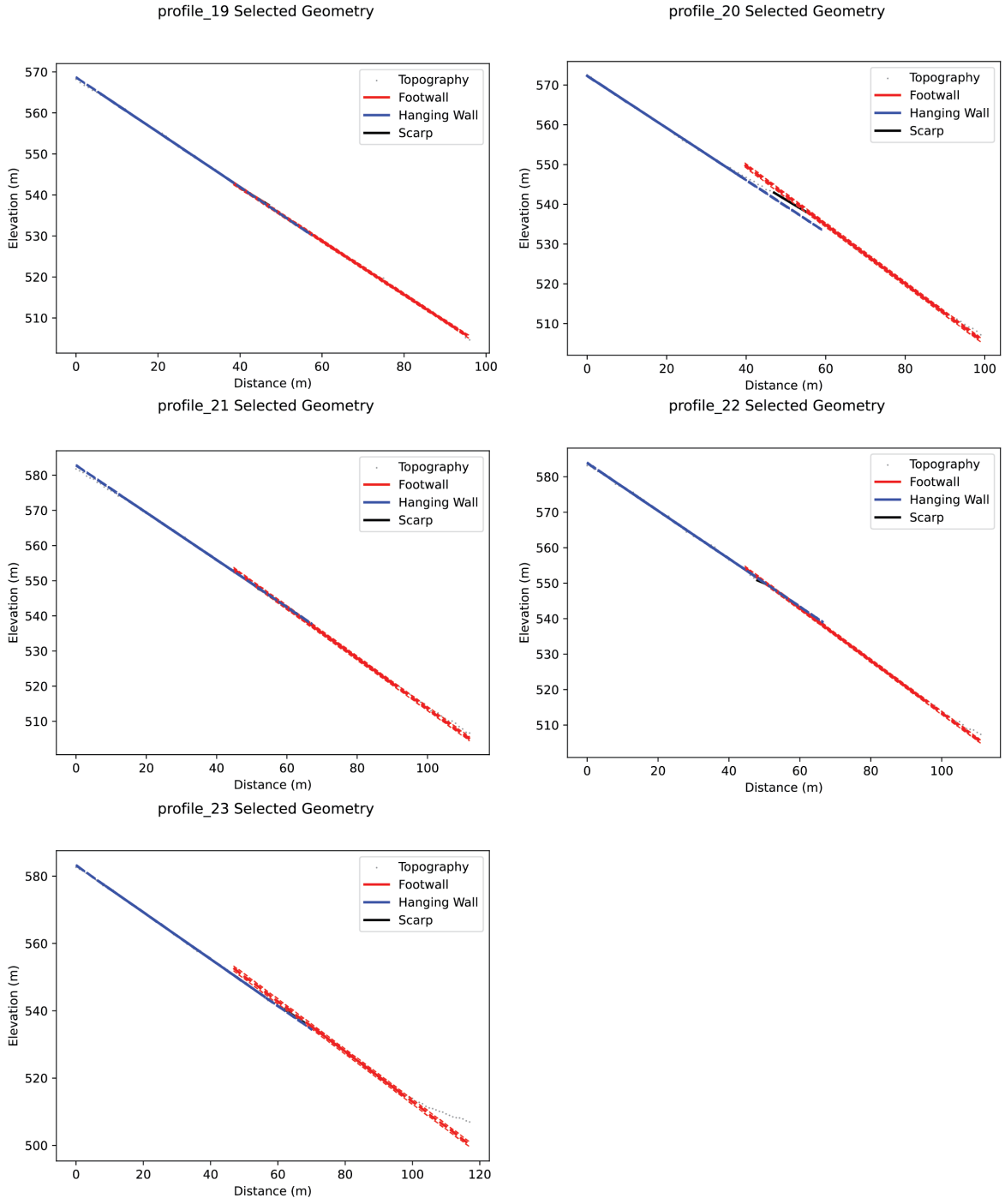

Figure C.9: Cross sections for profiles 19–23 from the the uphill facing scarp (UPSCARP). Short dashed lines show 95% error in linear regression fit.

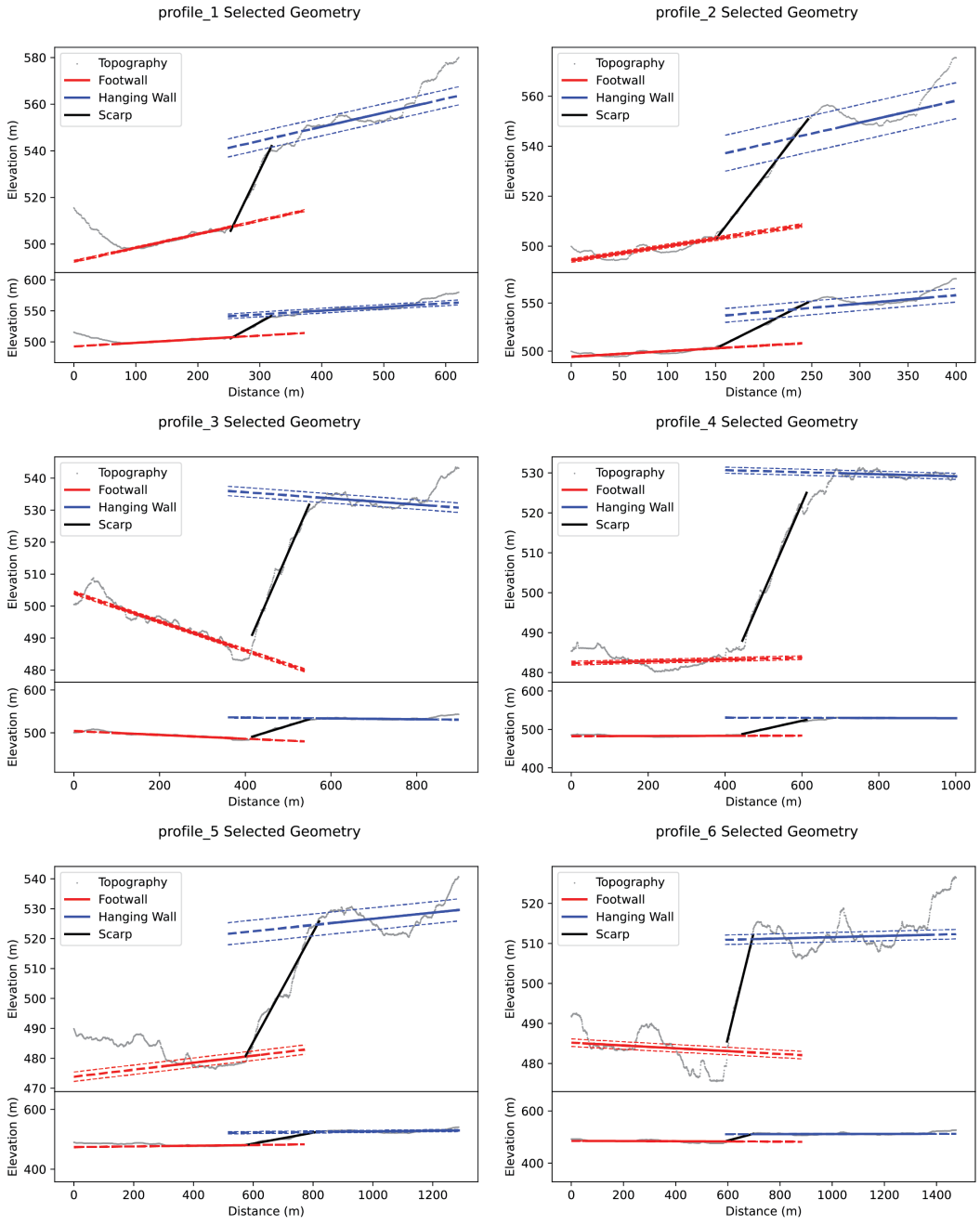

Figure C.10: Cross sections for profiles 1–6 from the glacially scoured surface (GSS). Top panel is vertically exaggerated, panel below has no exaggeration. Short dashed lines show 95% error in linear regression fit.

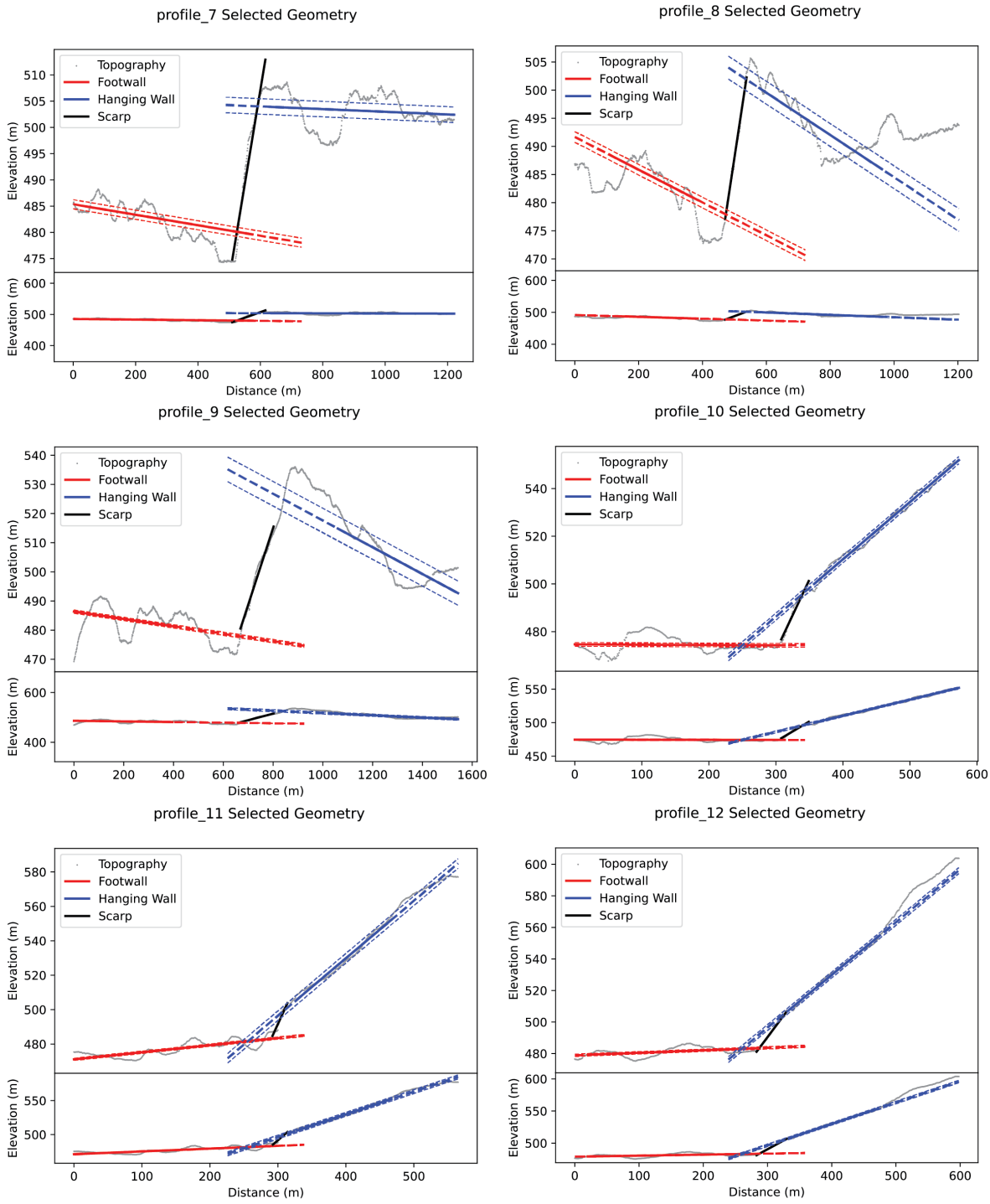

Figure C.11: Cross sections for profiles 7–12 from the glacially scoured surface (GSS). Top panel is vertically exaggerated, panel below has no exaggeration. Short dashed lines show 95% error in linear regression fit.

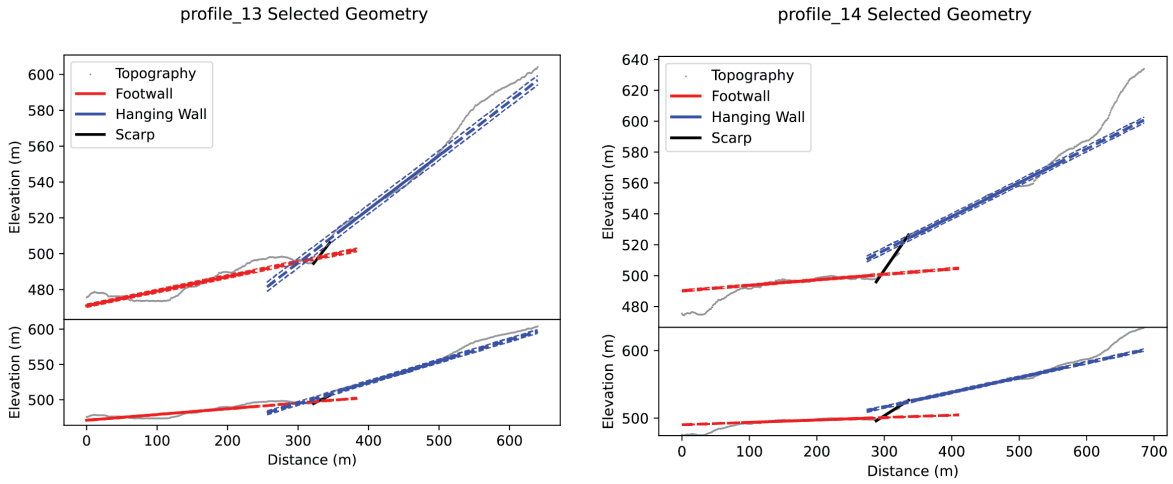

Figure C.12: Cross sections for profiles 13–14 from the glacially scoured surface (GSS). Top panel is vertically exaggerated, panel below has no exaggeration. Short dashed lines show 95% error in linear regression fit.

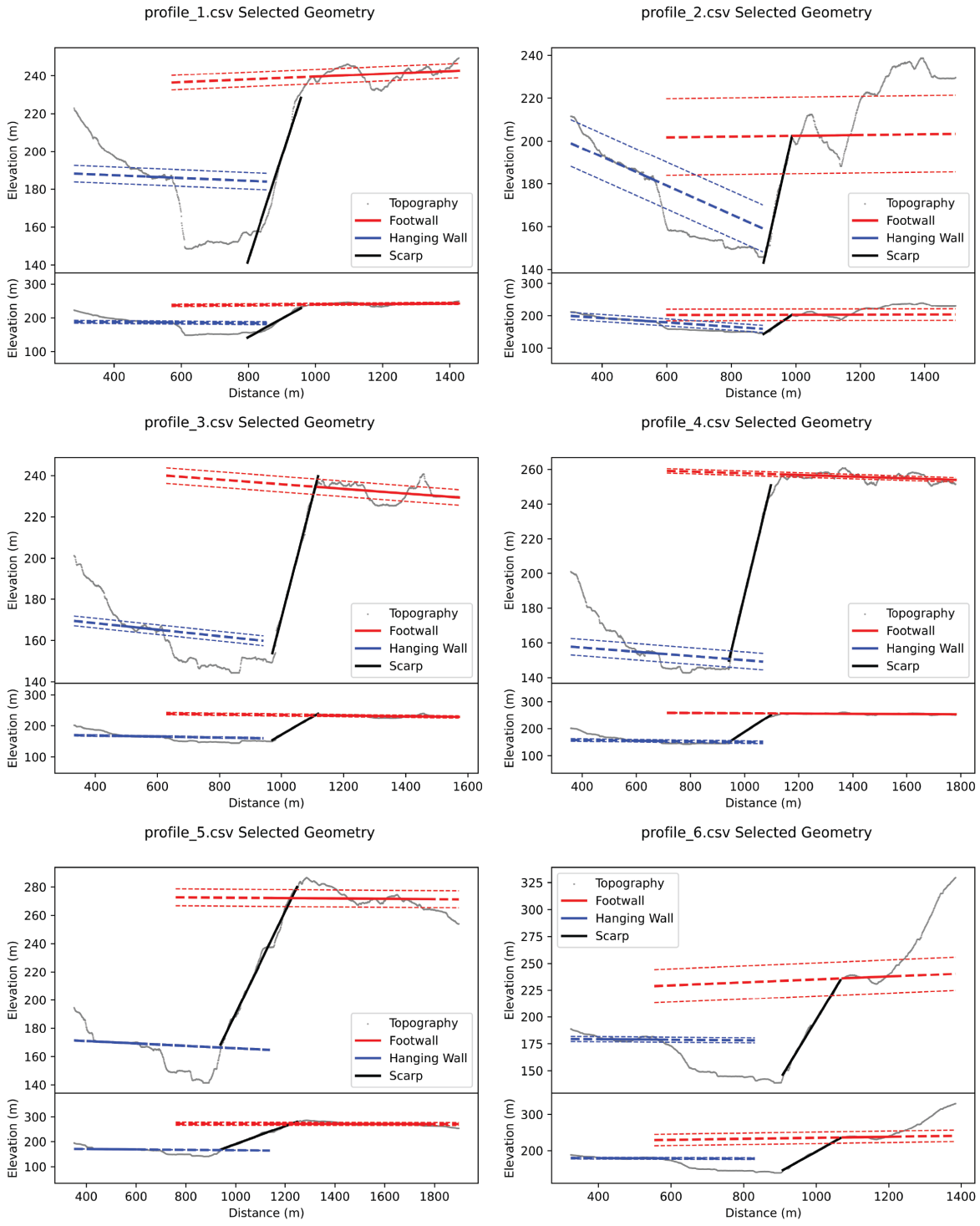

Figure C.13: Surface offset profiles 1–6 from Figure 4.4. Numbering begins in the West and increases eastwards. Top panel is vertically exaggerated, panel below has no exaggeration. Short dashed lines show 95% error in linear regression fit.

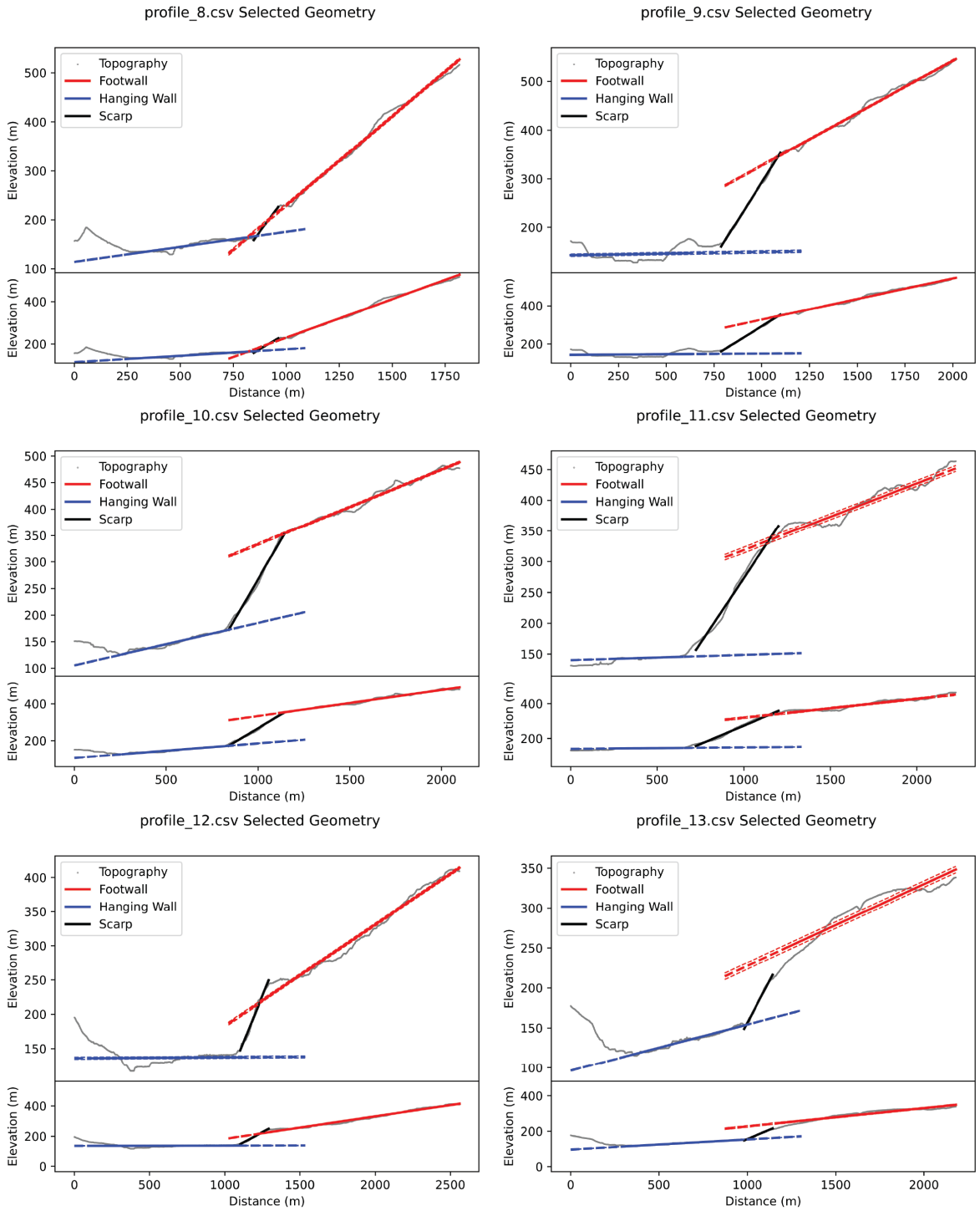

Figure C.14: Surface offset profiles 7–12 from Figure 4.4. Numbering begins in the West and increases eastwards. Top panel is vertically exaggerated, panel below has no exaggeration. Short dashed lines show 95% error in linear regression fit.

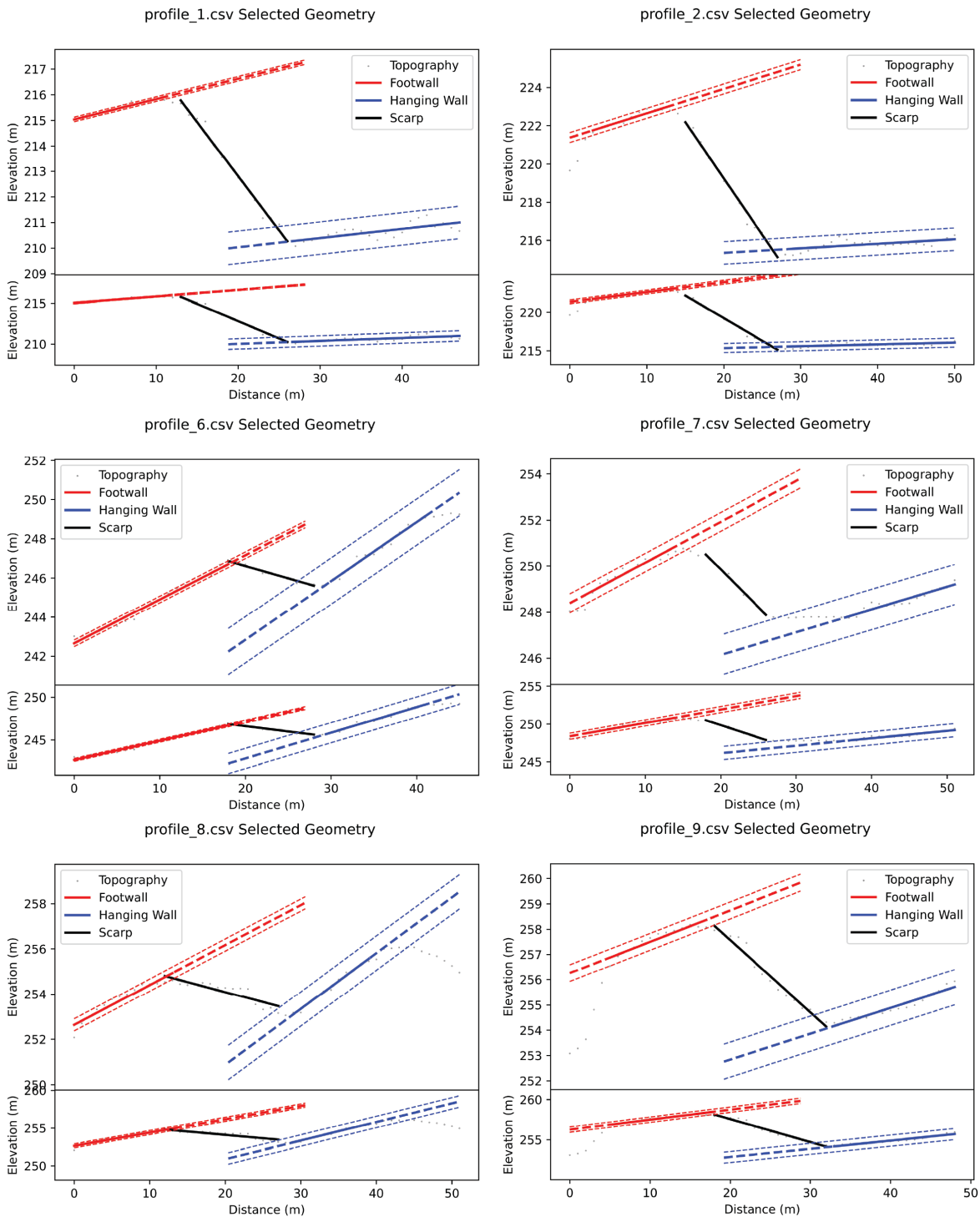

Figure C.15: Bedrock offset profiles 1–6 from Figure 4.4. Numbering begins in the West and increases eastwards. Top panel is vertically exaggerated, panel below has no exaggeration. Short dashed lines show 95% error in linear regression fit.

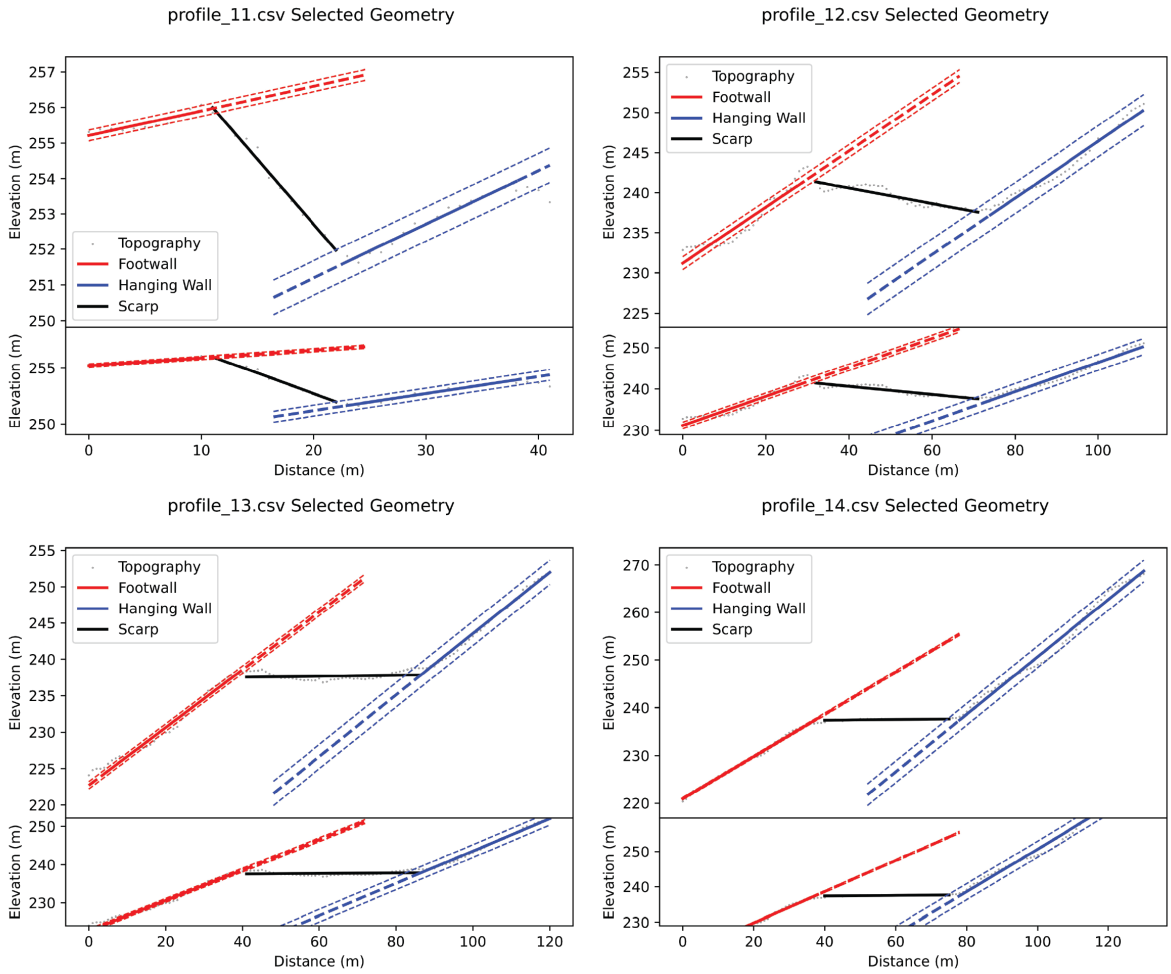

Figure C.16: Bedrock offset profiles 7–10 from Figure 4.4. Numbering begins in the West and increases eastwards. Top panel is vertically exaggerated, panel below has no exaggeration. Short dashed lines show 95% error in linear regression fit.

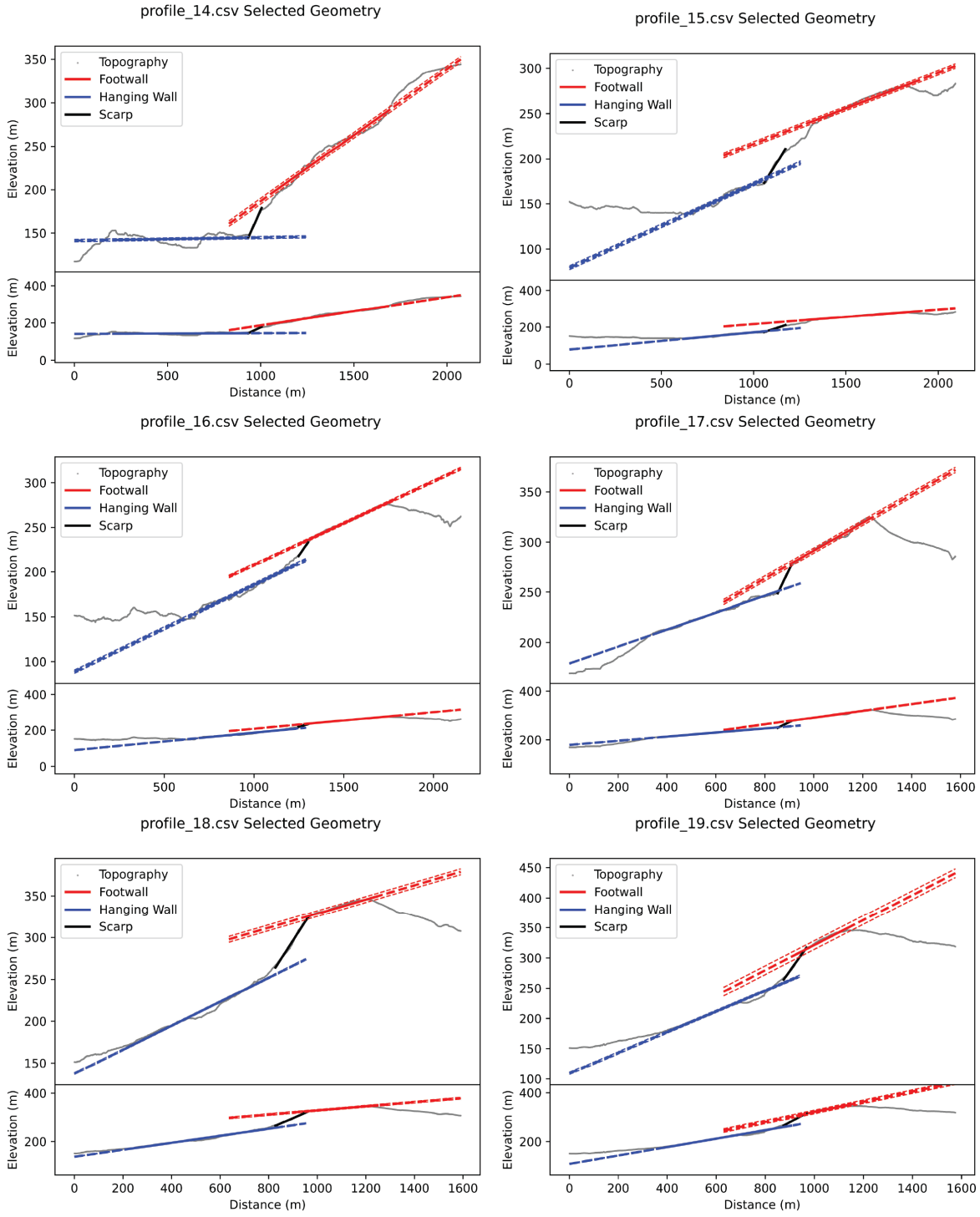

Figure C.17: Surface offset profiles 1–6 from Figure 4.4. Numbering begins in the West and increases eastwards. Top panel is vertically exaggerated, panel below has no exaggeration. Short dashed lines show 95% error in linear regression fit.

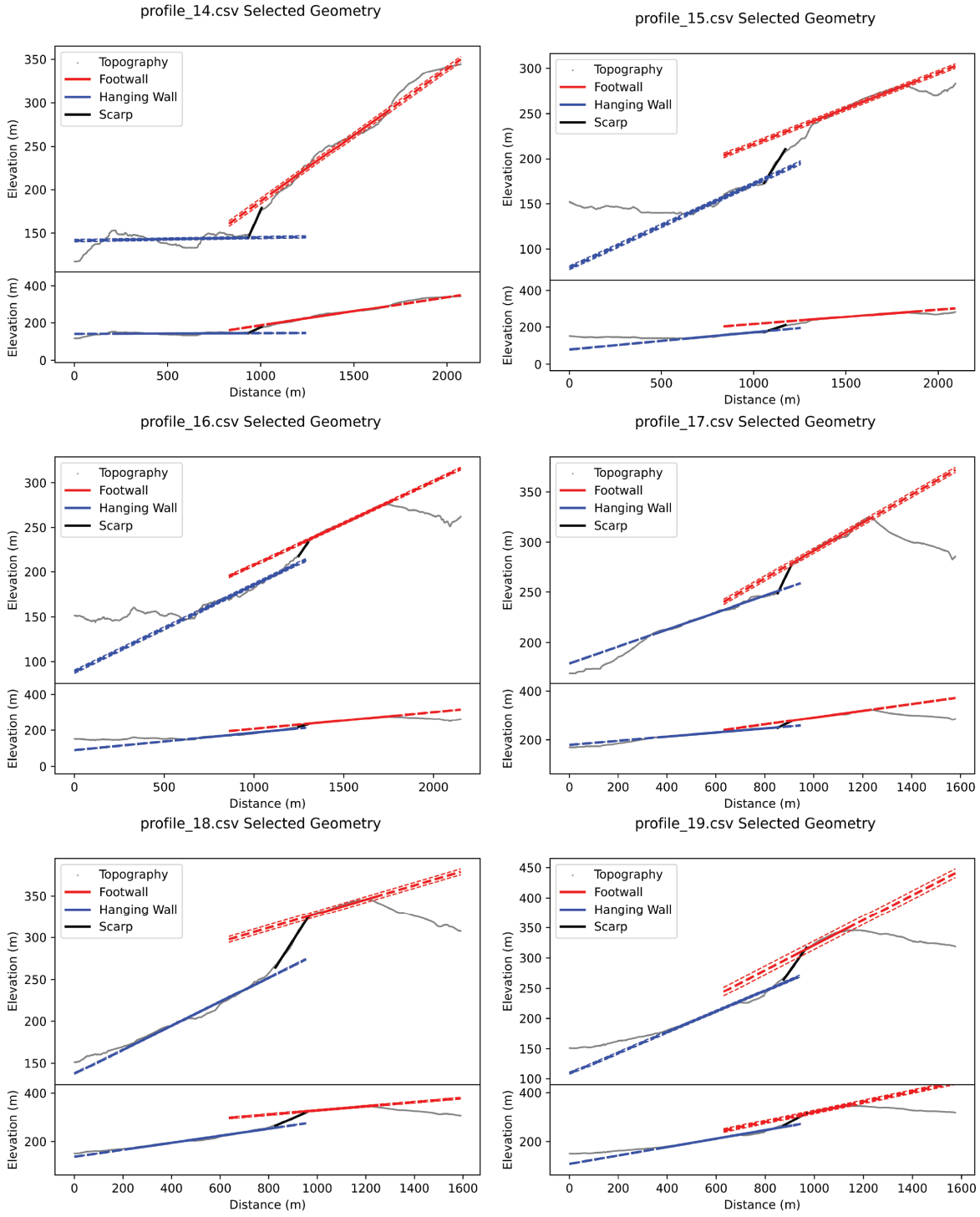

Figure C.18: Surface offset profiles 7–12 from Figure 4.4. Numbering begins in the West and increases eastwards. Top panel is vertically exaggerated, panel below has no exaggeration. Short dashed lines show 95% error in linear regression fit.

Figure C.19: Photographs from the Schmidt hammer data collection. a) Proceq N-type Schmidt hammer used for data collection. b) Sub-vertical fault shear zone located near the uphill facing scarp. c) Close-up of the serpentinized material. Some near-horizontal slickenlines present. d) Cleaning the surface for Schmidt hammer sampling. e) Taking a sample, most samples were collected from near vertical surfaces along roadsides.